

MMP-2 Sensitive Self-assembled Peptide Nanoscaffolds for Neural Tissue Engineering

by

Kyle Michael Koss

A thesis submitted in partial fulfillment of the requirements for the degree of

Doctor of Philosophy in

Chemical Engineering

Department of Chemical and Materials Engineering
University of Alberta

©Kyle Michael Koss, 2016

Abstract

Neurotrophic factor peptide analogues are capable of promoting healing by neurogenesis, enhancing neuronal survival and attenuating glial activation. In vivo peptide delivery is difficult due to susceptibility to proteases, but they are considered ideal therapeutics due to specificity, potency, and size (i.e. diffusion). Self-assembling peptide (RADA)₄ is a novel class of peptide that, upon injection, assembles into a 3D nanoscaffold, capable of storing water and molecules. Synthesizing peptide therapeutics onto this nanoscaffold may afford protection from proteases, whilst utilizing resident enzymes (i.e. Matrix Metalloproteinase 2 (MMP-2)) for localized, ‘on-demand’ release. In this thesis, we study the self-assembly of engineered peptides into enzymatically sensitive nanoscaffolds for proteolytic induced release kinetics, glial activity, and PC-12 neurite-outgrowth. Specifically, peptides with high ((RADA)₄-GG-GPQG+IASQ (CP1)) and low ((RADA)₄-GG-GPQG+PAGQ (CP2)) MMP-2 sensitivity were investigated ('+' = scissile bond). These peptides were shown to self-assemble, measured incrementally by morphology, over 24 hours and CP1 and CP2 favored bundles of nanofibers when compared to (RADA)₄ morphology. Fractal dimensions in these nanostructures were significant after 2 hours, suggesting diffusion limitations of fractal nanofibers. Methionine-Valine-Guanine (MVG; DP1), a brain-derived neurotrophic factor secretion stimulant, and Aspartic acid-Guanine-Guanine-Leucine (DGGL; DP2), a ciliary neurotrophic factor analogue, were tethered to CP1 and CP2, by automated peptide synthesis, and mixed with (RADA)₄-IKVAV as a means of promoting cell adherence. Nanoscaffold self-assembly, enzyme-induced release of DP1 and DP2, glial activation and resulting PC-12 acetylcholine-esterase signaling and neurite outgrowth were evaluated. Release kinetics were shown to be related to the high (CP1) and low (CP2) activity cut sites and by their concentrations. Peptide release could be controlled between 0 and 100%,

over 32 days, depending on nanoscaffold design. Nanoscaffold seeded microglia were visually ramified and MTT levels were found to be highest in pure (RADA)₄ nanoscaffolds; suggesting increased adhesion and survival. Ramified microglia, as well as negligible astrocyte scarring and axonal cell death were also observed upon an intra-cerebral injection into the brains of 2-day post-natal rat pups. MMP-2 released peptide-drugs promoted differentiation in PC-12 cells; observed neurite extension and increased acetylcholine esterase signaling for nanoscaffolds composed of 10% v/v (RADA)₄-IKVAV, 10% v/v (RADA)₄-CP1/CP2-MVG/DGGL, and 80% (RADA)₄. Finally, optimal seeding capacity was observed upon addition of 10% v/v (RADA)₄-IKVAV to the nanoscaffolds. (RADA)₄ nanoscaffolds were observed to self-assemble, exhibit microglia compatibility without affecting their response to lipopolysaccharide stimulation, and able to promote neural differentiation for PC-12 cells upon release of DP1 or DP2. Thus a biomimetic, fully synthetic self-assembling nanoscaffold has been demonstrated for a tuneable drug release system with good microglia and intra-cerebral biocompatibility capable of inducing neural differentiation by peptide cleavage.

Preface

All work was performed occurred at the University of Alberta under the principal supervision of Dr. L.D. Unsworth (LDU). As each chapter of this thesis was written in paper format and, due to the fact that some of these chapters have been published with other authors, each author's contribution to these works is outlined.

Chapter 1 – Self-Assembling Peptide-Based Materials for Intelligent Nanoscaffolds in Neural Tissue Engineering

Publication status: Accepted for Publication, Acta Biomaterialia

Both authors were involved in determining the scope of the review and discussing the work. Kyle Koss (KK) wrote entire first draft, incorporated revisions from LDU, wrote first draft of response to reviewer's critiques, and prepared documents for submission.

Chapter 2 - Towards Developing Bioresponsive, Self-Assembling Materials: Dynamic Morphology and Fractal Nature of Nanostructured Matrices

Publication status: To be submitted

Both authors were involved in determining the scope of the review. KK conducted experiments, collected and analyzed data, wrote entire first draft, incorporated revisions from LDU.

Chapter 3 - MMP-2 Cleavage of C-terminal Modified (RADA)₄ as a Platform for Peptide Delivery: Assembled Morphology and Cleavage Kinetics.

Publication status: To be submitted

KK and Christopher Tsui (CT) conducted experiments, collected and analyzed the data. CT wrote the first draft of the methods section and parts of the discussion, and KK conducted experiments, collected and analyzed data, wrote entire first draft, incorporated revisions from LDU.

Chapter 4 - Induced Neural Differentiation of MMP-2 Cleaved (RADA)₄ Drug Delivery Systems

Publication Status: Accepted with Revisions, Journal of Controlled Release

Cell culture and nanoscale/cell imaging was done by KK, assays and enzyme kinetics were conducted by both KK and CT. KK wrote entire first draft, with CT contributing to methods and result and discussion, incorporating revisions from LDU.

Chapter 5 - Brain Biocompatibility and Microglia Response Towards Engineered Self-Assembling (RADA)₄ Nanoscaffolds

Publication Status: Published, Acta Biomaterialia

The primary cell culture was performed by M.A. Churchward (MAC). Assays for this culture were shared with MAC and KK, imaging performed by KK. All animal work and related analysis was performed by A.T. Nguyen (ATN). KK was responsible for collating all components of writing from MAC and ATN, for forming first draft of manuscript. KK was responsible for incorporating all revisions requested from Drs. Todd, Yager, and LDU, as well as preparation for all manuscripts for submission and preparation of first drafts of the responses to all reviewer comments.

Dedication

This work is dedicated to my mother, late grandfather, and especially my father, who taught me EM and cell culture, but more than anything else, taught me to be a scientist. I would be nowhere without their unwavering support.

Acknowledgments

I would like to acknowledge Terry Sereda, Paul Semchuk, and Jack Moore for peptide synthesis assistance. Without you guys, none of this project would have started.

Thanks to Mike Xia and Nancy Zhang for their friendly help in their HPLC and Peptide Synthesis labs.

I want to give thanks to Arlene Oatway for the excellent electron microscopy support and George Braybrook for teaching me how to use the machines all those years ago.

I am eternally grateful to Emily Gruber, Theodore Ng, Zoe Collins, and Christopher Tsui; my assistants and closest comrades throughout it all. I love you guys.

I would like to gratefully thank Jerome Yager, Ed Armstrong Katherine Shen, and especially Antoinette Ngugen for all the wonderful collaboration and animal work.

I am deeply thankful to Kathyn Todd, Matthew Churchward, Kam Dhami, Sam Jerusadan, Erika Johnson, and Jocelyn Madeira for all help with cell culture and excellent collaboration.

My Sister, Mom, and Dad, for everything.

The Unsworth lab members: Mojtaba Binazadeh, Maryam Kabiri, Markian Bhaniuk, Aditi Saini, and Abdullah Alshememrey. You are my family away from my family.

All my friends at the CBS club. I'm happy to have played a small role in such a great group of people.

I am most thankful to my committee and my supervisor who carried through to the end.

I am grateful for financial support from NSERC, NINT-NRC, Women's and Children's Health Research Initiative (UofA) and Alberta-Gangwon Korea, AIHS, Alberta Health Services, the Davey Endowment for Brain Research, and WCHI grants.

Table of Contents

Abstract	ii
Preface	iv
Dedication	vi
Acknowledgements	vii
Table of Contents	viii
List of Tables	xiii
List of Figures	xiii
Introduction - Chapter 1 - Neural Tissue Engineering: Bioresponsive Nanoscaffolds using Engineered Self-Assembling Peptides	1
Abstract	2
1. Introduction	3
2. Self-Assembling Components for Nanoscaffolds	6
2.1. Ionic Self-Complimentary Peptides	11
2.2. Protein-Derived β -Sheet Peptides	13
2.3. α -Helical Peptides	13
2.4. Fmoc-PP Peptide	14
2.5. Multidomain Peptides	14
2.6. Co-Assembling Peptides	15
2.7. Peptide Amphiphile Hybrids	16
2.8. DNA-Peptide Composites	16
2.9. Lipid-Peptide Hybrids	17
3. Neural Bioactive Ligands	18
3.1. Neural Cell Adhesion Molecule (NCAM) Peptides	19
3.2. Tenascin-C (TN-C) Peptide	25

3.3.	Laminin-Based Peptides	25
3.4.	Fibronectin-Derived Peptides	27
3.5.	Other Peptide Derivatives	28
4.	Drug Candidates	29
4.1.	Neurotrophic Growth Factor Peptides	30
4.2.	Anti-inflammatory Peptides	35
5.	Release Cues for NanoscaffoldDrug Delivery	36
6.	Conclusion and Future Directions	38
7.	Acknowledgements	40
8.	References	41
Chapter 2 - Towards Developing Bioresponsive, Self-Assembling Materials: Dynamic Morphology and Fractal Nature of Nanostructured Matrices		64
	Abstract	65
1.	Introduction	66
2.	Materials and Methods	71
2.1.	Materials	71
2.2.	Peptide Synthesis	71
2.3.	MMP-2 Enzymatic Treatment	72
2.4.	Transmission Electron Microscopy	72
2.5.	Nanofiber Bundle and Hausdorff Dimension Analysis	73
3.	Results and Discussion	74
4.	Conclusions	91
5.	Acknowledgements	92
6.	References	93

Chapter 3 - MMP-2 Cleavage of C-terminal Modified (RADA)₄ as a Platform for Peptide Delivery: Assembled Morphology and Cleavage Kinetics	99
Abstract	100
1. Introduction	101
2. Materials and Methods	107
2.1. Materials	107
2.2. Peptide Synthesis	107
2.3. Transmission Electron Microscopy	108
2.4. MMP-2 Enzymatic Treatment	108
2.5. Hausdorff Dimension Analysis	110
3. Results and Discussion	112
3.1. Controls and Standard for Quantifying Mass Spectroscopy	112
3.2. Nanoscaffold Mass and MMP-2 Concentration Dependency	114
3.3. Morphology of MMP-2 Degraded Nanoscaffold	121
3.4. Time Series of MMP-2 Degraded Nanoscaffold	126
4. Conclusions	130
5. Acknowledgements	131
6. References	132
Chapter 4 - Induced Neuronal Differentiation of MMP-2 Cleaved (RADA)₄ Drug Delivery Systems	141
Abstract	142
1. Introduction	143
2. Materials and Methods	148
2.1. Materials	148
2.2. Peptide Synthesis	148

2.3.	Transmission Electron Microscopy	149
2.4.	<i>In vitro</i> Study	150
2.4.1.	PC-12 and Two-Dimension Cell Culture with SAP	150
2.4.2.	Live/Dead Viability	151
2.4.3.	Molecular Analyses	151
2.4.4.	Immunocytochemistry	152
2.4.5.	Statistical Analyses	153
2.5.	MMP-2 Enzymatic Treatment	153
3.	Results and Discussion	155
3.1.	Nanoscale Morphology and Cell Adhesion	155
3.2.	Enzymatic Product Formation	159
3.3.	PC-12 Neural Cell Response to MMP-2 Treatment	163
4.	Summary and Conclusion	170
5.	Acknowledgements	171
6.	References	171
Chapter 5 - Brain Biocompatibility and Microglia Response Towards Engineering Self-Assembling (RADA)₄ Nanoscaffolds		179
	Abstract	180
1.	Introduction	181
2.	Materials and Methods	185
2.1.	Materials	185
2.2.	Peptide Synthesis	185
2.3.	Transmission Electron Microscopy	186
2.4.	<i>In vitro</i> Study	186
2.4.1.	Primary Microglia Cell Culture and Treatments	186

2.4.2.	Two-Dimension Cell Culture with SAP	187
2.4.3.	Molecular Analyses	187
2.4.4.	Immunocytochemistry	188
2.4.5.	Cell Proliferation Assay	189
2.5.	<i>In vivo</i> Studies	189
2.5.1	Animals	189
2.5.2.	Intracerebral Injections	190
2.5.3.	Histology	190
2.6.	Statistical Analyses	191
3.	Results	191
3.1.	Nanoscale Morphology	191
3.2.	Primary Microglial Culture	193
3.3.	Animal Study	199
4.	Discussion	201
5.	Conclusions	204
6.	Acknowledgements	205
7.	References	206
	Chapter 6 - Summary and Outlook	213
	Sources Consulted	217
	Appendix A - Supplemental Figures	I
	Appendix B - MATLAB Code	IX
	Appendix C - Supplemental Methods	XIII

List of Tables

Table 1.1. Self-Assembling Materials for Neural Tissue Engineering

Table 1.2. Neural Bioactive Peptide Motifs

Table 1.3. Peptide Analogues for Neural Tissue Drug Delivery

List of Figures

Figure 2.1. Schematic of nanofiber formation and MMP-2 cleavage of (RADA)₄, (RADA)₄-GG-GPQG+IASQ (CP1), and (RADA)₄-GG-GPQG+PAGQ (CP2). '+' Denotes cleavage site and CP1, CP2, and CP products are IASQ, PAGQ, and (RADA)₄-GG-GPQG, respectively.

Figure 2.2. Transmission electron microscopy of (RADA)₄ (A), (RADA)₄-GG-GPQG+IASQ (CP1) (B), and (RADA)₄-GG-GPQG+PAGQ (CP2) (C). Low (i) and high (ii) magnification are shown to demonstrate fibers present in bundles. All samples were stained with 4% uranyl acetate and imaged at 0.5% w/v in TNC buffer upon 30 minutes of sonication and incubation at 37°C. Scale bars are all 100 nm.

Figure 2.3. Transmission electron microscopy of (RADA)₄ (A), (RADA)₄-GG-GPQG+IASQ (B), and (RADA)₄-GG-GPQG+PAGQ (C) at 0 (i), 1 (ii), 2 (iii), 4 (iv), 6 (v), and 24 hs (vi). All samples were stained with 4% uranyl acetate and imaged at 0.5% w/v in TNC buffer upon 30 minutes of sonication and incubation at 37°C. Scale bars are all 100 nm.

Figure 2.4. Transmission electron microscopy of 25%/75% (A), 50%/50% (B), and 75%/25% (C) (RADA)-GG-GPQG+IASQ / (RADA)₄ at 0 (i), 1 (ii), 2 (iii), 4 (iv), 6 (v), and 24 (vi) hs. All samples were stained with 4% uranyl acetate and imaged at 0.5% w/v in TNC buffer upon 30 minutes of sonication and incubation at 37°C. Scale bars are all 100 nm.

Figure 2.5. Transmission electron microscopy of 25%/75% (A), 50%/50% (B), and 75%/25% (C) (RADA)-GG-GPQG+PAGQ / (RADA)₄ at 0 (i), 1 (ii), 2 (iii), 4 (iv), 6 (v), and 24 (vi) hs. All samples were stained with 4% uranyl acetate and imaged at 0.5% w/v in TNC buffer upon 30 minutes of sonication and incubation at 37°C. Scale bars are all 100 nm.

Figure 2.6. Bundle thickness and fractal dimension analysis for (RADA)₄ systems. Bundle thickness (A) and Hausdorff box-count dimensions (B) of (RADA)₄-GG-GPQG+IASQ (i) and (RADA)₄-GG-GPQG+PAGQ (ii) mixtures with (RADA)₄. Example images of thickness measurement (C) and fractal contour tracing (D). Thickness image outlines the number of pixels across one bundle, which is used to calculate bundle width from scale bar. Mixtures include 100%, 75%, 50%, 25% (RADA)₄-GG-GPQG+IASQ/ (RADA)₄-GG-GPQG+PAGQ and 100% (RADA)₄-GG-GPQG+IASQ and (ii) (RADA)₄. By sample, 50 random thicknesses were chosen for three independent images (i.e. n=3). Data analyzed represents mean ± SD, where line is to guide the eye only.

Figure 2.7. Transmission electron microscopy of various magnifications (Ai-viii) and average Hausdorff box-count dimensions (B) over 10 incremental changes in magnification (1,400, 1,800, 22,000, 28,000, 36,000, 44,000, 56,000, 71,000, 89,000, and 110,000 x magnification). All samples were stained with 4% uranyl acetate and imaged at 0.5% w/v in TNC buffer upon 30 minutes of sonication and 24 hs of incubation at 37°C. Scale bars are all 100 nm, data analyzed represents mean ± SD, n=3.

Figure 2.8. MALDI TOF/TOF mass spectrometry of 0.5% w/v (RADA)₄-GG-GPQG+IASQ (Ai) and (RADA)₄-GG-GPQG+IASQ (Aii) proteolysis. Cleavage fragments are also shown (B). Incubated with 40 nM active MMP-2, in TNC buffer for three weeks at 37°C. Substrate peaks are labelled 2525.2 m/z and 2478.8 m/z, representing theoretical molecular weights of (RADA)₄-GG-GPQG+IASQ and (RADA)₄-GG-GPQG+IASQ, respectively. The peak 2125.1 m/z represents the molecular weight of the product for both substrates.

Figure 3.1. Schematic of self-assembled peptide hydrogel with incorporated cleavage motifs. Suggested MMP-2 digestion is shown. Theoretical peptides fragments and molecular weights are shown for both substrates and products for both cleavage peptides (CP1 and CP2).

Figure 3.2. MALDI TOF/TOF mass spectrometry of 0.5% w/v (A) (RADA)₄-GG-GPQG+IASQ ((RADA)₄-CP1) and (B) (RADA)₄-GG-GPQG+IASQ ((RADA)₄-CP2) proteolysis. Incubated with (i) 0 and 40 nM active MMP-2, in TNC buffer for three weeks at 37°C. Substrate peaks are labelled 2525.2 m/z and 2478.8 m/z, representing theoretical molecular weights of (RADA)₄-GG-CP1 and (RADA)₄-GG-CP2, respectively. The peak 2125.1 m/z represents the molecular weight of the product for both substrates. Also shown are product quantification with addition of the standard (RADA)₄-GG-GPQGD₈ to a (ii) 5 nM active MMP-2 3 day treatment. These are compared

to (iii) TNC buffer, (iv) 1 nM MMP-1, and (v) scrambled sequences (RADA)₄-GG-IQPGSAQG and (RADA)₄-GG-PQGAQGPQ. The standard peak, or average isotopic envelope is noted at 2132.1 m/z. (RADA)₄-CP2 and (RADA)₄-CP2 produced $31.6 \pm 0.3\%$ and $8.6 \pm 2.0\%$ in these conditions.

Figure 3.3. Product formation as a function of substrate (hydrogel) concentration from MMP-2 digestion of (RADA)₄-GG-GPQG+IASQ (CP1) calculated by area under the curve from MALDI TOF/TOF mass spectra of (A) raw product and (B) percent product of initial amount. Perspectives shown are (i) 2D and (ii) 3D. MMP-2 concentrations shown are 0.1, 0.5, 1.0, 5.0 nM. All reactions were performed in TNC buffer at 37°C for 32 days.

Figure 3.4. Product formation as a function of substrate (hydrogel) concentration from MMP-2 digestion of (RADA)₄-GG-GPQG+PAGQ (CP2) calculated by area under the curve from MALDI TOF/TOF mass spectra of (A) raw product and (B) percent product of initial amount. Perspectives shown are (i) 2D and (ii) 3D. MMP-2 concentrations shown are 0.1, 0.5, 1.0, 5.0 nM. All reactions were performed in TNC buffer at 37°C for 32 days.

Figure 3.5. Transmission electron microscopy of (RADA)₄-GG-GPQG+IASQ treated with (A) 0 and (B) 1 nM MMP-2, and (RADA)₄-GG-GPQG+PAGQ similarly treated with (C) 0 and (D) 1 nM MMP-2. Mixtures included (i) 0%/100%, (ii) 25%/75%, (iii) 50%/50%, and (iv) 75%/25% of (RADA)₄ / (RADA)₄-GG-GPQG+IASQ or (RADA)₄ / (RADA)₄-GG-GPQG+PAGQ. Fractal dimensions (E) as a function of (RADA)₄ addition, with and without MMP-2 treatment for (i) (RADA)₄-GG-GPQG+IASQ and (ii) (RADA)₄-GG-GPQG+PAGQ. Also, included is (F) (RADA)₄. All samples were 0.5% w/v, incubated at 37°C for 32 days, extracted, and stained with 4% uranyl acetate and imaged. Scale bars are all 100 nm.

Figure 3.6. Product formation as a function of time from MMP-2 digestion of (RADA)₄-GG-GPQG+IASQ calculated by area under the curve from MALDI TOF/TOF mass spectra of (A) raw product and (B) percent product of initial amount. Perspectives shown are (i) 2D and (ii) 3D. Mixtures included 0%/100%, 25%/75%, 50%/50%, and 75%/25% of (RADA)₄ / (RADA)₄-GG-GPQG+IASQ. All reactions were performed in TNC buffer at 37°C for 32 days.

Figure 3.7. Product formation as a function of time from MMP-2 digestion of (RADA)₄-GG-GPQG+PAGQ calculated by area under the curve from MALDI TOF/TOF mass spectra of (A) raw product and (B) percent product of initial amount. Perspectives shown are (i) 2D and (ii) 3D. Mixtures included 0%/100%, 25%/75%, 50%/50%, and

75%/25% of (RADA)₄ / (RADA)₄-GG-GPQG+PAGQ. All reactions were performed in TNC buffer at 37°C for 32 days.

Figure 4.1. PC-12 cells, seeded into a (RADA)₄ nanoscaffold, responding to bound and cleaved neurotrophic peptides without and with MMP-2 treatment, respectively. Cells are spherical when untreated and differentiate with outgrown neurites when treated with enzyme. Cells are adhering to IKVAV motifs. Full sequences for cleavage peptides (CP1 and CP2) and drug peptides (DP1 and DP2) are shown with (RADA)₄.

Figure 4.2. 1% w/v (A) transmission electron microscopy (TEM) (A), and phase contrast microscopy (B) of PC-12 cells seeded into 0% / 100% (i), 10% / 90% (ii), 25% / 70% (iii), 50% / 50% (iv), and 100% / 0% (v) mixtures of (RADA)₄-IKVAV / (RADA)₄. All TEM samples were stained with 4% uranyl acetate and imaged at 1% w/v in TNC buffer upon 30 minutes of sonication and 24 hours of incubation at 37°C. Cells were imaged after 3 days, while media was refreshed daily. Scale bars are 100 nm (A) and 50 μm (B). Measured MTT (C), cell counts (D), and percent live cells (E) for 10% increments of (RADA)₄ mixed with (RADA)₄-IKVAV. *n* = 3 for all groups (* *p* < 0.05) in a multi-way ANOVA. Data analyzed represents mean ± SD.

Figure 4.3. Enzymatic product formation of (RADA)₄-GG-GPQG+IASQ (CP1) (A) and (RADA)₄-GG-GPQG+PAGQ (CP2) (B). MALDI TOF/TOF mass spectrographic isotopic distribution (i) of product (2125.1 m/z) and standard (2132.1 m/z) from a 5 nM MMP-2 experiment. A 1 nM MMP-2 treatment with 2D (ii) and 3D (iii) calculated product formation from comparative area under isotopic distribution as a function of time, with 0%, 25%, 50% and 75% (RADA)₄ in (RADA)₄-CP1/CP2. All enzyme treatments were allowed to self-assemble for 24 hours in TNC buffer, post 30 minute sonication, and were incubated for 3 days at 37°C in TNC buffer, with 0.5 % w/v peptide. Scale bars are 100 nm. Transmission electron microscopy, 0% (iv), 25% (v), 50% (vi), and 75% (vii) mixtures of (RADA)₄ in (RADA)₄-CP1/CP2. Samples were stained with 4% uranyl acetate and imaged at 0.5% w/v in TNC buffer upon 30 minutes of sonication and 24 hours of incubation at 37°C. Scale bars are 100 nm. *n* = 3 for all groups. Data analyzed represents mean ± SD.

Figure 4.4. Phase contrast imaging of PC-12 cell neurite outgrowth. Cells were seeded into type IV Collagen treated with 100 nM CP1-DP1 (A), CP2-DP1 (B), CP1-DP2 (C), CP2-DP2 (D), where CP1/CP2 were projected cleaved peptide fragments IASQ/PAGQ, full DP1/DP2 sequences are MVG/DGGL, and scrambled sequences are GVM

/GLDG (i/ii). Also shown are 100ng/ml nerve growth factor (NGF (E)), a media control (F), and 1 nM MMP-2. Live images were taken at day 3. Scale bars are 25 μ m.

Figure 4.5. Acetylcholine esterase activity of PC-12 cells, measured over 3 days, seeded into 1% w/v (RADA)₄ nanoscaffolds with GPQG+IASQ (CP1) (A) and GPQG+PAGQ (CP2) (B), treated with 0 nM and 1 nM MMP-2. The embedded peptide neurotrophins were MVG (DP1) and DGGL (DP2). Fully the mixtures tested were 80% (RADA)₄, 10% (RADA)₄-IKVAV, and variations of 10% (RADA)₄-CP1-DP1, (RADA)₄-CP1-DP2, (RADA)₄-CP2-DP1, and (RADA)₄-CP2-DP2. Mixed DP groups were split 5% / 5% (RADA)₄-CP1-DP1 (mix 1) / (RADA)₄-CP1-DP2 and (RADA)₄-CP2-DP1 / (RADA)₄-CP2-DP2 (mix 2). $n = 3$ for all groups (* $p < 0.05$). Day 3 was compared to day 1 in a pairwise comparison. Data analyzed represents mean \pm SD.

Figure 4.6. Phase contrast imaging of PC-12 cell neurite outgrowth. Cells were seeded into 1% w/v (RADA)₄ nanoscaffolds with 0 nM (A) and 1 nM MMP-2 (B) treated GPQG+IASQ (CP1) and also 0 nM (C) and 1 nM (D) treated GPQG+PAGQ (CP2). The embedded peptide neurotrophins were MVG (DP1) (i), DGGL (DP2) (ii) and a 1:1 mixture of these (iii). Fully the mixtures tested were 80% (RADA)₄, 10% (RADA)₄-IKVAV, and variations of 10% (RADA)₄-CP1-DP1, (RADA)₄-CP1-DP2, (RADA)₄-CP2-DP1, and (RADA)₄-CP2-DP2. Mixed DP groups were split 5% / 5% (RADA)₄-CP1-DP1 (mix 1) / (RADA)₄-CP1-DP2 and (RADA)₄-CP2-DP1 / (RADA)₄-CP2-DP2 (mix 2). Confocal images (E) are labelled GAP43 (violet) (Ei) and beta(III) tubulin (green) (Eii), and nuclei were stained with Hoechst 33342 (blue) (Eiii). Also shown are phase contrast (Eiv) and fluorescent overlay (Ev). Images or fixations were taken at day 3. Scale bars are 50 μ m.

Figure 5.1. A potential host response is portrayed by active amoeboid microglia degrading and phagocytosing the material and astrocytes forming the dense interlinked networks of astrogliosis. Proposed biocompatibility of (RADA)₄ scaffold with inclusion laminin receptors and IKVAV peptides, where microglia are ramified and astrocytes are circular and non-fibrous.

Figure 5.2. Transmission electron microscopy of (A) 0% / 100%, (B) 10% / 90%, (C) 25% / 75%, (D) 50% / 50%, and (E) 100% / 0% mixtures of (RADA)₄-IKVAV / (RADA)₄. All samples were stained with 4% uranyl acetate and imaged at 1% w/v in TNC buffer upon 30 minutes of sonication and 24 hours of incubation at 37°C. Scale bars are all 100 nm.

Figure 5.3. Representative confocal immunofluorescence micrographs of microglia seed onto 1% w/v mixtures of (A) Poly-L Lysine, (B) 0% / 100%, (C) 10% / 90%, and (D) 25% / 75% mixtures of (RADA)₄-IKVAV / (RADA)₄. Labels include IBA1 (green), CD68 (red), and Hoescht. Scale bars are 25 μ m.

Figure 5.4. ELISA results for IL-1 β (A) and TNF- α (B) cytokine release of microglia culture. Analysis of nitrite release (C) and cell number from MTT assay (D). 1% w/v mixtures of 0:100, 10:90, 25:75(RADA)₄-IKVAV : (RADA)₄ were compared to the PLL control. Groups were exposed with 0 μ g/ml, 0.1 μ g/ml, and 1.0 μ g/ml LPS. All cytokine and nitrite groups were normalized with their respective MTT assay results. (-) represent PLL control. $n=4$ for all groups (* $p<0.05$, ** $p<0.1$). Data analyzed represents mean \pm SEM.

Figure 5.5. Proliferation analysis of primary microglia culture. Confocal immunofluorescent imaging visualizing proliferation of primary microglia activated with (A) 0 μ g/ml (con), (B) 0.1 μ g/ml, and (C) 1.0 μ g/ml LPS, and cultured on substrates (i) PLL, (ii) 0% / 100%, (iii) 10% / 90%, (iv) 25% / 75% (RADA)₄-IKVAV / (RADA)₄. EdU (orange) stained new DNA while morphology was labelled by IBA1 (green) and DAPI (blue). Scale bars are 50 μ m. Proliferation was imaged by epifluorescence and quantified (D) by counting EdU and DAPI labelled nuclei, in 12 sequential images per sample, where $n=4$ (* $p<0.05$). Mean cell counts (E) are also shown. (-) represent PLL control. Data analyzed represents mean \pm SEM.

Figure 5.6. Histology and immunohistochemistry of postnatal rat pup, 7 days post intracerebral injection. Areas of interest are located at 5x magnification, centered in the field of view, and analyzed at 40x. Injections of respective solutions occurred on P8 and brain tissue was analyzed one week post surgery. The first row represents CD68 (Ai-iv), a marker for active microglia. Exposure to treatments did not cause significant changes in microglia cell counts. The second row represents GFAP (Bi-iv), a marker for astrocytes. Treatments did not cause significant changes in GFAP immunodensity. Finally, the third row represents Fractin (Ci-iv), a marker for damaged axons. No positive cells were detected surrounding the injection site. Scale bars are 0.5 mm. Saline $n=2$, (RADA)₄ $n=4$, (RADA)₄-IKVAV $n=4$. Data analyzed represents mean \pm SEM.

Figure A2.1. Representative (i) HPLC (i) and (ii) MALDI TOF/TOF mass spectrometry (ii) of purified peptide (RADA)₄, (RADA)₄-GG-GPQG+IASQ, and (RADA)₄-GG-GPQG+PAGQ, shown in A, B, and C, respectively. Purities were determined to be above 95% by measuring the comparative areas under the major curve in the HPLC

spectra. Major peaks in the MALDI spectra are at 1671.8, 2525.2, and 2478.8 m/z which reflect the theoretical molecular weights. All peaks were normalized to their respective maxima.

Figure A2.2. Example of image processing for Hausdorff boxcount method. (A) Transmission electron microscopy, (B) gray scale and background filtering off image (MATLAB functions `im2bw` and `imfill`), various grid sizes used to count pixels ($D(r)$) based on radius or dimension (r) for points of the box-count line, and a linear plot from the log of the box count curve. The negative slope of the linear curve is the box-count dimension (D_H), this dimension being 1.8.

Figure A3.1. HPLC and MALDI TOF/TOF mass spectrometry, i and ii respectively, of purified peptide A) (RADA)₄, (B) (RADA)₄-GPQG+IASQ, (C) (RADA)₄-GPQG+PAGQ, (D) (RADA)₄-IQPGSAQG, (E) (RADA)₄-PQGAQQPG and (F) (RADA)₄-GPQG₈₊. Purities were determined to be above 95% by measuring the comparative areas under the major curve in the HPLC spectra. Respective major peaks in the MALDI spectra are at 1671.8, 2525.2, 2478.8, 2525.2, 2478.8, and 2132.1 m/z which reflect the theoretical molecular weights. All peaks were normalized to their respective maxima.

Figure A3.1. MALDI TOF/TOF mass spectrometry of worked example for enzyme product formation analysis. Raw spectra (A) of whole data set. Spectra of raw unfiltered data (B) in range of interest with product isotopic envelope (left) and standard envelope (right). Selected, filtered, and curve fitted spectra (C) where the area (trapezoidal rule) under the right envelope divided by the left equates to the product formed relative to the concentration of the standard.

Figure A4.1. HPLC and MALDI TOF/TOF mass spectrometry, i and ii respectively, of purified peptide (RADA)₄ (A), (RADA)₄-GPQG+IASQ (B), (RADA)₄-GPQG+PAGQ (C), and (RADA)₄-GPQG₈₊ (D) shown in A, B, and C, respectively. Purities were determined to be above 95% by measuring the comparative areas under the major curve in the HPLC spectra. Respective major peaks in the MALDI spectra are at 1671.8, 2525.2, 2478.8, and 2132.1 m/z which reflect the theoretical molecular weights. All peaks were normalized to their respective maxima.

Figure A4.2. HPLC and MALDI TOF/TOF mass spectrometry, i and ii respectively, of purified peptide (RADA)₄-IKVAV (A), (RADA)₄-GPQG+IASQ-MVG (B), (RADA)₄-GPQG+PAGQ-MVG (C), (RADA)₄-GPQG+IASQ-DGGL (D), and (RADA)₄-GPQG+PAGQ-DGGL (E). Purities were determined to be above 95% by measuring the

comparative areas under the major curve in the HPLC spectra. Respective major peaks in the MALDI spectra are at 2182.4, 2812.01, 2765.95, 2866.98, and 2820.91 m/z, which reflect the theoretical molecular weights. All peaks were normalized to their respective maxima.

Figure A5.1. HPLC and MALDI TOF/TOF mass spectrometry, i and ii respectively, of purified peptide (RADA)₄ and (RADA)₄-IKVAV, shown in A and B, respectively. Purities are above 95% and major peaks in the ms are at 1671.8 and 2182.4 m/z, which reflect the theoretical molecular weights. All peaks were normalized to their respective maxima.

Figure A5.2. Representative image for the histological analyses. The areas of interest were located under 5X (A) and (B) 10X magnification to ensure the location of the injection tract and site. The final image for analyses were taken at 40X magnification (C). The red boxes indicate the area that was magnified in the following sections. S = site of injection. Arrows refers to the injection tract. Scale bars are (A) 0.5 mm, (B) 0.25 mm, and (C) 50 μ m. Tract is immunolabelled by CD68.

Figure A5.3. Representative images for histological analyses. Areas of interest are located at 10X magnification and centered in the field of view (A). Positive cells are counted at 40X magnification in 4 areas surrounding the injection site. The areas are dorsal (B), lateral (C), medial (D), and ventral (E) to the injection site. Red boxes indicate positions where images were taken at 40X for counting. S = site of injection, D = dorsal, L = lateral, M = medial, V = ventral. Arrow represents the injection tract. Scale bars are (A) 0.25 mm and (B-E) 50 μ m. Tract is immunolabeled by CD68.

Chapter 1.

Neural Tissue Engineering: Bioresponsive Nanoscaffolds using Engineered Self-Assembling Peptides

Koss, KM^{a,b}; Unsworth, LD^{a,b,*}

a. Department of Chemical and Materials Engineering, University of Alberta, 9211 - 116 Street NW Edmonton, AB T6G 1H9
b. National Institute for Nanotechnology, 11421 Saskatchewan Dr NW, Edmonton, AB, T6G 2M9

*. To whom correspondence should be addressed lunswort@ualberta.ca

Keywords:

neural tissue engineering, nanoscaffold, drug delivery, engineered peptides, self-assembly

Abstract

Rescuing or repairing neural tissues is of utmost importance to the patient's quality of life after an injury. To remedy this, many novel biomaterials are being developed that are, ideally, noninvasive and directly facilitate neural wound healing. As such, this review surveys the recent approaches and applications of self-assembling peptides, and peptide amphiphiles, for building multi-faceted nanoscaffolds for direct application to neural injury. Specifically, methods enabling cellular interactions with the nanoscaffold and controlling the release of bioactive molecules from the nanoscaffold for the express purpose of directing endogenous cells in damaged or diseased neural tissues is presented. An extensive overview of recently derived self-assembling peptide-based materials and their use as neural nanoscaffolds is presented. In addition, an overview of potential bioactive peptides and ligands that could be used to direct behaviour of endogenous cells are categorized with their biological effects. Finally, a number of neurotrophic and anti-inflammatory peptides are described and discussed. Smaller therapeutic molecules are emphasized, as they are thought to be able to have less potential effect on the overall peptide self-assembly mechanism. Options for potential nanoscaffolds and drug delivery systems are suggested.

1. Introduction

The human nervous system comprises a grid of complicated dynamic neuronal networks that constantly use physicochemical signalling to send and receive 'information'. Upon injury, there is inherent capacity for wound healing, usually through attempting to direct outgrowth of neurons with reformed synapses and supporting glial cells. However, this process is very slow, and often attenuated by scar tissue replacing active nervous elements. Therefore, this healing process is generally inadequate in restoring structure and function to pre-injury levels. As such, damage to any component of this network may result in permanently affected sensory and motor function, neuropathic pain, as well as an inhibition of cognitive and memory processes, with a limited potential for repair. Medical treatment varies and challenges arise according to the position and type of injury alongwith the local anatomy.

In the peripheral nervous system (PNS), ie., the nerves and ganglia outside the brain and spinal cord, severed neurons are reconnected surgically. If the patient is lucky, the nerve is simply sutured back together. In contrast, surgery usually progresses *via* an autograph procedure, which reconnects nerves 'end to end'. This is the standard for repair; however this procedure requires a donor graft that can only be taken from a limited number of sites that usually results in a loss of site-based nerve function. Alternatively, allografts and xenografts can be used, but immunogenic rejection is a major concern [1].

In spinal and brain tissues of the central nervous system (CNS) tissue, healing requires support from a host of cell types such as microglia, astrocytes, and myelinating cells. In the event of a spinal cord injury, myelinating cells rapidly die and generally will not recover, reactive microglia and astrocytes secrete pro-inflammatory cytokines that may induce the death of surrounding healthy cells and result in the formation of an acellular void in the tissue

encapsulated by reactive astrocytes and a glycosaminoglycan-based scar tissue. This scar tissue largely prevents neurite growth and axonal extension into the injured area [2]. To date, there are no fully successful medical treatments for these types of injury. Regardless of the cause of brain injury (i.e. stroke, concussion, trauma) the patient outcome may be extremely complicated due to the presence of multi-functional, interlaced neural networks that are found in several anatomical regions and composed of a myriad of differing cell types. Brain inflammation-related injury is usually similar to the spinal CNS, but astrogliosis can also be diffuse or cystic, often initiated by severe inflammation [3]. Furthermore, brain tissue does not have the innate regenerative capacity of other tissues due to the immune response being primarily regulated by a single cell type, namely, microglia. In addition, neurons and white matter oligodendrocytes can be arranged in extremely complicated manners that are not well understood and can depend on regional anatomy. Unfortunately, this is further complicated by the type of injury or disease, be it stroke, trauma or a series of neurodegenerative disorders (i.e., Alzheimer's, Parkinson's, Huntington's disease). Any artificial materials used to support healing, should be as minimally invasive as possible, be degradable, and promote cell viability and infiltration. In order to access brain tissue, these materials have to be capable of passing through or going around the blood brain barrier (BBB); treatments using the circulatory system are limited as the BBB filters out many exogenous particles or molecules. As a result, the brain-injury system has to be defined before an appropriate tissue engineering strategy is chosen. It is not surprising that no successful regenerative therapies have been established to treat brain related injury.

Despite many emerging neural scaffolds, many of these biomaterials have limited success in beneficially changing and fully integrating surrounding tissues as full treatments. To address these shortcomings, drug therapy has been proposed using a combination of substances such as

neurotrophic growth factors (NTFs) to direct healthy regeneration, and anti-inflammatory agents to attenuate the deleterious effects of inflammation. However, some of these substances suffer from poor pharmacokinetic qualities, low solubility, potentially harmful activity in non-target cells and tissues, and cannot be passed through the BBB [4]. Multifunctional nanoscaffolds, comprised of integrated bioactive ligands and drug therapeutics, are thought to have potential in promoting neural regeneration. Nanoscaffolds, designed to function as an engineered mimic of the extra-cellular matrix (ECM), may be populated by neurons. Therefore these ECM-like scaffolds act as a medium to direct growth and axonal connection, promoting cell adhesion, division, outgrowth, migration, neurogenesis, and synaptogenesis [7]. They can also be used to support survival of myelinating Schwann cells and oligodendrocytes, prevent inflammation response from leukocytes and microglia, and reduce scar forming astrocytes. A myriad of natural and synthetic polymers [5-7] have been explored for use as engineered mimics of the ECM and have been used to guide nerve conduits, induce peripheral nerve regeneration, mitigate spinal cord injury, attenuate neuro-inflammation, and degradation based release to induce neurite extension and scaffold infiltration [8 - 16]. Unfortunately these polymer-based nanoscaffolds may suffer from: 1) toxic co-solvent media, and 2) addition of ligands and drugs may be imprecise and require multi-stage synthesis.

Over the past 15 years, peptide based self-assembling (SA) systems have emerged in the realm of neural tissue engineering, capable of emulating ECM properties and providing a platform for drug delivery. They are designed to self-assemble in aqueous conditions, their nanostructures often enhanced by physiological salts. Their fabrication is simple and systematic, and can be made with high purities by commercially available automated synthesis [17 - 19]. Due to similar biophysical self-assembly, bioactive ligands and drug release systems can be

mixed and matched for an exact and programmed cell or tissue response. One major, but seldom tested, advantage of SA systems is their capacity to disperse freely in the body as individual molecules and potentially aggregate and assemble at sites of interest due to incorporation of targeting moieties. With appropriate design, these molecules may be able to circumvent the BBB and accumulate as nanoscaffolds in crucially damaged brain sites [20 - 21]. For example, targeting and altering transport receptors to enhance transfer of substances across the BBB offers a noninvasive delivery of specific molecules into the brain. With these benefits in mind, this article serves as a review for peptide SA molecules used in neural tissue engineering applications, peptide ligands and drugs used as neural biochemical cues, and potential drug release systems in pro-inflammatory neural cells and tissues.

2. Self-Assembling Components for Nanoscaffolds

Several SA peptides have been defined over the past decade. Excellent reviews of their makeup and use in other tissue engineering applications are available [22 - 25]. Many new SA materials and neural tissue studies have emerged, which are summarized in Table 1.

Table 1.1. Self-Assembling Materials for Neural Tissue Engineering

Class	Sequence / Abbreviation	Cells / Tissue	Outcome	Citation
Ionic self-complimentary	Ac-RADARADARADARADA-NH ₂ (RAD16-1)	PC-12 cells, mouse and rat cerebellar granule and hippocampal neurons	Neurite outgrowth, synaptic formation, and <i>in vivo</i> cytotoxicity	[27]
		Rat hippocampal tissue slice (<i>ex vivo</i>)	Migration and proliferation	[33]
		Mouse NSCs	Cell adhesion and differentiation	[98]
		Hamster dorsal midbrain and retinal tract	Brain gap closure and repair, axonal regeneration in lesion, and functional vision return	[37]
		Rat Schwann cells, NPCs, and spinal tissue	Axonal integration of 3D scaffold implant in spinal lesion	[38]
		Rat cortical tissue	Tissue integration and gliosis reduction of lesion	[39]
		PC-12 cells	Neurite outgrowth	[28]
		Mouse NSCs	Proliferation, differentiation, and migration	[99]
		Mouse NSCs	Differentiation	[29]
		Rat spinal tissue	Infiltration, basement membrane deposition, and axon regeneration in spinal injury	[34]
	Rat spinal tissue	Guided regeneration of chronic spinal injury	[35]	

		Mouse NSCs	3D neural differentiation	[30]
		Mouse NSCs	Neural and glial differentiation	[31]
		Rat NSCs and rat cortical tissue	Tissue integration and reduced gliosis of lesion	[40]
		Rat NSCs and rat hippocampal tissue	Tissue integration and restored synaptic function for Alzheimer's model	[41]
		N2a cells, human EnSC and rat spinal tissue	Neural differentiation of EnSC and myelination and axonal regeneration in chronic spinal cord injury	[36]
		Microglia, rat cortical tissue	Microglia activation and brain biocompatibility	[32]
Protein-derived β-sheet	Biotin-GGG-AFASTKT-CONH ₂	Human NSCs and spinal cord tissue	Viability and biocompatibility	[43]
	Biotin-GGG-AFASAKA-CONH ₂	Murine NSCs	Viability	[44]
α-helical	hSAF _{AAA}	PC-12 Cells	Neural differentiation	[45]
		Murine EnSCs	Adhesion, migration, proliferation, and differentiation	[46]
Fmoc-FF	Fmoc-FF	Primary rat microglia	Proliferation and NGF secretion	[48]
Multidomain	Ac-E ₂ -(SL) ₆ -E ₂ -NH ₂	Human EmSCs	Secretome delivery	[53]

	Ac-K ₂ -(QL) ₆ -K ₂ -NH ₂	Mouse NPCs and rat spinal tissue	Spinal cord injury recovery and glial scarring and inflammation attenuation	[54]
		Mouse neural stem and progenitor cells in rat spinal tissue	Cervical spinal cord injury recovery	[55]
Co-assembling	Ac-LDLKLDLKLKLDL-NH ₂ (LDLK12)	Murine and human stem cells, and rat spinal tissue	Proliferation neural differentiation and spinal tissue regrowth and locomotor recovery	[56]
	Ac-LDLKLDLKLKLDL-NH ₂ (LDLK12)	Murine stem cells	Neural differentiation	[57]
	Ac-LKLKLLKLLKLLK-NH ₂ (LKLK12) / Ac-LDLDLLDLDDL-NH ₂ (LDLD12)	Human stem cells, murine stem cells, mouse NPCs, and rat spinal cord transection	Spinal cord regeneration	[58]
Peptide amphiphile hybrid	C ₁₆ -A ₄ G ₃ IKVAV	Murine NPCs and rat spinal tissue	Neural differentiation and assembly	[62]
		Mouse spinal tissue	Axon elongation and glial scar attenuation	[63]
DNA-peptide composite	C ₁₆ -V ₂ A ₃ E ₂ -NH ₂	Rat penis nervous tissue	Regenerate cavernous nerve	[64]
	M13phage-RGD complex	Rat hippocampal progenitor cells	Adhesion, differentiation, and alignment	[65]
	DNA-RGDS complex	Mouse NSCs	Adhesion and differentiation	[66]
Lipid-peptide hybrid	CSRARKQAASIKVAVSAD	Rat NPCs	Cell attachment and clustering	[68]
	R-EG ₂ -POPE / POPC layer			
	Bsp-RGD layer	Rat NSCs	Cell attachment and spherical clustering	[69]

DOPE / DOPG / DOTAP / GdDOTA(GAC ₁₂) ₂ complexes	N2a cells and rat corpus callosum and striatum tissue	Gene delivery enhancement	[70]
DOPE / DOTMA / DOPG / DPPE / DOPE-PEG2000 / K ₁₆ GACYGLPHKFCG / K ₁₆ RVRRGACRGDCLG complexes	N2a cells, rat striatum	SiRNA delivery enhancement	[71]

Abbreviations: Amino Acids: Alanine (A), Arginine (R), Asparagine (N), Aspartic acid (D), Cystein (C), Glutamine (Q), Glutamic Acid (E), Glycine (G), Histidine (H), Isoleucine (I), Leucine (L), Lysine (K), Methionine (M), Phenylalanine (F), Proline (P), Serine (S), Threonine, Tryptophan (W), Tyrosine (Y), Valine (V). Acyl (Ac), Bone Sialoprotein (Bsp), Pheochromocytoma12 (PC-12), Neural Stem Cell (NSC), Neural Progenitor Cell (NPC), Neuroblastoma2a (N2a), Fluorenylmethyloxycarbonyl (Fmoc), Nerve growth Factor (NGF), Embryonic Stem Cell (EnSC), Dorsal Root Ganglia (DRG), 1-Palmitoyl-2-oleoyl-sn-glycero-3-phosphoethanolamine (POPE), 1-Palmitoyl-2-oleoyl-sn-glycero-3-phosphocholine (POPC), 1,2-Dioleoyl-sn-glycero-3-phosphoethanolamine (DOPE), 1,2-di-(9Z-octadecenoyl)-sn-glycero-3-phospho-(1'-rac-glycerol) (DOPG), N-[1-(2,3-Dioleoyloxy)propyl]-N,N,N-trimethylammonium methyl-sulfate (DOTAP), Gadolinium-bound 1,4,7,10-tetraazacyclododecane-1,4,7,10-tetraacetic acid (GdDOTA), 1,2-di-O-octadecenyl-3-trimethylammonium propane (DOTMA), 1,2-dipalmitoyl-sn-glycero-3-phosphoethanolamine (DPPE), Polyethylene Glycol (PEG)

2.1. Ionic Self-Complimentary Peptides

Ionic self-complimentary peptides form ~10 nm thick nanofiber networks as a result of both hydrophobic and electrostatic interactions in physiological conditions [27]. Sequences include RADA16-I (RADARADARADARADA), RADA16-II (RARADADARARADADA), and EAK16-II (EAEAKAKAEAEAKAK). These were first used by Holmes and colleagues to observe cell attachment, neurite outgrowth, synaptic communication of rat adrenal pheochromomcytoma (PC-12) cells, and the formation of active synapses without deleterious inflammation in primary hippocampal and cerebellar neurons [27]. RADA16-I was chosen for future use in many projects due to its similarity to fibronectin, laminin, and collagen in that it has a similar sequence (RGD *vs.* RAD) that facilitates cell adhesion. A wide variety of cell adhesion peptides were assayed in a micro 3D environment composed of RADA16-I and the effect they had on the extent of neural stem cell (NSC) differentiation shown [98]. Neuritogenesis was studied with 2D and 3D PC-12 cell culture, by Li and Chau, using a laminin derived peptide to prime the cells for neural differentiation [28]. They found that IKAV did not induce differentiation, but enhanced it with the treatment nerve growth factors. In another study, cell adhesion, and neural differentiation of NSCs was demonstrated with a bone marrow homing peptide (BMHP) and varied glycine spacing [29]. 3D differentiation of mouse NSCs was studied in this matrix and enhanced viability, proliferation, and differentiation due to incorporated BMHP was observed [30]. Several bioactive peptide mixtures in RADA16-I were compared to Matrigel and Collagen I in 3D culture of stem cells, where it was shown that this system yielded comparable or improved long-term cell viability as well as favourable neural and glial differentiation [31]. In addition, neural biocompatibility was assessed for RADA16-I cultured

with primary microglia and injected intracerebrally in rat brains, where it was determined that no adverse effects were induced by the scaffold [32].

RADA16-I nanoscaffolds were placed upon a slice of hippocampal tissue and showed that neural progenitor cells (NPCs) and astrocytes fully migrated, and began proliferating in the adjoining nanoscaffold [33]. Many studies were performed to assess repair of lesions in acutely and chronically injured spinal tissues. In one case, a BMHP with varied glycine (G) spacing was used to repair a lesion, with the result being an observable recovery in locomotion [34]. In another situation, RADA16-I nanoscaffolds were used with an electrospun lamina to successfully guide regrowth for a 6 month chronic spinal injury [35]. BMHP was also studied in RADA16-I, *in vivo*, by Tavakol *et al.*, where neural differentiation of human endometrial stem cells, and the recovery of chronically injured spinal tissue was investigated [36]. Restoration of spinal and brain tissues were observed *in vivo* by several groups. Ellis-Behnke used RADA16-I to regenerate hamster midbrain tissue and a retinal tract [37], where functional vision was noted 30 and 45 days post-surgery. Guo, *et al.*, first observed spinal repair by transplanting Schwann cells and NPCs into the dorsal column of rats [38]. Axonal and arterial migration and integration into the nanoscaffold was reported. They also performed a study to assess the nanoscaffold assisted repair of a generated brain lesion [39]. It was shown that the nanoscale matrix assembled into the injury site, allowed reconstruction, and reduced inflammation and glia scarring. Stem cell transplants for brain tissues have been performed by two research groups. Cheng *et al.* noted neural cell differentiation and reduction in astrogliosis for a lesion transplant [40]. Synaptic function and learning/memory function was restored by Cui and colleagues in a Alzheimer's disease model [41].

2.2. Protein-Derived β -Sheet Peptides

A small number of SA peptides have been identified from existing β -sheet sources in full proteins. The Gelain lab discovered and evaluated several sequences derived from BMHP with the potential for bioactivity in neural systems [42]. From these, the Biotin-GGG-AFASTKT-CONH₂ sequence was considered a promising candidate, capable of forming nanofibers in cultured human stem cells and displayed general biocompatibility in spinal tissue [43]. Silva later cultured murine stem cells in another series of similar peptides, where biotin-GGG-AFASAKA-CONH₂ was determined to have favourable viability, nanofiber morphology, and physiologically comparable shear stress [44]. This particular sequence promoted adhesion and proliferation of the stem cells.

2.3. α -Helical Peptides

The Woolfson group discovered coiled SA sequences, known to form from two supercoiled α -helices. Banwell *et al.* describe two 28 amino acid peptides that co-assemble into an α -helical dimer with complimentary sticky ends that allow for longitudinal supercoiled nanofibers to form [45]. These networks are also called hydrogelating self-assembled fibers (hSAF_{XXX}) with *abcdefg* heptad repeats, where *a*, *d*, *e*, and *g* amino acids direct dimer interface, and the _{XXX} subscript is denoted by *b*, *c*, and *f*, which are the exposed residues of the coiled-coil structures. This group observed promising neural differentiation in a hSAF_{AAA} network, where PC-12 cells were seeded into mature nanofibers and, upon treatment with nerve growth factors, both growth and full differentiation occurred. Mehrban *et al.*, evaluated NSC culture with modified hSAF_{AAA} and showed full migration, differentiation of neurons and astrocytes, and voltage conductance was noted with enhancement due to RGD decoration, which increased the proliferative activity and maturity (differentiation) of NSCs [46].

2.4. *Fmoc-PP Peptide*

Reches and Gazit observed that a SA molecule composed of two F amino acids with a 9-fluorenylmethoxycarbonyl (Fmoc), typically used for N-terminus protection in solid phase synthesis [47], formed amyloid type fibril nanostructures when diluted from a hexafluoroisopropanol solution. Chronopoulou *et al.* seeded primary rat microglia in this nanoscaffold to assess biocompatibility and discovered ramified microglia that proliferated extensively and secreted nerve growth factor (NGF), which may have neurotrophic effects on endogenous cells [48].

2.5. *Multidomain Peptides*

Multidomain peptides (MDP) of 16 amino acids in length are composed of ABA blocks with an A block of either double K or E charged residues and an inner B block with three to six repeating QL, QF, or SL groups [49 - 51]. Briefly, the structures look like Ac-A-B-A-NH₂. Upon incubation in aqueous solutions, these constructs formed ~6 nm thick β -sheet-rich nanofibers that could be further cross-linked with lysyl oxidase [52]. As lysyl oxidase is a component of some culture media, nanoscaffold stiffness could potentially increase with cell culture time. The peptide, Ac-E₂-(SL)₆-E₂-NH₂, was the first MDP applied to tissue engineering, whereby a growth factor-rich solution was absorbed from an adjacent embryonic stem cell (ESC) culture and this secretome rich gel was tested *in vivo* to assess delivery and the fate of the nanoscaffold [53]. With Gd³⁺ magnetic resonant image contrast labels they were able to demonstrate localization with delivery over 24 hours. Although this system was not delivered to neural tissues, Ac-K₂-(QL)₆-K₂-NH₂ (QL6) was used for spinal injury recovery where mouse NPCs were cultured in the QL6 matrix and injected into an aneurysm clip compression-contusion spinal injury [54]. It was found, over 8 weeks, that the scaffold degraded, astrogliosis was

attenuated, and microglia activity and post-traumatic apoptosis were favourably demonstrated along with spinal tissue preservation. Iwasaki demonstrated forelimb functional recovery due to QL6 interaction with spinal injury repair [55]. NPCs were seeded into the QL6 nanoscaffold and this system was transplanted into the cervical enlargement in the spine. NPC fate was characterized by cellular differentiation and migration. A tremendous reduction in glia scarring and increased spinal preservation was noted. Several tests for motor recovery were performed and a fair (25%) recovery of motor function was noted.

2.6. Co-Assembling Peptides

Using intermolecular interactions of ionic self-complimentary peptides, the Gelain laboratory determined co-assembling peptides (CAPs) can form analogous 10-12 nm thick nanofibers and nanoscaffolds from double layer β -sheets. Specifically, by using hydrophobic leucine (L), positively charged lysine (K), and negatively charged aspartic acid (D), three peptides have been identified: Ac-LDLKLDLKLKLDLK-NH₂ (LDLK12), Ac-LKLKLLKLKLLK-NH₂ (LKLK12), and Ac-LDLDLDLDLDL-NH₂ (LDLD12). Novel biopanned differentiation promoting peptides, incorporated with LDLK12, influenced neural differentiation of human and murine NSCs, and promoted recovery in a spinal lesion and locomotor function [56]. Murine NSCs have also been seeded into assembled LDLK12 to assess its potential as a neural scaffold [57]. It was found that differentiation occurred in all cases, and that oligodendrocytes were comparable in all conditions. However, as the nanoscaffold stiffness increased, the subpopulation of astrocytes increased and neurons decreased. Co-assembly of LKLK12/LDLD12 in polycaprolactone (PCA) / polylactic-co-glycolic acid (PLGA) microtubes were used to assess viability and differentiation

into neurons, astrocytes, and oligodendrocytes (from human NSCs) and when combined with these microtubes were shown to guide axonal and synaptic development [58].

2.7. Peptide Amphiphile Hybrids

Many peptide hybrid SA nanoscaffolds have been investigated in the past decade. Peptide amphiphiles (PAs) were developed largely in the Stupp group and have showed promise for neural tissue engineering applications. With a general structure that incorporated a peptide head with a 16 carbon alkyl tail, peptide amphiphiles usually contained glutamic acid (E) to balance charge in cell culture media and hydrophobic residues, typically alanine (A) or valine (V). The hydrophobic residues and alkyl chain are thought to facilitate the assembly into β -sheets and 7 nm thick nanofibers due to unfavourable contact of non-polar hydrophobic segments with water. This forces any added bioactive motifs outwards to encourage aqueous and potential cell interaction. Assembly is triggered with reduced electrostatic repulsion, which can be the result of ion balancing solution or culture media washing, mixing with complimentary charged amphiphiles, or pH balancing [60 - 61]. Silva *et al.* was able to rapidly and favourable differentiate NPCs into neurons using this type of nanoscaffold (C_{16} -A₄G₃IKVAV), with fewer astrocytes present and acceptable neuron viability and migration [62]. Further work used this same nanoscaffold to treat spinal cord injury assessing biodegradation, astrogliotic and apoptotic reduction, descending cortical motor and ascending dorsal sensory axons regrowth, and long-term functional motor recovery [63]. A similar peptide amphiphile, (C_{16})-V₂A₂E₂-(NH₂), was used to regenerate a cavernous nerve using the Sonic hedgehog (SHH) pathway, demonstrating increased SHH protein accumulation and assistance in a penal cavernous peripheral nerve and Schwann myelin recovery [64].

2.8. DNA-Peptide Composites

Double stranded DNA (dsDNA) possesses inherent intermolecular properties favourable to self-assembly. As a result, a few research groups have experimented by combining DNA with bioactive peptides for novel SA nanostructures. A nanofibrous liquid crystal film was fabricated from M13 phage viruses, which are typically used to study protein-protein interactions by 'displaying' variable peptide motifs [65]. This film, enhanced by the bioactive peptides being displayed promoted rat NPC differentiation. Cell adhesion and alignment of NPCs was noteworthy, although neural differentiation was not thoroughly examined. Another study looked at a five strand DNA segment covalently bonded to RGDS, which assembled into a 'double-crossover tile' structure that resulted in the formation of a continuous nanotube in 14 by 4 nm segments [66]. Mouse NSC differentiation was studied in this system and neurons preferentially differentiated over astrocytes.

2.9. Lipid-Peptide Hybrids

Lipids self-assemble in aqueous environments to form structures like cell membranes in the form of lipid bilayers. Lipid-based drug delivery vehicles, like liposomes, have been thoroughly reviewed elsewhere [67]. Peptide modification of lipids have been conducted to both alter their assembly properties and alter their bioactivity. A laminin derived peptide-lipid was used to form a surface coating bilayer that housed NPCs, where cell adhesion was observed, without differentiation, and uncharacteristic cell clusters were found over full laminin substrates [68]. A similar bilayer coating system was later developed using a Bsp-RGD lipid-peptide (Fmoc-GGGNGEPRGDTYRAY-NH₂) hybrid [69]. In this study, rat NSC were again shown to spherically cluster (a configuration atypical to laminin) but the degree of cellular differentiation was comparable to laminin. Depending on their sequences, lipid-peptide hybrids have been

shown to be capable of penetrating phospholipid bilayers. As such, the Hart group has applied this concept to the design of enhanced gene delivery vehicles for targeting brain tissue. Kenny *et al.* used a gadolinium labelled GdDOTA(GAC₁₂)₂ that self-assembled into micelles, mixed with anionic and cationic polar lipids and integrated into liposomes, ultimately form aggregates, to deliver various fluorescent bearing DNA vectors to N2a cells, *in vitro*, and the corpus callosum and striatum, *in vivo* [70]. Among several groups, their anionic DOPG lipid formula effectively labelled and transfected the desired site. Tagalkis and colleagues made complexes with the same anionic lipids, PEG labelled lipids, bioactive peptides, and glyceraldehyde 3-phosphate dehydrogenase (GAPDH) siRNA [71]. Again, N2a cells and the striatum were targeted and the complex PRL^{AP1} provided the best transfection, where peptide and RNA were first incubated together followed by the addition of the liposome complex DOPG:DOPE:DPPE-PEG2000.

3. Neural Bioactive Ligands

Although many bare SA nanoscaffolds are capable of promoting cell adhesion and some minor behaviours, several desirable cell behaviours must be induced with bioactive ligands or peptides. Due to the nature of SA peptides, appended bioactive ligands are usually engineered to be as small as possible so as to not adversely impact the formation of assembled nanostructures. Furthermore, peptides in themselves, are desirable due to the investigator's ability to design their bioactivity, realize their potential for intelligent multipurpose bioengineering, and their relatively easy synthesis. In the realm of neural tissue engineering, several peptides have been derived from known functional proteins typically responsible for regulating cell viability, adhesion, migration, neuritogenesis, neurogenesis, synaptogenesis, the attenuation of neuro-inflammation and astrogliosis, and the potential regeneration of nerves and nervous tissues. Some of these molecules have been derived from full protein screening, while others have been obtained from

peptide libraries and biopanning techniques. Although not every molecule listed (Table 2) in this review has been used in neural nanoscaffolds, nor have all been joined with SA systems, several have been applied with recovery of like cells and tissues and show potential merit for nanoscaffold design options.

3.1. Neural Cell Adhesion Molecule (NCAM) Peptides

Neural cell adhesion molecule (NCAM) is a glycoprotein linked to cell-cell adhesion of neurons and glial cells and, ultimately, synaptic plasticity, memory, and learning [72]. NCAMs have yielded peptide motifs, exhibiting a variety of functions that have been used as a dual lysine tetramer structure in several studies. The EVYVVAENQQGKSKA (FGL) sequence has been shown to enhance both neuritogenesis in hippocampal neurons (*in vitro*) and synaptogenesis in the same cells while increasing spatial learning in rats [73 - 74]. This sequence was also found to promote neurite outgrowth in dopaminergic, cerebellar granule, and hippocampal neurons [75]. Furthermore, this peptide was used to enhance memory from sensorimotor recovery in postnatal rats and to promote long-term plasticity as seen in hippocampal and dentate gyrus tissue growth [76 - 77]. In addition, it has been demonstrated that the FGL peptide could attenuate glia activity in aged hippocampi for both astrocyte and microglia populations [78]. The BCL domain peptide, NLIKQDDGGSPIRHY, was used to assess viability and neuritogenesis in cerebellar granule neurons [79]. GRILARGEINFK (P2) sequence was used to stimulate neurite outgrowth, and ASKKPKRNIKA (CD3) was found to induce neuritogenesis, synaptogenesis, and modulate presynaptic function with different quantities of the peptide [80 - 81]. Other peptides were shown to interact with glia cells, an example of which was KHIFSDDSSE used to limit astrocyte proliferation [82 - 83]. Additionally, the DRVEPYSSSTA (FRM) sequence showed increased

survival and neurite outgrowth of cerebellar and hippocampal neurons, and promoted premyelinated oligodendrocyte survival [84 - 85].

Table 1.2. Neural Bioactive Peptide Motifs

Type	Sequence/Label	Study	Citation	
NCAM sequence	EVYVVAENQQGKSKA (FGL)	Rat hippocampal neurite outgrowth	[73]	
		Synaptogenesis, presynaptic function, and memory in rats	[74]	
		Neurite outgrowth and survival in dopaminergic hippocampal and cerebellar granule rat neurons	[75]	
		Early postnatal sensorimotor development and memory in rats	[76]	
		Facilitates long-term plasticity in dentate gyrus and hippocampus	[77]	
	NLIKQDDGGSPIRHY (BCL)	Glia activity attenuation in aged rat hippocampus	[78]	
		Viability and neurite outgrowth in rat cerebellar granule neurons	[79]	
		GRILARGEINFK (P2)	Neurite outgrowth in rat hippocampal neurons	[80]
		ASKKPKRNIKA (C3D)	Neuritogenesis, synaptogenesis, and presynaptic function in rat hippocampal neurons	[81]
		KHIFSDDSSE	Attenuation of rat astrocyte proliferation	[82]
Selective rat astrocyte adhesion on silica substrate	[83]			
DRVEPYSSTA (FRM)	Viability and neurite outgrowth in rat cerebellar and hippocampal neurons	[84]		
	Survival in rat premyelinated oligodendrocytes	[85]		
TN-C sequence	VFDNFVLK	Neurite outgrowth in rat cerebellar and cortical neurons	[87]	
		Neurite outgrowth and receptor identification in rat cerebellar granule neurons	[88]	

Laminin sequence	IKVAV	Rat septal neuron adhesion and neurite outgrowth	[94]
		Differentiation and neurite outgrowth PC-12 cells and mice granular neurons	[92]
		Neurite outgrowth of mouse hippocampal neurons	[96]
		Selective rat astrocyte adhesion and reduced proliferation on silica substrate	[83]
		Adhesion with PC-12 and T98-G cells	[93]
		Murine NPC differentiation and assembly in rat spinal tissue	[62]
		Regeneration of nerve tissue in rat sciatic nerve with chitosan tube implant	[101]
		Cell adhesion and neurite outgrowth of chick DRG neurons	[95]
		Mouse NSC adhesion and differentiation	[98]
		Axon elongation and glial scar attenuation in mouse spinal tissue	[63]
		Adhesion and clustering of rat neural progenitor stem cells	[68]
		Neurite outgrowth in PC-12 cells	[28]
		Biocompatibility of NSCs	[99]
		Infiltration, basement membrane deposition, and axon regeneration in rat spinal injury	[34]
		Stem cell integration and reduced gliosis of cortical lesion	[40]
		Improved 3D culture technique with DRG cells (collagen)	[97]
Viability and neural differentiation of NSCs	[100]		
Primary microglia activation and brain biocompatibility	[32]		

YIGSR	Neurite outgrowth and axonal differentiation of rat hippocampal neurons	[105]
	Adherence and aggregation of PC-12 and N2a cells	[102]
	Neurite outgrowth of mouse hippocampal neuron	[96]
	Selective rat astrocyte adhesion on silica substrate	[83]
	Adhesion and neurite outgrowth of N2a cells with alginate surface	[103]
	Regeneration of nerve tissue in rat sciatic nerve with chitosan tube implant	[101]
	Cell adhesion and neurite outgrowth of chick DRG neurons	[95]
	Mouse NSC adhesion and differentiation	[98]
	DRG neuron axonal response in embryonic chick spinal explant	[106]
	Comparative adhesion study using PC-12 cell neural differentiation	[104]
	Rat NSCs transplanted into rat hippocampal tissue; integration and restored synaptic function for Alzheimer's model	[41]
PPFLMLLKGSTR	Micropattern differentiation and neurite outgrowth of PC-12 cells	[107]
	Adhesion, differentiation, and viability of rat NSCs	[108]
	Differentiation and neurite outgrowth of PC-12 cells in enzymatically crosslinked system	[109]
Fibronectin RGD sequence	Adherence and aggregation of PC-12 and N2a cells	[102]
	3D migration of and neurite outgrowth of chick DRG neurons	[119]

	Neuron electrode contact and neurite outgrowth with chick DRG neurons	[118]
	Migration and potentiation of B35 neuroblastoma and HEK293 cells	[117]
	Adhesion with PC-12 and T98-G cells	[93]
	Mouse NSC adhesion and differentiation	[98]
	Neuroprotection of immature rat brain via glia mechanism upon NMDA exposure	[125]
	Comparative adhesion study using PC-12 cell neural differentiation	[104]
	Rat NSC adhesion, clustering, and proliferation	[69]
	Cell adhesion, cyclic, and differential pulse voltammetry of PC-12 cells into neural cell chip	[116]
	Adhesion, differentiation, and alignment of NPCs	[65]
	Isolation of radial glia like NSCs from fetal and adult mouse forebrain	[121]
	Nerve regeneration of rat sciatic nerve	[126]
	Proliferation, migration, outgrowth, signalling, and neural differentiation of N2a cells	[115]
	Neurite outgrowth, survival, proliferation, and differentiation of NSCs	[122]
	Adhesion and differentiation of human pluripotent stem cells	[123]
	Outgrowth and nerve guidance of human NSCs	[124]
	Neurite outgrowth in chick DRG neurons and Schwann interactions	[119]
PHSRN	Comparative adhesion study using PC-12 cell neural differentiation	[104]
MEGF10 / KLPGWSG	Enhanced neural differentiation of murine stem cells	[57]

**Notch1 /
Dll4
sequence**

		Differentiation of murine NSCs and regeneration in rat spinal transection	[58]
MARK1	FAQRVPP	Mouse NSC viability, proliferation, and differentiation, and spinal and locomotor recovery	[43]
BMHP sequence	PFSSTKT (BMHP1)	Mouse NSC adhesion and differentiation	[98]
		Mouse NSC differentiation	[29]
		Cell infiltration, basement membrane deposition, and axon regeneration in rat spinal injury	[34]
		Mouse NSC 3D differentiation	[30]
		Regeneration of rat chronic spinal injury	[35]
		Neural differentiation of human EnSCs, myelination, and axonal regeneration in spinal cord injury	[36]
	SKPPGTSS (BMHP2)	Mouse NSC adhesion and differentiation	[98]
		Mouse NSC 3D neural differentiation	[30]
		Mouse NSC and glial differentiation	[31]

Abbreviations: Amino Acids: Alanine (A), Arginine (R), Asparagine (N), Aspartic acid (D), Cystein (C), Glutamine (Q), Glutamic Acid (E), Glycine (G), Histidine (H). Isoleucine (I), Leucine (L), Lysine (K), Methionine (M), Phenylalanine (F), Proline (P), Serine (S), Theonine, Tryptophan (W), Tyrosine (Y), Valine (V).Neural Cell Adhesion Molecule (NCAM), Tenascin C (TN-C), Pheochromocytoma12 (PC-12), Dorsal Root Ganglia (DRG), Neuroblastoma2a (N2a), Neural Stem Cell (NSC), Human Embryonic Kidney (HEK293), Neural Progenitor Cell (NPC), Embryonic Stem Cell (EnSC), Multiple Embryonic Growth Factor-Like-Domains (MEGF10), Delta Like Ligand (Dll4), Serine/Theonine Kinase (MARK1), Bone Marrow Homing Peptide (BMHP)

3.2. Tenascin-C (TN-C) Peptide

Tenascin-C (TN-C) is an extracellular matrix protein family of spliced variants that has been shown to influence neuronal adhesion, growth, and migration [86]. The peptide VFDNFVLK, among other TN-C derived sequences, was found capable of supporting neurite outgrowth in rat cerebellar, cortical and cerebellar granule neurons [87 - 88].

3.3. Laminin-Based Peptides

Laminins are a class of glycoproteins (~400 kDa) that are a major component of basal lamina, which lines every organ and has major roles in cell attachment, migration, and adhesion [89 - 91]. As laminins self-assemble to promote basement membrane formation, their primary amino acid sequence has been extensively studied for the express purpose of designing better artificial nanoscaffolds. A handful of sequences have emerged that have experienced prolific use in neural tissue engineering design and applications. The most studied of these sequences is IKVAV, for which we intend only to review its application to neural tissue engineering. PC-12 and glioblastoma (T98-G) cell lines have been used to study the *in vitro* adhesion, differentiation, and neurite outgrowth to IKVAV-based, including free solution, culture coatings and nanoscaffolds [28, 92 - 93]. Similarly, this peptide has also been successfully observed using primary culture as an adhesive substrate coating or nanoscaffold and promoter of neurite outgrowth with septal, hippocampal, granular, and DRG neurons [94 - 97]. Full neural directed differentiation and viability of NPCs and NSCs have also been characterized by several researchers with IKVAV integrated coatings and nanoscaffolds [44, 68, 98 - 100]. In addition, it has been shown that inclusion of IKVAV has attenuated adhered astrocytes [83]. Several *in vivo* applications have been used with IKVAV. IKVAV has been combined with an SA amphiphile for favourably differentiating NPCs into neurons [44], added to chitosan to promote

regeneration of a rat sciatic nerve [100], and an IKVAV amphiphile was used to demonstrate axonal elongation and the attenuation of astrogliosis in a mouse spinal lesion [62]. A RADA16-I – IKVAV SA was used to promote axonal regeneration upon spinal injury and to integrate a stem cell transplant into cortical lesions to reduce glia scarring [34, 38]. Koss *et al.* also used this particular sequence to assess primary microglia activity in culture and in a 7 day intracerebral injection [32]. Despite reductions in glial scarring in other literature, they found that microglia were not attenuated by this particular sequence.

Another laminin-derived peptide motif, YIGSR, has been used to promote adherence, aggregation, neurogenesis and neurite outgrowth in PC-12 and N2a culture [102 - 104], and primary hippocampal and DRG neurons [95 - 96, 105]. Neural differentiation and adhesion of NSCs was assessed by Gelain *et al.*, and astrocyte adhesion was documented in the same study that Kam and colleagues performed with IKVAV [83, 98]. It was found that as a substrate, this peptide enhanced the assessed parameters. An *ex vivo* study used YIGSR to promote interaction and axonal regeneration of DRG neurons in a chick spinal explant [106]. In the study that Itoh *et al.* used IKVAV to regrow a sciatic nerve, YIGSR was also comparatively used in the chitosan tube implant [101]. In this case, YIGSR was capable of regenerating the tissue in epineurium-like layers within the tube layers. Ultimately, YIGSR was used with the most promising results by Cui and company, in a RADA16-I based NSC implant to restore synaptic function in an Alzheimer's model, where significant improvement in spatial learning and recovery from memory deficits in Alzheimer's Disease rats was observed, which is one of the first applications, with peptides of these kinds in developing therapeutics for neurodegenerative disorders [40].

The sequence PPFLMLLKGSTR was recently discovered from the G3 domain of laminin 5. Using this to functionalize a micropatterned PLGA film showed that the precise neurite

extension of PC-12 cells was enhanced by the peptide [107]. This peptide was also shown to promote adhesion, viability, and neural differentiation of NSCs in a collagen modified matrix [108]. Finally, extensive PC-12 cell neurite outgrowth in an enzymatically cross-linked collagen nanoscaffold was observed when this peptide was present [109].

3.4. Fibronectin-Derived Peptides

Similar to laminin, fibronectin is glycoprotein (~440 kDa) that binds to ECM components to instigate cell adhesion, migration, differentiation and is strongly linked to tissue regeneration and embryonic development [110 - 111]. By itself, it assembles into its own ECM that initiates cell adhesion [112]. As such, several amino acid sequences have been identified and used extensively in tissue engineering applications, especially in vascular and connective tissue systems. Fibronectin-based peptides have played no small role in neural tissue engineering design and implementation.

The most significant peptide used in cell and tissue nanoscaffolds is the RGD sequence, being widely applied to neural nanoscaffolds and neuronal adhesive materials [113]. Although originally derived from fibronectin, this sequence has been identified in many cell attachment proteins, including fibrinogen, laminin and collagen [114]. Like IKVAV, it has been used to assay adhesion, clustering, neurite outgrowth, and differentiation using PC-12, N2a, and T98-G cell lines [93, 102, 104, 115]. In addition, Kafi *et al.* used cyclic and differential pulse voltammetry to characterize signalling of PC-12 cells in a neural cell chip, where RGD peptides were nanopatterned and eventually improved cell-binding affinity with an Au substrate [116]. Other cell lines used include B35 neuroblastoma and HEK293 cells, in which RGD directed receptor and signalling-induced directional migration and potentiation [117]. Similar outcomes

were noted in primary culture; outgrowth, migration, and Schwann cell interactions of DRG neurons have been documented on electrodes and nanoscaffolds [118 - 120]. RGD has also been used to isolate radial glia progenitors by Markó *et al.* [122]. Rat and human NPC and NSC interactions with RGD substrates are also extensive, including adhesion, clustering, alignment, neuritogenesis, and differentiation of cells [65, 69, 98, 122 - 124]. Although many studies have used neural cell culture, only a few investigations have reached *in vivo* applications. This peptide was included as part of a genetic vector to enhance neuroprotection in rat brain lesions, and was shown to attenuate microglia and astrocyte activity [125]. An RGD-PLGA composite conduit, mixed with NGF, was shown to promote regeneration of a peripheral rat sciatic nerve, 3 months post severing [126].

The pentapeptide sequence PHSRN is a second peptide based on fibronectin, which has been confirmed to function similar to RGD and partially enhance cell adhesion synergistically [127]. PHSRN has also been studied with PC-12 cells, where it was shown to enhance cell adhesion [104]. Despite its potential, to date, this peptide has yet to be successfully applied to primary culture, neural stem cell engineering, nor any *in vivo* substrate or scaffold.

3.5. Other Peptide Derivatives

Several peptide sequences have been discovered from biopanning or phage display techniques, and have been linked to known proteins through established databases (ie. basic local alignment search tool, BLAST). The Gelain laboratory identified several sequences in such a manner, which were utilized to study and direct stem cell behaviour. One peptide, KLPGWSG, has apparent sequences in multiple proteins, including epidermal growth factor 10 (MEGF10), Notch1, and delta-like ligand 4 (Dll4). These proteins are often involved in angiogenesis, as well

as radial glia, astrocyte, and stem cell differentiation [57]. As previously mentioned, these peptides were used with co-assembling peptides to preferentially differentiate murine stem cells into neurons, and incorporated in PLGA microtube directed regeneration of a spinal transection [58]. Another sequence relevant to NSC differentiation, the microtubule affinity-regulating kinase (MARK1) peptide FAQRVPP, was discovered by Gelain *et al.* and used to functionalize LDLK12 nanoscaffolds to promote neural differentiation in mouse NSCs, and regrowth of spinal tissue for locomotor recovery [56]. Like the aforementioned β -sheet derived peptides, the Gelain group discovered promising bioactive sequences, as well as SA peptides, that appear in BMHP. PFSSTKT (BMHP1) was found to foster mouse neural and human endometrial stem cell (hEnSC) differentiation and repair spinal tissue when tethered to RADA16-I [29, 37 - 38, 41]. The peptide SKPPGTSS (BMHP2) was studied with RADA16-I to promote neural over glial differentiation in mouse stem cells [31, 98]. A comparative study noted similar NSC differentiation and proliferation upon treatment with both BMHP1 and BMHP2 in a 3D model [31].

4. Drug Candidates

Stationary bioactive peptides can greatly influence the therapeutic outcome of SA nanoscaffolds. However, they are limited in their capacity to influence surrounding systems. By artificially generating the nanoscaffold to release similar drugs and molecules, a new dimension of intelligent design can be integrated into a nanoscaffold. Several potential drugs candidates, with varying degrees of efficacy on different cell and tissue types within and without the nanoscaffold, can be engineered to be released by rate and dose. Furthermore, isolating release to a specific nanoscaffold location, can prevent these drugs from delivering unwanted responses, such as pain-related neural sprouting [128]. Careful choice in drug and timeline of release must

be taken as the desired biological outcome may be heavily influenced by these parameters. For example, anti-inflammation, axonal regrowth, or glia scar reduction may be desired in spinal recovery, but different drugs and release timelines may be essential to achieve this goal. As with stationary ligands, their use in neural tissues and SA nanoscaffolds may be limited to smaller molecules to retain expected formation of nanoscale architectures. This section will survey these molecules and summarize their recent uses (Table 3).

4.1. Neurotrophic Growth Factor Peptides

In neural tissues, neurotrophic growth factors (NTFs) are vital signalling molecules secreted and used by nearly every cell in the core CNS with their primary purpose being to initiate and promote neural survival and regeneration. With this in mind, several research groups have identified and tested analogues or promoters of these NTFs.

NGF targets the tyrosine kinase A (TrkA) receptor and is secreted by oligodendrocytes and Schwann cells for the recovery of nerves in several injury types [129]. NGF is used for the maintenance of sensory neurons and also linked to survival of cholinergic neurons in Huntington's and Alzheimer's disease states [130]. To date, YCTDEKQCY is the only documented analogue for NGF [131]. Designed by Beglova *et al.*, its NGF comparable 3D structure and interaction with the TrkA receptor was characterized by nuclear magnetic resonance. This peptide was later applied to rat septal neurons and reinforcement of synaptic communication was observed, demonstrating successful ligand-receptor interaction in cortical tissue.

Table 1.3. Peptide Analogues for Neural Tissue Drug Delivery

Type	Sequence/Label	Study	Citation
NGF analogue	YCTDEKQCY	3D solution structure compared to NGF	[131]
		Signalling and synaptic marker increase in rat septal neurons and cortical tissue	[132]
BDNF analogue	Tricyclic dimeric peptide	Neuronal survival in chick DRG neurons	[134]
	Trimeric MVG peptide	Increased H19-7 cell hippocampal tissue BDNF and TrkB expression and improved spatial learning and memory	[135]
	LM22A	Prevented neurodegeneration in mouse hippocampal neurons, <i>in vitro</i> Hippocampal and striatal TrkB activation, and improved motor learning in post-brain injury	[136]
GDNF analogue	ETMYDKILKNLSRSR (Gliafin)	Neurite outgrowth in rat hippocampal neurons	[137]
		Neurotrophin delivery for neural differentiation of mouse dorsal root ganglia and transplanted murine embryonic stem cells	[143]
CNTF analogue	DGGL	Neurogenesis and synaptogenesis of hippocampal tissue and synaptic plasticity in mice	[141]
		Neurogenesis, dendritic and synaptic plasticity in hippocampal neurons, and memory in mice	[140]
		DGGLFEKKLWGLKV (Cintrofin)	Attenuates spatial-learning deficit in rat epilepticus model
Cripto blocker	[_L -M(O)]-C(Bzl)-C(Bzl)	Neurotrophin delivery for neural differentiation of mouse DRG and transplanted murine embryonic stem cells	[143]
		Neural induction, differentiation, and integration of mouse embryonic stem cells in a Parkinson's rat	[144]

α-MSH	SYSMEHFRWGKPV	Plasmid vector transfection of this peptide into A-172 cells attenuated pro-inflammatory activation by lipopolysaccharide	[150]
		Controlled release of the peptide in electrode coating attenuated lipopolysaccharide activated microglia	[151]

Abbreviations: Amino Acids: Alanine (A), Arginine (R), Asparagine (N), Aspartic acid (D), Cystein (C), Glutamine (Q), Glutamic Acid (E), Glycine (G), Histidine (H), Isoleucine (I), Leucine (L), Lysine (K), Methionine (M), Phenylalanine (F), Proline (P), Serine (S), Theonine, Tryptophan (W), Tyrosine (Y), Valine (V). Nerve Growth Factor (NGF), Brain-Derived Neurotrophic Factor (BDNF), Tyrosine Kinase (Trk), Glial-Derived Neurotrophic Factor (GDNF), Ciliary Neurotrophic Factor (CNTF), Hydroxyl (O) and Benzyl (Bzl) Protecting Groups

Brain-derived neurotrophic factor (BDNF), tuned to the TrkB receptor, is another imperative NTF for neuroprotection and neural development that also is important to signalling and synaptic plasticity [133]. Early BDNF analogues were tricyclic dimeric peptides, connected with disulphide linkages, which emulated a flexible non-linear TrkB receptor interaction and was potent in promoting DRG neuron viability [134]. A trimeric neuropeptide, MVG, capable of significantly promoting BDNF secretion was discovered using a positional scanning synthetic peptide combinatorial library [135]. Although its pathway is unknown, this peptide stimulated BDNF and TrkB expression in H19-7 cells and rat hippocampal tissues, and was shown to improve spatial learning and memory in adult rats. More recently, several small molecular weight BDNF mimics (LM22A series) were shown to bind to TrkB with comparable affinity to BDNF and activate hippocampal and striatal TrkB, *in vivo* [136]. It was found that they prevented hippocampal neuronal degeneration with an *in vitro* culture-based Alzheimer, Huntington, and Parkinson disease models. In addition, spatial learning was effectively recovered using the LM22A-4 variant in rats upon a controlled cortical impact injury.

Glial derived neurotrophic factor (GDNF) is secreted by oligodendrocytes and Schwann cells for neural injury repair and interacts with dopaminergic neurons in a trophic manner [130]. As such, it can be used to treat CNS and peripheral nerve injury, as well as neurodegenerative disorders. A GDNF analogue (ETMYDKILKNLSRSR, Gliafin) demonstrated neurite outgrowth activity in primary rat hippocampal neurons, with a supposed pathway of NCAM interaction [137].

Another supporting growth factor is ciliary neurotrophic growth factor (CNTF), which has been linked to motor neuron viability, neurite outgrowth and subsequent recovery of CNS and PNS injury; results shown to be accomplished indirectly though induced angiogenesis [138 -

139]. The first series of CNTF peptides, DGGL from VGDGGLFEKKL, stimulated proliferation and maturation of NPCs in the dentate gyrus and improved synaptic plasticity and reference memory in mice [140]. Furthermore, a dual adamantane adamantine modified DGGL peptide was used to improve pharmacokinetics and BBB permeability [141], where peripheral administration to mice yielded proliferation, maturation, neurogenesis of neurons in the granular cell layer and dentate gyrus, along with enhanced learning through short term and spatial reference memory. This sequence is also present in the Cintrofin peptide (DGGLFEKKLWGLKV), which was used to treat the learning deficit associated with a rat post-status epilepticus model [142]. In the acute short term (5-9 days), Cintrofin was unable to promote neurogenesis or proliferation, however long-term treatment (13 weeks) in chronic conditions, normalized proliferation and neuroblast formation. Pre-treatment also prevented seizure-associated activity from basal dendrites and reduced anxiety-associated behaviour in the rats. Subsequent work released both Gliafin and Cintrofin from silica nanoparticles to assess neural differentiation of DRG neurons and implanted murine NSCs, where it was found to effectively promoted full differentiation, signalling, and long-term survival (2 months) [143].

Rescuing damaged neurons and neural tissues is not an exclusive characteristic of NTFs, because other indirectly derived peptides have been discovered and used in similar applications. One apt example is the cripto blocking peptide $[_L\text{-M(O)}]\text{-C(Bzl)-C(Bzl)}$, which is a glycosylphosphatidylinositol-anchored coreceptor in the epidermal growth factor-cripto-1/FRL-1/cryptic family of proteins that is vital in stem cell differentiation [144 - 146]. When attenuated, cripto has a strong effect on differentiating midbrain dopaminergic neurons, which makes it a potential candidate for Parkinson's treatment [147]. In this study, $[_L\text{-M(O)}]\text{-C(Bzl)-C(Bzl)}$ was transplanted in the striatum showing enhanced functional recovery of Parkinson's rats and

reduced tumour formation. Another example of a molecule that enhances the effect of NTFs are cyclic adenosine monophosphates (cAMPs), which blocks a Nogo receptor that inhibits overall neural regeneration [148]. It was shown to promote axonal regrowth Schwann cell myelination in a Schwann cell graft upon spinal injury. Supraspinal and proprioceptive axon sparing was noted with serotonergic fibers expanded beyond the graft, and eventually improved the locomotion of the tested rats. In preconditioned treatment, cAMP combined with NTFs was shown to further improve axonal regrowth with Schwann cells survival in a 3 month dorsal root injury [149]. It should be noted that cAMP is a highly non-specific molecule, which plays a fundamental role in many cellular pathways and should be explored for highly specific controlled delivery in the future.

4.2. Anti-inflammatory Peptides

Attenuating and halting the host-response or inflammation associated with foreign bodies or neural injury can be a great stride in mitigating chronic complications, scarring, and promoting accelerated healing. Nanoscaffolds designed to deliver anti-inflammatory drugs are often best served surrounding implants or used to bridge tissue gaps in the site of penumbras associated with stroke, or neurodegenerative diseases, that are exacerbated by excessive inflammation. α -Melanocyte-stimulating hormone (α -MSH, SYSMEHFRWGKPV) is capable of inhibiting secretion of inflammatory cytokines from downstream signalling of κ B activity [150]. α -MSH was loaded into the nitrocellulose coating surrounding brain electrodes and was observed to attenuate active microglia, reducing cytokine and nitric oxide secretion [151]. It was also discovered that adding repeating lysine residues (K5) to self-assembling peptides was enough to block the Tumour Necrosis α and other cytokine pathways, suppressing general inflammatory responses [152]. Although covalently attached, it may be capable of being released as a drug. A

host of anti-inflammatory drugs are available that could potentially be used in neural tissue engineering. Their use remains infrequent in neural nanoscaffolds due to the unpredictable timelines for treating acute bouts of severe inflammation or the complication of designing materials that can address chronic inflammation from sustained and controlled release.

5. Release Cues for Nanoscaffold Drug Delivery

The drugs and ligands discussed are highly capable of causing very specific cellular responses and, therefore, directing the fate of both healthy and damaged neural tissues. However, without a proper means of delivery, they are limited and unable to reach their full clinical potential. Delivery may only be effective during specific phases or time points in injury or disease states, require a sustained delivery for chronic treatment, ameliorate poor pharmacokinetic qualities such as half-life or improper distribution, or potentially prevent toxic effects or unwanted neurite sprouting from heavy or unwanted circulation. Several research groups have investigated the benefit of intelligent and controlled release. Within neural nanoscaffolds it has become a powerful tool in the precise directing and engineering of cells that oftentimes need guidance, alignment, and migration cues. With the goal of designing SA nanoscaffolds capable of circulating *in vivo* and forming nanostructures in targeted areas, drugs are preferably bound or tethered covalently or through strong intermolecular bonds. The section will highlight some of the design strategies used or may have potential merit in SA nanoscaffolds for neural tissue engineering.

5.1. Release Cues

Release techniques have been developed that respond to exogenous stimuli, including thermal, magnetic, ultrasound, ultraviolet, and electric [153]. Well-established biodegradable

polymers have been used extensively to delivery time-dependent drug doses, as reviewed elsewhere [154 - 155]. PLA, PGA, co-polymerized PLGAs, PCA and several blends of these poly(α -ester) materials are clinically approved, have well defined degradation rates, but have seldom been combined with SA peptides or amphiphiles as simple drug delivery vehicles or directed neural tissue engineered nanoscaffolds [6]. This may be due to the fact that these polyesters acidify environments as they degrade, or because they are not well tuned to respond to surrounding cellular behaviour, and therefore not effectively controlled. Some synthetic polymers have been developed to be responsive to lower pH, which is associated with injury and inflammation including various polymer linkages: acetals, hydrazones, vinyl esters, and ortho esters [156]. In neural tissue engineering, these polymers may only be relevant in the most drastic stroke penumbra microenvironments or tumours, where the pH is below 6.75 [157 - 159]. Few studies in neural tissues or SA peptides have been pursued with these materials.

Using the tightly regulated spatiotemporal profile of endogenous enzymes, specifically secreted *in situ* to cue drug release, has recently gained momentum in several drug delivery applications. This allows design for highly specific feed-back or feed-forward style delivery, specific to substrate sequence and enzyme activity, as reviewed elsewhere [160 - 162]. With respect to SA nanoscaffolds, only a few systems have been modified with proteolytic peptide sequences. Law and Tung designed a SA system (MPEG₂₀₀₀BK(FITC)SGRSANA-kldlkldlkldl-NH₂), which used trypsin or urokinase plasminogen activator (uPa) to initiate the release of fluorescent quenching molecules from SA fluorescent nanofibers. [163]. MMP-2 cleavable sequences were added to their SA MDP to direct cell proliferation and migration into their nanoscaffold [51]. Despite a scant record of neural SA nanoscaffolds with enzyme cued drug release, the tremendous potential of this approach remains untapped. Many enzymes, with a

plethora of peptide substrates with variable activities, have been recognized as key players in neural disorders, injury, and healing; especially those secreted by support microglia and astrocytes [166 - 167]. Cathepsins B, D, E, and S play key roles, including processing of host response related exogenous antigens, the degradation of A β plaques and ECMs, and neuronal apoptosis [168 - 172]. A β plaques are also degraded by insulin-degrading enzymes [173 - 174]. During multiple sclerosis, calpains are involved in degrading myelin [175 - 176]. In the event of microglia apoptosis, caspase 1 and 3 are secreted [169, 171, 177 - 178]. Certain proteasomes are also responsible for processing antigens, but also play a role in degrading I κ B, associated with HIV-1 dementia [177 - 178]. Tissue plasminogen activator (tPa) is secreted by active microglia, which can occur from neuroinflammation caused by injury and several neurodegenerative disease states, and during neuronal apoptosis [180 - 181]. uPa is secreted during microglial migration [182]. Elastase could be used in nanoscaffolds designed for microglia phagocytosis and neuritogenesis [183]. MMP-2 and MMP-9 are highly expressed by active microglia in stroke penumbras or as a result of cerebrovascular diseases [184 - 187].

6. Conclusion and Future Directions

To date, many advances in SA nanoscaffolds and nanostructures have been made in neural tissue engineering. Directing neural behaviour from incorporated multipurpose bioactivity and controlled drug release allows design for a tuneable and intelligent nanoscaffold, capable of addressing many sources of injury in the CNS. Applying small analogues of these to SA systems, could promote therapeutics that are simply manufactured for large-scale use and designed to potentially traverse the body and accumulate and self-assemble in recoverable tissues. As discussed in this article, a host of SA peptides and amphiphiles have been designed and implemented in a series of neural tissue engineering studies. These include well studied SA

peptides, such as RADA16-I, which have been used to regenerate spinal and cortical lesions with directed stem cell transplants and Alzheimer's models. Other peptides, such as co-assembling and multi-domain peptides have also shown similar merit in spinal cord regeneration. Peptide and DNA amphiphiles have similarly been applied. Other molecules, such as lipid-peptide forming layers have been studied with neurogenic cell culture, neural stem cell differentiation. Several bioactive peptides have been discovered to be associated with neural cell adhesion, proliferation, migration, outgrowth, axonal guidance, differentiation, the formation of synapses, learning and memory, motor recovery, and the attenuation of microglia and astrocyte related scar tissue formation. These peptides have many sources: NCAM, laminin, fibronectin, TN-C, and biopanned peptides that appear in MEGF10, Notch1, Dll4, MARK1 and BMHP. Many neurotrophic, neurotrophic-like, and anti-inflammatory drugs have also emerged for potential controlled drug release. With endogenous delivery cues, such as environmental degradation, pH, and enzyme response, these drugs can be delivered at different rates, doses, and mixtures to specifically direct cellular behaviour in a complex neural injury microenvironment.

Although many advances have been made in intelligent neural nanoscaffolds, the results have generated more questions than answers for the neural tissue engineer. This field is still in its infancy. Most of the systems studied for more than a decade have focused on cell culture and animal transplantation; their use in controlled drug delivery remains limited. Re-assembly and cell migration have been studied extensively, yet targeted drug delivery to neural cells is unknown. In contrast, a variety of enzymatic design choices for treating neural damage and disease are known and understood, as outlined in this article. This suggests that tremendous potential for research and therapeutics is awaiting study in enzymatically degradable nanoscaffolds. The protocols for synthesis are well-established and automated, with self-

assembly made to occur in physiological conditions without deleterious solvents. Generic circulation and distributed nanostructure assembly of SA systems are not feasible to date, as *in situ* injection is still required. Labour intensive investigation in identifying tethering peptides and molecules is ongoing with modifications for BBB penetration remaining little understood. Many puzzle pieces in the journey to unlocking powerful tools for intelligent neural tissue engineering may lay in enzymatic linked nanoscaffolds for the future.

7. Acknowledgements

The authors are grateful for financial support from Alberta-Gangwon, AET, NSERC, NINT-NRC, and WCHRI.

8. References

1. Janeway CA, Travers P, Walport M, Shlomchik MJ. Responses to alloantigens and transplant rejection. In: Immunobiology: the immune system in health and disease. New York: Garland Science; 2001.
2. Göritz C, Dias DO, Tomilin N, Barbacid M, Shupliakov O, Frisén J. A pericyte origin of spinal cord scar tissue. *Science*. 2011;333:238-42.
3. Huang L, Wu Z, Zhuge Q, Zheng W, Shao B, Wang B, et al. Glial scar formation occurs in the human brain after ischemic stroke. *Int J Med Sci*. 2014;11(4):344.
4. Lattera J, Keep R, Betz LA, Goldstein GW. Blood-brain barrier. In: Siegel GJ, Agranoff BW, Albers RW, Fisher SK, Uhler MD, editors. *Basic neurochemistry: molecular, cellular and medical aspects*, 6th edition. Philadelphia: Lippincott-Raven; 1999. p. 763.
5. Orive G, Anitua E, Pedraz JL, Emerich DF. Biomaterials for promoting brain protection, repair and regeneration. *Nat Rev Neurosci*. 2009;10(10):682-92.
6. Cao H, Liu T, Chew SY. The application of nanofibrous scaffolds in neural tissue engineering. *Adv Drug Deliv Rev*. 2009;61:1055-64.
7. Willerth SM, Sakiyama-Elbert SE. Approaches to neural tissue engineering using scaffolds for drug delivery. *Adv Drug Deliv Rev*. 2007;59(4):325-38.
8. Barras FM, Pasche P, Bouche N, Aebischer P, Zurn AD. Glial cell line-derived neurotrophic factor released by synthetic guidance channels promotes facial nerve regeneration in the rat. *J Neurosci Res*. 2002;70:746-55.

9. Bloch J, Fine EG, Bouche N, Zurn AD, Aebischer P. Nerve growth factor- and neurotrophin-3-releasing guidance channels promote regeneration of the transected rat dorsal root. *Exp Neurol.* 2001;172(2):425-32.
10. Fine EG, Decosterd I, Papalioezos M, Zurn AD, Aebischer P. GDNF and NGF released by synthetic guidance channels support sciatic nerve regeneration across a long gap. *Eur J Neurosci.* 2002;15(4):589-601.
11. Moore K, MacSween M, Shoichet M. Immobilized concentration gradients of neurotrophic factors guide neurite outgrowth of primary neurons in macroporous scaffolds. *Tissue eng.* 2006;12(2):267-78.
12. Yu X, Bellamkonda RV. Tissue-engineered scaffolds are effective alternatives to autografts for bridging peripheral nerve gaps. *Tissue eng.* 2003;9(3):421-30.
13. Houweling DA, Lankhorst AJ, Gispens WH, Bär PR, Joosten EAJ. Collagen containing neurotrophin-3 (NT-3) attracts regrowing injured corticospinal axons in the adult rat spinal cord and promotes partial functional recovery. *Exp Neurol.* 1998;153(1):49-59.
14. Burdick JA, Ward M, Liang E, Young MJ, Langer R. Stimulation of neurite outgrowth by neurotrophins delivered from degradable hydrogels. *Biomaterials.* 2006;27(3):452-9.
15. Piantino J, Burdick JA, Goldberg D, Langer R, Benowitz LI. An injectable, biodegradable hydrogel for trophic factor delivery enhances axonal rewiring and improves performance after spinal cord injury. *Exp Neurol.* 2006;201(2):359-67.
16. Winter JO, Cogan SF, Rizzo JF. Neurotrophin-eluting hydrogel coatings for neural stimulating electrodes. *J Biomed Mater Res Part B Appl Biomater.* 2007;81B(2):551-63.

17. Williams BAR, Chaput JC. Synthesis of peptide-oligonucleotide conjugates using a heterobifunctional crosslinker. *Curr Protoc Nucleic Acid Chem.* 2010;Chapter 4:Unit4.41.
18. Anderson DG, Levenberg S, Langer R. Nanoliter-scale synthesis of arrayed biomaterials and application to human embryonic stem cells. *Nat Biotechnol.* 2004 July;22(7):863-666..
19. Flaim CJ, Chien S, Bhatia SN. An extracellular matrix microarray for probing cellular differentiation. *Nat Methods.* 2005;2(2):119-25.
20. Ramos-Cabrer P, Campos F, Sobrino T, Castillo J. Targeting the ischemic penumbra. *Stroke.* 2011;42(1 Suppl):S11.
21. Nowakowski GS, Dooner MS, Valinski HM, Mihaliak AM, Quesenberry PJ, Becker PS. A specific heptapeptide from a phage display peptide library homes to bone marrow and binds to primitive hematopoietic stem cells. *Stem Cells.* 2004;22:1030-8.
22. Zhang S. Fabrication of novel biomaterials through molecular self-assembly. *Nat Biotechnol.* 2003;21(10):1171-8.
23. Seow WY, Hauser CAE. Short to ultrashort peptide hydrogels for biomedical uses. *Mater Today.* 2014;17(8):381-8.
24. Maude S, Ingham E, Aggeli A. Biomimetic self-assembling peptides as scaffolds for soft tissue engineering. *Nanomedicine.* 2013;8(5):823-47.
25. Kyle S, Aggeli A, Ingham E, McPherson MJ. Production of self-assembling biomaterials for tissue engineering. *Trends Biotechnol.* 2009;27(7):423-33.
26. Kabiri M, Bushnak I, McDermot MT, Unsworth LD. Toward a mechanistic understanding of ionic self-complementary peptide self-assembly: role of water molecules and ions. *Biomacromolecules.* 2013;14:3943-50.

27. Holmes TC, de Lacalle S, Su X, Liu G, Rich A, Zhang S. Extensive neurite outgrowth and active synapse formation on self-assembling peptide scaffolds. *Proc Natl Acad Sci U S A*. 2000;97(12):6728-33.
28. Li Q, Chau Y. Neural differentiation directed by self-assembling peptide scaffolds presenting laminin-derived epitopes. *J Biomed Mater Res A*. 2010;94(3):688-99.
29. Taraballi F, Natalello A, Campione M, Villa O, Doglia SM, Paleari A, et al. Glycine-spacers influence functional motifs exposure and self-assembling propensity of functionalized substrates tailored for neural stem cell cultures. *Front Neuroeng*. 2010;3:NA.
30. Cunha C, Panseri S, Villa O, Silva D, Gelain F. 3D culture of adult mouse neural stem cells within functionalized self-assembling peptide scaffolds. *Int J Nanomedicine*. 2011;6:943-55.
31. Koutsopoulos S, Zhang S. Long-term three-dimensional neural tissue cultures in functionalized self-assembling peptide hydrogels, Matrigel and Collagen I. *Acta Biomater*. 2012;9:5162-69.
32. Koss KM, Churchward MA, Nguyen AT, Yager JY, Todd KG, Unsworth LD. Brain Biocompatibility and microglia response towards engineering self-assembling (RADA)₄ nanoscaffolds. *Acta Biomater*. 2016
33. Semino CE, Kasahara J, Hayashi Y, Zhang S. Entrapment of migrating hippocampal neural cells in three-dimensional peptide nanofiber scaffold. *Tissue Eng*. 2004;10(3-4):643-55.
34. Cigognini D, Satta A, Colleoni B, Silva D, Donegà M, Antonini S, et al. Evaluation of early and late effects into the acute spinal cord injury of an injectable functionalized self-assembling scaffold. *PloS one*. 2011;6(5):e19782.

35. Gelain F, Panseri S, Antonini S, Cunha C, Donega M, Lowery J, et al. Transplantation of nanostructured composite scaffolds results in the regeneration of chronically injured spinal Cords. *ACS Nano*. 2011;5(1):227-36.
36. Tavakol S, Saber R, Hoveizi E, Aligholi H, Ai J, Rezayat SM. Chimeric self-assembling nanofiber containing bone marrow homing peptide's motif induces motor neuron recovery in animal model of chronic spinal cord injury; an in vitro and in vivo investigation. *Mol Neurobiol*. 2015.
37. Ellis-Behnke RG, Liang Y, You S, Tay DKC, Zhang S, So K, et al. Nano neuro knitting: peptide nanofiber scaffold for brain repair and axon regeneration with functional return of vision. *PNAS*. 2006;103(13):5054-9.
38. Guo J, Su H, Zeng Y, Liang Y, Wong WM, Ellis-Behnke RG, et al. Reknitting the injured spinal cord by self-assembling peptide nanofiber scaffold. *Nanomedicine*. 2007;3(4):311-21.
39. Guo J, Leung KKG, Su H, Yuan Q, Wang L, Chu T, et al. Self-assembling peptide nanofiber scaffold promotes the reconstruction of acutely injured brain. *Nanomedicine*. 2009;5(3):345-51.
40. Cheng T, Chen M, Chang W, Huang M, Wang T. Neural stem cells encapsulated in a functionalized self-assembling peptide hydrogel for brain tissue engineering. *Biomaterials*. 2013;34(6109):2005-16.
41. Cui G, Shao S, Yang J, Liu J, Guo H. Designer self-assemble peptides maximize the therapeutic benefits of neural stem cell transplantation for Alzheimer's disease via enhancing neuron differentiation and paracrine action. *Mol Neurobiol*. 2015.

42. Saracino GA, Gelain F. Modelling and analysis of early aggregation events of BMHP1-derived self-assembling peptides. *J Biomol Struct Dyn*. 2014;32(5):759-75.
43. Gelain F, Silva D, Caprini A, Taraballi F, Natalello A, Villa O, et al. BMHP1-derived self-assembling peptides: hierarchically assembled structures with self-healing propensity and potential for tissue engineering applications. *ACS nano*. 2011;5(3):1845.
44. Silva D, Natalello A, Sanii B, Vasita R, Saracino G, Zuckermann RN, et al. Synthesis and characterization of designed BMHP1-derived self-assembling peptides for tissue engineering applications. *Nanoscale*. 2013;5:704-18.
45. Banwell EF, Abelardo ES, Adams DJ, Birchall MA, Corrigan A, Donald AM, et al. Rational design and application of responsive α -helical peptide hydrogels. *Nat Mater*. 2009;8(7):596-600.
46. Mehban N, Zhu B, Tamagnini F, Young FI, Wasmuth A, Hudson KL, et al. Functionalized α -helical peptide hydrogels for neural tissue engineering. *ACS Biomater Sci Eng*. 2015;1(6):431-9.
47. Mahler A, Reches M, Rechter M, Cohen S, Gazit E. Rigid, self-assembled hydrogel composed of a modified aromatic dipeptide. *Adv Mater*. 2006;18(11):1365-70.
48. Chonopoulou L, Togna AR, Guarguaglini G, Masci G, Giammaruco F, Togna GI, et al. Self-assembling peptide hydrogels promote microglial cells proliferation and NGF production. *Soft Matter*. 2012;8:5784-90.
49. Dong H, Paramonov SE, Aulisa L, Bakota EL, Hartgerink JD. Self-assembly of multidomain peptides: balancing molecular frustration controls conformation and nanostructure. *J Am Chem Soc*. 2007;129(41):12468-72.

50. Galler KM, Aulisa L, Regan KR, D'Souza RN, Hartgerink JD. Self-assembling multidomain peptide hydrogels: designed susceptibility to enzymatic cleavage allows enhanced cell migration and spreading. *J Am Chem Soc.* 2010;132(9):3217.
51. Bakota EL, Sensoy O, Ozgur B, Sayar M, Hartgerink JD. Self-assembling multidomain peptide fibers with aromatic cores. *Biomacromolecules.* 2013;14(5):1370-8.
52. Bakota EL, Aulisa L, Galler KM, Hartgerink JD. Enzymatic cross-linking of a nanofibrous peptide hydrogel. *Biomacromolecules.* 2011;12(1):82-7.
53. Bakota EL, Wang Y, Danesh FR, Hartgerink JD. Injectable multidomain peptide nanofiber hydrogel as a delivery agent for stem cell secretome. *Soft Matter.* 2011;12:1651-7.
54. Liu Y, Ye H, Satkunendrarajah K, Yao GS, Bayon Y, Fehlings MG. A self-assembling peptide reduces glial scarring, attenuates post-traumatic inflammation and promotes neurological recovery following spinal cord injury. *Acta Biomater.* 2013;9:8075-88.
55. Iwasaki M, Wilcox JT, Nishimura Y, Zweckberger K, Suzuki H, Wang J, et al. Synergistic effects of self-assembling peptide and neural stem/progenitor cells to promote tissue repair and forelimb functional recovery in cervical spinal cord injury. *Biomaterials.* 2013;35:2617-29.
56. Gelain F, Cigognini D, Caprini A, Silva D, Colleoni B, Donegá M, et al. New bioactive motifs and their use in functionalized self-assembling peptides for NSC differentiation and neural tissue engineering. *Nanoscale.* 2012;4:2946-57.
57. Caprini A, Silva D, Zanoni I, Cunha C, Volontè C, Vescovi A, et al. A novel bioactive peptide: assessing its activity over murine neural stem cells and its potential for neural tissue engineering. *N Biotechnol.* 2013;30(5):552.

58. Raspa A, Saracino GAA, Pugliese R, Silva D, Cigognini D, Vescovi A, et al. Complementary co-assembling peptides: from In silico studies to in vivo application. *Adv Funct Mater.* 2014;24(40):6317-28.
59. Hartgerink JD, Beniash E, Stupp SI. Self-assembly and mineralization of peptide-amphiphile nanofibers. *Science.* 2001;294:23.
60. Niece KL, Hartgerink JD, Donners, Jack J J M, Stupp SI. Self-assembly combining two bioactive peptide-amphiphile molecules into nanofibers by electrostatic attraction. *J Am Chem Soc.* 2003;125(24):7146-7.
61. Beniash E, Hartgerink JD, Storrie H, Stendahl JC, Stupp SI. Self-assembling peptide amphiphile nanofiber matrices for cell entrapment. *Acta Biomater.* 2005;1:387-97.
62. Silva GA, Czeisler C, Niece KL, Beniash E, Harrington DA, Kessler JA, et al. Selective differentiation of neural progenitor cells by high-epitope density nanofibers. *Science.* 2004;303(5662):1352-5.
63. Tysseling-Mattiace VM, Sahni V, Niece KL, Birch D, Czeisler C, Fehlings MG, et al. Self-assembling nanofibers inhibit glial scar formation and promote axon elongation after spinal cord injury. *J Neurosci.* 2008;28(14):3814-23.
64. Angeloni NL, Bond CW, Tang Y, Harrington DA, Zhang S, Stupp SI, et al. Regeneration of the cavernous nerve by Sonic hedgehog using aligned peptide amphiphile nanofibers. *Biomaterials.* 2011;32(4):1091-101.
65. Chung W, Merzlyak A, Yoo SY, Lee S. Genetically engineered liquid-crystalline viral films for directing neural cell growth. *Langmuir.* 2010;26(12):9885.

66. Stephanopoulos N, Freeman R, North HA, Sur S, Jeong SJ, Tantakitti F, et al. Bioactive DNA-peptide nanotubes enhance the differentiation of neural stem cells into neurons. *Nano Lett.* 2015;15(1):603.
67. Allen TM, Cullis PR. Liposomal drug delivery systems: from concept to clinical applications. *Adv Drug Deliv Rev.* 2013;65:36-48.
68. Thid D, Holm K, Eriksson PS, Ekeröth J, Kasemo B, Gold J. Supported phospholipid bilayers as a platform for neural progenitor cell culture. *J Biomed Mater Res A.* 2008;84A(4):940-53.
69. Ananthanarayanan B, Little L, Schaffer DV, Healy KE, Tirrell M. Neural stem cell adhesion and proliferation on phospholipid bilayers functionalized with RGD peptides. *Biomaterials.* 2010;31:8706-15.
70. Kenny GD, Bienemann AS, Tagalakis AD, Pugh JA, Welser K, Campbell F, et al. Multifunctional receptor-targeted nanocomplexes for the delivery of therapeutic nucleic acids to the brain. *Biomaterials.* 2013;34:9190-200.
71. Tagalakis AD, Lee DHD, Bienemann AS, Zhou H, Munye MM, Saraiva L, et al. Multifunctional, self-assembling anionic peptide-lipid nanocomplexes for targeted siRNA delivery. *Biomaterials.* 2014;35:8406-15.
72. Weledji EP, Assobb JC. The ubiquitous neural cell adhesion molecule (N-CAM). *Ann Med Surg (Lond).* 2014;3(3):77-81.
73. Kiselyov VV, Skladchikova G, Hinsby AM, Jensen PH, Kulahin N, Soroka V, et al. Structural basis for a direct interaction between FGFR1 and NCAM and evidence for a regulatory role of ATP. *Structure.* 2003;11(6):691-701.

74. Cambon K, Hansen SM, Venero C, Herrero AI, Skibo G, Berezin V, et al. A synthetic neural cell adhesion molecule mimetic peptide promotes synaptogenesis, enhances presynaptic function, and facilitates memory consolidation. *J Neurosci*. 2004;24(17):4197-204.
75. Neiiendam JL, Køhler LB, Chistensen C, Li S, Pedersen MV, Ditlevsen DK, et al. An NCAM-derived FGF-receptor agonist, the FGL-peptide, induces neurite outgrowth and neuronal survival in primary rat neurons. *J Neurochem*. 2004;91(4):920-35.
76. Secher T, Novitskaia V, Berezin V, Bock E, Glenthøj B, Klementiev B. A neural cell adhesion molecule-derived fibroblast growth factor receptor agonist, the FGL-peptide, promotes early postnatal sensorimotor development and enhances social memory retention. *Neuroscience*. 2006;141(3):1289-99.
77. Dallérac G, Zerwas M, Novikova T, Callu D, Leblanc-Veyrac P, Bock E, et al. The neural cell adhesion molecule-derived peptide FGL facilitates long-term plasticity in the dentate gyrus in vivo. *Learn Memory*. 2011;18(5):306-13.
78. Ojo B, Rezaie P, Gabbott PL, Cowley TR, Medvedev NI, Lynch MA, et al. A neural cell adhesion molecule-derived peptide, FGL, attenuates glial cell activation in the aged hippocampus. *Exp Neurol*. 2011;232:318-28.
79. Jacobson J, Kiselyov V, Bock E, Berezin V. A peptide motif from the second Fibronectin module of the neural cell adhesion molecule, NCAM, NLIKQDDGGSPIRHY, is a binding site for the FGF receptor. *Neurochem Res*. 2008;33(12):2532-9.
80. Soroka V, Kiryushko D, Novitskaya V, Rønn LCB, Poulsen FM, Holm A, et al. Induction of neuronal differentiation by a peptide corresponding to the homophilic binding site of the

- second Ig module of the neural cell adhesion molecule. *J Biol Chem.* 2002;277(27):24676-83.
81. Kiryushko D, Kofoed T, Skladchikova G, Holm A, Berezin V, Bock E. A synthetic peptide ligand of neural cell adhesion molecule (NCAM), C3d, promotes neuritogenesis and synaptogenesis and modulates presynaptic function in primary cultures of rat hippocampal neurons. *J Biol Chem.* 2003;278(14):12325-34.
82. Sporns O, Edelman GM, Crossin KL. The neural cell adhesion molecule (N-CAM) inhibits proliferation in primary cultures of rat astrocytes. *Proc Natl Acad Sci.* 1995;92(2):542-6.
83. Kam L, Shain W, Turner JN, Bizios R. Selective adhesion of astrocytes to surfaces modified with immobilized peptides. *Biomaterials.* 2002;23(2):511-5.
84. Anderson AA, Kendal CE, Garcia-Maya M, Kenny AV, Morris-Triggs SA, Wu T, et al. A peptide from the first fibronectin domain of NCAM acts as an inverse agonist and stimulates FGF receptor activation, neurite outgrowth and survival. *J Neurochem.* 2005;95(2):570-83.
85. Palser AL, Norman AL, Saffell JL, Reynolds R. Neural cell adhesion molecule stimulates survival of premyelinating oligodendrocytes via the fibroblast growth factor receptor. *J Neurosci Res.* 2009;87(15):NA.
86. Joester A, Faissner A. The structure and function of tenascins in the nervous system. *Matrix Biol.* 2001;20(1):13-22.
87. Meiners S, Nur-e-Kamal MSA, Mercado MLT. Identification of a neurite outgrowth-promoting motif within the alternatively spliced region of human Tenascin-C. *J Neurosci.* 2001;21(18):7215.

88. Mercado MLT, Nur-e-Kamal A, Liu H, Gross SR, Movahed R, Meiners S. Neurite outgrowth by the alternatively spliced region of human Tenascin-C is mediated by neuronal $\alpha 7\beta 1$ integrin. *J Neurosci*. 2004;24(1):238-47.
89. Yurchenco P, Patton B. Developmental and pathogenic mechanisms of basement membrane assembly. *Curr Pharm Des*. 2009;15(12):1277-94.
90. Durbeej M. Laminins. *Cell Tissue Res*. 2010;339:259-68.
91. Timpl R, Rohde H, Robey PG, Rennard SI, Foidart JM, Martin GR. Laminin--a glycoprotein from basement membranes. *J Biol Chem*. 1979;254(19):9933.
92. Powell SK, Rao J, Roque E, Nomizu M, Kuratomi Y, Yamada Y, et al. Neural cell response to multiple novel sites on laminin-1. *J Neurosci Res*. 2000;61(3):302-12.
93. Massia SP, Holecko MM, Ehteshami GR. In vitro assessment of bioactive coatings for neural implant applications. *J Biomed Mater Res A*. 2004;68A(1):177-86.
94. Jucker M, Kleinman HK, Ingram DK. Fetal rat septal cells adhere to and extend processes on basement membrane, laminin, and a synthetic peptide from the laminin A chain sequence. *J Neurosci Res*. 1991;28:507-17.
95. Yu TT, Shoichet MS. Guided cell adhesion and outgrowth in peptide-modified channels for neural tissue engineering. *Biomaterials*. 2005;26(13):1507-14.
96. Tong YW, Shoichet MS. Enhancing the neuronal interaction on fluoropolymer surfaces with mixed peptides or spacer group linkers. *Biomaterials*. 2001;22:1029-34.
97. Hosseinkhani H, Hiraoka Y, Li C, Chen Y, Yu D, Hong P, et al. Engineering three-dimensional collagen-IKVAV matrix to mimic neural microenvironment. *ACS Chem Neurosci*. 2013;4(8):1229-35.

98. Gelain F, Bottai D, Vescovi A, Zhang S. Designer self-assembling peptide nanofiber scaffolds for adult mouse neural stem cell 3-dimensional cultures. *PloS one*. 2006;1(1):e119.
99. Zhang ZX, Zheng QX, Wu YC, Hao DJ. Compatibility of neural stem cells with functionalized self- assembling peptide scaffold In vitro. *Biotechnol Bioprocess Eng*. 2010;15:545-55.
100. Sun W, Incitti T, Migliaresi C, Quattrone A, Casarosa S, Motta A. Viability and neuronal differentiation of neural stem cells encapsulated in silk fibroin hydrogel functionalized with an IKVAV peptide. *J Tissue Eng Regen Med*. 2015.
101. Itoh S, Matsuda A, Kobayashi H, Ichinose S, Shinomiya K, Tanaka J. Effects of a laminin peptide (YIGSR) immobilized on crab-tendon chitosan tubes on nerve regeneration. *J Biomed Mater Res Part B Appl Biomater*. 2005;73B(2):375-82.
102. Dai W, Belt J, Saltzman WM. Cell-binding peptides conjugated to poly(ethylene glycol) promote neural cell aggregation. *Nat Biotechnol*. 1994;12:797-801.
103. Dhoot NO, Tobias CA, Fischer I, Wheatley MA. Peptide-modified alginate surfaces as a growth permissive substrate for neurite outgrowth. *J Biomed Mater Res A*. 2004;71A(2):191-200.
104. Cooke MJ, Zahir T, Phillips SR, Shah DSH, Athey D, Lakey JH, et al. Neural differentiation regulated by biomimetic surfaces presenting motifs of extracellular matrix proteins. *J Biomed Mater Res A*. 2010;93(3):NA.
105. Matsuzawa M, Weight FF, Potember RS, Liesi P. Directional neurite outgrowth and axonal differentiation of embryonic hippocampal neurons are promoted by a neurite outgrowth domain of the B2-chain of laminin. *Int J Devl Neuroscience*. 1996;14(3):283-95.

106. Masuda T, Sakuma C, Kobayashi K, Kikuchi K, Soda E, Shiga T, et al. Laminin peptide YIGSR and its receptor regulate sensory axonal response to the chemoattractive guidance cue in the chick embryo. *J Neurosci Res.* 2009;87(2):353-9.
107. Yao L, Wang S, Cui W, Sherlock R, O'Connell C, Damodaran G, et al. Effect of functionalized micropatterned PLGA on guided neurite growth. *Acta Biomater.* 2009;5(2):580-8.
108. Hiraoka M, Kato K, Nakaji-Hirabayashi T, Iwata H. Enhanced survival of neural cells embedded in hydrogels composed of collagen and laminin-derived cell adhesive peptide. *Bioconjugate Chem.* 2009;20(5):976-83.
109. Yao L, Damodaran G, Nikolskaya N, Gorman AM, Windebank A, Pandit A. The effect of laminin peptide gradient in enzymatically cross-linked collagen scaffolds on neurite growth. *J Biomed Mater Res A.* 2010;92(2):484-92.
110. Williams CM, Engler AJ, Slone RD, Galante LL, Schwarzbauer JE. Fibronectin expression modulates mammary epithelial cell proliferation during acinar differentiation. *Cancer Res.* 2008;68(9):3185-92.
111. Pankov R, Yamada K. Fibronectin at a glance. *J Cell Sci.* 2002;115:3861-563.
112. Wierzbicka-Patynowski I, Schwarzbauer JE. The ins and outs of fibronectin matrix assembly. *J Cell Sci.* 2003;116(16):3269-76.
113. Ruoslahti E. RGD and other recognition sequences for integrins. *Annu Rev Cell Dev Biol.* 1996;12(1):697-715.
114. Yamada KM. Adhesive recognition sequences. *J Biol Chem.* 1991;266(20):12809.

115. Jeon WB, Park BH, Choi SK, Lee K, Park J. Functional enhancement of neuronal cell behaviors and differentiation by elastin-mimetic recombinant protein presenting Arg-Gly-Asp peptides. *BMC Biotechnol.* 2012;12(1):61.
116. Kafi MA, Kim T, Kim H, Yea C, Choi J. Effects of nanopatterned RGD peptide layer on electrochemical detection of neural cell chip. *Biosens Bioelectron.* 2010;26(4):1359-65.
117. Thelen K, Kedar V, Panicker AK, Schmid R, Midkiff BR, Maness PF. The neural cell adhesion molecule L1 potentiates integrin-dependent cell migration to extracellular matrix proteins. *J Neurosci.* 2002;22(12):4918.
118. Romano NH, Madl CM, Heilshorn SC. Matrix RGD ligand density and L1CAM-mediated Schwann cell interactions synergistically enhance neurite outgrowth. *Acta Biomater.* 2015;11:48-57.
119. Sorribas H, Braun D, Leder L, Sonderegger P, Tiefenauer L. Adhesion proteins for a tight neuron–electrode contact. *J Neurosci Methods.* 2001;104(2):133-41.
120. Schense JC, Hubbell JA. Three-dimensional migration of neurites is mediated by adhesion site density and affinity. *J Biol Chem.* 2000;275(10):6813-8.
121. Markó K, Kohidi T, Hádinger N, Jelítai M, Mezo G, Madarász E. Isolation of radial glia-like neural stem cells from fetal and adult mouse forebrain via selective adhesion to a novel adhesive peptide-conjugate. *PloS one.* 2011;6(12):e28538.
122. Naghdi P, Tiraihi T, Ganji F, Darabi S, Taheri T, Kazemi H. Survival, proliferation and differentiation enhancement of neural stem cells cultured in three-dimensional polyethylene glycol RGD hydrogel with tenascin. *J Tissue Eng Regen Med.* 2014:n/a.

123. Knight GT, Sha J, Ashton RS. Micropatterned, clickable culture substrates enable in situ spatiotemporal control of human PSC-derived neural tissue morphology. *Chem Commun.* 2015;51:5238-41.
124. Jenkins P, Laughter M, Lee D, Lee Y, Freed C, Park D. A nerve guidance conduit with topographical and biochemical cues: potential application using human neural stem cells. *Nanoscale Res Lett.* 2015;10(1):1-7.
125. Peluffo H, González P, Arís A, Acarin L, Saura J, Villaverde A, et al. RGD domains neuroprotect the immature brain by a glial-dependent mechanism. *Ann Neurol.* 2007;62(3):251-61.
126. Yan Q, Yin Y, Li B. Use new PLGL-RGD-NGF nerve conduits for promoting peripheral nerve regeneration. *Biomed Eng Online.* 2012;11(1):36.
127. Aota S, Nomizu M, Yamada K. The short amino acid sequence Pro-His-Ser-Arg-Asn in human Fibronectin enhances cell-adhesive function. *J Biol Chem.* 1994;269(40):24756-61.
128. Romero MI, Rangappa N, Garry MG, Smith GM. Functional regeneration of chronically injured sensory afferents into adult spinal cord after neurotrophin gene therapy. *J of Neurosci.* 2001;21(21):8408-16.
129. Huang EJ, Reichardt LF. Neurotrophins: roles in neuronal development and function. *Annu Rev Neurosci.* 2001;24:677-736.
130. Siegel GJ, Chauhan NB. Neurotrophic factors in Alzheimer's and Parkinson's disease brain. *Brain Res Rev.* 2000;33:199-227.

131. Beglova N, LeSauter L, Ekiel I, Saragovi HU, Gehring K. Solution structure and internal motion of a bioactive peptide derived from nerve growth factor. *J Biol Chem.* 1998;273(37):23652-8.
132. Debeir T, Saragovi HU, Cuello AC. A nerve growth factor mimetic TrkA antagonist causes withdrawal of cortical cholinergic boutons in the adult rat. *Proc Natl Acad Sci.* 1999;96(7):4067-72.
133. Bramham CR, Messaoudi E. BDNF function in adult synaptic plasticity: The synaptic consolidation hypothesis. *Prog Neurobiol.* 2005;76:99-125.
134. O'Leary PD, Hughes RA. Design of potent peptide mimetics of brain-derived neurotrophic factor. *J Biol Chem.* 2003;278(28):25738-44.
135. Shin MK, Kim HG, Kim KL. A novel trimeric peptide, Neuropep-1-stimulating brain-derived neurotrophic factor expression in rat brain improves spatial learning and memory as measured by the Y-maze and Morris water maze. *J Neurochem.* 2011;116:205-16.
136. Massa SM, Yang T, Xie Y, Shi J, Bilgen M, Joyce JN, et al. Small molecule BDNF mimetics activate TrkB signaling and prevent neuronal degeneration in rodents. *J Clin Invest.* 2010;120(5):1774-85.
137. Nielsen J, Gotfryd K, Li S, Kulahin N, Soroka V, Rasmussen KK, et al. Role of glial cell line-derived neurotrophic factor (GDNF)-neural Cell adhesion molecule (NCAM) interactions in induction of neurite outgrowth and identification of a binding site for NCAM in the heel region of GDNF. *J Neurosci.* 2009;29(36):11360.

138. Grothe C, Haastert K, Jungnickel J. Physiological function and putative therapeutic impact of the FGF-2 system in peripheral nerve regeneration — lessons from in vivo studies in mice and rats. *Brain Res.* 2006;51(2):293-9.
139. Ishii K, Nakamura M, Dai H, Finn TP, Okano H, Toyama Y, et al. Neutralization of ciliary neurotrophic factor reduces astrocyte production from transplanted neural stem cells and promotes regeneration of corticospinal tract fibers in spinal cord injury. *Journal of Neuroscience Research.* 2006 December;84(8):1669-81.
140. Chohan MO, Li B, Blanchard J, Tung Y, Heaney AT, Rabe A, et al. Enhancement of dentate gyrus neurogenesis, dendritic and synaptic plasticity and memory by a neurotrophic peptide. *Neurobiol Aging.* 2011;32(8):1420-34.
141. Li B, Wanka L, Blanchard J, Liu F, Chohan MO, Iqbal K, et al. Neurotrophic peptides incorporating adamantane improve learning and memory, promote neurogenesis and synaptic plasticity in mice. *FEBS Lett.* 2010;584(15):3359-65.
142. Russmann V, Seeger N, Zellinger C, Hadamitzky M, Pankratova S, Wendt H, et al. The CNTF-derived peptide mimetic Cintrofin attenuates spatial-learning deficits in a rat post-status epilepticus model. *Neurosci Lett.* 2013;556:170-5.
143. Garcia-Bennett AE, Kozhevnikova M, König N, Zhou C, Leao R, Knöpfel T, et al. Delivery of differentiation factors by mesoporous silica particles assists advanced differentiation of transplanted murine embryonic stem cells. *Stem Cells Transl Med.* 2013;2(11):906-15.
144. Lonardo, E. Parish, C. L., Ponticelli S, Marasco D, Ribeiro D, Ruvo M, Falco SD, et al. A small synthetic cripto blocking peptide improves neural induction, dopaminergic

- differentiation, and functional integration of mouse embryonic stem cells in a rat model of Parkinson's disease. *Stem Cells*. 2010;28:1326-37.
145. Strizzi L, Bianco C, Normanno N, Salomon D. Cripto-1: a multifunctional modulator during embryogenesis and oncogenesis. *Oncogene*. 2005;24(37):5731-41.
146. Minchiotti G. Nodal-dependant Cripto signaling in ES cells: from stem cells to tumor biology. *Oncogene*. 2005;24(37):5668-75.
147. Parish CL, Arenas E. Stem-cell-based strategies for the treatment of Parkinson's disease. *Neurodegenerative Dis*. 2007;4:339-47.
148. Pearse DD, Pereira FC, Marcillo AE, Bates ML, Berrocal YA, Filbin MT, et al. cAMP and Schwann cells promote axonal growth and functional recovery after spinal cord injury. *Nat Med*. 2004;10(6):610-6.
149. Lu P, Yang H, Jones LL, Filbin MT, Tuszynski MH. Combinatorial therapy with neurotrophins and cAMP promotes axonal regeneration beyond sites of spinal cord injury. *J Neurosci*. 2004;24(28):6402-9.
150. Ichiyama T, Campbell IL, Furukawa S, Catania A, Lipton JM. Autocrine α -melanocyte-stimulating hormone inhibits NF- κ B activation in human glioma. *J Neurosci Res*. 1999;58(5):684-9.
151. Yang WS, Park YC, Kim JH, Kim H, Yu T, Byeon SE, et al. Nanostructured, self-assembling peptide K5 blocks TNF- α and PGE2 production by suppression of the AP-1/p38 pathway. *Mediators Inflamm*. 2012;2012:489810-8.
152. Zhong Y, Bellamkonda RV. Controlled release of anti-inflammatory agent α -MSH from neural implants. *J Control Release*. 2005;106(3):309-18.

153. Mura S, Nicolas J, Couvreur P. Stimuli-responsive nanocarriers for drug delivery. *Nat Mater.* 2013;12(11):991.
154. Ulery BD, Nair LS, Laurencin CT. Biomedical applications of biodegradable polymers. *J Polym Sci , Part B: Polym Phys.* 2011;49(12):832-64.
155. Gomes ME, Reis RL. Biodegradable polymers and composites in biomedical applications: from catgut to tissue engineering. *Int Mater Rev.* 2004;49(5):261-73.
156. Yoshida T, Lai TC, Kwon GS, Sako K. pH- and ion-sensitive polymers for drug delivery. *Expert Opin Drug Deliv.* 2013;10(11):1497-513.
157. Sun PZ, Zhou J, Sun W, Huang J, van Zijl, Peter C M. Detection of the ischemic penumbra using pH-weighted MRI. *J Cereb Blood Flow Metab.* 2007;27(6):1129-36.
158. Harston GWJ, Tee YK, Blockley N, Okell TW, Thandeswaran S, Shaya G, et al. Identifying the ischaemic penumbra using pH-weighted magnetic resonance imaging. *Brain.* 2015;138(1):36-42.
159. Zhou J, van Zijl P. Defining an acidosis-based ischemic penumbra from pH-weighted MRI. *Transl Stroke Res.* 2012;3(1):76-83.
160. Hu Q, Katti PS, Gu Z. Enzyme-responsive nanomaterials for controlled drug delivery. *Nanoscale.* 2014;6:12273-86.
161. Luo C, Sun J, Sun B, He Z. Prodrug-based nanoparticulate drug delivery strategies for cancer therapy. *Trends Pharmacol Sci.* 2014;35(11):556-66.
162. Law B, Tung C. Proteolysis: A biological process adapted in drug delivery, therapy, and imaging. *Bioconjugate Chem.* 2009;20(9):1683-965.

163. Law B, Tung C. Structural modification of protease inducible preprogrammed nanofiber precursor. *Biomacromolecules*. 2008;9(2):421-5.
164. Chau Y, Luo Y, Cheung ACY, Nagai Y, Zhang S, Kobler JB, et al. Incorporation of a matrix metalloproteinase-sensitive substrate into self-assembling peptides - A model for biofunctional scaffolds. *Biomaterials*. 2008;29:1713-9.
165. Lévesque SG, Shoichet MS. Synthesis of enzyme-degradable, peptide-cross-linked dextran hydrogels. *Bioconjugate Chem*. 2007;18(3):874-85.
166. Nakanishi H. Microglial functions and proteases. *Mol Neurobiol*. 2003;27:163-76.
167. Nakanishi H. Microglial proteases: strategic targets for neuroprotective agents. *Curr Neuropharmacol*. 2003;1(1):99-108.
168. Petanceska S, Canoll P, Devi LA. Expression of rat cathepsin S in phagocytic cells. *J Biol Chem*. 1996;271(8):4403-9.
169. Nishioku T, Hashimoto K, Yamashita K, Liou S, Kagamiishi Y, Maegawa H, et al. Involvement of cathepsin E in exogenous antigen processing in primary cultured murine microglia. *J Biol Chem*. 2002;277(7):4816-22.
170. Ryan RE, Sloane BF, Sameni M, Wood PL. Microglial cathepsin B: an immunological examination of cellular and secreted species. *J Neurochem*. 1995;65(3):1035-45.
171. Kingham PJ, Pocock JM. Microglial secreted cathepsin B induces neuronal apoptosis. *Journal of Neurochemistry*. 2001;76(5):1475-84.
172. Kakimura J, Kitamura Y, Takata K, Umeki M, Suzuki S, Shibagaki K, et al. Microglia activation and amyloid- β clearance induced by exogenous heat-shock proteins. *FASEB J*. 2002;16(6):601-3.

173. Qiu WQ, Ye Z, Kholodenko D, Seubert P, Selkoe DJ. Degradation of amyloid β -protein by a metalloprotease secreted by microglia and other neural and non-neural cells. *J Biol Chem.* 1997;272(10):6641-6.
174. Qiu WQ, Walsh DM, Ye Z, Vekrellis K, Zhang J, Podlisny MB, et al. Insulin-degrading enzyme regulates extracellular levels of amyloid b-protein by degradation. *J Biol Chem.* 1998;273:32730-8.
175. Shields DC, Tyor WR, Deibler GE, Hogan EL, Banik NL. Increased calpain expression in activated glial and inflammatory cells in experimental allergic encephalomyelitis. *PNAS.* 1998;95(10):5768-72.
176. Shields DC, Schaecher KE, Saido TC, Banik NL. A putative mechanism of demyelination in multiple sclerosis by a proteolytic enzyme, calpain. *PNAS.* 1999;96(20):11486-91.
177. Takai N, Nakanishi H, Tanabe K, Nishioku T, Sugiyama T, Fujiwara M, et al. Involvement of caspase-like proteinases in apoptosis of neuronal PC12 cells and primary cultured microglia induced by 6-hydroxydopamine. *J Neurosci Res.* 1998;54(2):214-22.
178. Ferrari D, Los M, Bauer MKA, Vandenabeele P, Wesselborg S, Schulze-Osthoff K. P2Z purinoreceptor ligation induces activation of caspases with distinct roles in apoptotic and necrotic alterations of cell death. *FEBS Lett.* 1999;447(1):71-5.
179. Stohwasser R, Giesebrecht J, Kraft R, Müller E, Häusler KG, Kettenmann H, et al. Biochemical analysis of proteasomes from mouse microglia: Induction of immunoproteasomes by interferon- γ and lipopolysaccharide. *Glia.* 2000;29(4):355-65.

180. Fine SM, Maggirwar SB, Elliott PR, Epstein LG, Gelbard HA, Dewhurst S. Proteasome blockers inhibit TNF- α release by lipopolysaccharide stimulated macrophages and microglia: implications for HIV-1 dementia. *J Neuroimmunol.* 1999;95(1):55-64.
181. Flavin MP, Zhao G, Ho LT. Microglial tissue plasminogen activator (tPA) triggers neuronal apoptosis in vitro. *Glia.* 2000;29(4):347-54.
182. Nakajima K, Tsuzaki N, Shimojo M, Hamanoue M, Kohsaka S. Microglia isolated from rat brain secrete a urokinase-type plasminogen activator. *Brain Res.* 1992;577(2):285-92.
183. Nakajima K, Shimojo M, Hamanoue M, Ishiura S, Sugita H, Kohsaka S. Identification of elastase as a secretory protease from cultured rat microglia. *J Neurochem.* 1992;58(4):1401-8.
184. Romanic AM, White RF, Arleth AJ, Ohlstein EH, Frank C B. Matrix metalloproteinase expression increases after cerebral focal ischemia in rats: inhibition of matrix metalloproteinase-9 reduces Infarct size. *Stroke.* 1998;29(5):1020-30.
185. Jiang X, Namura S, Nagata I. Matrix metalloproteinase inhibitor KB-R7785 attenuates brain damage resulting from permanent focal cerebral ischemia in mice. *Neurosci Lett.* 2001;305(1):41-4.
186. Asahi M, Asahi K, Jung J, Zoppo GJ, Fini ME, Lo EH. Role for matrix Metalloproteinase 9 focal cerebral ischemic: effects of gene knockout and enzyme inhibition with BB-94. *J Cereb Blood Flow Metab.* 2000;20:1681-9.
187. Rosenberg GA, Estrada EY, Dencoff JE. Matrix metalloproteinases and TIMPs are associated with blood-brain barrier opening after reperfusion in rat brain. *Stroke.* 1998;29(10):2189.

Chapter 2.***Towards Developing Bioresponsive, Self-Assembled Peptide Materials: Dynamic Morphology and Fractal Nature of Nanostructured Matrices***

Koss, K^{1,2}; Unsworth, LD^{1,2,*}

1. Department of Chemical and Materials Engineering, University of Alberta, 11487 89 ave, Edmonton, AB, T6G 2M7

2. National Institute for Nanotechnology, NRC, 11421 Saskatchewan Dr NW, Edmonton, AB, T6G 2M9

Corresponding Author Information: Larry D. Unsworth, larry.unsworth@ualberta.ca, [780-492-6020](tel:780-492-6020)

Abstract

(RADA)₄ nanoscaffolds have many inherent qualities that make them excellent candidates for use as peptide delivery vehicles: relatively easy synthesis, *in-situ* assembly, and molecularly programmable allowing for use of multiple release strategies whilst presenting a variety of bioactive ligands all on one ‘construct’. Local, on-demand release of peptides triggered *via* proteolysis of tethered peptide sequences is a novel means of delivering peptides that is seldom applied. However, the spatial-temporal morphology of engineered self-assembling nanoscaffolds may greatly influence the ability for enzymes to both diffuse into as well as actively cleave substrate. The dynamic nanoscaffold morphology is seldom observed and little understood, despite the fact that this property of the system may dramatically affect the overall peptide release. In addition, fractal networks observed in nanoscaffolds are linked to the fractal nature of diffusion from these systems. Thus, matrix morphology and fractal dimension of virgin (RADA)₄ and mixtures of (RADA)₄ and matrix metalloproteinase 2 (MMP-2) cleavable substrate modified (RADA)₄ were characterized over time. MMP-2 cleavable substrates of high (GPQG+IASQ, CP1) and low (GPQG+PAGQ, CP2) activity were chosen. Relatively large nanofiber bundles were observed upon incorporation of CP1 and CP2 domains, when compared to (RADA)₄ only. To further elucidate the effect of peptide composition on nanoscaffold morphology and fractal nature, mixtures of 25:75, 50:50 and 75:25 (RADA)₄:CP1 and 25:75 (RADA)₄:CP2 were studied. After 2 hs of incubation, nanofiber networks showed an established fractal nature, however nanofibers continued to bundle in all cases as incubation times increased. It was observed that despite extensive nanofiber bundling after 24 hs of incubation time, the CP1 and CP2 nanoscaffolds were susceptible to MMP-2 cleavage, even for the most bundled of the structures. The properties of these engineered nanoscaffolds characterized herein illustrate that they are an excellent candidate as an enzymatically initiated peptide delivery platform.

Keywords: Self-assembling peptides, (RADA)₄, MMP-2, Nanoscaffold, Hausdorff dimension, Fractal

1. Introduction

Peptides are the fastest growing segment of the pharmaceutical industry, and are generally considered the ideal therapeutic: specific, potent, small enough for diffusion, etc [1]. That said, peptide therapeutics suffer from a major drawback, they are easily cleaved by circulating proteases and are thus short lived; this factor makes them almost impossible to effectively deliver *in vivo*. To circumvent these issues, peptide therapeutics have been incorporated into delivery vehicles with 'on-demand' release cues, such as specific proteolytic cleavage sites [2 - 3]. Of these systems, hydrogels that form nanofiber networks have dynamic and novel applications due to their unique properties, including: capable of swelling with water, housing drugs and ligands, and being made with a multitude of mechanical and morphological features that provide multiple means of controlling release from these structures [4]. However, acquiring exact and tuneable release mechanisms and morphological features can be extremely complicated, needing additional chemical synthesis, and may require toxic co-solvents, chemical triggers, or full transplantation to provide a fully formed network *in vivo* [5]. In addition, high throughput and comprehensive studies that are often imperative to drug discovery, measuring precise timed drug release and cell response, are not easily performed with systematic processing on such materials [6 - 7]. With these limitations in mind, the ideal drug delivery hydrogel should incorporate accurate release cues, have reproducible gelation morphology, and be simple to synthesize. To this end, controlled release peptide content was precisely modulated and corresponding

nanoscale morphology was observed of a self-assembling peptide (SAP), capable of forming a three-dimensional (3-D) nanoscaffold upon injection into a physiologically relevant aqueous environment, which can be made using well-established automated peptide synthesis.

SAPs were created to spontaneously assemble into a nanoscaffolding material in the presence of aqueous salts, *in vivo*, by formation of non-covalent van der Waals forces, hydrogen bonds, and electrostatic interactions [8], resulting in materials capable of emulating pore and nanoscale fiber morphology of natural extra cellular matrices [9 - 12]. Further, these SAPs can be easily programmed with additional peptide groups, including cleavage sites and drugs, during solid-state synthesis, simplifying their overall fabrication into one predictable step. One such example of a relatively well characterized SAP candidate for molecular-level programming is the RADA16 or (RADA)₄ construct (arginine-alanine-aspartate-alanine)₄ [13 - 15]. *In situ* tissue engineering and diffusion based release of drug and protein factors has been demonstrated in this SAP as well as matrix metalloproteinase-2 (MMP-2) cleavable domain incorporation and digestion within the (RADA) sequence [12, 16 - 17]. Self-assembly morphology has been studied through various techniques, including circular dichroism, and atomic force, scanning, and transmission electron microscopy [18]. With the exception of short-term molecular modelling studies, few comprehensive time-based studies for (RADA)₄ assembly over a 24 h period have been conducted.¹⁸ Without clarification of the matrix morphology as a function of assembly time, it may be difficult to correlate the subsequent results (i.e., drug release through to cellular activity) obtained from different labs who are working on similar materials.

Various forms of proteolytically triggered drug release systems have been studied, including both nanoparticles and hydrogels, and have also been applied as therapy and imaging modalities [20]. The MMP family is comprised of multiple enzymes that are highly spatiotemporally

regulated within a large variety of diseases, including various forms of cancer and inflammatory responses [21]. In particular, MMP-2 is abundantly secreted during injury and is well known to cleave both high (GPQG+IASQ, CP1) and low (GPQG+PAGQ, CP2) affinity substrates, where the '+' indicates the sessile cleavage bond [22 - 23]. Previous work has incorporated these MMP-2 substrates into digestible polymer cross-linkers for the specific purpose of degrading dextran-based hydrogels to release embedded fluorophores [24]. That said, there are no known studies that have utilized these domains for the express purpose of understanding their effect on self-assembly of peptides and subsequent morphology.

Fractals are a measure of pattern symmetry that is present in every possible scale and appear in many facets of biology and life. In apparently disordered systems, fractal patterns may emerge and can indicate a relationship between the function of cells and biological materials, where no other information can be derived. In networked nanofibers, such as agarose and DNA-binding chomatin, fractal dimensions of morphology (ie. porosity) are highly related to protein binding and diffusion coefficients [25 - 26]. Therefore, fractal nature may be strongly indicative of both the substrate-enzyme interaction and the diffusion within a matrix. One commonly used technique for classifying a fractal is the Hausdorff dimension analysis, which is an image-based technique employed to observe common patterns in otherwise random cell growth, laminin polymerization, nanotubes and nanovesicles, and other β -sheet forming SAPs [17, 27 - 32]. Despite its wide use, no fractal or Hausdorff study has been observed in (RADA)₄, nor has it been linked to differences in growth and the addition of cleavage sites for drug release.

In this study, self-assembly kinetics of (RADA)₄ were assessed for systems that incorporated MMP-2 substrates (RADA)₄-GG-GPQG+IASQ (CP1) and (RADA)₄-GG-GPQG+PAGQ (CP2) to evaluate potential differences in resulting nanostructures, bulk bundling of nanofibers, fractal

dimension, and cleavage (Figure 1). Morphology and assembly kinetics may vary with CP1 and CP2 and precise doping may be desired in future studies, therefore 100%, 75%, 50%, and 25% (RADA)₄-CP1/CP2 were mixed with (RADA)₄, and observed over 0, 1, 2, 4, 6, and 24 hs. Resulting nanofibers were imaged using transmission electron microscopy (TEM). The resulting structures were statistically characterized by measuring bundle thickness and change in porosity. To estimate the fractal nature of these materials, which are related to protein binding and diffusion, the Hausdorff fractal dimensions were also estimated from these architectures, using box counting. MMP-2 was introduced to systems that exhibited extensive nanofiber bundling to evaluate if cleavage was still possible, where matrix-assisted laser desorption/ionization time of flight (MALDI-TOF/TOF) mass-spectrometry was used to characterize cleavage.

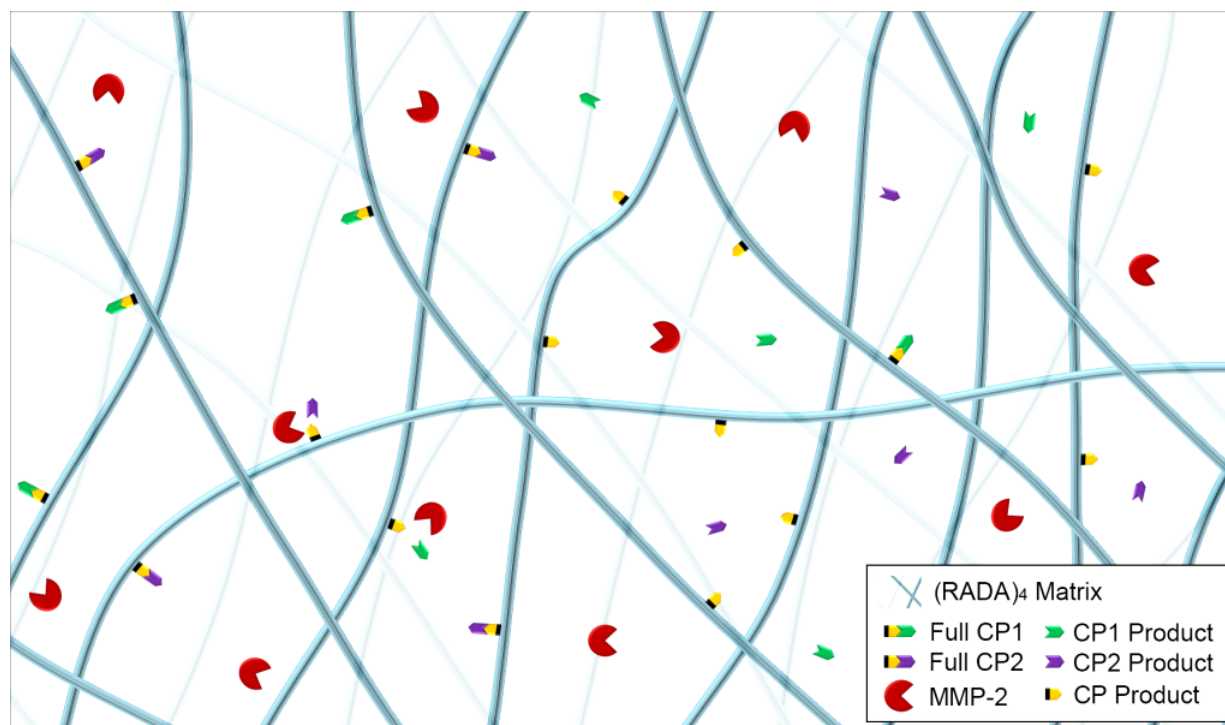


Figure 2.1. Schematic of nanofiber formation and MMP-2 cleavage of (RADA)₄, (RADA)₄-GG-GPQG+IASQ (CP1), and (RADA)₄-GG-GPQG+PAGQ (CP2). '+' Denotes cleavage site and CP1, CP2, and CP products are IASQ, PAGQ, and (RADA)₄-GG-GPQG, respectively.

2. Materials and Methods

2.1. Materials

Methanol (99.8%), dichloromethane (99.8%), acetonitrile (ACN) (99.8%), N-dimethylformamide (99.8%), piperidine (99.5% biotech. grade), N-diisopropylethylamine (99.5% biotech. grade), 1-cyano-2-ethoxy-2-oxoethylideneaminoxydimethylamino-morpholinocarbenium hexafluorophosphate (COMU) (97%), triisopropylsilane (99%), trifluoroacetic acid (TFA) (99%), α -cyano-4-hydroxycinnamic acid (HCCA) were acquired from Sigma (Oakville, ON) and used without further purification. Fmoc amino acids and wang resins were purchased from ChemPep (Wellington, FL). (Redding, CA). Active human recombinant MMP-2 was acquired from EMD Millipore (Etobicoke, ON). Uranyl acetate and TEM grids were obtained from Ted Pella Inc.

2.2. Peptide Synthesis

All self-assembling peptides, (RADA)₄, (RADA)₄-GG-GPQG+IASQ, and (RADA)₄-GG-GPQG+PAGQ were synthesized using an ABI 433A Peptide Synthesizer. Fmoc chemistry was chosen and coupling was performed using 500 mM concentrations of COMU and ethyl (hydroxyimino)cyanoacetate. Fastmoc protocols were chosen and coupling was doubled and cycles were extended 15 minutes. All other protocols and methods were specified by the ABI 433A manual [33]. A cleavage cocktail of (96/2/2) TFA, water, and triisopropylsilane was used. ABI 4800 matrix-assisted laser desorption/ionization time of flight (MALDI-TOF/TOF) mass-spectrometry was used to assess sample masses. HCCA matrix concentrations of 10 mg/mL were suspended in 1:1 ACN:H₂O (0.1% TFA). Peptides were purified to 95% or greater using high performance liquid chromatography (HPLC) and a Zorbax Eclipse C18 reverse-phase semi-preparative 9.4 x 250 mm column (Agilent Technologies) using a H₂O-ACN (0.1% TFA)

loading. Purity was determined with HPLC with a Luna C18 reverse phase 4.6 x 250 mm column, by comparing the areas under the major curve to the minor curve areas in the HPLC spectra using Agilent's in-house software. MALDI mass spectra and chromatographs are presented in the supplemental section (Figure A2.1).

2.3. MMP-2 Enzymatic Treatment

Preparation for MMP-2 treatment was adapted from Chau *et al.* [17]. The gel was prepared by dissolving 1 % (w/v) of the peptides (RADA)₄-CP1/CP1 in TNC buffer (pH 7.4, 50 mM tris-HCl, 150 mM NaCl, 1 mM CaCl₂). These solutions were sonicated for 30 minutes and allowed to gel over 24 hs. TNC buffer was carefully removed from the surface of the gel (10% of the volume) and refreshed, until pH of the removed buffer was balanced to 7.4. Active MMP-2 in TNC buffer was added as the final refreshed treatment 1:9 by volume for 40 nM enzyme concentration. TNC buffer, without MMP2, was added as a control. These mixtures were incubated for 2 weeks at 37°C to assure full digestion of the hydrogel. The samples were made soluble by diluting 1:1000 in 1:1 water/acetonitrile (0.1% TFA) and were subsequently sonicated for 30 minutes. The substrate and product fragments were measured by MALDI mass spectra, using the previously mentioned protocol.

2.4. Transmission Electron Microscopy

(RADA)₄ samples were pipetted, in 5 µl aliquots, onto 200 mesh perforated formvar carbon coated copper grids (Ted Pella, Redding, CA). All samples were collected after 30 minutes of sonication, and 0, 1, 2, 4, 6, and 24 hours of incubation at 37°C. 5 µl of a 4% aqueous uranyl acetate stain was then applied to samples for 5 minutes. In between steps, sample and stain were filter-dried using filter paper wedges cut from Whatman filter paper pieces. The negative staining

technique was after Dawes [34], and labels the peptide surrounding buffer with a uranium-based heavy metal salt, where images are generated by electron transmission through the sample. Grids were placed into the grid holder of a transmission electron microscope. All TEM was performed on a Philips FEI Morgagni transmission electron microscope with a 80 kV accelerating voltage and a tungsten thermionic emission source. Representative images were chosen for each group.

2.5. Nanofiber Bundle and Hausdorff Dimension Analyses

All image processing and analysis was done using MATLAB® R2012b (The Mathworks Inc. Natick, MA). Bundles were measured by perpendicular distance across whole continuous nanofibers. These were chosen randomly 50 times for three images, repeated over three samples, for a total of 150 random measurements for each sample. The standard error mean was chosen across the three images.

Fractal dimensions were derived using a box counting method, similarly performed by Hochman-Mendez *et al.* in laminin protein fibers [28]. MATLAB code was modified from French and Costa and an example is shown in the appendices [35 - 36]. The Hausdorff dimension is an indication of likewise shapes in complex geometries based on specified points or members [37]. It is a method of quantifying fractals, but image-base calculation is not implied, therefore box counting was used to estimate these dimensions in this study. Using fixed grids with varying box sizes r , images were processed and the amount of boxes associated with a set $D(r)$ were counted [38 - 40]. The following equation (1) was then used to estimate the fractal dimension:

$$D_H = - \frac{\Delta[\log D(r)]}{\Delta \log(1/r)} \quad (1)$$

where D_H is the Hausdorff-Besicovitch dimension or simply the box count fractal dimension. All images were processed as full images in greyscale, and the functions `im2bw` and `imfill` were used to convert to binary and fill regions, respectively. An example of this and the resulting box count curve is shown in the supplemental material (Figure A3.2). All samples were analyzed based on the mean and standard deviation of $n=3$, where significance was based on $p < 0.05$ (t -test) for individual discussed values.

3. Results

3.1. Nanoscale Morphology

Nanoscale morphology of 0.5% w/v peptide solutions of (RADA)₄, (RADA)₄-CP1, and (RADA)₄-CP2 were inspected using TEM upon 24 hs assembly with higher magnifications (Figure 2.2.). Also shown are images at 0, 1, 2, 4, 6, and 24 hs post-sonication (Figure 2.3.). Nanofibers are present in all images past 1 hour and networks continue to develop with time. At 0 hs, small 5-10 nm diameter particles seem present in all images, but (RADA)₄ and (RADA)₄-CP2 seem to already have individual nanofibers present, speaking to the rapidity in which nanofibers form. After 1 h, individual nanofibers have formed in (RADA)₄, (RADA)₄-CP1 and (RADA)₄-CP2 and by 2 hs, a mesh network of nanofibers exists in all groups. The network in (RADA)₄ grows more defined and interconnected with time and has a consistent structure by 6 hs. Individual nanofiber thickness remains between 5-15 nm. Both (RADA)₄-CP1 and (RADA)₄-CP2 seem to assemble into thick bundled and branched networks up to 150 nm, which were not observed for (RADA)₄. These systems seem to losing their mesh-like morphology after 2 hs for (RADA)₄-CP1 and 6 hs for (RADA)₄-CP2.

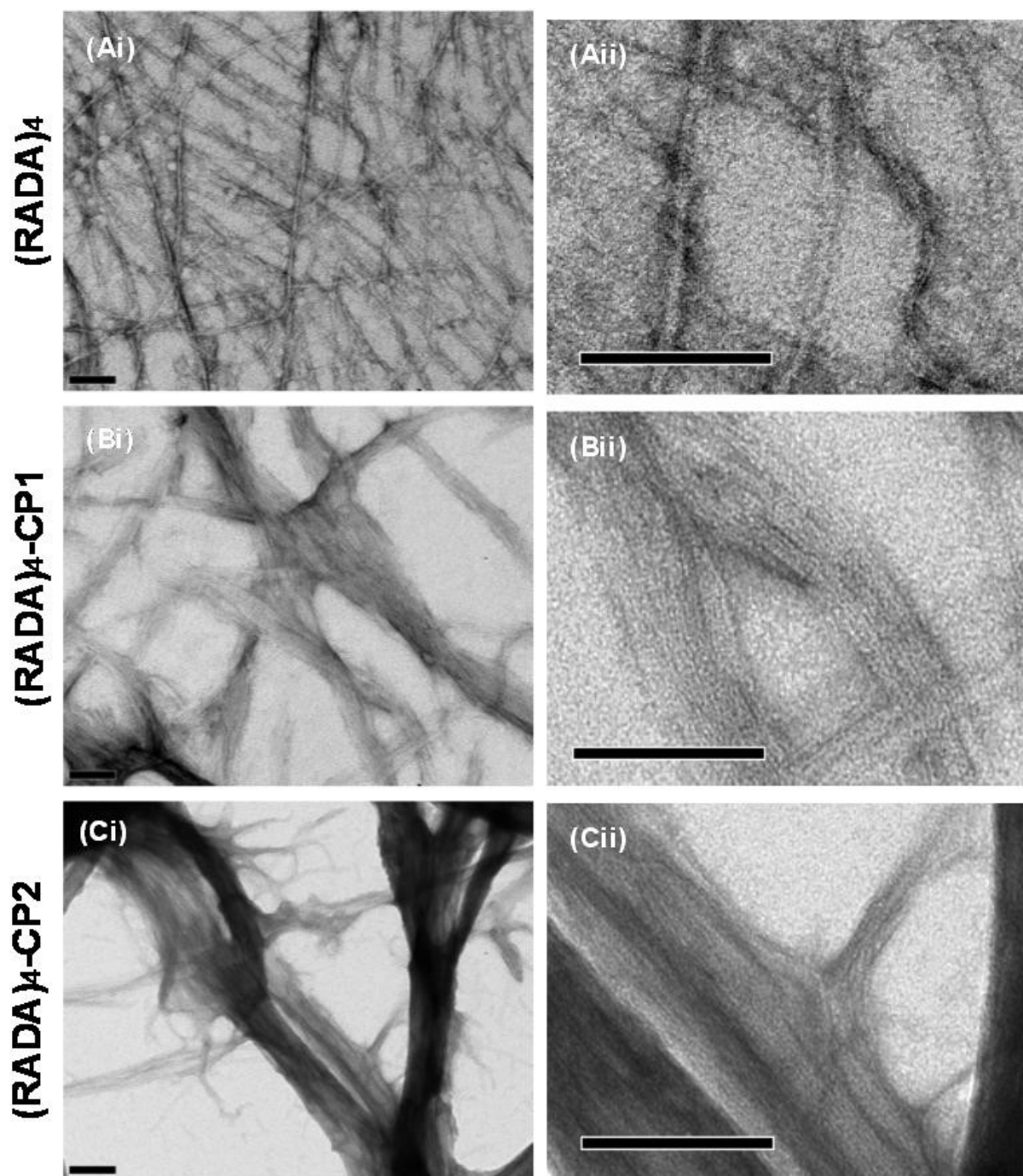


Figure 2.2. Transmission electron microscopy of (A) (RADA)₄, (B) (RADA)₄-GG-GPQG+IASQ (CP1), and (C) (RADA)₄-GG-GPQG+PAGQ (CP2). Low (i) and high (ii) magnification are shown to demonstrate fibers present in bundles. All samples were stained with 4% uranyl acetate and imaged at 0.5% w/v in TNC buffer upon 30 minutes of sonication and incubation at 37°C for 24 hs. Scale bars are all 100 nm.

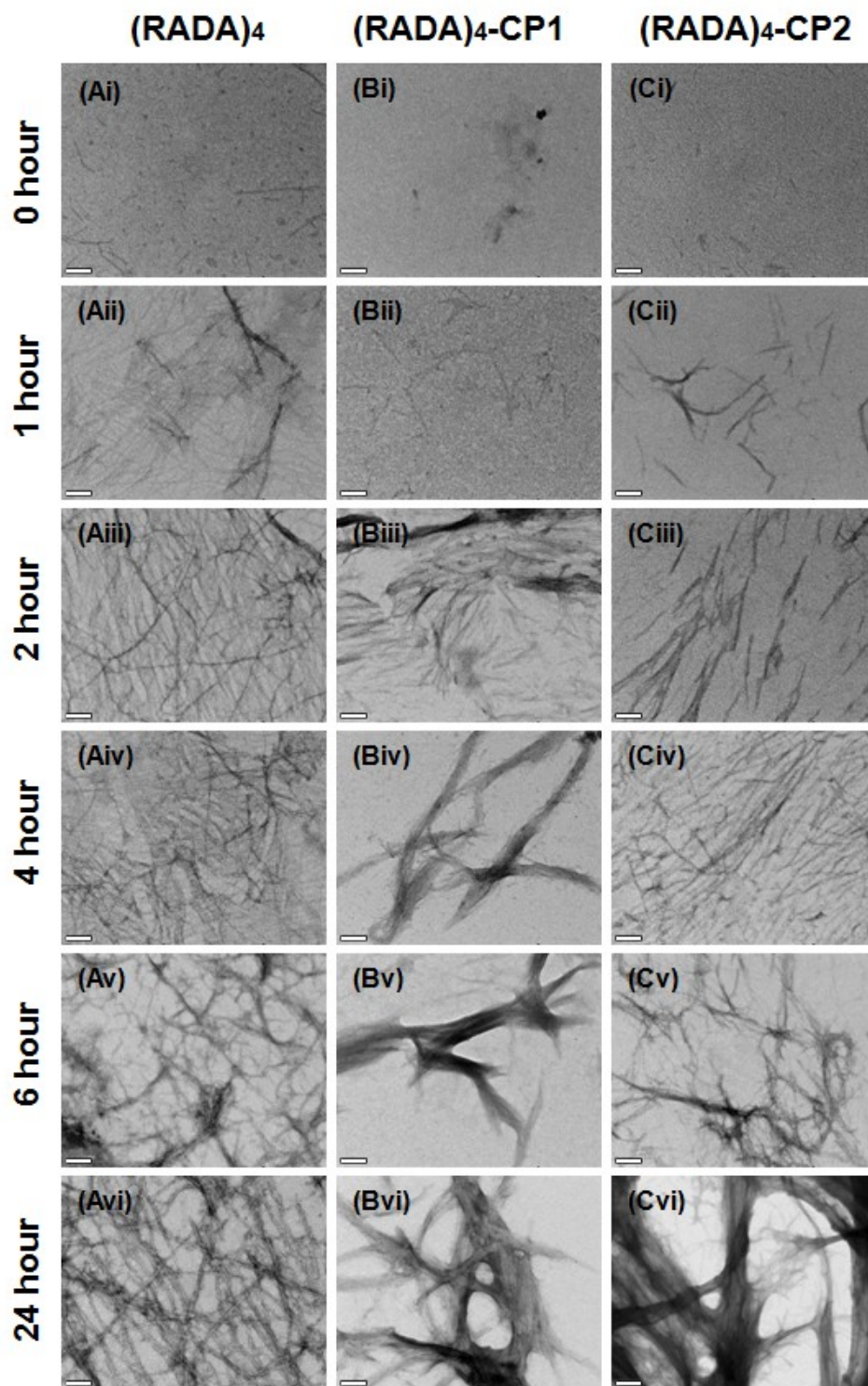


Figure 2.3. Transmission electron microscopy of (A) (RADA)₄, (B) (RADA)₄-GG-GPQG+IASQ, and (C) (RADA)₄-GG-GPQG+PAGQ. Samples were pipetted onto the grid at (i) 0, (ii) 1, (iii) 2, (iv) 4, (v) 6, (vi) and 24 hs of 37°C incubation upon 30 minutes sonication. All samples were stained with 4% uranyl acetate and imaged at 0.5% w/v in TNC buffer upon . Scale bars are all 100 nm.

TEM was used to observe nanofiber structures for 25%, 50%, and 75% v/v (RADA)₄ in (RADA)₄-CP1, at 0, 1, 2, 4, 6, and 24 hs after sonication (Figure 4). Like its pure component images, nanofibers are present in all images past 1 hour and these continue to develop more interconnected networks with time. Discontinuous nanofiber fragments at least 15 nm in length are apparent in 50% and 75% v/v of (RADA)₄. At 1 h, individual 5-10 nm nanofiber meshes are comparable for 25%, 50%, and 75% (RADA)₄ in (RADA)₄-CP1 mixtures. This complexity was similar to the network visible in pure samples. At 2 hs, a mesh morphology is present CP1 mixtures and are similar in complexity to their pure unmixed forms, however it is more distinct and porous in 75% (RADA)₄ than the other CP1 mixtures. In 25% mixtures after 4 hs, this network becomes more bundled but retains a mesh-like arrangement. By 24 hs, it bears the porous and curved architecture of its pure CP1 counterpart but is meshed and networked like pure (RADA)₄. For 50%, it similarly loses its mesh structure at 6 hs but does not effectively bundle and rather clusters in arrays of individually visible nanofibers. This morphology for 75% remains consistent after 2 hs while the networks and overall porosity become thicker and more defined by 24 hs. At 24 hs, none of these morphologies were thickly bundled like CP1, but bears similar structure to pure (RADA)₄.

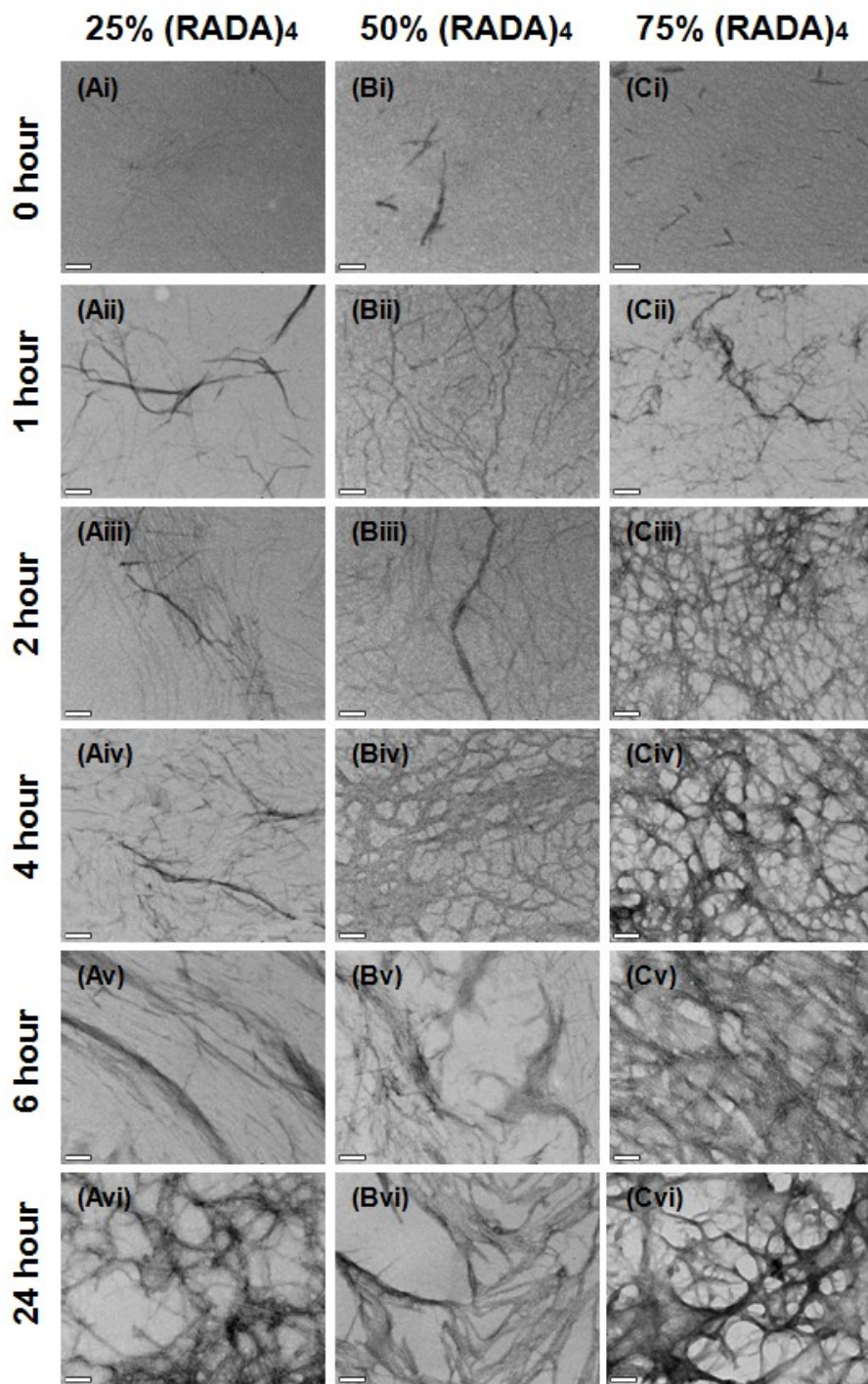


Figure 2.4. Transmission electron microscopy of (A) 25%/75%, (B) 50%/50%, and (C) 75%/25% (RADA)-GG-GPQG+IASQ/(RADA)₄ at (i) 0, (ii) 1, (iii) 2, (iv) 4, (v) 6, (vi) and 24 hs. All samples were stained with 4% uranyl acetate and imaged at 0.5% w/v in TNC buffer upon 30 minutes of sonication and incubation at 37°C. Scale bars are all 100 nm.

Nanostructures were observed using TEM for 25%, 50% and 75% (RADA)₄, mixed with (RADA)₄-CP2, at 0, 1, 2, 4, 6, and 24 hs upon applying sonication (Figure 5). Like all previous peptide mixtures, nanofibers are visible 1 h and grow into more defined structures with time. Also similar to peptide mixtures of (RADA)₄ in (RADA)₄-CP1, the discontinuous nanofiber fragments larger than 15 nm in length are also present in 50% and 75% v/v of (RADA)₄ in (RADA)₄-CP2. The nanoscale network complexity shown in pure samples and (RADA)₄-CP1 mixtures are also present at 1 h; individual 5-10 nm nanofiber meshes are comparable for all (RADA)₄ in (RADA)₄-CP2 mixtures. From 1 until 6 hs, a mesh morphology is present in CP2 mixtures and are comparable in complexity to their pure peptide groups with continuous nanofiber meshed matrices, except 75% (RADA)₄ in (RADA)₄-CP2 at 6 hs, which bears similarly porous and thicker networks to 75% (RADA)₄ in (RADA)₄-CP1. Major differences are noteworthy at 24 hs for (RADA)₄ in (RADA)₄-CP2 mixtures: at 25%, a dense meshed coating with few 50-100 nm pores overshadows the sample, at 50%, a less dense version of this is present for with a greater amount of 10-50 nm pores, and at 75%, a finer mesh exists that also reflects the morphology noted in 75% (RADA)₄ in (RADA)₄-CP1.

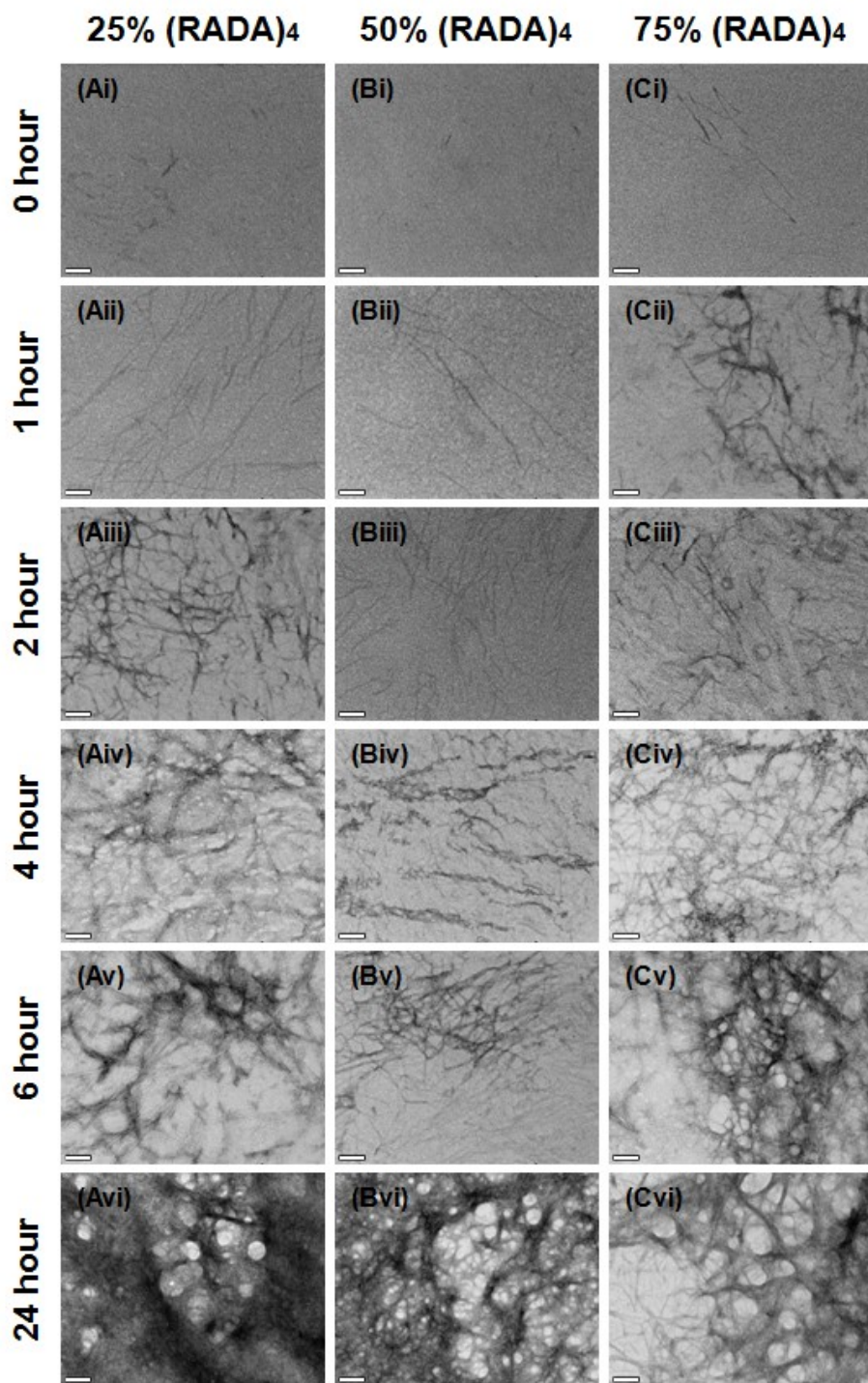


Figure 2.5. Transmission electron microscopy of (A) 25%/75%, (B) 50%/50%, and (C) 75%/25% (RADA)-GG-GPQG+PAGQ / (RADA)₄ at (i) 0, (ii) 1, (iii) 2, (iv) 4, (v) 6, (vi) and 24 hs. All samples were stained with 4% uranyl acetate and imaged at 0.5% w/v in TNC buffer upon 30 minutes of sonication and incubation at 37°C. Scale bars are all 100 nm.

3.2. Bundle Thickness and Fractal Dimension Analysis

Bundle thicknesses of TEM images were quantified using a MATLAB counting tool and summarized as a function of time for 0%, 25%, 50%, 75%, and 100 % v/v (RADA)₄ mixed with (RADA)₄-CP1 and (RADA)₄-CP2 (Figures 2.6Ai, and 2.6Aii). Hausdorff fractal dimension were determined using a MATLAB box count program at the same time points and systems as the bundle analysis (Figures 4Bi, and 4Bii). All bundle thicknesses increase with time, which reflects the TEM images. (RADA)₄ does not bundle too great a extent having nanofibers 15±4 nm thick at 24 hs. 25% and 75% v/v (RADA)₄ in (RADA)₄-CP1 share similar bundle thickness growth, 25% being 5-8 nm higher than 75% after 4 hs and both approaching 50±3 nm at 24 hs. 50% v/v (RADA)₄ in (RADA)₄-CP1 has comparatively higher bundle thicknesses than its 25% and 75% counterparts, having an average of 60±8 nm at 24 hs. Pure (RADA)₄-CP1 bundle thicknesses are higher than these, being 100±4 nm. (RADA)₄-CP2 and all subsequent mixtures with (RADA)₄ have similar bundle growth kinetics up until 6 hs, and all within 20-40 nm thick by 6 hs. By 24 hs, 25% and 50% (RADA)₄ in (RADA)₄-CP2 also have similar bundle sizes both becoming 50±5 nm. Pure (RADA)₄-CP2, however, approaches 100±15 nm and 25% (RADA)₄ in (RADA)₄-CP2 bundles become as thick as 119±18 nm, both being extensively thicker than other CP2 related mixtures. Each CP1 mixture rapidly reaches a plateau at 6 hs, where a marginal increase of 10 nm occurred by 24 hs. On the other hand, the CP2 mixtures are continuously increasing in a slower and linear manner until 24 hs and have ultimately thicker bundling only when mixed with 25% (RADA)₄. Fractal dimensions increase with time in every group. At 0 hs, all experimental groups have lower range Hausdorff dimensions of approximately 1 or below except pure (RADA)₄ and 75% (RADA)₄ in (RADA)₄-CP2. All systems reach a maximum dimension of 1.3-1.6 by 2 hs.

These dimensions were also observed across several magnifications (14, 18, 22, 28, 36, 44, 56, 71, 89, 110 K x) and the variance in Hausdorff dimension were negligible (Figure A2.3).

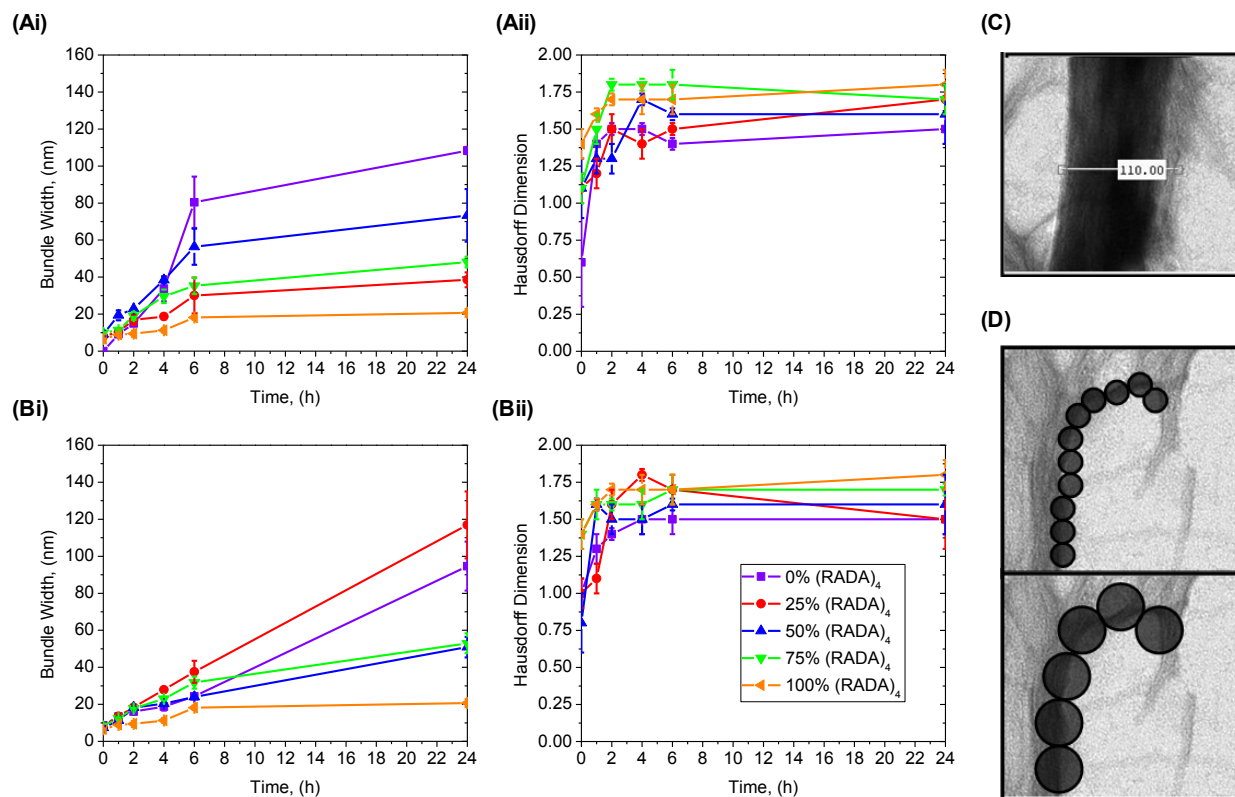


Figure 2.6. Bundle thickness and fractal dimension analysis for $(RADA)_4$ systems. (A) Bundle thickness and (B) Hausdorff box-count dimensions of $(RADA)_4$ -GG-GPQG+IASQ (i) and $(RADA)_4$ -GG-GPQG+PAGQ (ii) mixtures with $(RADA)_4$. Example images of (C) thickness measurement and (D) fractal contour tracing. Thickness image outlines the number of pixels across one bundle, which is used to calculate bundle width from scale bar. Mixtures include 100%, 75%, 50%, 25% $(RADA)_4$ -GG-GPQG+IASQ/ $(RADA)_4$ -GG-GPQG+PAGQ and 100% $(RADA)_4$ -GG-GPQG+IASQ and (ii) $(RADA)_4$. By sample, 50 random thicknesses were chosen for three independent images, from three independent experiments (i.e., $n=3$, with 150 random measurements). Data analyzed represents mean \pm SD, where line is to guide the eye only.

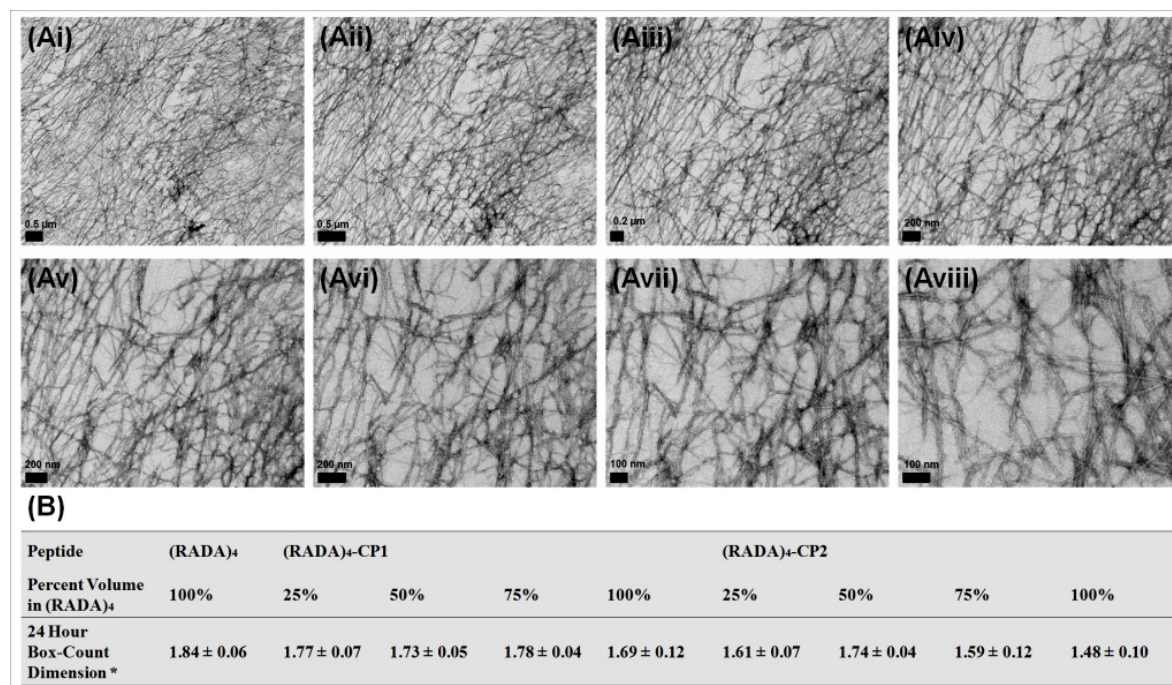


Figure 2.7. Transmission electron microscopy of (Ai-viii) various magnifications and (B) average Hausdorff box-count dimensions over 10 incremental changes in magnification (1,400, 1,800, 22,000, 28,000, 36,000, 44,000, 56,000, 71,000, 89,000, and 110,000 x magnification). All samples were stained with 4% uranyl acetate and imaged at 0.5% w/v in TNC buffer upon 30 minutes of sonication and 24 hs of incubation at 37°C. Scale bars are all 100 nm, data analyzed represents mean ± SD over the magnifications and $n=3$ experimental repeats.

As these fractals are a measure of continuous contour mapping present at any magnification, this was assessed with 10 magnifications (1,400, 1,800, 22,000, 28,000, 36,000, 44,000, 56,000, 71,000, 89,000, and 110,000), referenced from the scale. Averages and standard deviations for these were calculated (Figure 2.7). Continuous morphology appeared comparable by scale, and dimensions did not significantly change, no matter the magnification, nor were they below values expected in fractals. The previously discussed fractals bear significance at the observed scale.

3.3. MMP-2 Induced Peptide Cleavage

Enzymatic cleavage of high activity (RADA)₄-CP1 and low activity (RADA)₄-CP2 were observed using MALDI TOF/TOF mass spectrometry (Figure 2.8). These groups were chosen as the most bundled conditions, being the most proteolytically limited groups. The MMP-2 concentration of 40 nM was compared to the 0 nM control, in which no enzyme was present, over 3 weeks at 37°C. Enzyme activity was quality controlled with zymography. Excessive enzyme and time was used to assure visible product formation in a diffusion limited system once all conditions of gelation have become static. Substrate peaks of 2525.2 m/z and 2478.8 m/z are visible in the enzyme and control groups for (RADA)₄-CP1 and (RADA)₄-CP2, respectively. A high and low product peaks are also present at 2125.1 m/z in the enzyme group for these respective groups. Although MALDI results are typically semi-quantitative, as peaks are influenced by both ionization potential and quantity, the peak for (RADA)₄-CP1 was relatively higher than that of (RADA)₄-CP2, showing that the sequence activity influences the product formation when present in nanoscaffold form. These values all matched the theoretical molecular weight of the substrates and products, showing that upon nanoscaffold formation substrate cleavage was possible.

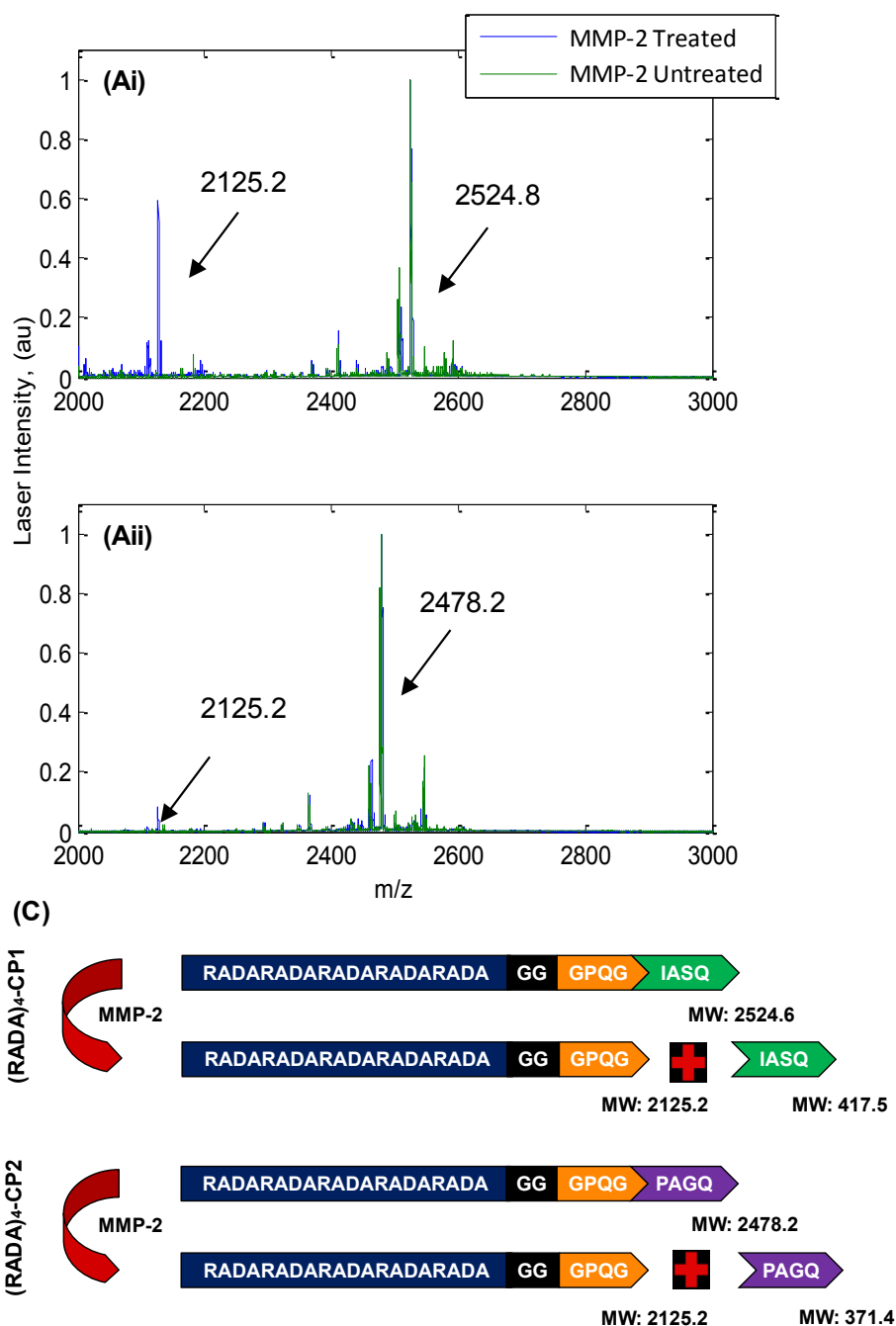


Figure 2.8. MALDI TOF/TOF mass spectrometry of (Ai) 0.5% w/v (RADA)₄-GG-GPQG+IASQ and (Aii) (RADA)₄-GG-GPQG+IASQ proteolysis. (B) Cleavage fragments are also shown. Incubated with 40 nM active MMP-2, in TNC buffer for three weeks at 37°C. Substrate peaks are labelled 2525.2 m/z and 2478.8 m/z, representing theoretical molecular weights of (RADA)₄-GG-GPQG+IASQ and (RADA)₄-GG-GPQG+IASQ, respectively. The peak 2125.1 m/z represents the molecular weight of the product for both substrates.

4. Discussion

As long as the (RADA)₄ peptide sequence is present, all peptides form a nanofiber matrix. Small nanoparticles at 0 hs suggest visible nucleation for (RADA)₄ which may be due to more rapid self-assembly of (RADA)₄ monomers. Individual nanofibers are formed by 1h in each condition indicating any initial self-assembly of nanofibers (not bundles) is finalized at this point. Both nucleation and rapid assembly were also noted in initial studies by Zhang *et al.* [18]. Bundle structures form with the addition of CP sequences, and are likely a result of the amino acids added by CP1 and CP2. GGGPQG, A and Q are shared between peptides. Glycines have no variable side chains, and are often used as spacers in synthetic peptide combinations. Present in the both CPs, they may attenuate the bundling due to CP residues on, and are not likely altering, the morphology of (RADA)₄. Taraballi *et al.* showed that by increasingly adding glycines spacers to SAPs, the behaviours of self-assembly and other peptides were better segregated [41]. Glutamine may affect the electrostatic interaction associated with self-assembly, however hydrophobic interactions have been determined by Kabiri to be dominant in (RADA)₄ self-assembly [42]. Alanine residues are hydrophobic and may contribute to the bundle formation. The presence of a cyclic pyrrolidine group integrated into the peptide backbone from proline may cause a cis-trans 'bend' in the peptide backbone and promote a bundle formation rather than the cross-linked mesh noted in pure (RADA)₄ [43 - 45]. Proline containing sequences, even in small amounts, have been shown to increasingly disrupt various mechanisms of secondary protein structures; especially the hydrogen bonding required in anti-parallel β -sheet formation, which occurs in (RADA)₄ assembly [45]. It has been shown that the presence of proline results in the formation of 'bulges' within the β -sheets, which may further favour hydrophobic interactions from this peptide. Proline interactions have also allowed for other types

of limited β -sheets protein conformations, such as β -turns. For example, proline-rich peptides have been studied in naturally forming zein maize storage proteins and implemented in vesicular SAPs [46 - 49]. Comparing the two CPs, growth of the bundles is apparently faster in (RADA)₄-CP1, but are ultimately thicker in (RADA)₄-CP2. This quicker self-assembly may be due to the increased hydrophobicity added by the isoleucine residue in CP1, however another proline in CP2 potentially enhances the bundle thickness as further anti-parallel β -sheet disruption may be occurring. As these systems vary in bundling type morphologies, their potential for proteolytic cleavage may change due to steric or diffusive hindrance, no longer reflecting their sequence specificity. Introducing pure (RADA)₄ to these peptides in mixtures may allow a comparable morphology with higher surface area and ultimately assure cleavage.

Any addition of the pure (RADA)₄ peptide sequence to the (RADA)₄-CP1 and (RADA)₄-CP2 allows self-assembly. Small nanofiber fragments are visible at 0 hs for 50% and 75% v/v for (RADA)₄-CP1 and all mixture of (RADA)₄-CP2 with the addition of (RADA)₄, but not the nanoparticles noted in (RADA)₄. If nucleation does occur (noted previously as nanoparticles) it may be missed at the time points observed or is only visible in pure (RADA)₄. Similar to pure (RADA)₄ and (RADA)₄-CP1, individual nanofibers are formed by 1 hour in each condition suggesting any initial self-assembly of individual nanofibers is finalized at this point. Overall, the nanofibers form in similar patterns when comparing (RADA)₄ mixtures in (RADA)₄-CP1 to its pure counterparts up until 2 hs, except for a thicker porous matrix present in 75% (RADA)₄ in (RADA)₄-CP1. After this time point, the structures are more akin to (RADA)₄ as no bundles are present in any time point. The thick porous matrix morphology persists in the 75% (RADA)₄ group up until 24 hs, which may be an alternately shaped matrix for potential drug delivery than individual meshes or large bundles. Overall morphology is similar to between (RADA)₄,

(RADA)₄-CP2 and its mixtures up until 6 hs with 75% (RADA)₄ in (RADA)₄-CP2. This may be due to (RADA)₄ having a dominant influence on the rate self-assembly at 75%, and at 50%. However, at 25% this may be slower or have the same rate. The extensive bundling shown at 24 hs for pure (RADA)₄-CP2, may form thicker and more layered meshed networks when (RADA)₄ is introduced to the mixture. This appears as a trend with the highest for 25% (RADA)₄ in (RADA)₄-CP2 and lowest for 75% (RADA)₄ in (RADA)₄-CP2, suggesting that the two peptides form alternate nanostructures that interact synergistically for form a composite when (RADA)₄-CP2 is the larger part of the mixture. This was similarly noted in 75% (RADA)₄ in (RADA)₄-CP1, although this mixture was mostly (RADA)₄. Self-assembly of (RADA)₄-CP2 appears to be slower, forms thicker structures, and is better able to integrate with (RADA)₄ than (RADA)₄-CP1. The additional 'bending' of the second proline may allow (RADA)₄ to favourably integrate into bigger structures over longer periods of time.

When quantified with bundle measurements, the (RADA)₄ peptide sequence promoted self-assembly with added peptide groups. For (RADA)₄-CP1 and its related mixtures, growth kinetics are higher in the pure CP1 group and thicker bundles are produced. The second to this is when 50% v/v (RADA)₄ is added, not 25% v/v, which may be a result of counting the sparse clusters of nanofibers as bundles (Fig. 2.1, at 6 and 24 hours). 25% and 75% (RADA)₄ in (RADA)₄-CP1 are much closer to (RADA)₄ in bundle thickness. Overall, this suggests that (RADA)₄ plays a dominant role in self-assembly over (RADA)₄-CP1, allowing for a matrix that retains similar bundle thickness and can load up to 75% drug bearing peptides. The bundle self-assembly is slower and more linear and allows for thicker structures in pure CP2 and its mixtures when compared to CP1. As noted previously (Fig. 1), pure (RADA)₄-CP2 visibly does this over (RADA)₄-CP1 and this trend appears in bundle thickness for mixtures whenever these peptides

are present. It is possible that the molecular bending from proline (once for CP1 and twice for CP2), which may enhance bundling, and the added hydrophobicity from isoleucine in CP1, which results in faster initial kinetics, are still present and progressively attenuated when (RADA)₄ is introduced in mixture form.

With enough time, all meaningful fractal dimensions (above 1.3) are present in any mixture of (RADA)₄, (RADA)₄-CP1, and (RADA)₄-CP2 and is comparable across multiple magnifications by 24 hs. These values were equal or greater to that of a dendritic julia set, which is typically seen in neurite outgrowth [32]. Lomander et al. derived a similar dimension of 1.34 for another β -sheet forming peptide SAP [50]. This occurs by 2hs in every case, suggesting that growth kinetics of these shapes changes by this time point. Similarly, no significant bundling was visible in the TEM images nor was there statistically relevant bundling derived from these images (Fig. 4a) for any mixture up to 2 hs. This may be due to initial self-assembly requiring some nucleation to occur to generate full nanofibers from individual peptide monomers. Once full nanofibers are present, the fractal dimension reached a maximum, and growth was noted in further networking and bundling. Characteristic nanofiber growth is expected to be finished by this point [18]. Previous work by Fatin-Rouge and Bancaud have suggested that fractal properties in nanofiber networks may result in a system with a reduced apparent diffusion rate compared to non-fractal materials, whilst still allowing for protein-matrix interactions. This suggests that our system may perform as a proteolytic cued peptide delivery vehicle upon 2 hs, which requires fractal dependent diffusive and protein-matrix (enzyme-substrate) interactions [25 - 26]. Even in the most highly structured bundles, MMP-2 cleavage is necessary to demonstrate this.

Adding the cleavage sequences of CP1 and CP2 to the (RADA)₄ SAP allows for cleavage in the presence of high MMP-2 levels. However, their morphologies and growth kinetics vary extensively with increased bundling and lowered matrix density and networking. Cleavage rates and subsequent drug release may no longer be represented by their sequences and variable morphology related diffusion limitations, steric hindrances, and bulk release from bundles likely play a great role. Mixing these peptides allows for comparable nanostructures to pure (RADA)₄ with the exception of 50% and 75% (RADA)₄ in (RADA)₄-CP2. As a result, this system can be modulated for exact drug loading in these morphologies, which can ultimately be tuned for on-demand delivery with MMP-2 endogenous to cancerous or inflammatory cells and tissues.

5. Conclusions

The temporal growth morphology and fractal dimension for a (RADA)₄ hydrogel were studied as a function of C-terminal tethered MMP-2 substrate (GPQG+IASQ (CP1), GPQG+PAGQ (CP2)) and overall substrate concentration within the matrix. This was done for the express purpose of elucidating the effect these parameters have upon matrix morphology with assembly time, and the ability of the system to be enzymatically cleaved; all of which is crucial to the development of MMP-2 induced release of peptides from these SAP systems. Both substrate modified (RADA)₄ peptides self-assembled into nanofibers and resulted in a significant bundled morphology compared to (RADA)₄. To maintain a similar morphology to (RADA)₄, (RADA)₄-CP1/CP2 were doped with 25%, 50%, and 75% v/v pure (RADA)₄. Any amount of (RADA)₄ added to CP1 mixtures demonstrated consistent architecture to its unmodified parent peptide, however the CP2 formula was only comparable to (RADA)₄ with 75% addition. A densely meshed architecture was noted with 50% and 25% (RADA)₄ in (RADA)₄-CP2, potentially allowing for different release kinetics. Fractal dimension reached a meaningful

plateau at 2 hs, however, nanofiber bundling continued after this time in all cases. The systems that exhibited the most bundling, (RADA)₄-CP1/CP2, were still susceptible to MMP-2 cleavage. As a potential drug delivery system, these peptide mixtures are capable of predictable morphologies for *in situ* nanoscaffold formation, and tuneable cleavage substrate addition for on-demand release. Undergoing enzyme kinetic and cell response studies, this system may demonstrate tremendous merit in tissue engineering applications and as a therapeutic for several inflammation and cancer related illnesses.

6. Acknowledgements

The Authors would like to acknowledge T. Sereda, P. Semchuk, and J. Moore for peptide synthesis assistance, R. Koss and A. Oatway for electron microscopy support, and E. Gruber and T. Ng for exceptional assistance with everything else. The authors are grateful for financial support from NSERC, NINT-NRC, Women's and Children's Health Research Initiative (UofA) and Alberta-Gangwon Korea grants.

References

1. Uhlig T, Kyprianou T, Martinelli FG, Oppici CA, Heiligers D, Hills D, Calvo XR, Varhaert P. The emergence of peptides in the pharmaceutical business: From exploration to exploitation. *EuPA*. 2014;4:58-69
2. Tiwari G, Tiwari R, Sriwastawa B, Bhati L, Pandey S, Pandey P, et al. Drug delivery systems: An updated review. *Int J Pharm Investig*. 2012;2(1):2-11.
3. Hoffman AS. Hydrogels for biomedical applications. *Adv Drug Deliv Rev*. 2012;64:18-23.
4. Lee KY, Mooney DJ. Hydrogels for Tissue Engineering. *Chem Rev*. 2001;101(7):1869-78.
5. Hoare TR, Kohane DS. Hydrogels in drug delivery: Progress and challenges. *Polymer*. 2008;Volume 49(Number 8):1993-2007.
6. Anderson DG, Levenberg S, Langer R. Nanoliter-scale synthesis of arrayed biomaterials and application to human embryonic stem cells. *Nat Biotechnol*. 2004 July;22(7):863-666.
7. Flaim CJ, Chien S, Bhatia SN. An extracellular matrix microarray for probing cellular differentiation. *Nat Methods*. 2005 February;2(2):119-25.
8. Zhang S. Fabrication of novel biomaterials through molecular self-assembly. *Nat Biotechnol*. 2003 October;21(10):1171-8.
9. MacPhee CE, Woolfson DN. Engineered and designed peptide-based fibrous biomaterials. *Curr Opin Solid State Mater Sci*. 2004;8(2):141-9.
10. Stupp SI. Biomaterials for regenerative medicine. *MRS Bull*. 2005;30(7):546-53.
11. Holmes TC. Novel peptide-based biomaterial scaffolds for tissue engineering. *Trends Biotechnol*. 2002 January;20(1):16-21.

12. Gelain F, Unsworth LD, Zhang S. Slow and sustained release of active cytokines from self-assembling peptide scaffolds RID A-7231-2011. *J Controlled Release*. 2010;145(3):231-9.
13. Kisiday J, Jin M, Kurz B, Hung H, Semino C, Zhang S, et al. Self-assembling peptide hydrogel fosters chondrocyte extracellular matrix production and cell division: implications for cartilage tissue repair. *Proc Natl Acad Sci U S A*. 2002 July 23;99(15):9996-10001.
14. Zhang S, Holmes TC, DiPersio CM, Hynes RO, Su X, Rich A. Self-complementary oligopeptide matrices support mammalian cell attachment. *Biomaterials*. 1995 March 23;16:1385-93.
15. Holmes TC, de Lacalle S, Su X, Liu G, Rich A, Zhang S. Extensive neurite outgrowth and active synapse formation on self-assembling peptide scaffolds. *PNAS*. 2000 June;97(12):6728-33.
16. Koutsopoulos S, Zhang S. Long-term three-dimensional neural tissue cultures in functionalized self-assembling peptide hydrogels, matrigel and collagen I. *Acta Biomater*. 2012(<http://dx.doi.org/10.1016/j.actbio.2012.09.010>).
17. Chau Y, Luo Y, Cheung ACY, Nagai Y, Zhang S, Kobler James B, et al. Incorporation of a matrix metalloproteinase-sensitive substrate into self-assembling peptides - A model for biofunctional scaffolds. *Biomaterials*. 2008;29:1713-9.
18. Hauser CAE, Zhang S. Designer self-assembling peptide nanofiber biological materials. *Chem Soc Rev*. 2010 August;39(8):2780-90.
19. Englander O, Oates W, Paravastu A, Cheng L. An effective continuum approach for modeling non-equilibrium structural evolution of protein nanofiber networks. *J Chem Phys*. 2011;135(5):15. <http://dx.doi.org/10.1063/1.3622489>. doi: 10.1063/1.3622489.

20. Law B, Tung C. Proteolysis: a biological process adapted in drug delivery, therapy, and imaging. *Bioconjugate Chem.* 2009;20(9):1683-95.
21. Turk BE, Huang LL, Piro ET, Cantley LC. Determination of protease cleavage site motifs using mixture-based oriented peptide libraries. *Nat Biotechnol.* 2001 July;19(7):661-7.
22. Nagase H, Fields GB. Human matrix metalloproteinase specificity studies using collagen sequence-based synthetic peptides. *Biopolymers.* 1996;40:399-416.
23. Netzel-Arnett S, Sang QX, Moore WG, Navre M, Birkedal-Hansen H, Van Wart HE. Comparative sequence specificities of human 72- and 92-kDa gelatinases (type IV collagenases) and PUMP (matrilysin). *Biochemistry.* 1993 June 29;32(25):6427-32.
24. Lévesque SG, Shoichet MS. Synthesis of enzyme-degradable, peptide-cross-linked dextran hydrogels. *Bioconjug Chem.* 2007;18(3):874-85.
25. Fatin-Rouge N, Starchev K, Buffle J. Size effects on diffusion processes within agarose gels. *Biophysical Journal.* 2004;86(5):2710-9.
26. Bancaud A, Beaudouin J, Ellenberg J, Huet S, Daigle N, Mozziconacci J. Molecular crowding affects diffusion and binding of nuclear proteins in heterochromatin and reveals the fractal organization of chromatin. *EMBO J.* 2009;28(24):3785-3798. <http://onlinelibrary.wiley.com/doi/10.1038/emboj.2009.340/abstract>. doi: 10.1038/emboj.2009.340.
27. Montague PR, Friedlander MJ. Expression of an intrinsic growth strategy by mammalian retinal neurons. *Proc Natl Acad Sci U S A.* 1989;86:7223-7.
28. Hochman-Mendez C, Cantini M, Moratal D, Salmeron-Sanchez M, Coelho-Sampaio T. A fractal nature for polymerized laminin. *PloS one.* 2014;9(10):e109388.

29. Vauthey S, Santoso S, Gong H, Watson N, Zhang S. Molecular self-assembly of surfactant-like peptides to form nanotubes and nanovesicles. *Proc Natl Acad Sci U S A*. 2002 April 16;99(8):5355-60.
30. Santoso S, Hwang W, Hartman H, Zhang S. Self-assembly of surfactant-like peptides with variable glycine tails to form nanotubes and nanovesicles. *Nano Lett*. 2002;2(7):687-91.
31. von Maltzahn G, Vauthey S, Santoso S, Zhang S. Positively charged surfactant-like peptides self-assemble into nanostructures. *Langmuir*. 2003;19:4332-7.
32. Lomander A, Hwang W, Zhang S. Hierarchical self-assembly of a coiled-coil peptide into fractal structure. *Nano Lett*. 2005;5.
33. Applied Biosystems. ABI 433A peptide synthesizer user guide. 2004.
34. Dawes JC, Biological techniques for transmission and scanning electron microscopy. Ladd Research Industries, Inc. 1984.
35. French P. Hausdorff dimension by the box counting method. 2007. <<http://www.mathworks.com/MATLABcentral/fileexchange/15918-hausdorff-dimension-by-the-box-counting-method>>
36. Costa A. Hausdorff (box-counting) fractal dimension, 2011. <<http://www.mathworks.com/MATLABcentral/fileexchange/30329-hausdorff--box-counting--fractal-dimension>>
37. Hausdorff F. Dimension und äußeres Maß. *Mathematische Annalen*. 1919;79:157-9.
38. Lopes R, Betrouni N. Fractal and multifractal analysis: A review. *Med Image Anal*. 2009;13:634-49.
39. Theiler J. Estimating fractal dimension. *J Opt Soc Am A*. 1990;7(6):1055-73.

40. Soille P, Rivest J. On the validity of fractal dimension measurements in image analysis. *J Vis Commun Image Represent.* 1996;7(3):217-29.
41. Taraballi F, Natalello A, Campione M, Villa O, M. Doglia S, Paleari A, et al. Glycine-spacers influence functional motifs exposure and self-assembling propensity of functionalized substrates tailored for neural stem cell cultures. *Front Neuroeng.* 2010 February;3:1-9.
42. Kabiri M, Bushnak I, McDermot MT, Unsworth LD. Toward a mechanistic understanding of ionic self-complementary peptide self-assembly: role of water molecules and ions. *Biomacromolecules.* 2013 September;14:3943-50.
43. Stewart DE, Sarkar A, Wampler JE. Occurrence and role of cis peptide bonds in protein structures. *J Mol Biol.* 1990;214(1):253-260. <http://www.sciencedirect.com/science/article/pii/002228369090159J>. doi: 10.1016/0022-2836(90)90159-J.
44. Pal D, Chakrabarti P. Cis peptide bonds in proteins: Residues involved, their conformations, interactions and locations. *J Mol Biol.* 1999;294(1):271. <http://www.ingentaconnect.com/content/ap/mb/1999/00000294/00000001/art03217>.
45. MacArthur MW, Thornton JM. Influence of proline residues on protein conformation. *J Mol Biol.* 1991;218(2):397-412. <http://www.ncbi.nlm.nih.gov/pubmed/2010917>. doi: 10.1016/0022-2836(91)90721-H.
46. Kogan M, Dalcol I, Gorostiza P, Lopez-Iglesias C, Pons R, Pons M, et al. Supramolecular properties of the proline-rich γ -zein N-terminal domain. *Biophys J.* 2002;83:1194-204.

47. Creasey RG, Voelcker NH, Schultz CJ. Investigation of self-assembling proline- and glycine-rich recombinant proteins and peptides inspired by proteins from a symbiotic fungus using atomic force microscopy and circular dichroism spectroscopy. *Biochim Biophys Acta*. 2012;1824:711-22.
48. Fernández-Carneado J, Kogan MJ, Castel S, Giralt E. Potential peptide carriers: amphipathic proline-rich peptides derived from the N-terminal domain of γ -zein. *Angw Chem Int Ed*. 2004;43:1811-4.
49. del Pozo-Rodríguez A, Pujals S, Delgado D, Solinís MA, Gascón AR, Giralt E, et al. A proline-rich peptide improves cell transfection of solid lipid nanoparticle-based non-viral vectors. *J Control Release*. 2008;133(2009):52-9.
50. Jelinek HF, Elston N, Zietsch B. Fractal analysis: pitfalls and revelations in neuroscience. In: Alt W, editor. *Fractals in biology and medicine mathematics and biosciences in interaction*. ; 2005. p. 85-94.

Pending Publication

Chapter 3.

MMP-2 Cleavage of C-terminal Modified (RADA)₄ as a Platform for Peptide Delivery: Assembled Morphology and Cleavage Kinetics.

Koss, K^{1,2}; Tsui, C^{1,2}; Unsworth, LD^{1,2,*}

1. Department of Chemical and Materials Engineering, University of Alberta, 13-390 Floor - Donadeo Innovation Centre for Engineering (ICE), 9211-116 Street NW, Edmonton, AB, T6G 1H9

2. National Institute for Nanotechnology, NRC, 11421 Saskatchewan Dr NW, Edmonton, AB, T6G 2M9

Abstract

(RADA)₄ self-assembling peptide (SAP) hydrogels are excellent candidates for drug delivery, with several beneficial qualities. They are a class of materials with uncomplicated fabrication and potentially allow for a diverse set of release strategies for many types of bioactive ligands. Enzyme-induced release of peptide sequences, synthesized with the SAP, for on-demand drug delivery could prove impactful to a plethora of human health applications. However, product formation and the degradation products from such modified nanoscaffolds, due to various substrate and enzyme conditions, can greatly affect the overall drug release potential of the system. To address this, enzyme kinetics in self-assembled hydrogels was studied by tethering matrix metalloproteinase 2 (MMP-2) cleavable peptide substrates of differing activities to the C-terminus of (RADA)₄. High and low activity sequences, GPQG+IASQ (CP1) and GPQG+PAGQ (CP2), were respectively chosen for tunable release. When incubated with 5 nM MMP-2, over 3 days, both CP1 and CP2 sequences showed product formation ~32 and ~9% of the original substrate, respectively. On-demand product formation was found to be dependent upon both SAP composition and enzyme concentrations, and could be tuned over the course of several days and weeks. Nanoscaffold morphology was visibly degraded by the protease, resulting in lower fractal dimensions for the matrix, suggesting that diffusion and post-delivery clearance of these materials may be possible over time.

Keywords: Self-assembling peptides, Drug delivery, (RADA)₄, MMP-2, Nanoscaffold, Hausdorff dimension, Fractal

1. Introduction

Peptide drugs have several beneficial traits; they are generally highly specific in their action and exhibit reduced side-effects compared to systemically delivered small drug molecules. However, peptides generally suffer from poor pharmacokinetics and may be rapidly digested before being effective. Supplying a dynamic dose that is tuned to the environmental conditions of the target tissue is challenging. Polymer drug delivery vehicles are capable of housing a variety of release triggers cued to physiology, as such as proteolysis, pH, and temperature, have been explored [1 - 4], and have taken many forms like reservoirs, micelles, liposomes, and nano/micro particles[5 - 6]. Hydrogels, made from nanofiber matrices composed of cross-linked polymers, can be fabricated with a wide spectrum of morphological and mechanical features that may emulate a natural extracellular matrix (ECM) and, when swollen with water, they are capable of controlled and diffuse release of housed molecules. Furthermore, they can be engineered to be a multi-faceted system that incorporates bioactive peptides for the express purpose of directing endogenous cell action: recruitment, differentiation, proliferation, activation, etc. [7]. Despite their potential, polymer hydrogels have inherent properties that limit their application in drug delivery. For example, deleterious host responses towards either the intact polymer matrix or the polymer degradation products may significantly reduce the application of polymer hydrogels. Drug release may be rapid, due to forming large pores and gaps in the nanostructured matrix, or unpredictable due to differences in the bulk morphology that may arise from uncontrolled aggregation[8]. Designing a polymer system with precisely tuned release can be tremendously intricate and ultimately impractical, requiring multi-stage chemical synthesis, *in-situ* precipitation with toxic co-solvents, chemical or photosensitive triggers, or invasive transplantation. As a result, comprehensive studies relating cell response to

precise timed drug release cannot be performed systematically with high-throughput analysis [9 - 11]. An optimal hydrogel for peptide delivery should be simple to fabricate, biocompatible, have reproducible morphology, include accurate drug loading, and specific release cues. Considering these ideals, enzymatically-triggered peptide release kinetics and matrix morphology were investigated for a hydrogel matrix formed from self-assembling peptides (SAP), which are biocompatible molecules generated reproducibly with automated synthesis.

Specifically, SAPs form nanoscaffolds spontaneously and preferably in aqueous salts, or *in vivo*, through hydrogen bonds, electrostatic interactions, and van der Waals forces [12 - 14]. They emulate ECMs and have demonstrated biocompatibility in many tissues [15 - 20]. A commonly employed SAP is (RADA)₄(arginine-alanine-aspartate-alanine)[21 - 23]. This SAP is biocompatible, has been used in many cell culture and tissue engineering studies, and diffuse drug and protein release profiles have been characterized from fully formed (RADA)₄ networks [17, 24 - 25]. Although proteolysis of MMP-2 substrate linked dimers of (RADA)₄ has been reported for the purpose of inducing morphological re-assembly, this technique has not been applied as a drug delivery mechanism[26]. Furthermore, due to the fact that the properties of the peptides facilitate their self-assembly, for enzymatically cleavable release of peptides it is crucial to understand how the C-terminus addition of enzymatically cleavable domains may affect the resulting matrix morphology and, as such, the in-gel enzyme activity. A systematic evaluation of *in situ* enzyme kinetics, directly relating to drug release, as a function of substrate type, substrate concentration, and enzyme levels over weeks have not been conducted with this self-assembling system.

Fractals are a measure of symmetry in patterns that are comparable at any scale. They appear in a variety of biological systems from nanoscale to the macroscale. Fractals have been derived

to understand the interaction between cells and changing ECMs (fractones) [27]. In the diffusion from agarose hydrogel systems, they have been related to the movement of particles where the proper diffusion suggests a higher fractal dimension [28]. In DNA-chromatin they are highly indicative of protein-protein interactions [29]. These dimensions have also been observed in various nanostructures, including laminin polymerization, nanovesicles, and nanotubes, and SAPs that form β -sheets. [30 - 35]. Despite fractals being observed in nanoarchitectures, diffusion, and protein interactions, studies are scarce on image and fractal dimension analysis of SAP hydrogels that have undergone enzymatic degradation. As such, fractal dimensions yielded from morphology may be highly related to diffusion and enzyme interactions which are essential properties of any proteolytically triggered drug delivery system.

Enzyme triggered drug release systems have been studied in several forms, including hydrogels, and have been used in medical imaging and therapeutic applications[36]. Several specific enzymes are secreted in cancer and inflammatory response circumstances, in which, drug delivery therapies are highly desirable. One such family of proteases are the matrix metalloproteinases (MMP), which include a multitude of different enzymes that specifically digest several ECM-based substrates and are, thus, ideal for the design of on-demand release from synthetic ECMs [37]. MMP-2 has several consensus peptide sequences with variable activity and is amply secreted by cancer cells and by other tissues during injury. Two substrate motifs glycine-proline-gluatamine-glycine+isoleucine-alanine-serine-gluatamine (GPQG+IASQ, CP1) and glycine-proline-gluatamine-glycine+proline-alanine-glycine-gluatamine (GPQG+PAGQ, CP2), have a respective high and low activity for MMP-2 and are promising candidates for modulating release ('+' denotes the scissile bond); reaction rates are 320 for CP1 and < 5.0 for CP2, measured as the relative reaction rate to MMP-1 hydrolysis of GPQG+IAGQ

[38 - 39]. These sequences have been employed, by the Shoichet group, to cleave sections of a dextran hydrogel allowing for effective release of fluorophores [40]. Incorporating these peptides into (RADA)₄ hydrogels is accurate, reproducible, and simpler, as these molecules can be made during initial peptide synthesis with predictable purity.

To evaluate the practicality of this drug delivery system, fully formed SAPs with incorporated MMP-2 cleavable sequences were treated with protease, product amounts were measured with time for a range of hydrogel compositions and MMP-2 concentrations. The CP1 and CP2 motifs were tethered to the C-terminus of (RADA)₄, and spaced by two glycine residues. The proposed system, with substrate and product fragments, is noted in Figure 3.1. The product fragment (RADA)₄-GG-GPQG was detected using matrix-assisted laser desorption/ionization time of flight (MALDI-TOF/TOF) mass-spectrometry. Product formation was quantified using anisotopically labelled product standard for high-throughput analysis of product formation [41]. Specifically, the 3rd and 4th alanines were deuterated for a total mass increase of 8, which retains the same ionization potential, but does not have overlapping isotopic envelopes. In a 32 day study, hydrogel concentrations represented range for SAP systems seen in literature for cell studies and drug delivery [42 - 44]. Similarly, MMP-2 concentrations were chosen to emulate polar states of physiology from healthy serum to late stage cancer tissue [45 - 46]. Additionally, morphology of these SAP hydrogels, when exposed to MMP-2, was assessed with transmission electron microscopy (TEM). The Hausdorff dimensions were derived from these images to observe unpredictable, but substantial, sized-based pattern changes due to enzymatic digestion; this may indicate potential for post-delivery dissolution and removal. Finally, product formation was measured periodically, over the course of 32 days, to observe sustained cleavage and understand the time-frame of controlled release. These SAPs were

gradually doped with (RADA)₄ 25%, 50%, and 75% by volume, to assess the effect available cleavages site may have on the amount of peptide product formed. With predictable product formation in various conditions, this system is capable of delivering a variety of drug amounts, on-demand, modulated to MMP-2 levels, with visible degradation.

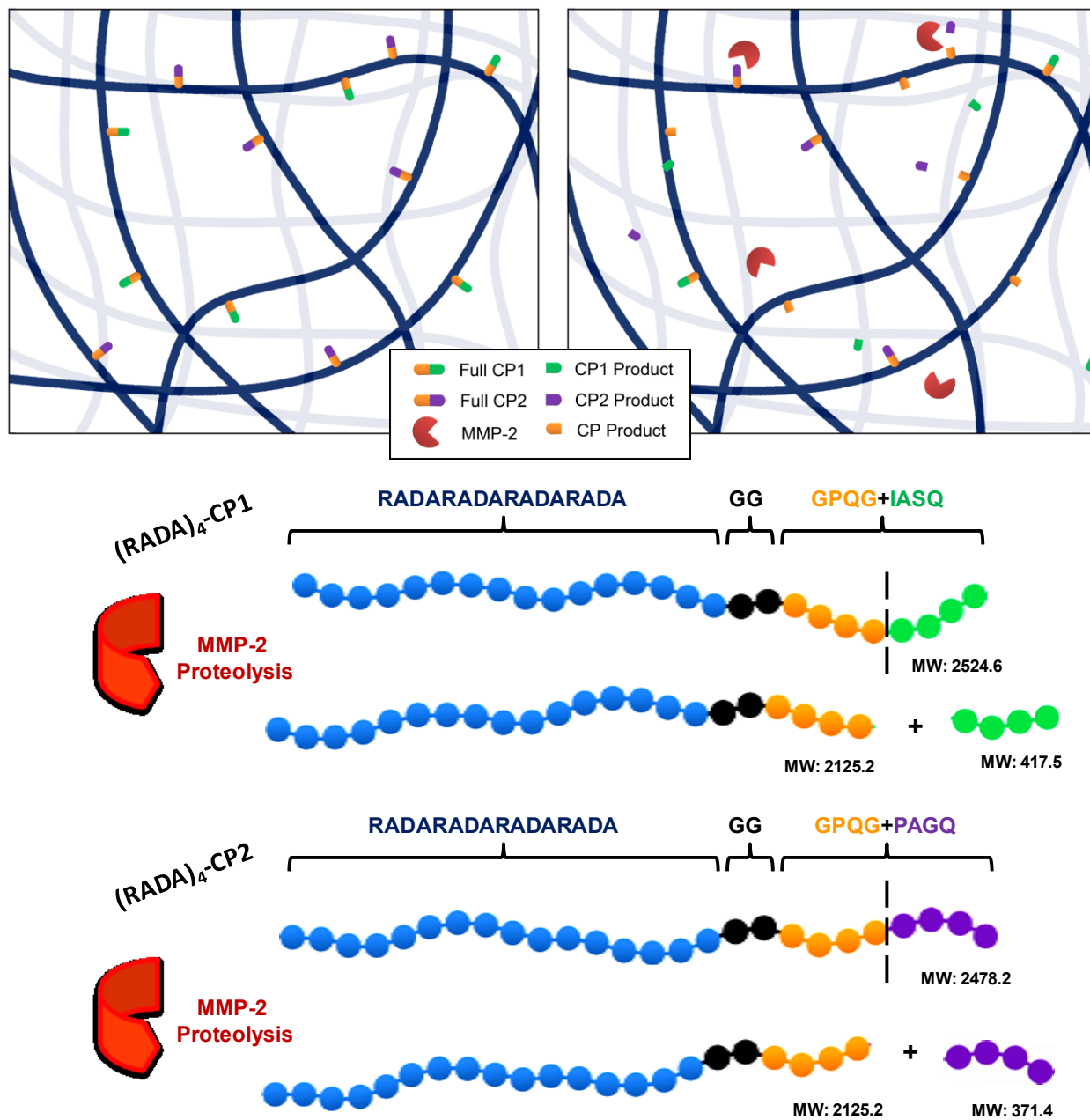


Figure 3.1. Schematic of self-assembled peptide hydrogel with incorporated cleavage motifs. Proposed MMP-2 digestion is shown. Theoretical peptide fragments and molecular weights are shown for both substrates and products for both cleavage peptides (CP1 and CP2).

2. Materials and Methods

2.1. Materials

Acetonitrile (ACN) (99.8%), dichloromethane (99.8%), N-dimethylformamide (99.8%), piperidine (99.5% biotech. grade), methanol (99.8%), N-diisopropylethylamine (99.5% biotech. grade), trifluoroacetic acid (TFA) (99%), triisopropylsilane (TIPS) (99%), α -cyano-4-hydroxycinnamic acid (HCCA), diethyl ether, and Fmoc-Ala-OH-2,3,3,3-d₄, were acquired from Sigma (Oakville, ON). All other Fmoc amino acids and Wang resins were purchased from ChemPep (Wellington, FL). 1-cyano-2-ethoxy-2-oxoethylideneaminoxydimethylamino-morpholino-carbenium hexafluorophosphate (COMU) (98%) and ethyl (hydroxyimino)cyanoacetate (OXYMA) (98%) from Oakwood Products, Inc (West Columbia, SC). Active human recombinant MMP-1 and MMP-2 were acquired from ProSci Inc. (Poway, CA) and EMD Millipore (Etobicoke, ON), respectively. All MMP-2 purchased contained 9% TIMP-2 inhibitor to prevent MMP-2 regulatory domain. Uranyl acetate and TEM grids were from Ted Pella, Inc (Redding, CA). Other materials used in subsequent substrate preparation and enzyme kinetics stages included Tris-HCl from Fisher Scientific (Fair Lawn, NJ), NaCl from EMD Chemicals Inc. (Darmstadt, Germany), and CaCl₂·2 H₂O from EMD Chemicals Inc. (Darmstadt, Germany). Unless specified otherwise, all water used in these experiments was Milli-Q grade.

2.2. Peptide Synthesis

Fully, the peptide synthesized were (RADA)₄, (RADA)₄-GG-GPQG+IASQ (CP1), (RADA)₄-GG-GPQG+PAGQ (CP2), (RADA)₄-GG-IQPGSAQG (SP1), (RADA)₄-GG-PQGAQGPG(SP2), and (RADA)₄-GG-GPQGD₈ using a ABI 433A Peptide Synthesizer. Fmoc chemistry was chosen and coupling was performed using 500 mM concentrations of COMU and

OXYMA. Fastmoc protocols were chosen and coupling was doubled and cycles were extended 15 minutes. All other protocols methods were specified by the ABI 433A manual[44]. A cleavage cocktail of (96/2/2) TFA, water, and triisopropylsilane was used. ABI 4800 matrix-assisted laser desorption/ionization time of flight (MALDI-TOF/TOF) mass-spectrometry was used to assess sample masses. HCCA matrix concentrations of 10 mg/mL were suspended in 1:1 ACN:H₂O (0.1% TFA). Peptides were purified to 95% or greater using high performance liquid chromatography (HPLC) and a Zorbax Eclipse C18 reverse-phase semi-preparative 9.4 x 250 mm column (Agilent Technologies) using a H₂O-ACN (0.1%TFA) loading. Purity was determined with HPLC. MALDI mass spectra and chromatographs are available in the supplemental section (Figure A3.1).

2.3. Transmission Electron Microscopy

All protocols were followed from Dawes *et al.* [45]. (RADA)₄ samples were pipetted from the center of the sample container, inserted onto perforated formvar carbon coated copper grid and a 4% uranyl acetate stain applied. The sample and stain were filter-dried in between steps. Samples were collected on day 32 alongside the time-based study. All TEM was performed on a Philips FEI Morgagni electron microscope.

2.4. MMP-2 Enzymatic Treatment

Enzyme treatment was adapted from Chau *et al.* [26]. MMP-2 activity was assessed with zymography. Each peptide was diluted to the desired experimental percent weight / volume (0.25 - 2.00 % w/v) in a modified TNC buffer (50 mM TrisHCl, 150 mM NaCl, 1 mM CaCl₂, pH 7.4) and sonicated for 30 minutes. All CP1 and CP2 samples were normalized using a (RADA)₄ % w/v basis for all mixed solution concentrations to match self-assembly conditions. As such, final concentrations were in excess multiplied by the molar weight ratio of (RADA)₄-CP / (RADA)₄.

Groups were centrifuged to force the gel into a pellet upon overnight self-assembly. Half of the supernatant was removed and replaced with TNC buffer at least 10 times until the pH of the supernatant was 7.4. During this process, soluble peptides were removed so that all labile substrates are in nanofibers. Following this, a 5:3 ACN:H₂O solution was added to this solution for a final 5-fold dilution and 1:1 ACN:H₂O ratio. This was done to dissolve nanofibers for stock solutions and reduce future error in multi-sample aliquots that undergo drying and small volume resolubilization procedures.

To prepare hydrogel samples (10 μ l), the diluted peptide solutions were sonicated for 30 minutes, aliquoted 50 μ l in 0.2 mL PCR Tubes and vacuum dried. Each tube was filled with 7.5 μ l water and sonicated for 60 minutes. The tubes were very briefly spun down in a Corning LSETM Mini Microcentrifuge at 2000 x g to maintain level of fluid. The samples self-assembled at 4°C for 24 hours and, under cold-room condition, 2.5 μ l of four times working concentration active MMP-2 was carefully pipetted onto the sample surface. To initiate experiments, samples were incubated at 37°C. Addition of a 75 μ l ACN, 65 μ l H₂O and 0.1% TFA solution, to a final 150 μ l volume, was used to halt the reaction. 5 μ l of this mixture was pipetted and mixed with a solution of deuterated standard for quantitative mass spectrometry: 100 μ l H₂O, 0.1% TFA, and 5 μ l of the 0.3 mg/ml deuterated standard. These mixtures were spotted onto a MALDI plate and the HCCA matrix protocol used for synthesized peptides was applied (Section 2.2). Using the trapezoidal rule, product was determined by comparing the area under the curve of the product (2122 - 2130 m/z) and standard (2132 - 2140 m/z) isotopic envelopes. Concentrations were back calculated from the molar quantity of deuterated standard. In MATLAB (The MathWorks®), data was smoothed and filtered with *smooth* and *filter* functions. Data was curve-fitted and areas

were calculated with *spline* and *trapz* functions, respectively. The baseline was normalized by this division and filter process. Sample code is available in the appendices.

Initially, 0.5 % w/v (RADA)₄-CP1 and (RADA)₄-CP2 samples were treated with 40 nM MMP-2 for 32 days, which is a considerably high amount relative to stock concentration and a long time to ensure full digestion of the hydrogel. This sample was diluted 1:1000 in 1:1 ACN/H₂O, 0.1% TFA, and spotted for MALDI, directly without standard. This was repeated at 5 nM for 3 days, and compared with the TNC buffer, MMP-1 (5 nM), (RADA)₄-SP1, (RADA)₄-SP2 negative controls. MMP-1 was used to test substrate specificity and SP1/SP2 were used to test sequence specificity. 5 nM MMP was chosen as a high concentration, similar to that found in cancerous tissues and inflammation [46, 49]. The standard was added to these groups and all subsequent experiments. Following this, a 32 day dose response experiment was performed where substrate concentrations were 0.25% w/v to 2.00% w/v, with 0.25% w/v increments. Additionally MMP-2 was varied at 0, 0.1, 0.5, 1.0, and 5.0 nM. A time-based kinetics study was also conducted over this 32-day span. Cleavage sequences were 0.50% w/v and 1 nM MMP-2 was used due to their common conditions for hydrogels and MMP-2 physiology in literature [46, 49]. For each cleavage sequence, hydrogels were doped with (RADA)₄ at 25 to 100%, with 25% increments. Samples were quenched daily in order to help establish a time-based kinetics profile of the enzymatic reaction. All samples were analyzed based on the mean and standard deviation of n=3, where significance was based on $p < 0.05$ (*t*-test) for individual discussed values.

2.5. Hausdorff Dimension Analyses

All image processing and analysis was done using MATLAB R2012b (The Mathworks Inc. Natick, MA).

Fractal dimensions were determined using a box counting method performed by Hochman-Mendez, used for laminin nanostructures[30]. MATLAB code was modified from French and Costa and an example is shown in the appendices [50 - 51]. The fractal Hausdorff dimension is a measure of size-based similarities in complex geometries based on specified members or points [52]. These dimensions are quantified fractals, but these are not directly determined through image-based calculation, therefore box counting was used to estimate them. Using varying box sizes r within represented grids for each image, the amount of boxes $D(r)$ were counted associated with a set[53 - 55]. The following equation (1) was applied:

$$D_H = - \frac{\Delta[\log D(r)]}{\Delta \log(1/r)} \quad (1)$$

where D_H is the Hausdorff-Besicovitch or box count fractal dimension. All images were processed in greyscale and binary with the function *im2bw* and blank regions were filled with the *imfill* function.

3. Results

3.1. Controls and Standard for Quantifying Mass Spectroscopy Results

Proteolysis of (RADA)₄-CP1 and (RADA)₄-CP2, bearing respective high and low MMP-2 activity sequences, was performed at 37°C and characterized throughout this entire study using MALDI TOF/TOF mass spectrometry. Initially, the peptide substrates (0.5% w/v) were treated with 40 nM active MMP-2 for 32 days to observe apparent product fragments. Excessive enzyme and incubation time was used to ensure that an appreciable amount of product and substrate signal could be captured in one spectrum. The untreated group introduced enzyme free-TNC buffer. Peaks of 2525.2 and 2478.8 m/z are shown in the MMP-2 and buffer-control groups and reflect the theoretical molecular weights for (RADA)₄-CP1 and (RADA)₄-CP2, respectively (Fig. 3.2 Ai and Bi). Upon incubation with MMP-2, a peak at 2125.1 m/z was observed for the CP1 and CP2 systems, the molecular weight of which was consistent with the expected formed product. Moreover, the intensity of these peaks coincided with high and low affinity substrates.

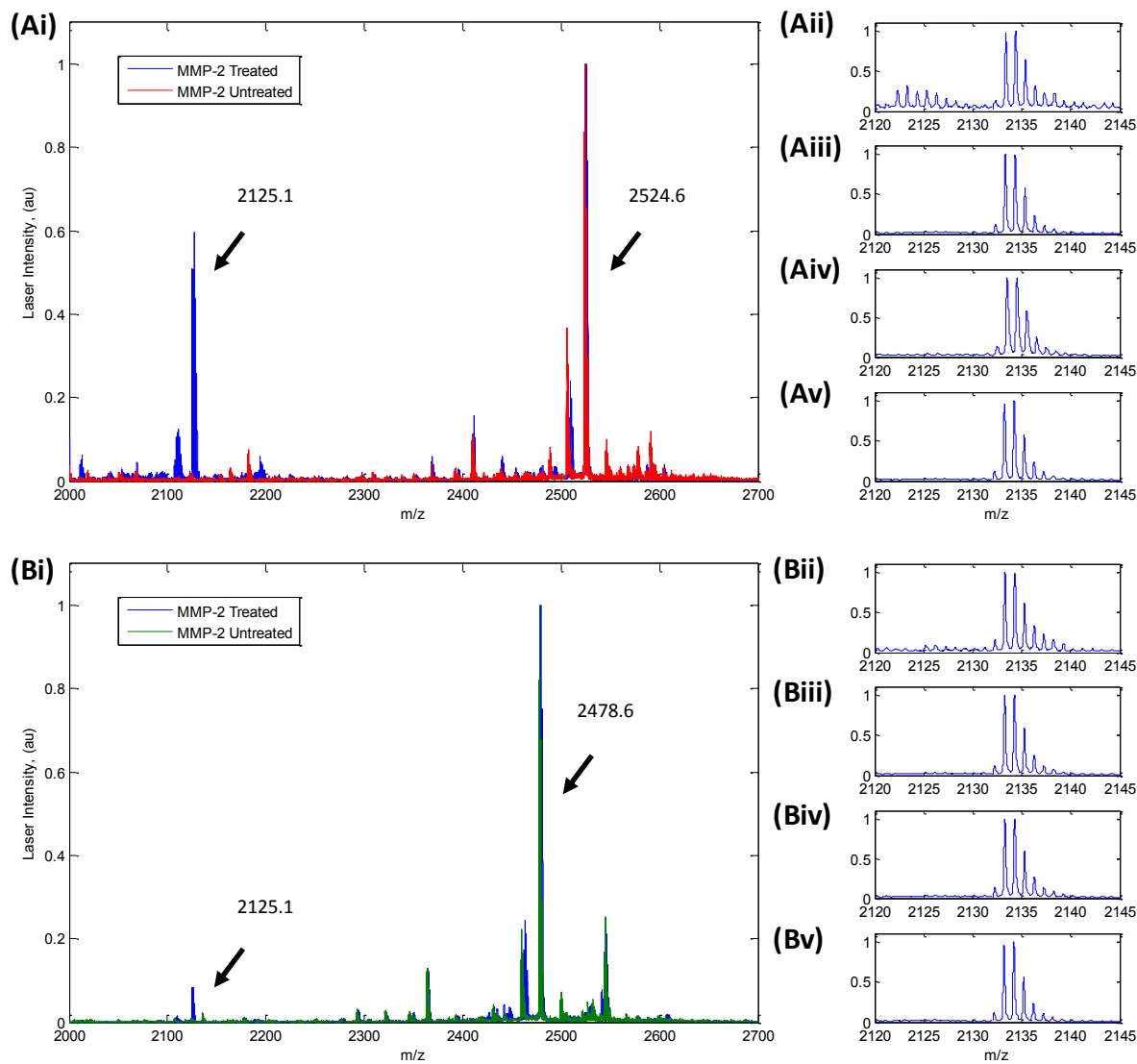


Figure 3.2. MALDI TOF/TOF mass spectrometry of 0.5% w/v (A) $(\text{RADA})_4\text{-GG-GPQG+IASQ}$ ($(\text{RADA})_4\text{-CP1}$) and (B) $(\text{RADA})_4\text{-GG-GPQG+PAGQ}$ ($(\text{RADA})_4\text{-CP2}$) proteolysis. Incubated with (i) 0 and 40 nM active MMP-2, in TNC buffer for 32 days at 37°C. Substrate peaks are labelled 2525.2 m/z and 2478.8 m/z , representing theoretical molecular weights of $(\text{RADA})_4\text{-CP1}$ and $(\text{RADA})_4\text{-CP2}$, respectively. The peak 2125.1 m/z represents the molecular weight of the product for both substrates. Also shown are product quantification with addition of the standard $(\text{RADA})_4\text{-GG-GPQGd}_8$ to a (ii) 5 nM active MMP-2 3 day treatment. These are compared to (iii) TNC buffer, (iv) 5 nM MMP-1, and (v) scrambled sequences $(\text{RADA})_4\text{-GG-IQPGSAQG}((\text{RADA})_4\text{-SP1})$ and $(\text{RADA})_4\text{-GG-PQGAQGPG}((\text{RADA})_4\text{-SP1})$. The standard peak, or average isotopic envelope is noted at 2132.1 m/z . $(\text{RADA})_4\text{-CP2}$ and $(\text{RADA})_4\text{-CP2}$ produced $31.6 \pm 0.3\%$ and $8.6 \pm 2.0\%$ in these conditions.

MALDI peak areas cannot be accurately quantified due to the complexity added due to ionization. To adequately shift the isotopic envelope, without overlap or inconsistent ionization, a+8 deuterated product standard was employed [41, 56]. The substrates were similarly exposed to 5 nM for three days and quantified with the equimolar addition of this standard in the following groups: MMP-2, TNC buffer, MMP-1, and scrambled peptide substrates as illustrated in Fig.3.2 A/B ii, iii, iv, and v, respectively. The expected isotopic envelopes for the product (2122 - 2130 m/z) and standard (2132 - 2140 m/z) are shown and the area under the curve was calculated and compared to derived product percentages. (RADA)₄-CP1 and (RADA)₄-CP2 sequences yielded $31.6 \pm 0.3\%$ and $8.6 \pm 2.0\%$ in MMP-2 conditions, respectively (Fig. 3.2Aii/Bii) (*t*-test, $p < 0.05$). Product formation was negligible for all negative controls, including the enzyme free system, MMP-1, and scrambled cleavage sequences (Fig. 3.2 Aiii/Aiv/Av and Biii/Biv/Bv). The greater CP1 product formation over CP2 is reflected in the first full spectra result (Fig. 3.2Ai and 3.2Bi), which was expected due to their MMP-2 affinities. The lack of product formation with MMP-1 proves that these substrate sequences are performing as expected, *viz.*, with specificity for MMP-2. Even CP2, despite being cleavable by many MMP types, has an order of magnitude lower specificity for MMP-1, which was chosen to contrast these differences [38].

3.2.Nanoscaffold Mass and MMP-2 Concentration Dependency

Utilizing a range of physiologically relevant MMP-2 concentrations that have been identified for various cancer and inflammation states (0, 0.1, 0.5, 1.0, and 5.0 nM) the total product formed and the percentage formed after 32 days of incubation was quantified for a range of pure (RADA)₄-CP1 (Figure 3.3) or (RADA)₄-CP2 (Figure 3.4) hydrogel constructs (0.25 – 2.0% w/v) [46, 49].

The total molar product formation increased, on average, with increasing (RADA)₄-CP1 substrate and MMP-2 concentrations (Figure 3.3). These were all significantly greater than the 0 nM MMP-2 control that remained at a baseline between 0 to 100 μM , within error. It was apparent that for all (RADA)₄-CP1 concentrations studied, the total product formed was similar for MMP-2 concentrations of 0.1 and 0.5 nM. Although higher on average relative to 0.1 and 0.5 nM, the total product formation for 1.0 and 5.0 nM MMP-2 concentrations also yielded similar values throughout the range of (RADA)₄-CP1 concentrations studied. (RADA)₄-CP1 incubation with 0.1 and 0.5 nM MMP-2 showed a total amount of product formation of $\sim 550 \mu\text{M}$ at 0.25% w/v, that increased in a relatively stepwise manner, to $\sim 1150 \mu\text{M}$ at 1.5% w/v. From 1.5 and 2.0% w/v, a rapid increase to $\sim 2250 \mu\text{M}$ occurred. On the other hand, 0.25 to 0.75 %w/v (RADA)₄-CP1, 1.0 and 5.0 nM MMP-2 systems showed a slight increase in total product formation from ~ 700 to $\sim 875 \mu\text{M}$. From 1.0 to 1.5 %w/v (RADA)₄-CP1, both 1.0 and 5.0 nM concentrations yielded a drastic increase in product formation from ~ 1000 to $\sim 1500 \mu\text{M}$, and from 1.5 to 2.0% w/v, these MMP-2 concentrations continued to yield similar amounts of product formed with $\sim 2750 \mu\text{M}$ of total product formed under these conditions. The higher two concentrations of MMP-2 started to deviate from the lower concentrations at (RADA)₄-CP1 values of 1.5% with total product formations of ~ 1500 and $\sim 1150 \mu\text{M}$, respectively.

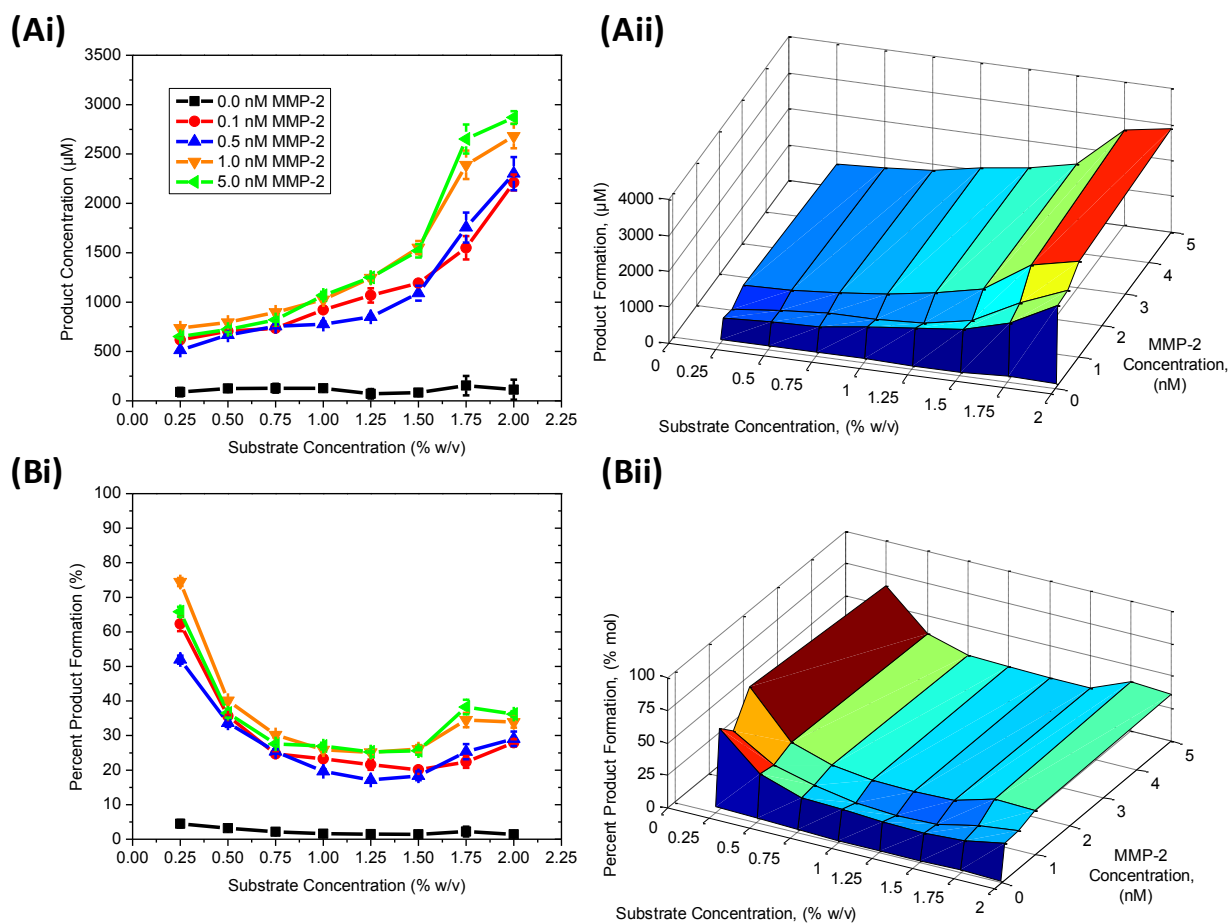


Figure 3.3. Product formation as a function of substrate $(\text{RADA})_4\text{-GG-GPQG+IASQ}((\text{RADA})_4\text{-CP1})$ and MMP-2 concentration calculated using the area under the curve from MALDI TOF/TOF mass spectra of (A) raw product and (B) percent product of initial amount. Perspectives shown are (i) 2D and (ii) 3D. MMP-2 concentrations shown are 0, 0.1, 0.5, 1.0, 5.0 nM. All reactions were performed in TNC buffer at 37°C for 32 days, where data represent average and error bars are ± 1 SD for $n = 3$ (experiments repetitions).

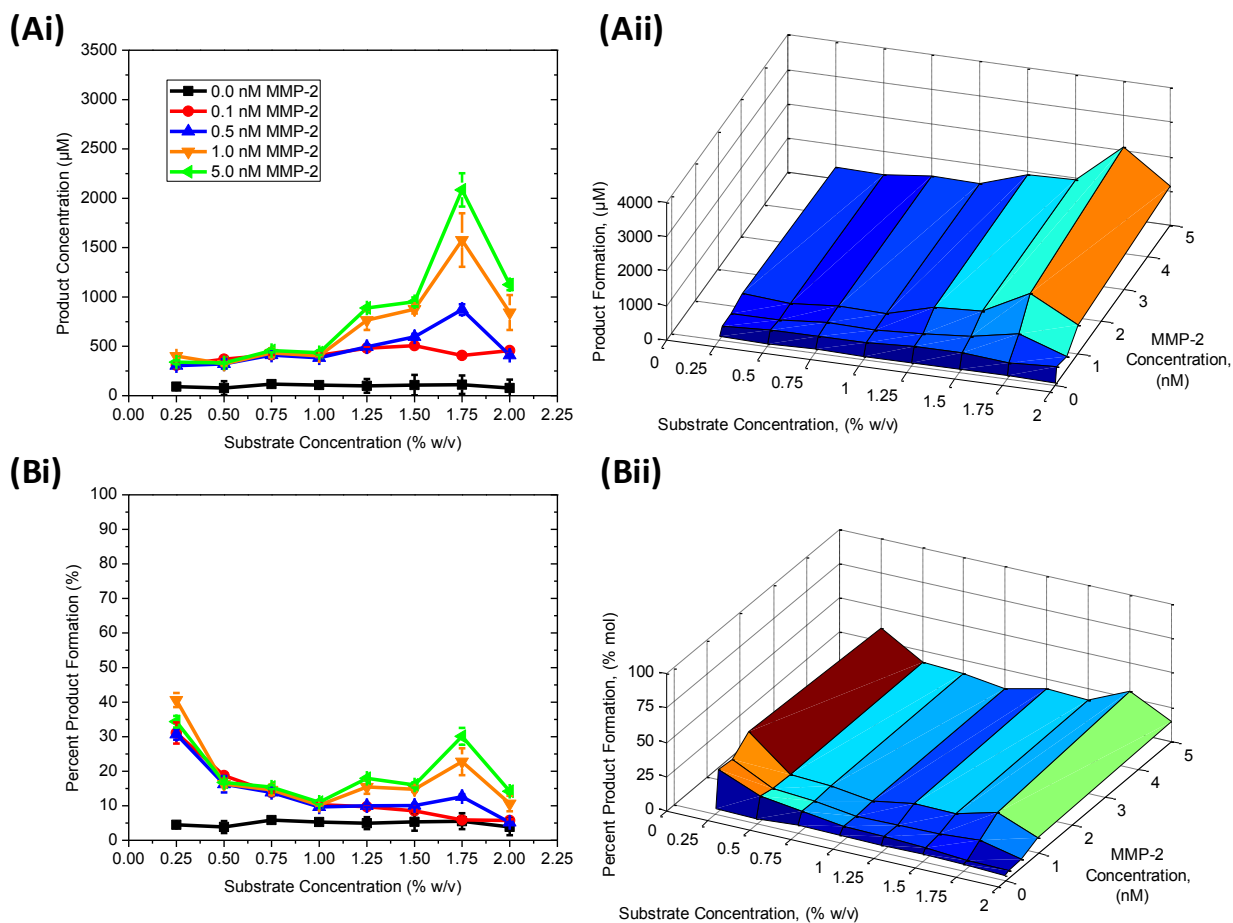


Figure 3.4. Product formation as a function of substrate ($((\text{RADA})_4\text{-GG-GPQG+PAGQ}((\text{RADA})_4\text{-CP2}))$) and MMP-2 concentration calculated using the area under the curve from MALDI TOF/TOF mass spectra of (A) raw product and (B) percent product of initial amount. Perspectives shown are (i) 2D and (ii) 3D. MMP-2 concentrations shown are 0, 0.1, 0.5, 1.0, 5.0 nM. All reactions were performed in TNC buffer at 37°C for 32 days. All reactions were performed in TNC buffer at 37°C for 32 days, where data represent average and error bars are ± 1 SD for $n = 3$ (experiments repetitions).

The percent product formation results provide further insight into the ability of these hydrogels to be cleaved by MMP-2. For example, there was relatively little difference in total amount of product formed for all 0.25% w/v systems. However, it was apparent that the 5.0 nM MMP-2 concentration released ~75% of the total available product in 32 days, but only ~50% of the total available product was liberated for the same system exposed to 0.5 nM MMP-2. These don't follow the trend of increasing proteolysis due to increasing enzyme concentration and may be somewhat confounded due to the error in the raw product to percent conversion. Moreover, for all cases, any significant increase in cleavage domains within the hydrogel did not result in an increase in the percent cleavage observed after 32 days incubation. In fact, all MMP-2 systems showed a drastic decrease in percent product formation to a plateau value between 1.0 and 1.5 % w/v (RADA)₄-CP1; this plateau value was slightly affected by MMP-2 concentration but had a tight range between 20 and 30%. For (RADA)₄-CP1 concentrations greater than 1.5% w/v, however, an average increase in percent release was observed for all systems. These data suggest that varying peptide concentration, changing the available cleavage sites and hydrogel surface area, may directly affect the enzymatic action and outcome of these systems.

The effect of cut site affinity for MMP-2 on peptide release was studied using similar hydrogel systems composed of the lower affinity cut site, *viz.*, (RADA)₄-CP2 (Figure 3.4). Regardless of the enzyme concentration for (RADA)₄-CP2 concentrations less than 1.0% w/v an average of ~375 μM of product was formed. Every group was significantly higher than the 0 nM MMP-2 baseline and, like (RADA)₄-CP1, did not deviate above ~100μM. For (RADA)₄-CP2 concentrations of 1.25% w/v and greater, the effect of increasing enzyme and substrate concentration become noticeable: for enzyme concentrations less than 0.5 nM, similar amounts of product were formed (~375 μM), with more being formed for 1.0 nM concentrations and

greater. Similar to (RADA)₄-CP1, product formation was greater for higher amounts of MMP-2, at substrate concentrations greater than 1.0% w/v. However, unlike (RADA)₄-CP1, this increasing trend is not continuous at the highest hydrogel content. A decrease from 1.75 - 2.00% w/v is significant with all MMP-2 levels above and equal to 0.5 nM, effectively returning to the 1.50% w/v product amount, displaying a clear maximum at 1.75% w/v in these trends. As with (RADA)₄-CP1, 0.1 and 0.5 nM MMP-2 showed negligible differences in product formed for 1.25% w/v and greater, and product levels 1.0 and 5.0 nM MMP-2 are likewise grouped, but higher by ~500 μM. For a substrate concentration of 1.75% w/v, a marked increase in product formation for all enzyme concentrations, other than 0.1 nM, was observed: 0.1, 0.5, 1.0, and 5.0 nM MMP-2 exposure resulted in 408 ± 19, 873 ± 54, 1577 ± 271, and 2085 ± 170 μM product formed, respectively (*t*-test, *p* < 0.05). That said, however, the amount of product formed is significantly comparable between the two high (1.0 and 5.0 nM) and low (0.1 and 0.5 nM) enzyme concentrations for substrate concentrations around 1.75% w/v.

With (RADA)₄-CP2 peptides, MMP-2 groups allow for the greatest percent product formation at 0.25 % w/v being 30 - 40 %. This was likewise noted in (RADA)₄-CP1 and also gradually decreased to a value of ~ 10 % at 1.0% w/v, as substrate concentration increased (for all MMP-2 groups). Above concentrations of 1.0% w/v, product percentages do not deviate from 10 % in 0.1 and 0.5 nM MMP-2 groups until they separate approximately 6 % by 1.75 % w/v (5.8 ± 0.3 and 12.6 ± 0.8 %, for 0.1 and 0.5 nM MMP-2, respectively), and both approach 6 % by 2.00 % w/v being indistinguishable from the 0 nM control. On the other hand, 1.0 and 5.0 nM enzyme groups remain 5 - 10 % higher than 0.5 nM MMP-2, follow an inverted curve, and the 5.0 nM group is significantly greater by 7.0 % at the 1.75% w/v maxima (23 ± 4 and 30 ± 2 %, for 1.0 and 5.0 nM MMP-2 respectively) (*t*-test, *p* < 0.05).

3.3. Morphology of MMP-2 Degraded Nanoscaffold

Nanoscale morphology of (RADA)₄-CP1 and (RADA)₄-CP2, with and without MMP-2 for 32 days, were characterized using TEM. From these data fractal Hausdorff dimensions were generated (Fig. 3.5). Pure (RADA)₄ was added to these systems at 0, 25, 50, and 75% by volume, normalized to the (RADA)₄ sequence, so as to investigate the addition of cleavage domain only on the morphology of assembled nanofibers. To observe degradation, a frequently-used hydrogel concentration (0.5 % w/v) and a physiological relevant MMP-2 level (1 nM) were chosen as a subset of the previous dataset to understand how packing of the cleavage domain on the nanofiber may affect enzyme kinetics. It was observed that multiple phases of peptides were not present in all mixtures prior to enzyme incubation, indicating that the substrate bearing RADAs were incorporated into the nanofibers. Without MMP-2 treatment, thick bundles of nanofibers are present in both pure (RADA)₄-CP1 and (RADA)₄-CP2 samples that ranged in thicknesses between 20 - 100 nm and 20 - 300 nm, respectively (Fig. 3.5 Ai and Ci). Upon addition of (RADA)₄ the untreated (RADA)₄-CP1 groups showed thinner bundles and individual nanofibers (5 - 20 nm thick) that were closer in shape to pure (RADA)₄ nanofibers (Fig 3.5 Aii-iv). Mixing 25% (RADA)₄ with (RADA)₄-CP2, without the presence of MMP-2, thick bundles of nanofibers were present with pores no greater than 100 nm in apparent diameter (Fig. 3.5 Cii). Increasing the (RADA)₄ content to 50% and 75%, the networks lose complexity and density in a trend-wise manner (Fig. 3.5 Cii-iv). MMP-2 treated groups all have the same morphology of discontinuous networks of nanofibers that were 5-10 nm thick (Fig. 3.5 Bi-iv, Di -iv). These were similar to pure untreated and MMP-2 treated (RADA)₄ (Fig. 3.5Fi-ii), in which the treated group was slightly discontinuous compared to the untreated group. Fractal dimensions for both MMP-2 untreated and treated (RADA)₄-CP1 have a decreasing 0.3 trend as (RADA)₄ content increased

from 0 to 50%; however at 75% (RADA)₄, MMP-2 treated systems were ~ 0.5 lower than untreated systems, being 1.74 ± 0.12 (Fig. 3.5 Ei). On the other hand, MMP-2 treated (RADA)₄-CP2 groups have a decreasing trend in Hausdorff dimension to 1.11 ± 0.13 with the addition of (RADA)₄, while the untreated groups dimensions remain close to 1.6 - 1.7 (Fig. 3.5 Eii) (*t*-test, *p* < 0.05). Dimensions were considered meaningful above or close to 1.3, which is fractal behaviour similar to what was noted in nature, such as dendritic Julia sets of similar morphology or other SAPs [35, 58].

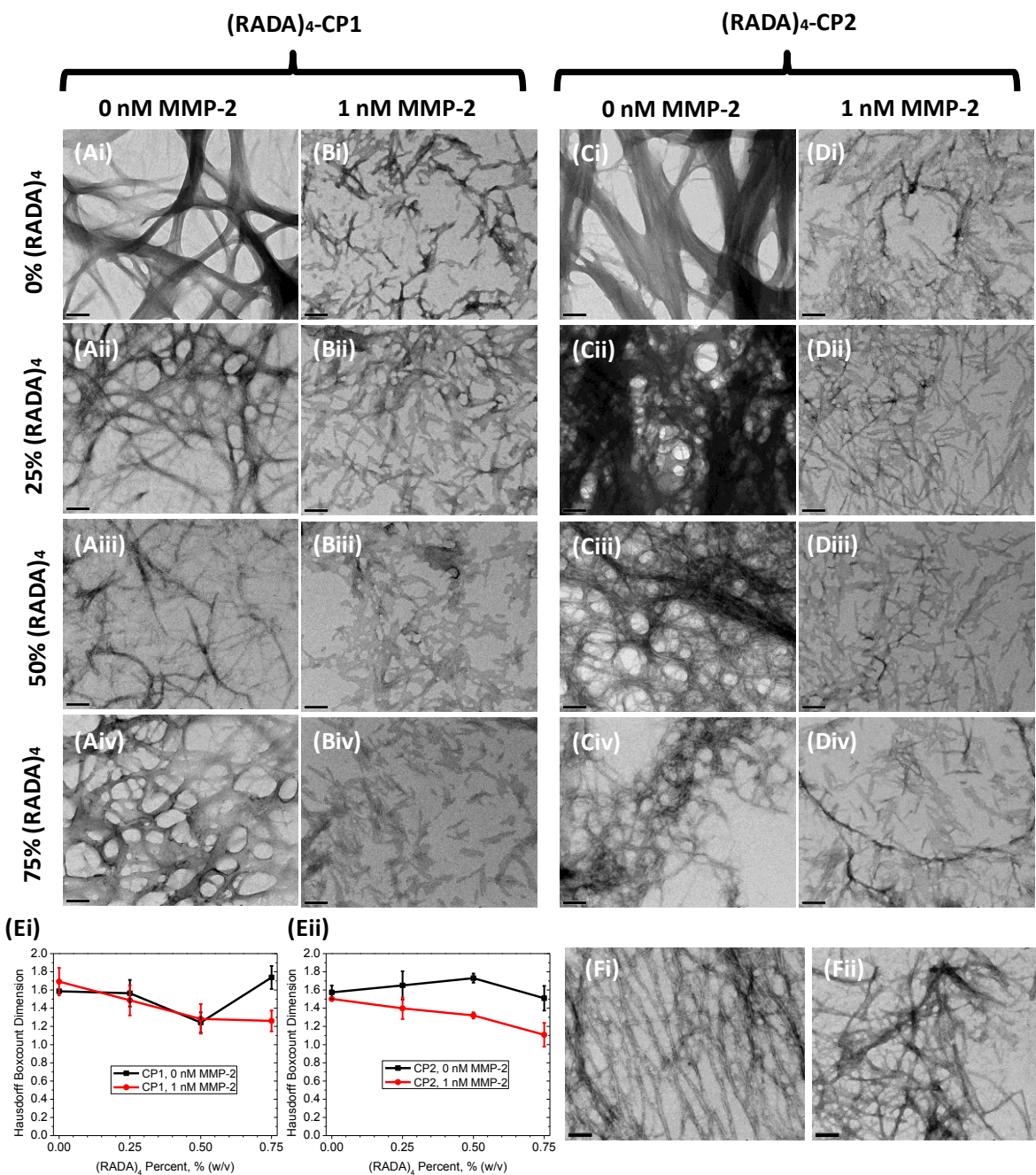


Figure 3.5. Transmission electron microscopy of $(RADA)_4$ -GG-GPQG+IASQ ($(RADA)_4$ -CP1) treated with (A) 0 and (B) 1 nM MMP-2, and $(RADA)_4$ -GG-GPQG+PAGQ ($(RADA)_4$ -CP2) similarly treated with (C) 0 and (D) 1 nM MMP-2. Mixtures included (i) 0%/100%, (ii) 25%/75%, (iii) 50%/50%, and (iv) 75%/25% of $(RADA)_4$ / $(RADA)_4$ -CP1 or $(RADA)_4$ / $(RADA)_4$ -CP2. Fractal dimensions (E) as a function of $(RADA)_4$ addition, with and without MMP-2 treatment for (i) $(RADA)_4$ -CP1 and (ii) $(RADA)_4$ -CP2. Also, included is (Fi) 0 nM and (Fii) 1 nM MMP-2 treated $(RADA)_4$ control. All samples were 0.5% w/v, incubated at 37°C for 32 days, extracted, and stained with 4% uranyl acetate and imaged. Scale bars are all 100 nm. Data represent average and error bars are ± 1 SD for $n = 3$ (experiments repetitions).

3.4. Time Series of MMP-2 Degraded Nanoscaffold

Product formation kinetics for (RADA)₄-CP1 (Fig. 3.6) and (RADA)₄-CP2 (Fig. 3.7) were observed, using the same conditions as the morphology study (Fig. 3.7). In all conditions for CP1 product formation increases as a function of time. Molar and percent product levels reach a plateau by day 4 in CP1 mixtures, but between day 12 and 15, this trend increases in an apparently linear manner, although this is not noteworthy in 50% (RADA)₄ content due to error. This trend is not visible in CP2 mixtures, where product levels are overall lower than CP1 groups, increase gradually after day 1, and cease rising by day 24 for 50% and 75% (RADA)₄. Raw molar product from both CP1 and CP2 peptides increases with the reduction of (RADA)₄ except at 0%, where a decrease is noted. The opposite trends are shown when observing percent product formation, where the higher product curve is dictated by the lower (RADA)₄ content. The highest amounts of product are formed with 25% (RADA)₄ content, which are 438.3 ± 52.2 and 418.8 ± 52.2 μM at day 4, and progress to 598.5 ± 48.3 and 573.9 ± 8.0 μM by day 32, for (RADA)₄-CP1 and (RADA)₄-CP2, respectively. Alternatively, the greatest percent product are made with the 75% (RADA)₄ mixtures, which are 65.2 ± 4.3 and 70.8 ± 5.0 % at day 4, and progress to 94.2 ± 2.4 and 79.4 ± 7.0 % by day 32, for (RADA)₄-CP1 and (RADA)₄-CP2, respectively (*t*-test, *p* < 0.05).

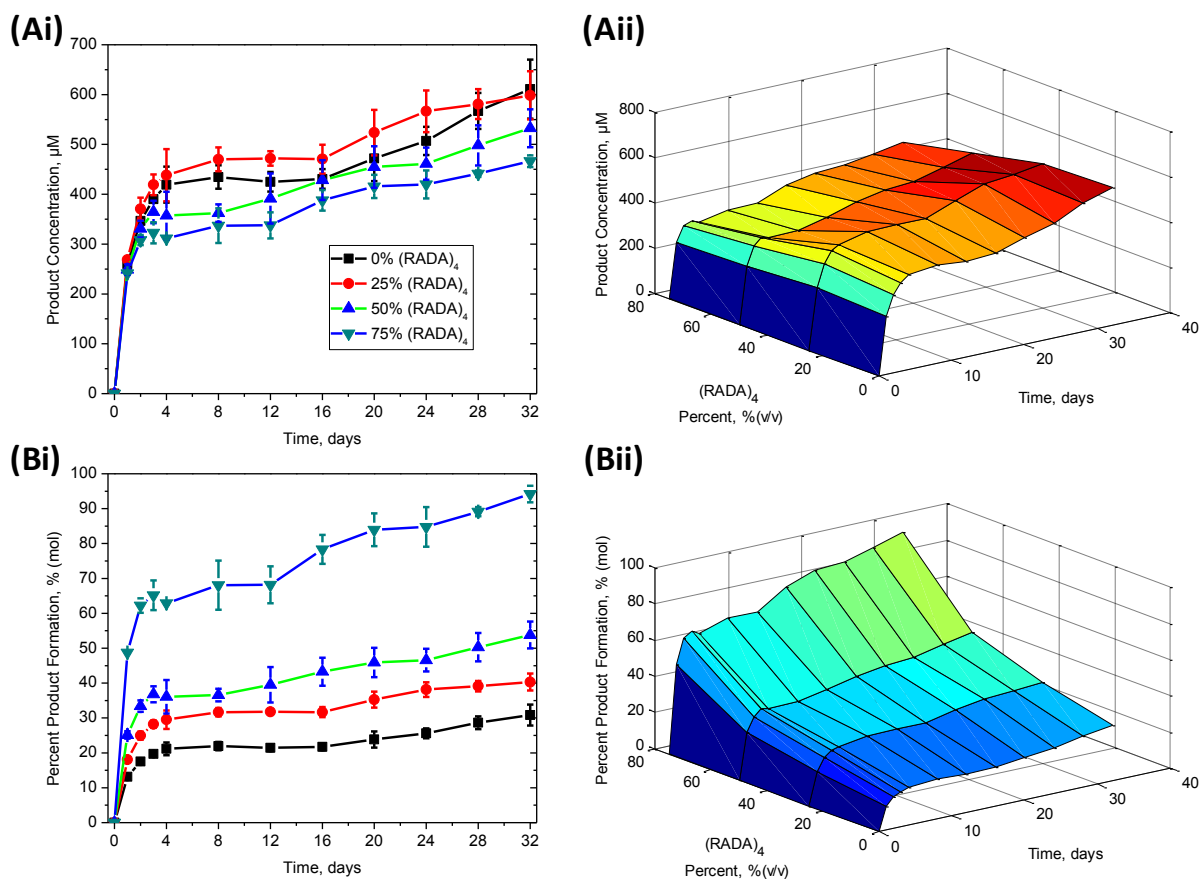


Figure 3.6. Product formation as a function of time from MMP-2 digestion of 0.5% w/v (RADA)₄-GG-GPQG+IASQ((RADA)₄-CP1) calculated by area under the curve from MALDI TOF/TOF mass spectra of (A) raw product and (B) percent product of initial amount. Perspectives shown are (i) 2D and (ii) 3D. Mixtures included 0%/100%, 25%/75%, 50%/50%, and 75%/25% of (RADA)₄/ (RADA)₄-CP1. All reactions were performed in TNC buffer at 37°C for 32 days, 24 hours upon self-assembly. Data represent average and error bars are ± 1 SD for $n = 3$ (experiments repetitions).

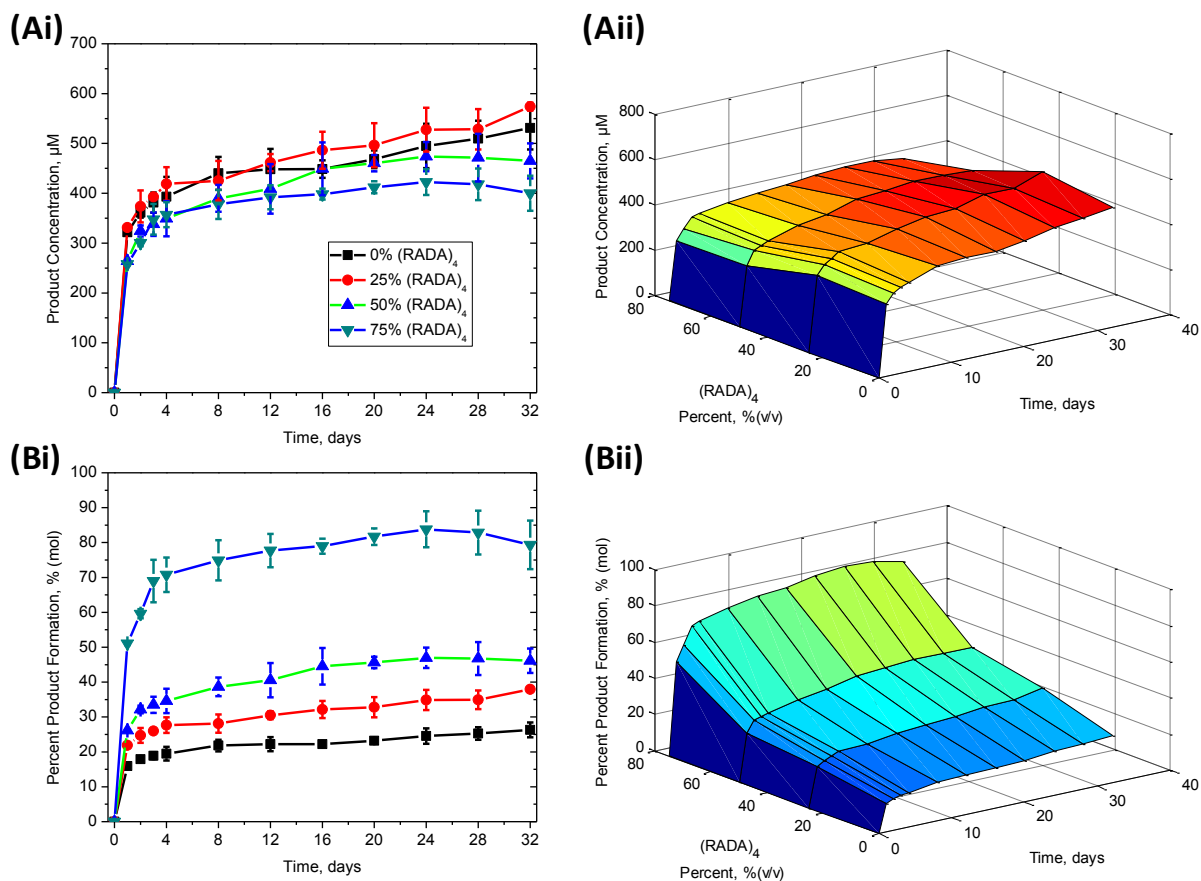


Figure 3.7. Product formation as a function of time from MMP-2 digestion of 0.5% w/v (RADA)₄-GG-GPQG+PAGQ (CP2) calculated by area under the curve from MALDI TOF/TOF mass spectra of (A) raw product and (B) percent product of initial amount. Perspectives shown are (i) 2D and (ii) 3D. Mixtures included 0%/100%, 25%/75%, 50%/50%, and 75%/25% of (RADA)₄/ (RADA)₄-CP2. All reactions were performed in TNC buffer at 37°C for 32 days, 24 hours upon self-assembly. Data represent average and error bars are ± 1 SD for $n = 3$ (experiments repetitions).

4. Discussion

The amount of active enzyme present has a significant effect on product formation, especially for (RADA)₄-CP2 above 1.0% w/v, despite 0.1/0.5 nM and 1.0/5.0 nM groups being indistinguishable from each other over many of the substrate concentrations. The changes from 0.5 to 1.0 nM may be important for modulating drug release. With the increased addition of the (RADA)₄-CP1 substrate, more raw product is formed upon exposure to MMP-2, which would be expected from soluble form of the CP1 peptide. Augmenting (RADA)₄-CP2 content yields increased product formation at concentrations greater than 1.0% w/v and has maxima at 1.75 % w/v, which is also a point of interest in the CP1 groups. Due to the ceiling of product formation noted near 2.0% w/v, the substrate concentration may be high enough to hinder MMP-2 efficacy in both SAPs, and may be a result of more complex matrices, nanofiber bundles, or steric hindrances typical in higher concentration hydrogels and (RADA)₄ [57]. The morphology formed by CP2 groups may actually be more complex and have greater steric and diffusion limitations than those formed with CP1 SAPs, as less product is generated for these groups at 2.00 % w/v. Higher concentrations greatly change the visible networking of (RADA)₄ as shown by the authors in a previous study with Saini *et al.*[19].

The trends present in the raw product curves for both CP1 and CP2 are not the same when percent product is observed because more is formed in lower concentration. This highest raw product from both SAPs are formed at 1.75 - 2.00 % w/v, however the highest percent products are formed at 0.25 % w/v. This may be artificially enhanced during the percent conversion, but could be an indication of the matrix content digested. Conversely to the product levels formed by concentrated SAPs, lower concentrations likely form less dense networks with lower aggregation and are subsequently digested to a greater extent due to potential greater surface area. The

differences in product formation, comparing lower to higher MMP-2 content, provides strong evidence that drug release can be modulated to protease secretion from endogenous cells, especially at higher substrate concentrations. Alternatively, having up to 75 % product formation, or hydrogel digestion, may prove an excellent strategy to prime the subsequent removal of the matrix upon delivering its dose. This can prevent a potential chronic host response from the material due to any persisting undigested presence. To demonstrate the potential limitations introduced by the architecture of these SAPs, or the visual fate of the digested delivery system, morphology must be studied.

Pure constructs of 0.5%w/v (RADA)₄-CP1 or (RADA)₄-CP2 formed drastically different matrix morphologies as compared to (RADA)₄ alone (Fig. 3.5 Ai, Ci, F). Both CP1 and CP2 constructs formed thick bundles composed of nanofibers, whereas pure (RADA)₄ constructs formed individual nanofibers as expected. The fact that the appended amino acids may cause the bundling of nanofibers to occur may be somewhat expected as the driving force for (RADA)₄ assembly has been shown to be dominated by hydrophobic interactions and, to a lesser degree, electrostatic interactions [59]. Both CP1 (GPQG+IASQ) and CP2 (GPQG+PAGQ) motifs include amino acids with a range of physicochemical properties. Glutamine could potentially alter the formation of anti-parallel β -sheets [60]. Although there are different scales to rank amino acid hydrophobicity at a pH of 7, glycine (G) is generally considered marginally hydrophobic (0 hydrophobicity) and phenylalanine (F) is generally considered the most hydrophobic (100 hydrophobicity) [61]. The inclusion of hydrophobic amino acids isoleucine (I, 99) and alanine (A, 41) in CP1 may facilitate nanofiber interactions leading to bundle formation. In comparison, CP2 has a proline (P, -46) instead of isoleucine (I, 99) and glycine (G, 0) is similar to serine (S, -5). This slight difference in amino acid composition may explain why CP1,

with the more hydrophobic isoleucine, may not only show bundle formation, but the formed bundles seemed generally more dense and thinner (Fig. 3.5 Ai vs. Ci) than those formed in the CP2 system. That said, proline (P), which has a cyclic residue embedded into the peptide backbone, potentially 'bends' the molecule and potentially disrupts β -sheets in repeated sequences, which has been shown in protein secondary structures, and allows hydrophobic interactions to make bundling preferable. Proline rich peptides are the core component of a vesicular SAP and are present in naturally forming and highly robust protein constructs such as zein maize storage proteins [62 - 65]. In fact, proline may be the residue that strongly influences bundle formation, for when cleaved off of the sequence by MMP-2 (Fig 3.5 Di-iv) the morphology returns to a more individual nanofiber state, as seen for CP2 systems.

Differences in bundling architectures were drastic for both CP1 and CP2 as (RADA)₄ is added to the system. Pure CP2 groups appear to have the thicker bundles when compared to CP1, which may hinder enzyme turnover and explain why there is a series of molar product maxima in CP2 mixtures and plateaus in CP1 mixtures when substrate concentrations approach 2.0 % w/v (Fig. 3.3 and 3.4). Despite these differences discussed together, morphology is drastically different for MMP-2 treated when compare to untreated, appearing digested and fragmented (Fig. 3.5). This resulted in comparable architecture for both CP1 and CP2 groups across all additions of (RADA)₄ and bears a similarity to MMP-2 untreated/treated (RADA)₄, being somewhat thinner and fragmented. Coupled with MALDI results, this is strong evidence suggesting that MMP-2 cleaved the peptides at the labile site, reducing the general complexity of the morphology, which is typically seen in nanofibers from gelatin, collagen, elastin, and laminin [66]. Cleavage of the peptides also lowers the fractal dimension with greater (RADA)₄ content and may be a result of the contour shapes being deteriorated. With this in mind, pure

groups retain their dimension and scaling patterns from this type of proteolysis, despite major differences in architecture, and are potentially more robust when exposed to biological stimulus. On the other hand, increasing (RADA)₄ may result in a less stable morphology that can potentially be cleared with greater ease upon delivering its drug contents. Though fluorescence correlated spectroscopy, Fatin-Rouge demonstrated that lower fractal coefficients were indicative of increasing relative diffusion within the hydrogel. Similar to our situation, a lower fractal dimension due to peptide cleavage may likewise indicate the potential for greater diffusivity of molecules within the hydrogel [28]. To further gauge the practical controlled digestion of this system, as MMP-2 is prone to sustained levels, enzymatic-based product formation should be gauged over the course of this 32 day study.

A quick burst of product, potentially due to a rapidly digested bulk portion of the nanostructure, is present the first 4 days of this study which may account for the great amount of initial product. The MMP-2 may lose some of its activity though auto-catalysis in this period as well, however this is likely insignificant as product formation was continuous in many groups, and the tissue inhibitor of MMP-2 (TIMP-2) was present in minute amounts in the supplier stock solution to prevent enzyme auto-degradation. The presence of non-uniform curves in the CP1 groups suggests a potential turning point in hydrogel degradation. At the noteworthy time points (day 12- 14), bulk nanostructures may have succumbed to proteolysis, as was noted in the microscopy, and another series of cleavable motifs have become exposed to further digestion. This was similarly seen when cleavage sites are exposed in collagen microtubules with reduced aggregation by proteolysis [67 - 68]. This is not apparently occurring with CP2 mixtures - cleavage may be more gradual and degradation ceases in some cases. It is also possible that self-assembly, or rather re-assembly, is occurring during proteolysis with CP1, as was observed with

the MMP-2 cleavable SAP (RADA)₃-PVGLIG-(RADA)₃ by Chau *et al.* [26]. The addition of (RADA)₄ alters raw product formation, at most, by 200 μ M, but appears to push the most product out with 25% for both CP1 and CP2 peptides. This is potentially due to (RADA)₄ reducing the bundling architecture, as is noteworthy in the TEM images, and promoting MMP-2 molecular movement and steric access to the cleavage motifs, while having a higher substrate content than the other groups. By percent product, formation is related to (RADA)₄ content for both CP1 and CP2 groups and reflects the results noted in low substrate concentrations (Fig. 3.3 and 3.4). This may be dependent on thinner networks of individual nanofibers that once again, promote greater MMP-2 digestion. Overall, product levels comparing CP1 and CP2 are not greatly different, although CP1 was generally higher in most cases observed. This is counter-intuitive as the activity expected from the cleavage sequences is contrastingly high and low. This may be an important observation for the cleavage kinetics for these substrate sequences were determined in a well-mixed (ie. not diffusion limited) system with surfactants. By introducing rigid nanostructures that are capable of reforming and constantly resisting dissolution, cleavage kinetics may be dominated by diffusion and accessing the substrates more than the substrate composition itself. The nanoscale morphology may be imperative in engineering predictable MMP-2 deterioration, drug loading, and the ultimate delivery of these systems.

5. Conclusions

The self-assembling peptide hydrogel (RADA)₄ was tethered to and modulated with the matrix metalloproteinase 2 (MMP-2) cleavable peptide sequences GPQG+IASQ (CP1) and GPQG+PAGQ (CP2) to create a peptide release system that is able to form *in situ* and deliver product when exposed to various protease concentrations observed in inflammatory and cancerous protease secretion. As such, these self-assembling mixtures of high and low activity

self-assembling MMP-2 cleavable peptides ((RADA)₄-CP1 and (RADA)₄-CP2)) are capable of delivering on-demand product, over the course several weeks, in the presence of varying hydrogel concentrations, MMP-2 levels, and dose altering (RADA)₄ SAP contents. A variety of product amounts were noted for potential application, and sustained formation was noted over time, under typical hydrogel and enzymatic conditions. For both CP1 and CP2, the highest product formed at 1.75% w/v peptide hydrogel and the greatest percent product, or hydrogel digestion, was noteworthy at 0.25 - 0.5 % w/v. Product formation amounts and percentages acquired for the CP1 and CP2 sequences agree with their relative level of proteolytic activity when exposed to MMP-2. Furthermore, visible degradation was observed in the presence of MMP-2, and lower fractal dimensions were reported, suggesting a diminishing on continuous morphology which can allow for ample release diffusion upon degradation. Measured daily over a month, MMP-2 induced raw product formation more rapidly in 100% and 75% (RADA)₄-CP1/(RADA)₄-CP2 mixtures in (RADA)₄ (0.5% w/v). However, percent product was more prevalent in 25% of these mixtures, which is likely due to higher surface areas from thin and complexly interwoven networks. The MMP-2-cued drug delivery capacity, i.e. product formation, of these nanoscaffolds are highly dependent on matrix concentration, active MMP-2 present, cleavage site, and time, suggesting for a dynamically tuneable, but specifically controlled on-demand release potentially able to mirror cell and tissue response.

6. Acknowledgements

The Authors would like to acknowledge Terry, Sereda, Paul Semchuk, and Jack Moore for peptide synthesis assistance, Ron Koss and Arlene Oatway for electron microscopy support, and Emily Gruber and Theodore Ng for support with everything else. The authors are grateful for

financial support from NSERC, NINT-NRC, Women and Children's Health Research Institute, and Alberta Gangwon Korea

6. References

1. Singh HD, Bushnak I, Unsworth LD. Engineered peptides with enzymatically cleavable domains for controlling the release of model protein drug from “soft” nanoparticles. *Acta Biomater.* 2012(8):636-45.
2. Hu Q, Katti PS, Gu Z. Enzyme-responsive nanomaterials for controlled drug delivery. *Nanoscale.* 2014;6:12273-86.
3. Ulery BD, Nair LS, Laurencin CT. Biomedical applications of biodegradable polymers. *J Polym Sci , Part B: Polym Phys.* 2011;49(12):832-64.
4. Yoshida T, Lai TC, Kwon GS, Sako K. pH- and ion-sensitive polymers for drug delivery. *Expert Opin Drug Deliv.* 2013;10(11):1497-513.
5. Romano NH, Sengupta D, Chung C, Heilshorn SC. Protein-engineered biomaterials: nanoscale mimics of the extracellular matrix. *Biochim Biophys Acta.* 2011;1810(3):339-49.
6. Mayet N, Choonara YE, Kumar P, Tomar LK, Tyagi C, Du Toit LC, et al. A comprehensive review of advanced biopolymeric wound healing systems. *J Pharm Sci.* 2014 August;103(8):2211-30.
7. Lee KY, Mooney DJ. Hydrogels for Tissue Engineering. *Chem Rev.* 2001;101(7):1869-78
8. Toh WS, Loh XJ. Advances in hydrogel delivery systems for tissue regeneration. *Mater Sci Eng C Mater Biol Appl.* 2014;45:690-7.

9. Peters A, Brey DM, Burdick JA. High-throughput and combinatorial technologies for tissue engineering applications. *Tissue Eng Part B Rev.* 2009 September;15(3):225-39.
10. Rodríguez-Seguí S, Pla-Roca M, Engel E, Planell J, Martínez E, Samitier J. Influence of fabrication parameters in cellular microarrays for stem cell studies. *J Mater Sci: Mater Med.* 2009 July;20(7):1525-33.
11. Fichman G, Gazit E. Self-assembly of short peptides to form hydrogels: design of buildingblocks, physical properties and technological applications. *Acta Biomater.* 2014;10:1671-82.
12. Hamley IW. Self-assembly of amphiphilic peptides. *Soft Matter.* 2011;7:4122-38.
13. Zhang S. Fabrication of novel biomaterials through molecular self-assembly. *Nat Biotechnol.* 2003 October;21(10):1171-8.
14. Zhao X, Zhang S. Designer self-assembling peptide materials. *Macromol Biosci.* 2007 January 5;7(1):13-22.
15. Geckil H, Xu F, Zhang X, Moon S, Demirci U. Engineering hydrogels as extracellular matrix mimics. *Nanomedicine.* 2010 April;5(3):469-84.
16. MacPhee CE, Woolfson DN. Engineered and designed peptide-based fibrous biomaterials. *Curr Opin Solid State Mater Sci.* 2004;8(2):141-9.
17. Gelain F, Unsworth LD, Zhang S. Slow and sustained release of active cytokines from self-assembling peptide scaffolds RID A-7231-2011. *J Controlled Release.* 2010;145(3):231-9.

18. Holmes TC. Novel peptide-based biomaterial scaffolds for tissue engineering. *Trends Biotechnol.* 2002 January;20(1):16-21.
19. Saini A, Serrano K, Koss K, Unsworth LD. Evaluation of the hemocompatibility and rapid hemostasis of (RADA)₄ peptide-based hydrogels. *Acta Biomater.* 2016;31:71-9.
20. Koss KM, Churchward MA, Nguyen AT, Yager JY, Todd KG, Unsworth LD. Brain Biocompatibility and microglia response towards engineering self-assembling (RADA)₄ nanoscaffolds. *Acta Biomater.* 2016
21. Zhang S, Holmes TC, DiPersio CM, Hynes RO, Su X, Rich A. Self-complementary oligopeptide matrices support mammalian cell attachment. *Biomaterials.* 1995 March 23;16:1385-93.
22. Worthington P, Pochan DJ, Langhans SA. Peptide Hydrogels - Versatile Matrices for 3D Cell Culture in Cancer Medicine. *Front Oncol.* 2015;5:92.
23. Cheng T, Chen M, Chang W, Huang M, Wang T. Neural stem cells encapsulated in a functionalized self-assembling peptide hydrogel for brain tissue engineering. *Biomaterials.* 2013;34:2005-16.
24. Koutsopoulos S, Zhang S. Long-term three-dimensional neural tissue cultures in functionalized self-assembling peptide hydrogels, matrigel and collagen I. *Acta Biomater.* 2012(<http://dx.doi.org/10.1016/j.actbio.2012.09.010>).
25. Schneider A, Garlick JA, Egles C. Self-assembling peptide nanofiber scaffolds accelerate wound healing. *PloS one.* 2008;3(1):e1410.

26. Chau Y, Luo Y, Cheung ACY, Nagai Y, Zhang S, Kobler James B, et al. Incorporation of a matrix metalloproteinase-sensitive substrate into self-assembling peptides - A model for biofunctional scaffolds. *Biomaterials*. 2008;29:1713-9.
27. Fonseca KB, Granja PL, Barrias CC. Engineering proteolytically-degradable artificial extracellular matrices. *Prog Polym Sci*. 2014;39:2010-29.
28. Fatin-Rouge N, Starchev K, Buffle J. Size effects on diffusion processes within agarose gels. *Biophysical Journal*. 2004;86(5):2710-9.
29. Bancaud A, Beaudouin J, Ellenberg J, Huet S, Daigle N, Mozziconacci J. Molecular crowding affects diffusion and binding of nuclear proteins in heterochromatin and reveals the fractal organization of chromatin. *EMBO J*. 2009;28(24):3785-3798. <http://onlinelibrary.wiley.com/doi/10.1038/emboj.2009.340/abstract>. doi: 10.1038/emboj.2009.340.
30. Hochman-Mendez C, Cantini M, Moratal D, Salmeron-Sanchez M, Coelho-Sampaio T. A fractal nature for polymerized laminin. *PloS one*. 2014;9(10):e109388.
31. Santoso S, Hwang W, Hartman H, Zhang S. Self-assembly of surfactant-like peptides with variable glycine tails to form nanotubes and nanovesicles. *Nano Lett*. 2002;2(7):687-91.
32. Vauthey S, Santoso S, Gong H, Watson N, Zhang S. Molecular self-assembly of surfactant-like peptides to form nanotubes and nanovesicles. *Proc Natl Acad Sci U S A*. 2002 April 16;99(8):5355-60.
33. von Maltzahn G, Vauthey S, Santoso S, Zhang S. Positively charged surfactant-like peptides self-assemble into nanostructures. *Langmuir*. 2003;19:4332-7.

34. Wang W, Chau Y. Self-assembled peptide nanorods as building blocks of fractal patterns. *Soft Matter*. 2009;5:4893-8.
35. Lomander A, Hwang W, Zhang S. Hierarchical self-assembly of a coiled-coil peptide into fractal structure. *Nano Lett*. 2005;5.
36. Law B, Tung C. Proteolysis: a biological process adapted in drug delivery, therapy, and imaging. *Bioconjugate Chem*. 2009;20(9):1683-95.
37. Turk BE, Huang LL, Piro ET, Cantley LC. Determination of protease cleavage site motifs using mixture-based oriented peptide libraries. *Nat Biotechnol*. 2001 July;19(7):661-7.
38. Nagase H, Fields GB. Human matrix metalloproteinase specificity studies using collagen sequence-based synthetic peptides. *Biopolymers*. 1996;40:399-416.
39. Netzel-Arnett S, Sang QX, Moore WG, Navre M, Birkedal-Hansen H, Van Wart HE. Comparative sequence specificities of human 72- and 92-kDa gelatinases (type IV collagenases) and PUMP (matrilysin). *Biochemistry*. 1993 June 29;32(25):6427-32.
40. Lévesque SG, Shoichet MS. Synthesis of enzyme-degradable, peptide-cross-linked dextran hydrogels. *Bioconjug Chem*. 2007;18(3):874-85.
41. Anderson NL, Razavi M, Pearson TW, Kruppa Gary, Paape R, Suckau D. Precision of heavy-light peptide ratios measured by MALDI-TOF mass spectrometry. *J Proteome Res*. 2012;11:1878.
42. MacPhee CE, Woolfson DN. Engineered and designed peptide-based fibrous biomaterials. *Curr Opin Solid State Mater Sci*. 2004;8(2):141-9.

43. Barbucci R. Hydrogels. Milan, Italy: Springer-Verlag; 2009.
44. Korsmeyer RW. Diffusion controlled systems: hydrogels. In: Tarcha PJ, editor. Polymers for controlled drug delivery. CRC Press Inc.; 1991.
45. Baker AE, Bergin FG, Leaper DJ. Matrix metalloproteinases, their tissue inhibitors and colorectal cancer staging. *Br J Surg.* 2000;87(9):1215-21.
46. Tutton MG, George ML, Eccles SA, Burton S, Swift RI, Abulafi AM. Use of plasma MMP-2 and MMP-9 levels as a surrogate for tumor expression in colorectal cancer patients. *Int J Cancer.* 2003 June;107:541-50.
47. Applied Biosystems. ABI 433A peptide synthesizer user guide. 2004;1.
48. Dawes JC, Biological techniques for transmission and scanning electron microscopy. Ladd Research Industries, Inc. 1984.
49. Groblewska M, Mroczko B, Gryko M, Poczynicz A, Guzińska-Ustymowicz K, Kędra B, et al. Serum levels and tissue expression of matrix metalloproteinase 2 (MMP-2) and tissue inhibitor of metalloproteinases 2 (TIMP-2) in colorectal cancer patients. *Tumor Biol.* 2014 January;35:3793-802.
50. French P. Hausdorff dimension by the box counting method. 2007. <<http://www.mathworks.com/MATLABcentral/fileexchange/15918-hausdorff-dimension-by-the-box-counting-method>>
51. Costa A. Hausdorff (box-counting) fractal dimension, 2011. <<http://www.mathworks.com/MATLABcentral/fileexchange/30329-hausdorff--box-counting--fractal-dimension>>

52. Hausdorff F. Dimension und äußeres Maß. *Mathematische Annalen*. 1919;79:157-9.
53. Lopes R, Betrouni N. Fractal and multifractal analysis: A review. *Med Image Anal*. 2009;13:634-49.
54. Theiler J. Estimating fractal dimension. *J Opt Soc Am A*. 1990;7(6):1055-73.
55. Schneider A, Garlick JA, Egles C. Self-assembling peptide nanofiber scaffolds accelerate wound healing. *PloS one*. 2008;3(1):e1410.
56. Miyagi M, Rao KCS. Proteolytic 18O-Labeling Strategies for Quantitative Proteomics. *Mass Spectrom Rev*. 2007;26:121-36.
57. Hule R, Nagarkar R, Hammouda B, Schneider J, Pochan D. Dependence of self-assembled peptide hydrogel network structure on local fibril nanostructure. *Macromolecules*. 2009;42(18):7137-45.
58. Jelinek HF, Elston N, Zietsch B. Fractal analysis: pitfalls and revelations in neuroscience. In: Alt W, editor. *Fractals in biology and medicine mathematics and biosciences in interaction*. ; 2005. p. 85-94.
59. Kabiri M, Bushnak I, McDermot MT, Unsworth LD. Toward a mechanistic understanding of ionic self-complementary peptide self-assembly: role of water molecules and ions. *Biomacromolecules*. 2013;14:3943-50.
60. Jha RK, Chakraborti S, Kern TL, Fox DT, Strauss CEM. Rosetta comparative modeling for library design: Engineering alternative inducer specificity in a transcription factor. *Proteins*. 2015;83:1327-40.

61. Monera OD, Sereda TJ, Zhou NE, Kay CM, Hodges RS. Relationship of sidechain hydrophobicity and alpha-helical propensity on the stability of the single-stranded amphipathic alpha-helix. *J Pept Sci.* 1995;1(5):319-29.
62. Creasey RG, Voelcker NH, Schultz CJ. Investigation of self-assembling proline- and glycine-rich recombinant proteins and peptides inspired by proteins from a symbiotic fungus using atomic force microscopy and circular dichroism spectroscopy. *Biochim Biophys Acta.* 2012;1824:711-22.
63. Fernández-Carneado J, Kogan MJ, Castel S, Giralt E. Potential peptide carriers: amphipathic proline-rich peptides derived from the N-terminal domain of γ -zein. *Angw Chem Int Ed.* 2004;43:1811-4.
64. del Pozo-Rodríguez A, Pujals S, Delgado D, Solinís MA, Gascón AR, Giralt E, et al. A proline-rich peptide improves cell transfection of solid lipid nanoparticle-based non-viral vectors. *J Control Release.* 2008;133(2009):52-9.
65. Kogan M, Dalcol I, Gorostiza P, Lopez-Iglesias C, Pons R, Pons M, et al. Supramolecular properties of the proline-rich γ -zein N-terminal domain. *Biophys J.* 2002;83:1194-204.
66. Nagase H, Woessner JF. Matrix metalloproteinases. *J Biol Chem.* 1999 July 30;274(31):21491-4.
67. Kim SI, Na H, Ding Y, Wang Z, Lee SJ, Choi ME. Autophagy promotes intracellular degradation of type I collagen induced by transforming growth factor (TGF)- β 1*. *J Biol Chem.* 2012;287(15):11677-88.

68. Hansen U, Bruckner P. Macromolecular specificity of collagen fibrillogenesis: fibrils of collagens I and XI contain a heterotypic alloyed core and a collagen I sheath. *J Biol Chem.* 2003 September 26;278(39):37352-9.

Chapter 4.

Induced Neuronal Differentiation of MMP-2 Cleaved (RADA)₄ Drug Delivery Systems

Koss, K^{1,2}; Tsui, C^{1,2}; Unsworth, LD^{1,2}

1. Department of Chemical and Materials Engineering, University of Alberta, 11487 89 ave, Edmonton, AB, T6G

2M7

2. National Institute for Nanotechnology, NRC, 11421 Saskatchewan Dr NW, Edmonton, AB, T6G 2M9

Abstract

(RADA)₄ self-assembling peptides (SAPs) are promising for neural nanoscaffolds with on-demand drug delivery capabilities due to their automated synthesis, *in-situ* assembly, and potential for interaction with and release of biomolecules. Neuroinflammation cued on-demand drug release, due to up-regulated proteases, may well be vital in the treatment of several neurological diseases. In these conditions, releasing neurotrophic growth factors (NTFs) could potentially lead to neuroprotection and neurogenesis. As such, (RADA)₄ was made with the high and low activity matrix metalloproteinase 2 (MMP-2) cleaved sequences, GPQG+IASQ (CP1) and GPQG+PAGQ (CP2), the brain-derived NTF secretion stimulating peptide MVG (DP1) and the ciliary NTF analogue DGGL (DP2). PC-12 cell culture was performed to assess bioactive substrate cell adhesion and NTF specific neuronal differentiation. The laminin-derived IKVAV peptide, known for neural cell attachment and interaction, was tethered to (RADA)₄-IKVAV and mixed in increasing increments with (RADA)₄ for this purpose. Using nanoscale morphology, metabolism, and viable cell count, 10%(v/v) IKVAV content was deemed optimal for cell-nanoscaffold interactions. With 1 nanomolar MMP-2 treatment, product formation was observed to increase over a three day period, with (RADA)₄ / (RADA)₄-CP1/CP2 mixture, however there was little difference between groups. Smaller CP1/CP2 concentrations displayed comparable (RADA)₄ nanoscale morphology to higher concentrations. Acetylcholine esterase and neural differentiation was observed over 3 days with 1 nM MMP-2 treatment according to the following makeup: 8/1/1 (RADA)₄/(RADA)₄-IKVAV/(RADA)₄-CP1/CP2-DP1/DP2. Signalling gradually increased in all groups, and neurite outgrowth was visible after three days.

Keywords: Self-assembling peptides, Drug Delivery, (RADA)₄, MMP-2, Nanoscaffold, PC-12, Neural Differentiation

1. Introduction

Neurotrophic factors (NTFs) make ideal drug candidates in several neuro-inflammatory and neurodegenerative conditions, capable of targeting specific neuro anti-inflammatory, protective, rescue, and regenerative functions [1 - 4]. Nonetheless, they almost always suffer from poor pharmacokinetics and are rapidly digested before action, or ultimately fail to breach the blood brain barrier. Site-specific injections have yielded limited results, and continual doses are short lived and require invasive techniques, such as osmotic pumps [5 - 6]. Supplying a dynamic dose of substances, tuned to surrounding tissues is a challenging but may show true merit as a solution. Many have opted to use drug delivery vehicles that are capable of housing a variety of release triggers cued to physiology, such as proteolysis, pH, and temperature [7]. These systems have been limited to protease related pro-form activation and nanofiber matrices acting together as nanoscaffolds [8 - 10]. Nanoscaffolds are promising drug delivery vehicles composed of cross-linked polymers, can be fabricated with a wide spectra of morphological and mechanical features, and when swollen with water, are capable of diffuse release of attached molecules. Furthermore, they emulate a natural extracellular matrix (ECM) and can be engineered in one system, to recruit, differentiate, proliferate, and release cells [11].

However, designing a nanoscaffold system with precisely tuned NTF release can be intricate and impractical when using polymer systems requiring complex synthesis, *in-situ* assembly with toxic co-solvents, external triggers, or transplantation. As such, cell response to precisely timed drug release studies cannot be performed systematically with high-throughput analysis on such materials [12 - 13]. A drug delivery nanoscaffold should be simply made, ultimately biocompatible and bioactive, have reproducible morphology and NTF loading, and on-demand

release due to neurological cues. Considering these concepts, spatiotemporal proteolytic triggered product formation was related to neurogenic signalling and neuritogenesis of a NTF sensitive cell line. This was assessed in a self-assembling peptide (SAP), made with automated peptide synthesis, capable of forming a (3-D) nanoscaffold upon injection into physiological conditions.

SAPs form spontaneous nanoscaffolds, according to specific physiological salts, through intermolecular interactions, including van der Waals, electrostatic, and hydrogen bonds [14]. Of these peptides, (arginine-alanine-aspartic acid-alanine)₄ (RADA16 or (RADA)₄) has a rich history [15 - 17]. This SAP has been used in many cell culture and tissue engineering studies, as it structurally emulates natural ECMs [18 - 21]. Specific to neural tissues, it has been applied to mouse, rat, and human neural stem cells, full rat hippocampal neural tissues, and has been used in brain transplantation of seeded stem cells [22 - 24]. Diffuse drug and protein release profiles have also been characterized from fully formed (RADA)₄ networks [25]. Proteolysis triggered re-assembly of (RADA)₄ nanofibers has been demonstrated, but this concept has not been applied as a drug delivery mechanism [26]. Time-paced full enzyme kinetics directly relating to controlled drug release, would greatly enhance this system's capacity as a dynamic neural nanoscaffold.

Enzyme triggered drug release systems have been studied in several forms, including nanoparticles, nanoscaffolds, and hydrogels [27]. Countless drug therapeutics target neuroinflammation in several diseases, in which several types of proteases are secreted. One protease family, the matrix metalloproteinases (MMP), are tuned to several ECM-derived peptide sequences and are fitting trigger candidates for on-demand release [28]. MMP-2 has several consensus substrates with a variable selection of activity, and is secreted by active glia

during inflammation [29]. Two potential cleavage peptides (CPs) for modulating release are glycine-proline-glutamine-glycine+isoleucine-alanine-serine-glutamine (GPQG+IASQ, CP1), having high MMP-2 activity, and glycine-proline-glutamine-glycine+proline-alanine-glycine-glutamine (GPQG+PAGQ, CP2), having low MMP-2 activity [30 - 31]. The '+' is the scissile bond [32]. Incorporating these peptides into (RADA)₄ hydrogels is simple and reproducible as these molecules can be made during initial peptide synthesis with predictable purity.

Full NTF proteins are delicate, relying on 3-D structure to function, and are 10-20 times larger than SAP molecule. This can seriously complicate and hinder a balance of NTF function and self-assembly mechanics of (RADA)₄ nanoscaffold. Using peptide analogues or drug peptides (DPs) could potentially solve these issues, being small enough to allow characteristic self-assembly and simply integrated with (RADA)₄ and CPs, being made during automated peptide synthesis. Two peptide NTF analogues show merit. The first, brain derived neurotrophic factor (BDNF) associated to the sequence, MVG (DP1), and known as Neuro-pep-1, was discovered in positional scanning synthetic peptide combinatorial library [33]. This peptide stimulated BDNF and TrkB expression in H19-7 cells and rat hippocampal tissues, and was shown to improve spatial learning and memory in adult rats. The second analogue, ciliary neurotrophic factor (CNTF) associated to the sequence DGGL (DP2), modified for blood brain barrier intrusion, has promoted dentate gyrus neurogenesis and synaptic plasticity in the rat brain [34 - 35]. Being small and effective, the application of the analogues in a drug delivery systems could be potent, yet remains unexplored.

To assay this drug delivery system in a simple neural scheme, fully formed SAPs, incorporated with MMP-2 CPs and the peptide drugs, were seeded into culture with NTF sensitive cells. PC-12 cells were chosen due to their specific adherence to bioactive substrates,

such as collagen IV, and obvious subsequent neural differentiation with NTF treatment [36 - 37]. Cell adhesion was enhanced by tethering the laminin derived peptide isoleucine-lysine-valine regeneration after spinal cord injury, and used in rat brain transplants [24, 26, 38 - 40]. All treatments were exposed to protease, and neural signalling and neurite outgrowth was evaluated. Control treatments included media only, scrambled peptide sequences, and MMP-2 alone used to assess attachment/differentiation of cells. (RADA)₄ was incrementally mixed with (RADA)₄-IKVAV to find an optimal content. Transmission electron microscopy (TEM) was used to assess differences in nanoscale morphology of these mixtures, and cells were visualized using phase contrast microscopy (PCM), assayed for metabolic activity using MTT, and counted using a live/dead assay with confocal microscopy. Product formation was observed, over 3 days, mixing (RADA)₄-CP1/CP2 with (RADA)₄ to determine the ideal CP quantity. This was measured using MALDI TOF/TOF ms by mixing the product solution with an equimolar standard peptide isotope ((RADA)₄-GG-GPQGd₈). These results were coupled with TEM to assess differences in morphology that may influence MMP-2 kinetics. The optimal CP and IKVAV mixtures, with DP groups, were then treated with MMP-2, and neural signalling, using an acetylcholine esterase assay, and cell differentiation was measured. This was done over 3 days to match product formation.

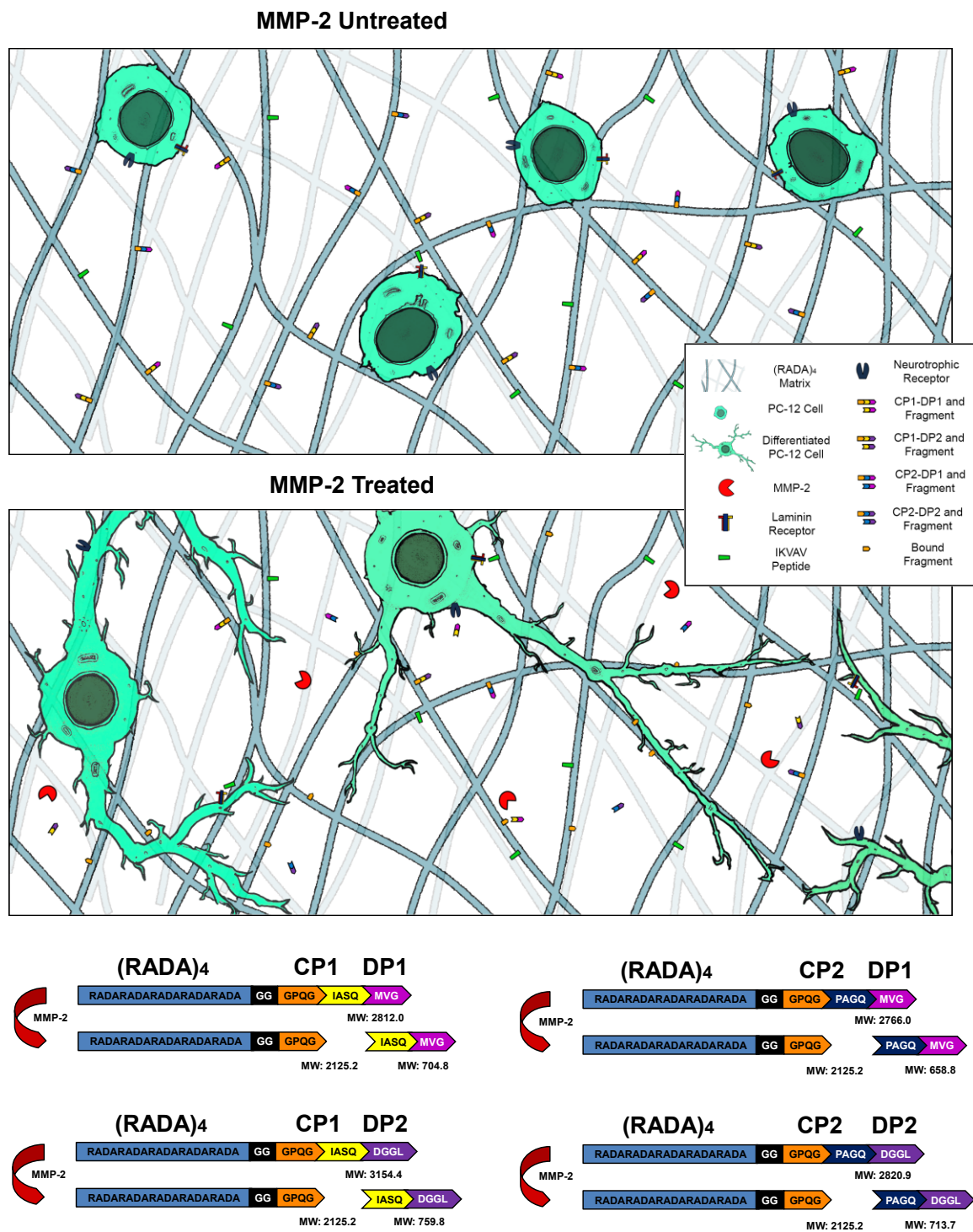


Figure 4.1. PC-12 cells, seeded into a (RADA)₄ nanoscaffold, responding to bound and cleaved neurotrophic peptides without and with MMP-2 treatment, respectively. Cells are spherical when untreated and differentiate with outgrown neurites when treated with enzyme. Cells are adhering to IKVAV motifs. Full sequences for cleavage peptides (CP1 and CP2) and drug peptides (DP1 and DP2) are shown with (RADA)₄.

2. Materials and Methods

2.1. Materials

Acetonitrile (ACN) (99.8%), diethyl ether, dichloromethane (99.8%), methanol (99.8%), N-dimethylformamide (99.8%), N-diisopropylethylamine (99.5% biotech. grade), piperidine (99.5% biotech. grade), trifluoroacetic acid (TFA) (99%), 1,2-ethanediol (EDT) (97%), triisopropylsilane (TIPS) (99%), formalin (10%), glutaraldehyde (25%), dimethyl sulfide (99%), α -cyano-4-hydroxycinnamic acid (HCCA), trypan blue (0.4%), and Fmoc-Ala-OH-2,3,3,3-d₄, were acquired from Sigma (Oakville, ON). All other Wang resins and Fmoc amino acids and were purchased from ChemPep (Wellington, FL). Ethyl (hydroxyimino)cyanoacetate (OXYMA) (98%) and 1-cyano-2-ethoxy-2-oxoethylidenaminoxy)dimethylamino-morpholino-carbenium hexafluorophosphate (COMU) (98%) were from Oakwood Products, Inc (West Columbia, SC). Active human recombinant MMP-2 was acquired from EMD Millipore (Etobicoke, ON). TEM grids and uranyl acetate were from Ted Pella, Inc (Redding, CA). Other materials used in subsequent substrate preparation and enzyme kinetics included NaCl and CaCl₂·2H₂O from EMD Chemicals Inc. (Darmstadt, Germany), and Tris-HCl from Fisher Scientific (Fair Lawn, NJ). Syto13 green, and SytoxOrange were also purchased from Fisher Scientific, Advanced RPMI, horse serum (HS), fetal bovine serum (FBS), l-glutamine, and penicillin/streptomycin were from Gibco (Life Technologies, Burlington, ON). All other reagents were of the highest quality available. Milli-Q grade water used in these experiments.

2.2. Peptide Synthesis

The peptide were synthesized using an ABI 433A Peptide Synthesizer. They are listed as (RADA)₄, (RADA)₄-IKVAV, (RADA)₄-GG-GPQG+IASQ, (RADA)₄-GG-GPQG+PAGQ, (RADA)₄-GG-GPQG+IASQ-DGGL, (RADA)₄-GG-GPQG+IASQ-MVG, (RADA)₄-GG-

GPQG+PAGQ-DGGL, (RADA)₄-GG-GPQG+PAGQ-MVG, and (RADA)₄-GG-GPQGD₈. Fmoc chemistry was used. Coupling concentrations of 500 mM concentrations of COMU and OXYMA were chosen. Fastmoc coupling protocols were doubled with 15 minute extended reaction cycles per coupling. All other methods were unchanged and followed the ABI 433A guidelines. [41] Cleavage cocktails were (96/2/2) TFA, H₂O, and triisopropylsilane except with methionine containing sequences, which the cocktail mixture was otherwise (84/2/2/2/10) TFA, H₂O, and triisopropylsilane, ethandithiol, and dimethyl sulphide. To assure sample mass, an ABI 4800 matrix-assisted laser desorption/ionization time of flight (MALDI-TOF/TOF) mass-spectrometry was used. Matrix concentrations of 10 mg/ml HCCA were suspended in 1:1 H₂O:ACN (0.1% TFA). Minimum 95% purification was achieved by high performance liquid chromatography (HPLC). A Zorbax Eclipse C18 reverse-phase semi-preparative 9.4 x 250 mm column (Agilent Technologies) was used with a H₂O-ACN (0.1% TFA) loading. Purity was also observed by HPLC. Chromatographs and MALDI mass spectra and are displayed in the supplemental information (Figure A4.1).

2.3. Transmission Electron Microscopy

All protocols were followed from Dawes *et al.* [42]. (RADA)₄ samples were pipetted onto perforated formvar carbon coated copper grids. A 4% uranyl acetate stain was applied. In between steps, sample and stain were filter-dried. All samples were collected 24 hours upon 30 minutes sonication. All TEM was performed on a Philips FEI Morgagni electron microscope.

2.4. In vitro study

2.4.1. PC-12 and Two-Dimensional Cell Culture with SAP

PC-12 cells (CRL-1721TM) were purchased from ATCC (Manassas, VA) and thawed according to supplier protocol. Cells were cultured in Advanced RPMI (10% v HS, 5% v FBS, 0.5% v l-glutamine, 10 mg/ml penicillin, and 10 I.U. streptomycin), suspended in standard 200 mL flasks, at 37°C and 5% CO₂. Cells were passaged 4 times before discarding. Viability was routinely assessed by centrifuging cells 200 x g for 5 minutes, flushing pellets with fresh media through a 20 ml syringe with a 22g needle, staining with 1:1 trypan blue (0.4%), mounting the mixed solution onto a BIO-RAD TC10 dual chamber counting slide, and inserting the slide into a BIO-RAD TC10 Automated Cell Counter. A viability of 80% live counted cells was acceptable for seeding.

1 % (w/v) (RADA)₄ mixtures in H₂O were sonicated for 60 minutes and 20 µL was pipetted into each well of a 24-well plate. Carefully, 80 µl of modified TNC buffer was added and incubated for 24 hours at 4° C. Buffer was aspirated and wells were washed with 200µL of advanced RPMI three times before addition of cells. Cells were seeded onto SAP scaffolds 200 µl volumes at 5×10⁴ cells / ml. Seeding was repeated two more times, with a 1 hour period between and set to rest overnight before an experiment.

2.4.2. Live/Dead Viability

Cell viability was performed using a live/dead cell assay. In brief, cells were treated 5 μ M Syto13 green for 60 min, then 30 min with SytoxOrange for 30 min. Syto13 stains all cell nuclei due to cell permeability and SytoxOrange stains cell nuclei with compromised membranes, or dying cells. For quantification and cell counts, images were systematically acquired using epifluorescence microscopy (Leica DMI6000-B microscope) on a 4×4 grid resulting in 16 images per condition, to eliminate acquisition bias. A sample size of $n = 3$ was used. Images were quantified by automated analysis using custom written macros in Image J.

2.4.3. Molecular Analyses

Viability was assessed for by 30 min incubation with 0.5 mg/ml 3-(4,5-dimethylthiazol-2-yl)-2,5-diphenyltetrazolium bromide (MTT, Fisher Scientific). Measurement of the oxidized formazan end-product was performed at 540 nm. To account for variance in cell number between conditions where cell count was not the goal, all acetylcholine esterase measurements were normalized to the MTT absorbance level of the cell lysate

Acetylcholine esterase was measured with an Amplex® acetylcholine/acetlycholinesterase assay kit (Life Technologies). Experimental procedures were adapted from the manufacturer's protocol. A 20 mM AR stock solution was prepared in DMSO and stored in a -20°C environment and protected from light until ready to be used. Reaction buffer was prepared in stock at 5X concentration (250 mM TrisHCl, pH 8.0), followed by a dilution down to 1X when needed. A 200 U/ml HRP stock solution was prepared by dissolving the contents of the kit's HRP vial into 1.0 ml of 1X reaction buffer, followed by division into small aliquots and storage at -20°C . A 20 mM H_2O_2 working solution was also prepared via dilution of the $\sim 3\%$ H_2O_2 provided in the kit. A 20 U/mL choline oxidase stock solution was prepared by dissolving the

contents of the kit's choline oxidase vial into 600 μL of 1X reaction buffer, followed by division into small aliquots and storage at -20°C . A 100 mM acetylcholine chloride solution was prepared in H_2O . Finally, a 100 U/mL acetylcholinesterase stock solution was prepared by dissolving the contents of the kit's acetylcholinesterase vial into 600 μL of 1X reaction buffer, followed by division into small aliquots and storage at -20°C .

A 400 μM AR/HRP/choline oxidase/acetylcholine solution containing 200 μL AR stock solution, 100 μL HRP stock solution, 100 μL choline oxidase stock solution, 10 μL acetylcholine stock solution. Samples containing acetylcholinesterase were diluted in 1X reaction buffer, for a reaction volume of 100 μL . Acetylcholinesterase positive controls were prepared by serial diluting the acetylcholinesterase stock solution with 1X reaction buffer, for a standard curve. The 1X reaction buffer was used as the negative control. Both positive and negative control sample volumes were kept at 100 μL . Samples were collected from cell secretions, gently rocked for 5 minutes, and diluted 1:10 in reaction buffer. All diluted samples and controls were pipetted in 100 μL quantities into separate microplate wells. The reactions were then started by adding 100 μL of the 400 μM AR/HRP/choline oxidase/acetylcholine solution to each microplate well. Reactions were incubated for over 30 minutes at room temperature while being protected from light. Fluorescence readings were taken at various time points in the reaction using an excitation range of 530-560 nm and an emission detection at 590 nm. Corrections were made at each point for background fluorescence interference by subtracting the negative control sample values.

2.4.4. Immunocytochemistry

At the end of treatment, cells were washed 3x with PBS (7.4) supplemented and fixed in 5% PBS-buffered formalin, with 1 % glutaraldehyde (pH 7.4) for 1 hour. Each of the following sequential steps was preceded by washing 3x with PBS: fixed cells were blocked and

permeabilized (PBS pH 7.4 supplemented with 1% HS and 0.1% Triton X-100 for 10 min). This was proceeded by incubation with primary polyclonal anti-beta III tubulin, Alexa Fluor[®] 488 (1:500, Millipore EMD) and monoclonal mouse anti-growth associated protein-43 (GAP43) (1 µg/ml, Syd Labs, Inc.) antibodies (PBS pH 7.4 with 0.1% HS, overnight at 4° C), secondary incubation with Alexafluor[®] 647 conjugated donkey-anti-mouse (1:100, Life Technologies) antibody (PBS with 0.1% HS, 2 h at room temperature), 15 min staining with Hoechst 33342 (1 µg/ml, Life Technologies), and mounting using Fluoromount-G (Southern Biotech). Confocal microscopy was performed on a Leica TCS-SPE inverted microscope. Post-processing was performed using ImageJ.

2.4.5. Statistical Analyses

Overall significance was assessed using one-way ANOVA, with Tukey's post-hoc analysis, and multi-way ANOVA analysis of variance with Bonferroni's multiple comparison post-hoc analysis between groups. Pairwise comparisons were assessed using a Mann-Whitney U test. A **p* value of ≤ 0.05 was considered significant. Data are presented as the mean \pm standard deviation (SD).

2.5. MMP-2 Enzymatic Treatment

MMP-2 (RADA)₄ product measurement was adapted from Chau *et al.* [26] Each peptide was diluted to 1.0% w/v in a modified TNC buffer (50 mM TrisHCl, 150 mM NaCl, 1 mM CaCl₂, pH 7.4) and underwent 30 minutes of sonication. Peptides with additional sequences were normalized to (RADA)₄, specifically adjusted to 1% w/v of (RADA)₄. Groups were centrifuged to force the gel into a pellet. Half of the supernatant removed and refreshed TNC buffer at least 10 times until the pH of the supernatant was 7.4. Following this, a 5:3 ACN:H₂O solution was

added for a final 1:1 ACN:H₂O ratio. This was done to dissolve nanofibers for stock solutions and reduce error in multiple samples of small volume.

In order to prepare 10 μ l hydrogel samples (peptide sequences listed), the cleavage sequence mixtures were sonicated for 60 minutes, aliquoted into Axygen 0.2 mL Polypropylene PCR tubes and dried under vacuum. Each PCR tube was next filled with 7.5 μ l water and left to sonicate for 60 minutes. In order to keep the samples from vaporizing during sonication, the PCR tubes were very briefly spun down in a Corning LSETM Mini Microcentrifuge at 2000 x g. The samples were left to self-assemble into hydrogels for 24 hours, and 2.5 μ l of active MMP-2 was then carefully pipetted onto the sample surface under cold-room conditions four times greater than the desired concentration to reach the working concentration. All samples were incubated at 37°C and for each sample group, $n = 3$ replicates were used for reproducibility and data analyzed represents mean \pm SD. Following incubation each sample was quenched to halt the reaction with a mixture comprising of 75 μ l ACN, 65 μ l H₂O and 0.1% TFA, for a final sample volume of 150 μ l. Then, 5 μ l of this mixture was taken and added to a new mixture comprising of 100 μ l H₂O, 0.1% TFA, and 5 μ l of the deuterated standard sequence at 0.3 mg/ml. This mixture was then spotted directly onto a MALDI plate for analysis with the aforementioned HCCA matrix protocol. Product was quantified by comparing the area under the curve, using the trapezoidal rule, of the product (2122 - 2130 m/z) and standard (2132 - 2140 m/z) envelopes and back calculating by the molar quantity of standard. All CP1 and CP2 samples were normalized to (RADA)₄ % w/v concentrations to match self-assembly, meaning that their overall concentrations in excess by the molar weight ratio (RADA)₄-CP:(RADA)₄. In MATLAB (The MathWorks®), data was smoothed and filtered with smooth filter functions. A baseline was determined from a curvefit for each dataset without the product/standard peak. Data was curve-fitted and areas were

calculated with spline and trapz functions, respectively. Sample code is available in the appendices.

Initially, 0.5 % w/v samples were treated with 0 and 5 nM for 3 days, which is a considerably high dose to assure full digestion of the nanoscaffold. This sample was mixed with standard, diluted 1:1000 in 1:1 ACN/H₂O, 0.1% TFA and spotted for MALDI, directly without standard. Following this, a kinetics study was also conducted over this 3-day span, with daily sampling. Cleavage sequences were 0.50% w/v and 1 nM MMP-2 was used due to their common conditions in literature [43 - 44]. For each cleavage sequence, (RADA)₄ was doped at 25% to 100%, with 25% increments in between. The standard was added to these groups upon quenching.

3. Results and Discussion

3.1. Nanoscale Morphology and Cell Adhesion

These PC-12 cells do not typically seed (adhere) during cell culture without some form of bioactive scaffolding such as collagen. Thus, the (RADA)₄-IKVAV peptide was introduced to pure (RADA)₄ in percent volumetric increments. Nanoscale morphology was visualized using TEM to determine the effect of IKVAV on self-assembly (Fig. 2 A). Cell adhesion was matched *via* PCM to these groups to determine an optimum IKVAV content for subsequent studies (Fig 2 B). Cell metabolism was assayed by MTT signal, overall cell count/mm² were determined using a nuclear stain, and percent viability was assessed with a cell-lysed nuclear counter-stain (Fig. 3 C, D, and E).

Nanofiber morphology was compared to cell adhered morphology in (RADA)₄-IKVAV mixtures of 0, 10, 50, 75, 90, and 100%(v/v) (RADA)₄ (Figure 2). Nanofibers with 5-10 nm

thickness were observed in all nanoscaffold constructs. These fibers appear dispersed and individual in 0 and 10%, formed a meshed network in 25%, and were thickly aggregated at 50 and 100% (RADA)₄-IKVAV. The IKVAV peptide introduces charged lysine and hydrophobic residues isoleucine, valine, and alanine which comprise most of this sequence and are likely responsible for the aggregation noted for 50 and 100% (RADA)₄ systems [45]. As shown from work in this lab previously, hydrophobic interactions dominate the self-assembly of (RADA)₄ [46].

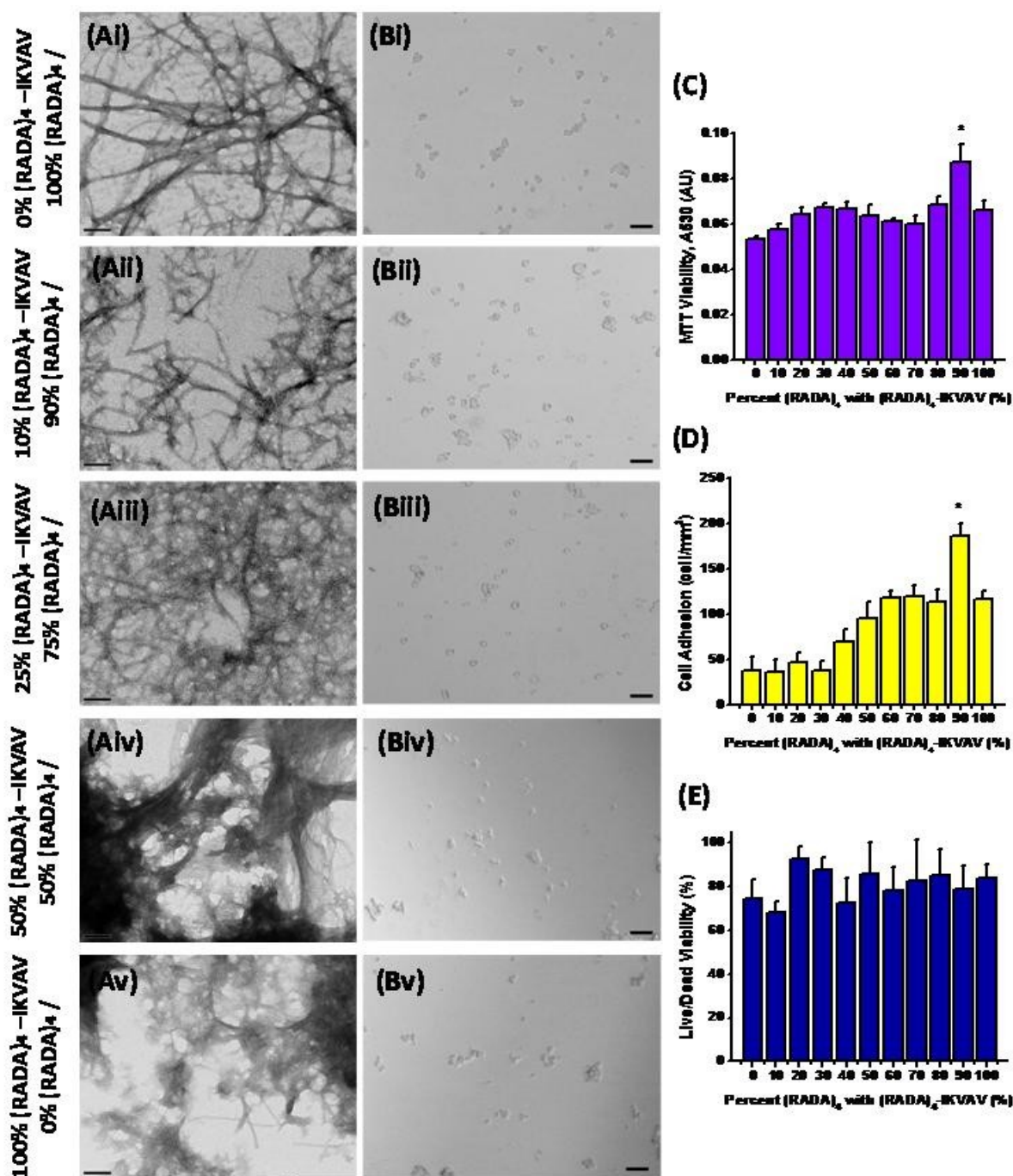


Figure 4.2. 1% w/v (A) transmission electron microscopy (TEM) (A), and phase contrast microscopy (B) of PC-12 cells seeded into 0% / 100% (i), 10% / 90% (ii), 25% / 70% (iii), 50% / 50% (iv), and 100% / 0% (v) mixtures of (RADA)₄-IKVAV / (RADA)₄. All TEM samples were stained with 4% uranyl acetate and imaged at 1% w/v in TNC buffer upon 30 minutes of sonication and 24 hours of incubation at 37°C. Cells were imaged after 3 days, while media was refreshed daily. Scale bars are 100 nm (A) and 50 μm (B). Measured MTT (C), cell counts (D), and percent live cells (E) for 10% increments of (RADA)₄ mixed with (RADA)₄-IKVAV. *n* = 3 replicates for all groups (* *p* < 0.05) in a multi-way ANOVA. Data analyzed represents mean ± SD.

All cells were spherical (~10 μm diameter) and undifferentiated after three days of seeding for all conditions. This may be expected as (RADA)₄-IKVAV was recently shown to prime these cells for neurite outgrowth, not incite changes in morphology [26]. That said, greater number of cells was observed for both 90 and 100%(v/v) (RADA)₄ groups, with 90%(v/v) systems showing the highest cell count. An MTT assay was performed on 10%(v/v) (RADA)₄ increments to substantiate this observation and it was found the 10%(v/v) (RADA)₄-IKVAV system had significantly higher metabolism than all other groups (Figure 2C). These results have low absorbance values by the assay standard, and any significance in other group variation may be lost due to a low plateau of sensitivity. Furthermore, this result only represents metabolism, and not necessarily cell quantity. Full cell counts corroborated the greater significance in the 10%(v/v) (RADA)₄-IKVAV group and counts have a trend-wise increase with decreasing IKVAV content, being lowest and comparable between 0% to 30% (RADA)₄ (Figure 2D). Although cells were present, their MTT levels were low, and viability may suffer during the seeding process. IKVAV, a five amino acid (2091 - 2108) sequence in a 900 kDa mosaic glycoprotein, is not naturally present in highly concentrated pockets in any ECM physiology [47]. In addition, the nanofiber clustering observed with increased amounts of IKVAV, may reduce cell adhesion due to the IKVAV sequence being inaccessible to the cells due to being buried within the aggregates, as well as reduced IKVAV flexibility for cell interactions to occur. The 10% (RADA)₄-IKVAV ratio promotes the benefit of the IKVAV ligand, without oversaturating cell receptors, and maintains the nanoscale morphology successfully used in original neural tissue engineering applications, which were characterized by 10 nm thick nanofibers in sparse networks [21]. Finally, the live/dead assay demonstrated that the cell viability (%) did not decrease compared to the pre-seeding viability measurement using Trypan blue exclusion.

Therefore, the 10% (RADA)₄-IKVAV system was chosen for drug release-related studies to enhance cell adhesion and drug release-related neuriteogenesis.

3.2. Enzymatic Product Formation

Controlled proteolysis was introduced by incorporating (RADA)₄-CP1 and (RADA)₄-CP2, (known for their high and low activity, respectively) into the self-assembling system, and treating them with MMP-2 (Fig. 3 and 4). Specifically 1 and 5 nM MMP-2 concentrations were applied to the CP's. Product formation was assessed and observed with MALDI TOF/TOF ms by mixing equimolar quantities of a deuterated standard for the shared product ((RADA)₄-GG-GPQGd₈). The experiment was conducted over a three day period and performed on 100% (RADA)₄-CP1 and (RADA)₄-CP2 (Fig. 3 and 4). This timeline and enzyme profile coincides with typical known window for neuroinflammation and up-regulation of MMP-2 [48 - 50]. A 5.21 ± 0.05 and 1.42 ± 0.3 mM product was detected from the enzyme treated CP1 and CP2 groups, respectively, while the controls were negligible. To maintain similar morphology to ECMs and subsequent cell behaviour, these sequences were increasingly doped with (RADA)₄ by % v/v, ie., 0, 25, 50 and 75, treated with 5 nM MMP-2, and portrayed in a 2D and 3D manner (Fig. 3 Aii, Bii, Aiii, and Biii). Product increases as a function of time in both CP groups ranging 300 - 400 μ M in both cases. The trend is apparently logarithmic for both, but is more rapid for CP2, producing almost all of product within one day. Overall product formation is slightly higher in CP1 groups, but this was not significant. The most product was formed with the addition of 25% (RADA)₄.

The 0, 25, 50 and 75% v/v (RADA)₄ were observed with TEM to relate nanostructure architecture to product formation (Fig. 3 Aiv-vii, and Biv-vii). Highly bundled structures are

visible in pure CP1, being 20 - 100 nm, and CP2, being 20 - 300 nm in diameter. However, all CP1 groups containing (RADA)₄ bear similar morphology; thin networks 5 - 20 nm in diameter, not unlike (RADA)₄ (Fig. 2 Ai). CP2 groups have thickly meshed nanostructures, with 20 - 80 nm diameter pores between bundles, which decrease in complexity and density with increasing (RADA)₄ percent. Only the 25% (RADA)₄-CP2 groups bear similar morphology to pure (RADA)₄.

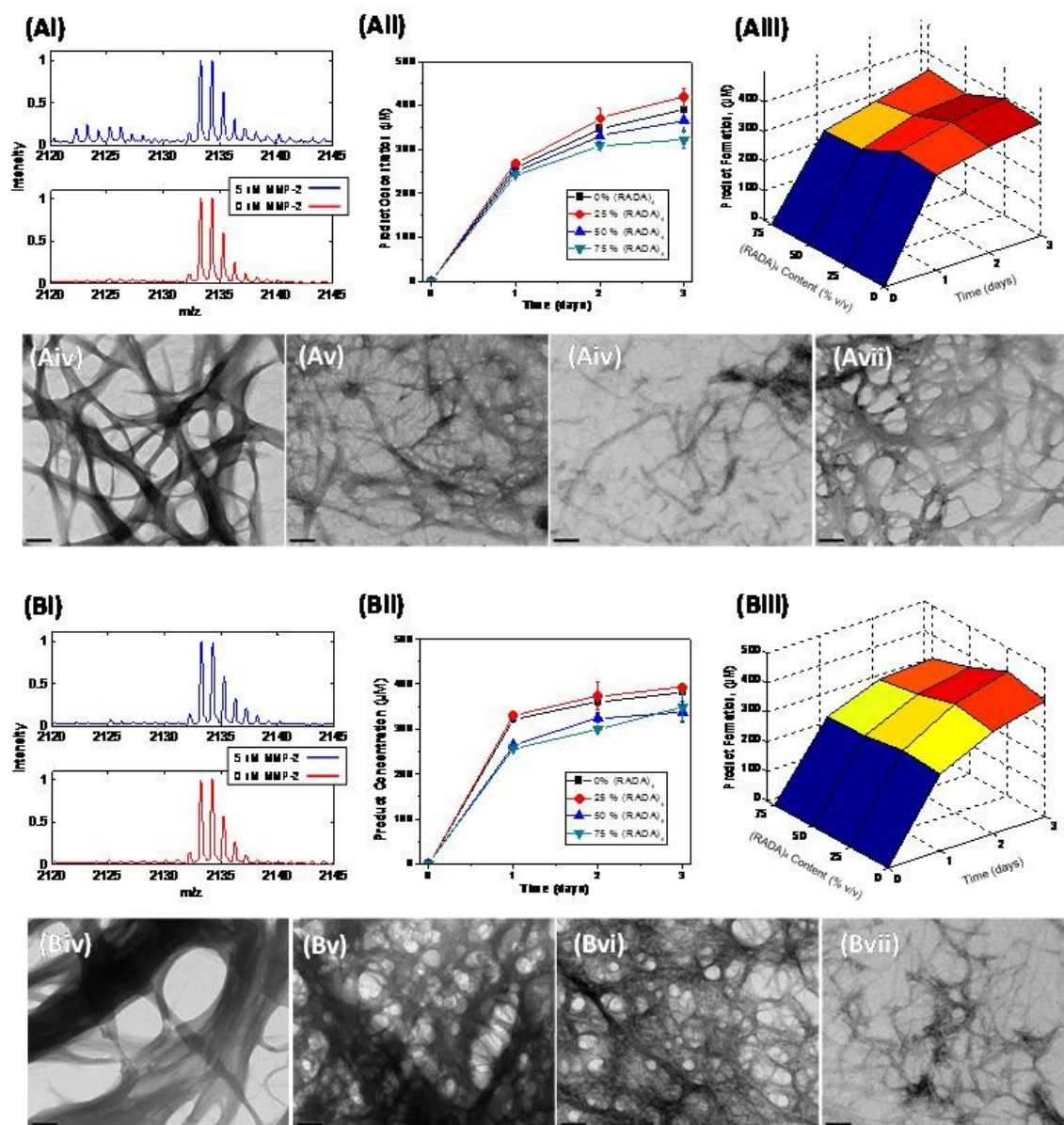


Figure 4.3. Enzymatic product formation of (RADA)₄-GG-GPQG+IASQ (CP1) (A) and (RADA)₄-GG-GPQG+PAGQ (CP2) (B). MALDI TOF/TOF mass spectrometric isotopic distribution (i) of product (2125.1 m/z) and standard (2132.1 m/z) from a 5 nM MMP-2 experiment. A 1 nM MMP-2 treatment with 2D (ii) and 3D (iii) calculated product formation from comparative area under isotopic distribution as a function of time, with 0%, 25%, 50% and 75% (RADA)₄ in (RADA)₄-CP1/CP2. All enzyme treatments were allowed to self-assemble for 24 hours in TNC buffer, post 30 minute sonication, and were incubated for 3 days at 37°C in TNC buffer, with 0.5 % w/v peptide. Scale bars are 100 nm. Transmission electron microscopy, 0% (iv), 25% (v), 50% (vi), and 75% (vii) mixtures of (RADA)₄ in (RADA)₄-CP1/CP2. Samples were stained with 4% uranyl acetate and imaged at 0.5% w/v in TNC buffer upon 30 minutes of sonication and 24 hours of incubation at 37°C. Scale bars are 100 nm. $n = 3$ replicates for all groups. Data analyzed represents mean \pm SD.

CP groups were capable of being cleaved when treated with MMP-2. When treated with 5 nM MMP-2, CP1 is significantly higher than CP2, which is expected from the sequence activity. However this was not the case with 1 nM MMP-2, and higher enzyme turnover may be necessary to degrade bulk nanostructures and allow sequence dominant activity [51]. Therefore, as 1 nM is more representative of neural inflammation, this concentration will be used in further investigations [50]. Similar to the observations in pure (RADA)₄-IKVAV groups, the hydrophobic residues from CP groups, such as isoleucine and alanine, may enhance clustering of nanofibers. However, these residues are not dominant in CP sequences, and proline may play a greater role in self-assembly. It has a cyclic ring, which is part of the backbone, that may 'bend' the peptide and allow bundling. Images of CP2 display thicker bundles, and bear two prolines. Proline-rich SAPs, derived from naturally forming zein maize storage proteins, have been engineered with this in mind [52 - 55]. Product formation was slightly higher in 25% (RADA)₄ groups for both CPs, and may be due to reduced bundling allowing free access to MMP-2 digestion. Despite this and a drastic difference in self-assembled morphology, there is little overall significant difference in product formation between (RADA)₄ and CP groups. Steric hindrances created by complex nanoscale architecture, such as those observed in microtubule digestion, may attenuate any differences in expected product formation and may be induced by nanofibers with or without bundling [56]. Differences may be noteworthy at higher enzyme turnover with greater concentrations or longer time studies. Nanoscale morphology better reflects natural ECMs at high (RADA)₄ contents in these CP groups, and these groups do not differ greatly in overall product formation. Similar reasoning for choosing 10% (RADA)₄-IKVAV, 10% v/v (RADA)₄-CP-DP was also chosen for studying cell response to drug release.

3.3. PC-12 Neural Cell Response to MMP-2 Treatment

A 3 day study of 100 nM soluble peptide drug on PC-12 neurite outgrowth was performed to assay the initial efficacy of the peptide drugs. The peptide fragments IASQ from CP1 and PAGQ from CP2 were included as they are expected to cleave with the DP1 and DP2 molecules. Controls include scrambled peptides, which are GMV for DP1 and GLDG for DP2, 100 ng/ml nerve growth factor (NGF), and media (Fig 4). Also included was a 1 nM MMP-2 group to test any deleterious effect on PC-12 morphology. Compared to the media control, neurite outgrowth was apparent in the expected NGF group and all drug groups to a lesser extent. Some neurite outgrowth was present in the scrambled sequences as well, suggesting that these peptides are too small to change their bioactivity through sequence change. None was present in the MMP-2 group suggesting no apparent change due the protease. Therefore, both drug peptides were used in further studies.

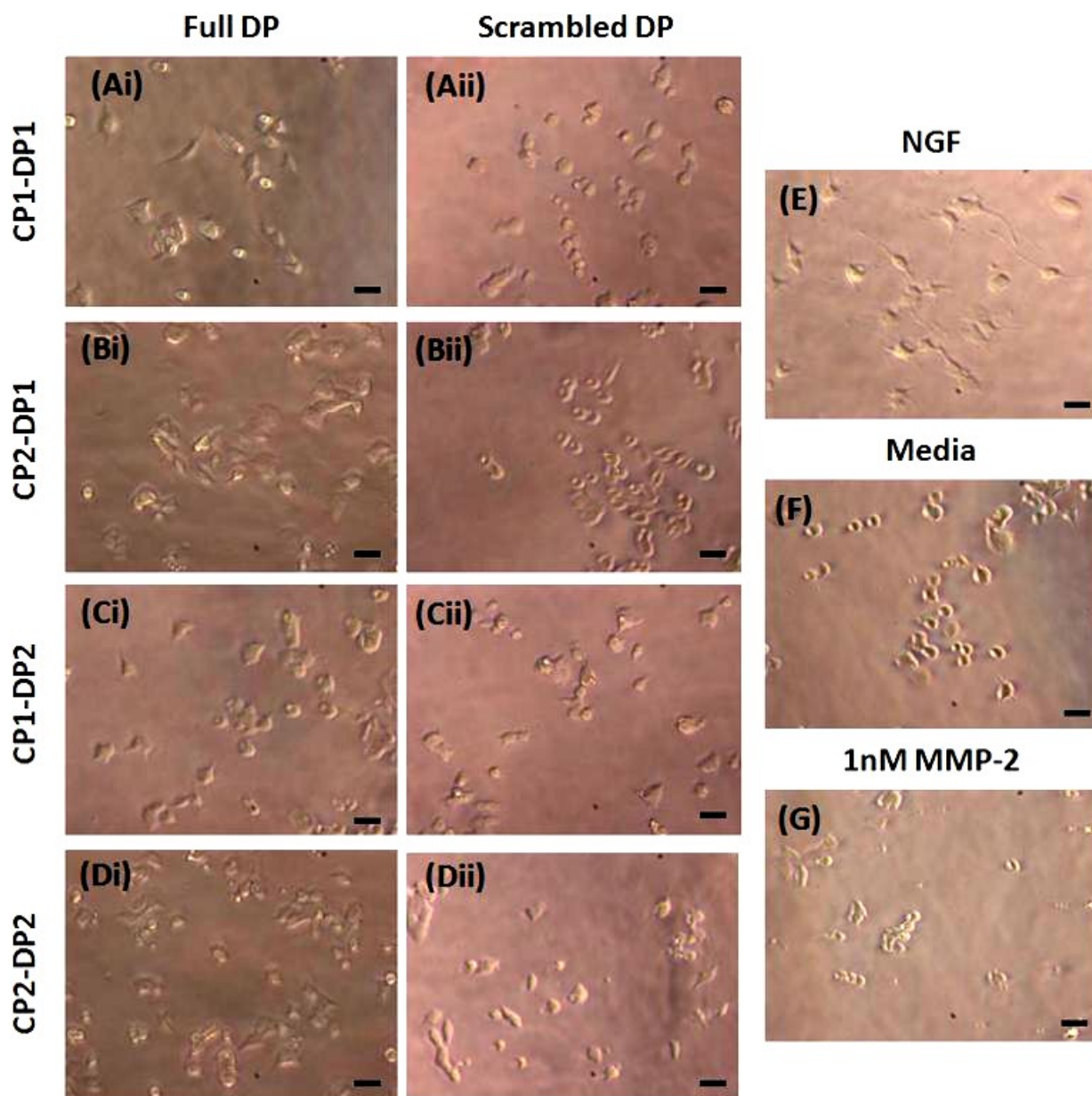


Figure 4.4. Phase contrast imaging of PC-12 cell neurite outgrowth. Cells were seeded into type IV Collagen treated with 100 nM CP1-DP1 (A), CP2-DP1 (B), CP1-DP2 (C), CP2-DP2 (D), where CP1/CP2 were projected cleaved peptide fragments IASQ/PAGQ, full DP1/DP2 sequences are MVG/DGGL, and scrambled sequences are GVM/GLDG (i/ii). Also shown are 100ng/ml nerve growth factor (NGF (E), a media control (F), and 1 nM MMP-2. Live images were taken at day 3. Scale bars are 25 μ m.

To assess active daily neural signaling and its interplay with product formation, acetylcholine esterase activity was assayed for 0 and 1 nM MMP-2 treated mixtures of 10% (RADA)₄-IKVAV, 10% (RADA)₄-CP1/CP2-DP1/DP2, and 80% (RADA)₄ groups, and is portrayed in 2D and 3D (Fig. 5A and B). Mixed drug groups were 5% / 5% DP1 / DP2. MTT measurements were used to normalize differences in cell quantity, as protein levels could create an artifact from excessive peptide substrate (i.e., tissue culture plate coating) . All MMP-2 untreated groups do not display any significant increase in esterase activity with time, while treated groups do increase by day. Noteworthy observations are visible at day 3, where the effect of DP1 is significantly higher than DP2 and the DP mixture, which is 1 mU for CP1 and 0.5 mU for CP2 groups. DP2 effects from both CP1 and CP2 groups are comparable to DP1/DP2 mixtures.

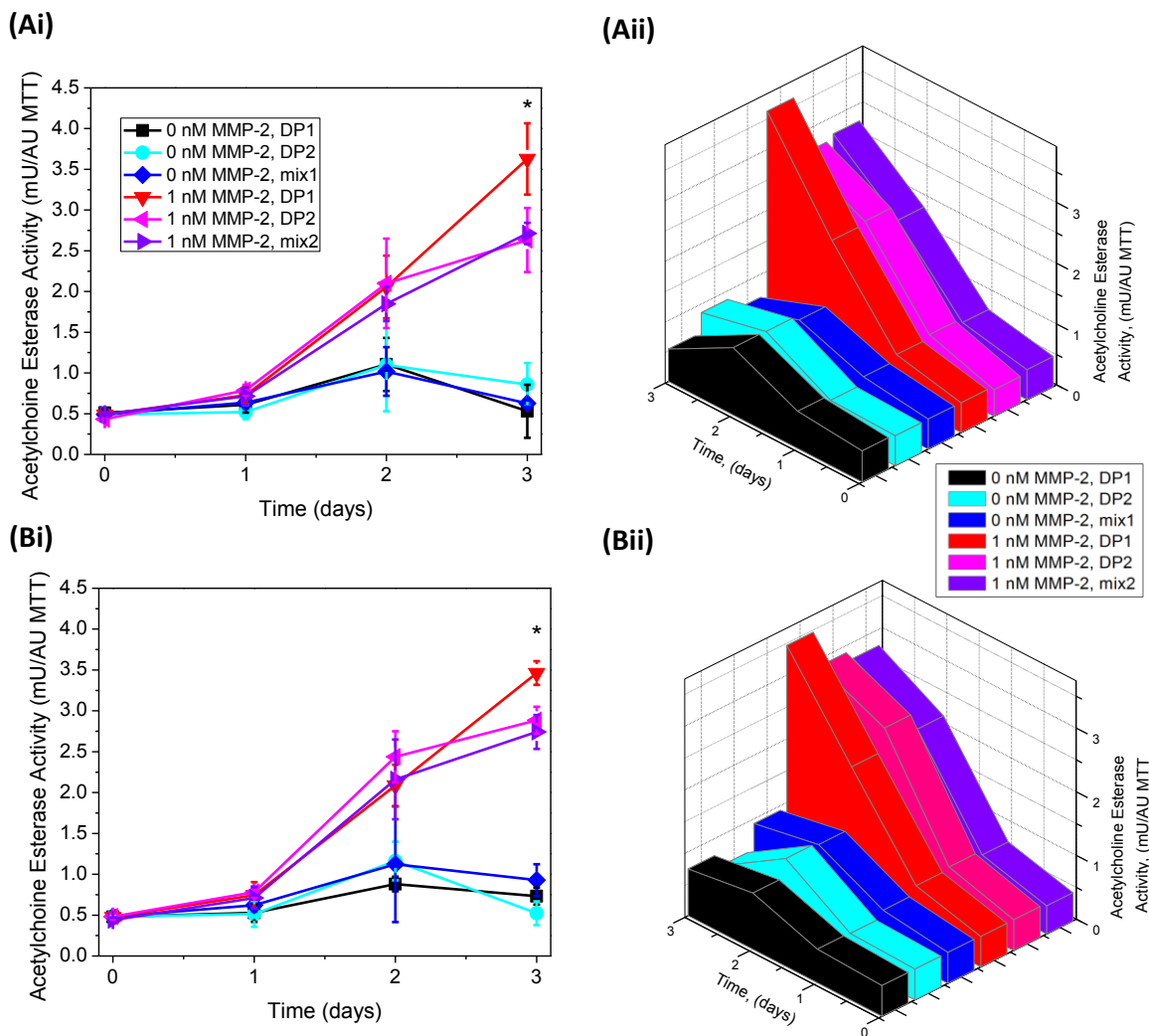


Figure 4.5. Acetylcholine esterase activity of PC-12 cells, measured over 3 days, seeded into 1% w/v (RADA)₄ nanoscaffolds with GPQG+IASQ (CP1) (A) and GPQG+PAGQ (CP2) (B), treated with 0 nM and 1 nM MMP-2. The embedded peptide neurotrophins were MVG (DP1) and DGGL (DP2). Fully the mixtures tested were 80% (RADA)₄, 10% (RADA)₄-IKVAV, and variations of 10% (RADA)₄-CP1-DP1, (RADA)₄-CP1-DP2, (RADA)₄-CP2-DP1, and (RADA)₄-CP2-DP2. Mixed DP groups were split 5% / 5% (RADA)₄-CP1-DP1 (mix 1) / (RADA)₄-CP1-DP2 and (RADA)₄-CP2-DP1 / (RADA)₄-CP2-DP2 (mix 2). $n = 3$ for all groups (* $p < 0.05$). Day 3 was compared to day 1 in a pairwise comparison. Data analyzed represents mean \pm SD.

For these groups, neurite outgrowth was observed by PCM and confocal microscopy (Fig.6). Gap junctions and microtubules were immunolabeled with GAP43 (green) and β -III tubulin (violet), respectively, and nuclei were stained with hoechst 33342 (blue). Overall, the cell body maintained a spherical shape $\sim 10 \mu\text{m}$ in diameter in all conditions. Occasional minor neurite budding is visible in untreated MMP-2 groups. With MMP-2 treatment, extensive neurite outgrowth, ranging from 2 - 100 μm in length, are present in some cells and cell clusters. Visible differences are indistinguishable between CP and DP groups, and were minor in esterase activity, therefore neurite quantification was not performed. Neurites are labelled by their gap junctions, but appear to have very little microtubule structure.

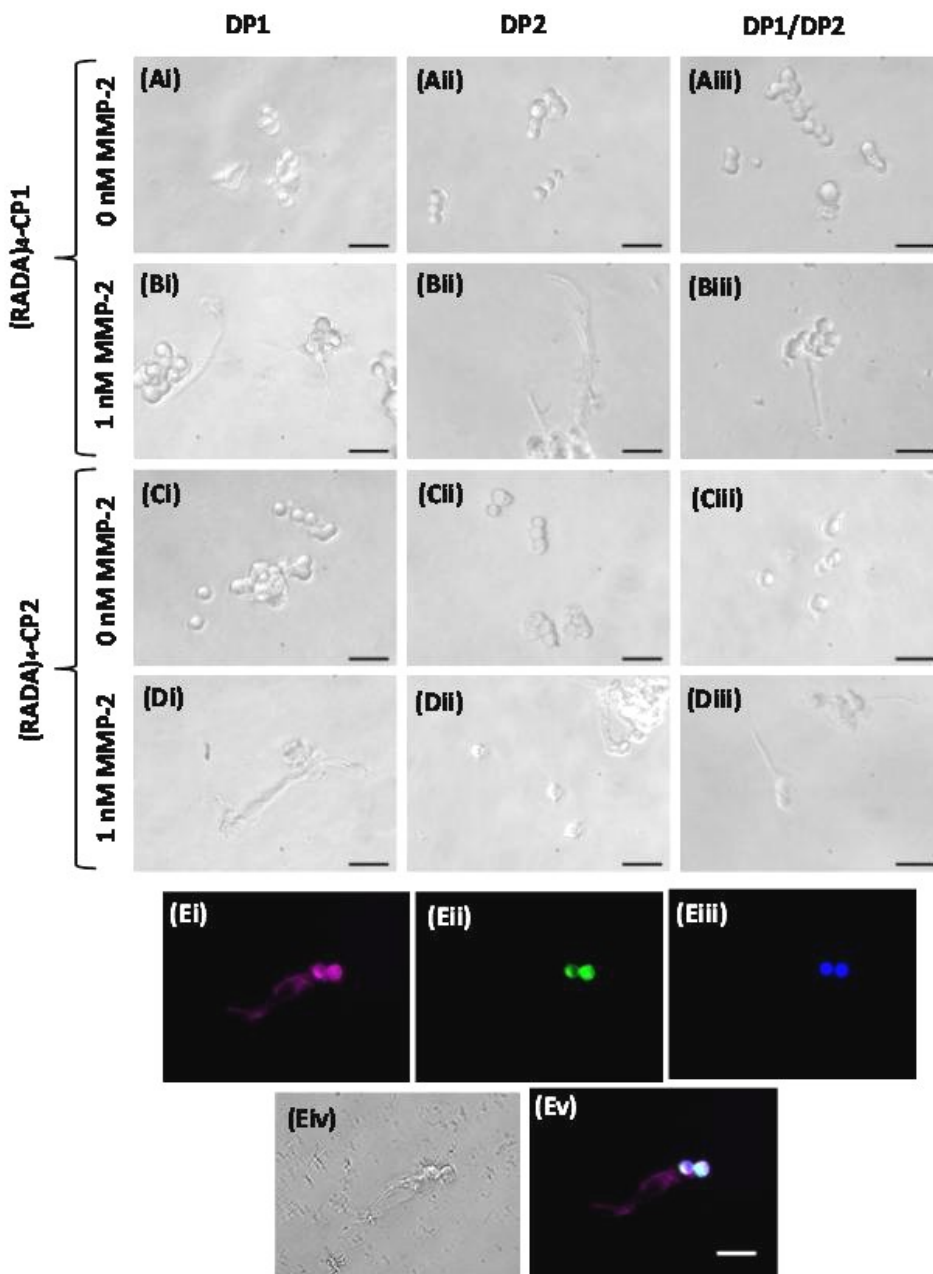


Figure 4.6. Phase contrast imaging of PC-12 cell neurite outgrowth. Cells were seeded into 1% w/v (RADA)₄ nanoscaffolds with 0 nM (A) and 1 nM MMP-2 (B) treated GPQG+IASQ (CP1) and also 0 nM (C) and 1 nM (D) treated GPQG+PAGQ (CP2). The embedded peptide neurotrophins were MVG (DP1) (i), DGGL (DP2) (ii) and a 1:1 mixture of these (iii). Fully the mixtures tested were 80% (RADA)₄, 10% (RADA)₄-IKVAV, and variations of 10% (RADA)₄-CP1-DP1, (RADA)₄-CP1-DP2, (RADA)₄-CP2-DP1, and (RADA)₄-CP2-DP2. Mixed DP groups were split 5% / 5% (RADA)₄-CP1-DP1 (mix 1) / (RADA)₄-CP1-DP2 and (RADA)₄-CP2-DP1 / (RADA)₄-CP2-DP2 (mix 2). Confocal images (E) are labelled GAP43 (violet) (Ei) and beta(III) tubulin (green) (Eii), and nuclei were stained with Hoechst 33342 (blue) (Eiii). Also shown are phase contrast (Eiv) and fluorescent overlay (Ev). Images or fixations were taken at day 3. Scale bars are 50 μ m.

MMP-2 digestion and subsequent drug release is the apparent cause of temporally increased acetylcholine esterase activity, and acetylcholine signaling, as well as differentiation and neuritogenesis. This is typically shown with NGF treatment, in a wide range of doses with cells seeded into other substrates, such as collagen [36 - 37]. There is some small increase noted in the control group, which is likely due to some interaction of the cells with bound drugs. In addition, PC-12 cells are known to secrete small quantities of MMPs while neurite growth cones attempt to reorganize collagen [57 - 58]. Little difference was noted in product formation from CP1 to CP2, which reflects the result in esterase activity. On the other hand, DP1 seems to have better efficacy than DP2 and there was no apparent synergistic increase from combining the two. BDNF is typically a more effective growth factor than CNTF, so this response is expected [59]. However these proteins should be able to enhance neurogenesis together, being capable of activating different pathways. It is noted in this study that PC-12 cells may not respond to these ligands as little is known about the combined BDNF and CNTF analogue interaction with this cell line. Neurites had excessive gap junctions over structural microtubules, suggesting that their purpose was initial probing rather than committing to synaptic contact. This system is moderate compared to the typical response from NGF treatment, although the amount of present drug is far less than NGF introduced to media. Furthermore, this system has potential for controlled and time-based release tuned to protease secreting cells and tissues. In addition, the cells do not appear flat and stretched out as with collagen substrates; they are rounded and may be seeded in a pseudo 3D manner close to the plate surface rather than the surface itself [60]. This is likely due to the manner the matrix was formed in solution, and not dried down in ethanol like typical collagen protocols [61]. Primary neurons may adhere and weave themselves into the matrix in more natural morphology, and this may be a promising next step to studying this biomaterial.

4. Summary and Conclusion

The self-assembling peptide (SAP) nanoscaffold (RADA)₄ was modified to create a drug delivery system capable of developing in physiological salts and delivering on-demand drug in neuro-inflammatory conditions. A laminin derived peptide motif IKVAV was tethered to (RADA)₄ to enhance neuronal cell-type attachment and enhance the neurogenic outcome of the system. Initially (RADA)₄ was mixed with (RADA)₄-IKVAV incrementally, and 2D cell culture to determine ideal adhesion. A PC-12 cell line was used because of their preferential adhesion to bioactive substrates and sensitivity to neurotrophic growth factors. Adding 10% v/v on the IKVAV modified SAP allowed for the greatest MTT activity and cell attachment, while all cells were comparably viable by live/dead assay. The self-assembling peptide (SAP) nanoscaffold (RADA)₄ was modified with matrix metalloproteinase (MMP-2) cleavable sites and neurotrophic peptide analogues. The chosen cleavage sites were GPQG+IASQ (CP1) and GPQG+PAGQ (CP2), which are known to have high and low MMP-2 activity, respectively. Neurotrophic analogues were chosen due to their potential anti-inflammatory and neuro-protective roles. The peptide drugs used were MVG (DP1), shown to increase expression of brain derived neurotrophic factor, and a ciliary neurotrophic factor analogue, DGGL (DP2). Upon 1 nM MMP-2 treatment, measured daily for 3 days, there was little difference in product formation with the incremental addition of (RADA)₄ to (RADA)₄-CP1/CP2 groups. As a result, the following mixtures were chosen for neurotrophic cell response with 1 nM MMP-2: 80% v/v (RADA)₄, 10% v/v (RADA)₄-IKVAV, and 10% v/v of the CP groups with combinations of DP1, DP2, and 1:1 DP1:DP2 mixed. Acetylcholine esterase activity and neurite outgrowth was assayed over a three day period in tandem with product formation results. Significant esterase signaling and neurite outgrowth was noted by day 3 for each DP group. There was little

difference between CP groups, but DP1 had significantly higher esterase activity over other DPs including the mixtures. Cells seeded into this system successfully demonstrated a neurogenic response, parallel to product formation, with a MMP-2 concentration typically seen in neuroinflammation. The above provides evidence demonstrating the overall efficacy of this drug delivery system as a baseline for future study. It should be clarified that PC-12 cells are adrenal tumour derived, and do not represent true neuronal physiology. Nor are they expected to secrete relevant levels of MMP-2. Primary culture with neurons and MMP-2 secreting glia would best represent the next step in this system's clinical evolution.

5. Acknowledgements

The Authors would like to acknowledge Terry Sereda, Paul Semchuk, and Jack Moore for peptide synthesis assistance, Arlene Oatway for electron microscopy support, Emily Gruber and Theodore Ng technical assistance, and Ron Koss for cell culture advice and guidance. The authors are grateful for financial support from NSERC, NINT-NRC, and Alberta Gangwon Korea, WISEST, AET.

6. References

1. Huang EJ, Reichardt LF. Neurotrophins: roles in neuronal development and function. *Annu Rev Neurosci.* 2001;24:677.
2. Skaper SD. Neuronal growth-promoting and inhibitory cues in neuroprotection and neuroregeneration. In: Skaper SD, editor. *Neurotrophic factors methods in molecular biology.* New York: Springer; 2012. p. 13-22.
3. Reichardt LF. Neurotrophin-regulated signalling pathways. *Phil Trans R Soc B.* 2006;361(1473):1545-64.

4. Skaper SD. The biology of neurotrophins, signalling pathways, and functional peptide mimetics of neurotrophins and their receptors. *CNS Neurol Disord Drug Targets*. 2008;7(1):46-62.
5. Hollis ER, Tuszynski MH. Neurotrophins: potential therapeutic tools for the treatment of spinal cord injury. *Neurotherapeutics*. 2011;8:694-703.
6. Kelamangalath L, Smith GM. Neurotrophin treatment to promote regeneration after traumatic CNS injury. *Front Biol*. 2013;8(5):486-95.
7. Tiwari G, Tiwari R, Sriwastawa B, Bhati L, Pandey S, Pandey P, et al. Drug delivery systems: An updated review. *Int J Pharm Investig*. 2012 March;2(1):2-11.
8. Cuello AC, Bruno M, Leon W. P3-380: A β -induced nerve growth factor trophic disconnection in Alzheimer's disease. *Alzheimers Dement*. 2008;4(4):T633.
9. Madduri S, Gander B. Growth factor delivery systems and repair strategies for damaged peripheral nerves. *J Control Release*. 2012;161:274-82.
10. Haller MF, Saltzman WM. Nerve growth factor delivery systems. *J Control Release*. 1998;53:1-6.
11. Lee KY, Mooney DJ. Hydrogels for Tissue Engineering. *Chem Rev*. 2001;101(7):1869-78.
12. Fichman G, Gazit E. Self-assembly of short peptides to form hydrogels: design of buildingblocks, physical properties and technological applications. *Acta Biomater*. 2014;10:1671-82.
13. Flaim CJ, Chien S, Bhatia SN. An extracellular matrix microarray for probing cellular differentiation. *Nat Methods*. 2005 February;2(2):119-25.

14. Zhang S. Fabrication of novel biomaterials through molecular self-assembly. *Nat Biotechnol.* 2003 October;21(10):1171-8.
15. Holmes TC, de Lacalle S, Su X, Liu G, Rich A, Zhang S. Extensive neurite outgrowth and active synapse formation on self-assembling peptide scaffolds. *PNAS.* 2000 June;97(12):6728-33.
16. Worthington P, Pochan DJ, Langhans SA. Peptide Hydrogels - Versatile Matrices for 3D Cell Culture in Cancer Medicine. *Front Oncol.* 2015;5:92.
17. Kisiday J, Jin M, Kurz B, et al. Self-assembling peptide hydrogel fosters chondrocyte extracellular matrix production and cell division: Implications for cartilage tissue repair. *Proc Natl Acad Sci U S A.* 2002;99(15):9996-10001.
18. Zhang S, Gelain F, Zhao X. Designer self-assembling peptide nanofiber scaffolds for 3D tissue cell cultures. *Semin Cancer Biol.* 2005 October;15(5):413-20.
19. MacPhee CE, Woolfson DN. Engineered and designed peptide-based fibrous biomaterials. *Curr Opin Solid State Mater Sci.* 2004;8(2):141-9.
20. Holmes TC. Novel peptide-based biomaterial scaffolds for tissue engineering. *Trends Biotechnol.* 2002 January;20(1):16-21.
21. Geckil H, Xu F, Zhang X, Moon S, Demirci U. Engineering hydrogels as extracellular matrix mimics. *Nanomedicine.* 2010 April;5(3):469-84.
22. Koutsopoulos S, Zhang S. Long-term three-dimensional neural tissue cultures in functionalized self-assembling peptide hydrogels, matrigel and collagen I. *Acta Biomater.* 2012(<http://dx.doi.org/10.1016/j.actbio.2012.09.010>).

23. Zhao X, Zhang S. Designer self-assembling peptide materials. *Macromol Biosci.* 2007 January 5;7(1):13-22.
24. Cheng T, Chen M, Chang W, Huang M, Wang T. Neural stem cells encapsulated in a functionalized self-assembling peptide hydrogel for brain tissue engineering. *Biomaterials.* 2013;34:2005-16.
25. Gelain F, Unsworth LD, Zhang S. Slow and sustained release of active cytokines from self-assembling peptide scaffolds RID A-7231-2011. *J Controlled Release.* 2010;145(3):231-9.
26. Chau Y, Luo Y, Cheung ACY, Nagai Y, Zhang S, Kobler James B, et al. Incorporation of a matrix metalloproteinase-sensitive substrate into self-assembling peptides - A model for biofunctional scaffolds. *Biomaterials.* 2008;29:1713-9.
27. Law B, Tung C. Proteolysis: a biological process adapted in drug delivery, therapy, and imaging. *Bioconjugate Chem.* 2009;20(9):1683-95.
28. Turk BE, Huang LL, Piro ET, Cantley LC. Determination of protease cleavage site motifs using mixture-based oriented peptide libraries. *Nat Biotechnol.* 2001 July;19(7):661-7.
29. Könnecke H, Bechmann I. The role of microglia and matrix metalloproteinases involvement in neuroinflammation and gliomas. *Clin Dev Immunol.* 2013;2013:914104.
30. Nagase H, Fields GB. Human matrix metalloproteinase specificity studies using collagen sequence-based synthetic peptides. *Biopolymers.* 1996;40:399-416.
31. Netzel-Arnett S, Sang QX, Moore WG, Navre M, Birkedal-Hansen H, Van Wart HE. Comparative sequence specificities of human 72- and 92-kDa gelatinases (type IV collagenases) and PUMP (matrilysin). *Biochemistry.* 1993 June 29;32(25):6427-32.

32. Lévesque SG, Shoichet MS. Synthesis of enzyme-degradable, peptide-cross-linked dextran hydrogels. *Bioconjug Chem.* 2007;18(3):874-85.
33. Shin MK, Kim HG, Kim KL. A novel trimeric peptide, Neuropep-1-stimulating brain-derived neurotrophic factor expression in rat brain improves spatial learning and memory as measured by the Y-maze and Morris water maze. *J Neurochem.* 2011;116:205-16.
34. Li B, Wanka L, Blanchard J, Liu F, Chohan MO, Iqbal K, et al. Neurotrophic peptides incorporating adamantane improve learning and memory, promote neurogenesis and synaptic plasticity in mice. *FEBS Lett.* 2010;584(15):3359-65.
35. Chohan MO, Li B, Blanchard J, Tung Y, Heaney AT, Rabe A, et al. Enhancement of dentate gyrus neurogenesis, dendritic and synaptic plasticity and memory by a neurotrophic peptide. *Neurobiol Aging.* 2011;32(8):1420-34.
36. Tomaselli KJ, Damsky CH, Reichardt LF. Interactions of a neuronal cell line (PC12) with laminin, collagen IV, and fibronectin: identification of integrin-related glycoproteins involved in attachment and process outgrowth. *J Cell Biol.* 1987;105:2347-58.
37. Li R, Kong Y, Ladisch S. Nerve growth factor-induced neurite formation in PC12 cells is independent of endogenous cellular gangliosides. *Glycobiology.* 1998;8(6):597-603.
38. Silva D, Natalello A, Sani B, et al. Synthesis and characterization of designed BMHP1-derived self-assembling peptides for tissue engineering applications. *Nanoscale.* 2013;5:704-718. <http://search.credoreference.com/content/entry/igidictist/nanoscale>.

39. Parmar M, Skogh C, Björklund A, Campbell K, Regional specification of neurosphere cultures derived from subregions of the embryonic telencephalon, *Mol Cell Neurosci* 2002;21:645–656.
40. Tysseling-Mattiace VM, Sahni V, Niece KL, Birch D, Czeisler C, Fehlings MG, et al. Self-assembling nanofibers inhibit glial scar formation and promote axon elongation after spinal cord injury. *J Neurosci*. 2008;28(14):3814-23
41. Applied Biosystems. ABI 433A peptide synthesizer user guide. 2004;1.
42. Dawes JC, Biological techniques for transmission and scanning electron microscopy. Ladd Research Industries, Inc. 1984.
43. Tutton MG, George ML, Eccles SA, Burton S, Swift RI, Abulafi AM. Use of plasma MMP-2 and MMP-9 levels as a surrogate for tumor expression in colorectal cancer patients. *Int J Cancer*. 2003 June;107:541-50.
44. Groblewska M, Mroczko B, Gryko M, Pryczynicz A, Guzińska-Ustymowicz K, Kędra B, et al. Serum levels and tissue expression of matrix metalloproteinase 2 (MMP-2) and tissue inhibitor of metalloproteinases 2 (TIMP-2) in colorectal cancer patients. *Tumor Biol*. 2014 January;35:3793-802.
45. Zhang S, Holmes T, Lockshin C, Rich A. Spontaneous assembly of a self-complementary oligopeptide to form a stable macroscopic membrane. *Proc Natl Acad Sci*. 1993;90:3334-8.
46. Kabiri M, Bushnak I, McDermot MT, Unsworth LD. Toward a mechanistic understanding of ionic self-complementary peptide self-assembly: role of water molecules and ions. *Biomacromolecules*. 2013 September;14:3943-50.

47. Beck K, Hunter I, Engel J. Structure and function of laminin: anatomy of a multidomain glycoprotein. *FASEB J.* 1990;4(2):148-60.
48. Ceulemans A, Zgavc T, Kooijman R, Hachimi-Idrissi S, Sarre S, Michotte Y. The dual role of the neuroinflammatory response after ischemic stroke: modulatory effects of hypothermia. *J Neuroinflammation.* 2010;7(1):74.
49. Lakhan SE, Kirchgessner A, Hofer M. Inflammatory mechanisms in ischemic stroke: therapeutic approaches. *J Transl Med.* 2009;7(1):97.
50. Lucivero V, Prontera M, Mezzapesa DM, Petruzzellis M, Sancilio M, Tinelli A, et al. Different roles of matrix metalloproteinases-2 and -9 after human ischaemic stroke. *Neurol Sci.* 2013 December 1;28:165-70.
51. Sun W, Valloran JJ, Zabara A, Mezzenga R. Controlling enzymatic activity and kinetics in swollen mesophases by physical nano- confinement†. *Nanoscale.* 2014;6:6853-9.
52. del Pozo-Rodríguez A, Pujals S, Delgado D, Solinís MA, Gascón AR, Giralt E, et al. A proline-rich peptide improves cell transfection of solid lipid nanoparticle-based non-viral vectors. *J Control Release.* 2008;133(2009):52-9.
53. Creasey RG, Voelcker NH, Schultz CJ. Investigation of self-assembling proline- and glycine-rich recombinant proteins and peptides inspired by proteins from a symbiotic fungus using atomic force microscopy and circular dichroism spectroscopy. *Biochim Biophys Acta.* 2012;1824:711-22.
54. Kogan M, Dalcol I, Gorostiza P, Lopez-Iglesias C, Pons R, Pons M, et al. Supramolecular properties of the proline-rich γ -zein N-terminal domain. *Biophys J.* 2002;83:1194-204.

55. Fernández-Carneado J, Kogan MJ, Castel S, Giralt E. Potential peptide carriers: amphipathic proline-rich peptides derived from the N-terminal domain of γ -zein. *Angw Chem Int Ed.* 2004;43:1811-4.
56. Tzafiriri AR, Bercovier M, Parnas H. Reaction Diffusion Model of the Enzymatic Erosion of Insoluble Fibrillar Matrices. *Biophys J.* 2002;83(2):776-93.
57. Andrew T. Jacovina, Fengming Zhong, Elena Khazanova, Emil Lev, Arunkumar B. Deora, Katherine A. Hajjar. Neuritogenesis and the nerve growth factor-induced differentiation of PC-12 cells requires annexin II-mediated plasmin generation. *J Biol Chem.* 2001;276(52):49350-8.
58. Pittman RN, Williams AG. Neurite penetration into collagen gels requires Ca^{2+} -dependent metalloproteinase activity. *Dev Neurosci.* 1989;11(1):41-51.
59. Segal RA, Greenberg ME. Intracellular signaling pathways activated by neurotrophic factors. *Annual review of neuroscience.* 1996;19(1):463-89.
60. Oh HH, Lu H, Kawazoe N, Chen G. Differentiation of PC12 cells in three-dimensional collagen sponges with micropatterned nerve growth factor. *Biotechnol Prog.* 2012 May;28(3):773-9.
61. Teng KK, Angelastro JM, Cunningham ME, Greene LA. Cultured PC12 cells chapter 21: a model for neuronal function, differentiation, and survival. In: *Cell Biology.* Elsevier Inc.; 2006. p. 171-6.

Published in Acta Biomaterialia

Chapter 5.

Brain Biocompatibility and Microglia Response Towards Engineered Self-Assembling (RADA)₄ Nanoscaffolds

Koss, KM^{a, b, Δ}; Churchward, MA^{c, Δ}; Nguyen AT^d; Yager, JY^d; Todd KG^c; Unsworth, LD^{a, b, *}

a. Department of Chemical and Materials Engineering, University of Alberta, 11487-89 Ave., Edmonton, AB, T6G 2M7

b. National Institute for Nanotechnology, NRC, 11421 Saskatchewan Dr NW, Edmonton, AB, T6G 2M9

c. Neurochemical Research Unit, Department of Psychiatry, University of Alberta, 11487-89 Ave., Edmonton, AB, T6G 2M7

d. Department of Pediatrics and Neuroscience, University of Alberta, 11487-89 Ave., Edmonton, AB, T6G 2M7

^Δ Authors contributed equally

*. To whom correspondence should be addressed lunswort@ualberta.ca

Abstract

(RADA)₄-based nanoscaffolds have many inherent properties making them amenable to tissue engineering applications: ease of synthesis, ease of customization with bioactive moieties, and amenable *for in situ* nanoscaffold formation. There is a dearth in the literature on their biocompatibility in brain tissues; where the glia response is key to regulating the local host response. Herein, nanoscaffolds composed of (RADA)₄ and (RADA)₄-IKVAV mixtures were evaluated in terms of their effect on primary microglia in culture and general tissue (*in vivo*) biocompatibility (astrocyte and microglia). Laminin-derived IKVAV peptide was chosen to promote beneficial cell interaction and attenuate deleterious glial responses. Microglia remained ramified when cultured with these nanoscaffolds, as observed using TNF- α and IL-1 β , NO, and proliferation assays. Evidence suggests that cultured microglia phagocytose the matrix whilst remaining ramified and viable, as shown visually and metabolically (MTT). Nanoscaffold intracerebral injection did not lead to microglia migration or proliferation, nor were glial scarring and axonal injury observed over the course of this study. IKVAV had no effect on microglia activation and astrogliosis. (RADA)₄ should be advantageous for localized injection as a tuneable-platform device, which may be readily cleared without deleterious effects on tissue-resident microglia.

Keywords: Self-assembling peptides, Biocompatibility, Microglia, Brain tissue, Primary cell culture, Nanoscaffold, Neural Tissue Engineering

1. Introduction

Extracellular matrices (ECM) are essential structures, containing a variety of bioactive molecules that guide tissue growth and regeneration. Developing synthetic ECM for tissue engineering and wound healing applications is an active area of research. A variety of scaffolding materials, comprised of synthetic and natural polymers, have been studied for neural tissue application [1]; however, many of these polymers systems are difficult to modify with tuneable biochemical and morphological features, requiring additional chemical synthesis, toxic co-solvents, transplantation, or a chemical trigger to maintain or form an adequate network. Many do not biodegrade effectively, potentially causing chronic inflammation as they remain at the site of administration, or their degradation products may be cytotoxic in themselves. Furthermore, high-throughput and comprehensive studies of synthetic ECM - cellular interaction may require a systematic processing, which cannot be easily performed on such materials [2, 3]. Herein, we examine the potential biocompatibility of (arginine-alanine-aspartate-alanine)₄ [(RADA)₄], a self-assembling peptide (SAP) capable of forming a three-dimensional (3-D) nanoscaffold upon exposure to physiological saline conditions that can be readily synthesized and functionalized using automated peptide synthesis.

SAPs are a novel class of nanoscaffolding material that spontaneously assembles and emulates the nanoscale fiber and pore morphology of natural ECMs [4-7]. They also bear similarities to brain ECMs, with regards to hydration and stiffness [8-10]. The mechanisms of formation are non-covalent in nature and include electrostatic forces, hydrogen bonds, and van der Waals forces [11]. The most widely used SAP for *in situ* tissue engineering application is the hexadecapeptide (RADA)₄ [12-14]. This SAP has been studied extensively using a variety of cell and tissue types, from mouse, rat, and human neural stem cells to full rat hippocampal neural

tissues [15]. Despite active use in neural tissue applications, the potential host response incurred by (RADA)₄ has not been evaluated with brain cells or tissues, where foreign material is rejected in a characteristically different manner compared to other host tissues.

A typical host response to a foreign material in peripheral tissues is initiated by the localization of leukocytes, followed by inflammation and granulation of tissue [16]. In brain tissue, leukocytes are not normally present, and their role in innate immunity is carried out by microglia, which are multifunctional cells that normally survey and provide support to surrounding cells when ramified, but when exposed to antigens take on an active 'macrophage' phenotype capable of surrounding and phagocytosing foreign bodies [17]. Microglia are identified through the expression of characteristic antigens including cluster of differentiation 68 (CD68) and ionized calcium-binding adaptor molecule 1 (IBA1), noted in cytoplasmic lysosomes and the cytoplasm, respectively [18]. In their active state, these cells secrete pro-inflammatory molecules, such as nitric oxide (NO) and cytokines including interleukin-1 beta (IL-1 β) and tumour necrosis factor alpha (TNF- α). While acute inflammation is critical for tissue defence and repair, prolonged or inappropriate inflammation ultimately results in the death of neuronal cells, and diffuse axonal and grey matter injury [19]. Furthermore, gliosis occurs in response to the continued presence of foreign materials and is characterized by the presence of active, hypertrophic astrocytes (expressing elevated levels of glial fibrillary acidic protein (GFAP)) surrounding the material to form a dense layer to protect adjacent vulnerable neurons [20]. To adequately assay biocompatibility of any potential material for brain tissue application, observing the response of microglia and astrocytes is crucial.

In the present study, the neural biocompatibility of (RADA)₄ was assessed *in vitro* using primary rat microglia and *in vivo* by rat pup intracerebral injection, noting microglia activation,

astrocyte mobilization and grey matter injury. The laminin-derived peptide isoleucine-lysine-valine-alanine-valine (IKVAV) has been shown to inhibit glial scar formation and promote axonal regeneration after spinal cord injury, and was tethered to the (RADA)₄ to attenuate potential glia-regulated host response and promoted beneficial cell interaction [20-24]. This system was used recently to transplant stem cells into the brain [25]. To find an optimal reduction, mixtures of (RADA)₄/(RADA)₄-IKVAV were evaluated in volumetric ratios of 100%/0%, 90%/10%, 75%/25%, 50%/50%, and 0%/100%. Transmission electron microscopy (TEM) was performed to assess the morphology of the self-assembled matrices. Microglia were seeded onto (RADA)₄/(RADA)₄-IKVAV scaffolds, and the morphology, proliferation, and release of pro-inflammatory factors were assayed. The *in vivo* host response to the formed nanoscaffolds was measured at the site of injection using histology to characterize the presence of microglia, astrocytes, and grey matter injury. The proposed system is summarized in Figure 5.1.

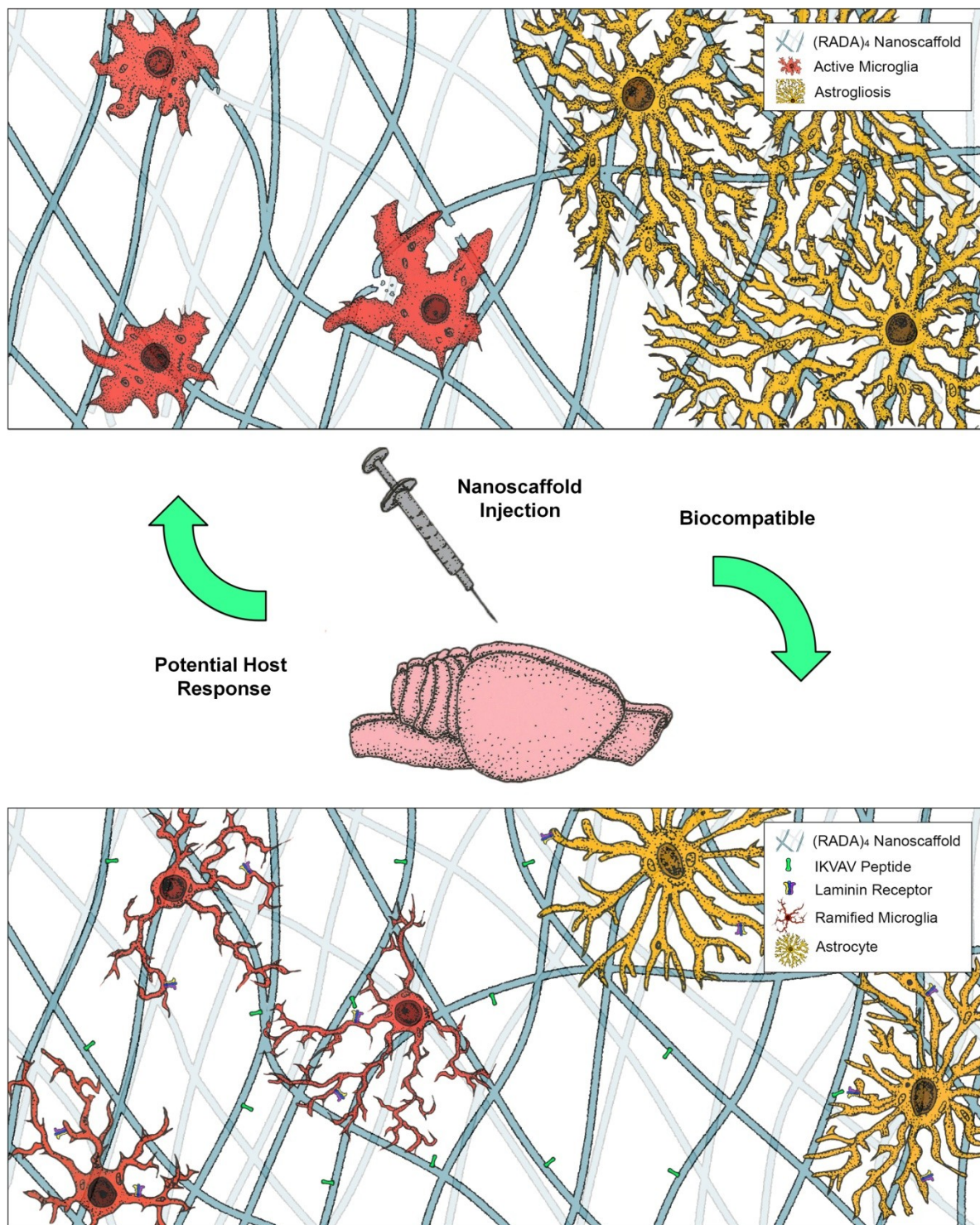


Figure 5.1. A potential host response is portrayed by active amoeboid microglia degrading and phagocytosing the material and astrocytes forming the dense interlinked networks of astrogliosis. Proposed biocompatibility of (RADA)₄ scaffold with inclusion laminin receptors and IKVAV peptides, where microglia are ramified and astrocytes are circular and non-fibrous.

2. Materials and Methods

2.1. Materials

Acetonitrile (ACN) (99.8%), methanol (99.8%), N,N-dimethylformamide (99.8%), dichloromethane (99.8%), N,N-diisopropylethylamine (99.5% biotech. grade), piperidine (99.5% biotech. grade), 1-cyano-2-ethoxy-2-oxoethylideneaminoxydimethylamino-morpholinocarbenium hexafluorophosphate (COMU) (97%), ethyl (hydroxyimino)cyanoacetate (97%), trifluoroacetic acid (TFA) (99%), triisopropylsilane (99%), and α -cyano-4-hydroxycinnamic acid (HCCA), and lidocaine HCl were all purchased from Sigma (Oakville, ON). Loaded Wang resins and Fmoc amino acids were from ChemPep (Wellington, FL). Dulbecco's modified Eagle Medium/Ham's F-12 (DMEM/F-12, 1:1), horse serum (HS), fetal bovine serum (FBS), 0.25% trypsin/EDTA, penicillin/streptomycin, and Hank's balanced saline solution (HBSS) were from Gibco (Life Technologies, Burlington, ON). All other reagents were of the highest quality available.

2.2. Peptide Synthesis

Self-assembling peptides, (RADA)₄ and (RADA)₄-IKVAV were synthesized using an ABI 433A Peptide Synthesizer. Fmoc chemistry was chosen and coupling was performed using 500 mM concentrations of COMU and ethyl (hydroxyimino) cyanoacetate. Fast-moc protocols were chosen and coupling was doubled and cycles were extended 15 minutes. All other protocols and methods were specified by the ABI 433A manual [26]. A cleavage cocktail of (96/2/2) TFA, water, and triisopropylsilane was used. ABI 4800 matrix-assisted laser desorption/ionization time of flight (MALDI-TOF/TOF) mass-spectrometry was used to assess sample masses. HCCA matrix concentrations of 10 mg/mL were suspended in 1:1 ACN:H₂O (0.1% TFA). Peptides were purified to 95% or greater using high performance liquid chromatography (HPLC) and a

Zorbax Eclipse C18 reverse-phase semi-preparative 9.4 x 250 mm column (Agilent Technologies) using an H₂O-ACN (0.1%TFA) loading. Purity was determined using HPLC with a Luna C18 reverse phase 4.6 x 250 mm column. MALDI mass spectra and chromatographs are available in the supplemental section.

2.3. Transmission Electron Microscopy

All protocols were followed from Dawes *et al.* [27]. (RADA)₄ samples at 1% (w/v) were sonicated in modified TNC buffer (pH 7.4, 50 mM tris-HCl, 150 mM NaCl, 1 mM CaCl₂) Samples were loaded onto perforated formvar carbon coated copper grids (Ted Pella, Inc.). A 4% uranyl acetate stain was applied to the peptide samples. All TEM was performed on an Philips FEI Morgagni.

2.4. In-vitro Studies

2.4.1. Primary microglial cell culture and treatments

Rat primary microglia were isolated from mixed glial cultures at 14 days *in vitro* (d.i.v.) essentially according to the method of Siao and Tsirka [28, 29]. Briefly, whole brains were dissected from male postnatal day 1-2 Sprague-Dawley rat pups. Meninges were removed and tissues were dissociated by trypsinization and mechanical trituration. Mixed cultures were grown in poly-L-lysine coated 75 cm² flasks and sustained in basal media consisting of Dulbecco's modified Eagle medium / Ham's F-12 supplement (1:1, DMEM/F-12) with 10% FBS and 200 U/mL penicillin, 200 µg/mL streptomycin in a 37° C, 5% CO₂ humidified incubator. Upon reaching confluence, microglia were isolated by treatment with 15 mM lidocaine in DMEM/F-12 containing 20 mM HEPES for 10 minutes, followed by gentle agitation (100 rpm at 37° C) for 5 minutes. Microglia were washed with DMEM/F-12 prior to plating in wells. Microglia were

treated overnight (16 hours) with glial conditioned media (basal media conditioned on 14 *d.i.v.* glial cultures for 24-hours, mixed 1:1 with fresh DMEM/F-12) to promote adhesion and recovery from the isolation procedure before replacement of media with DMEM/F-12 supplemented with 1% FBS for the duration of the experiments. Culture purity was routinely assessed by immunofluorescence microscopy for microglia-specific markers (IBA1) and were compared to total DAPI nuclear staining and was consistently $\geq 95\%$ microglia. Animal procedures were approved by The Animal Care and Use Committee, Health Sciences, at the University of Alberta.

2.4.2. Two-Dimensional Cell Culture with SAP

1 % (w/v) (RADA)₄ mixtures in 18 M Ω reverse osmosis H₂O were sonicated for 60 minutes and 20 μ L was pipetted into each well of a 24-well plate. Carefully, 180 μ L of modified TNC buffer was added and incubated for 24 hours at 4° C. Buffer was aspirated and wells were washed with 500 μ L of DMEM/F-12 three times before addition of cells. Microglia were seeded onto SAP scaffolds or poly-L-lysine in 500 μ L volumes at 1×10^6 cells / ml. All assays were performed 24 hours upon seeding.

2.4.3. Molecular Analyses

Nitric oxide levels were estimated by measuring the major metabolite nitrite using the Griess reaction [30, 31]. Enzyme-linked immunosorbant assays (ELISA) for TNF- α and IL-1 β were performed according to the manufacturer's instructions, with modifications (R&D Systems, Minneapolis, MN). Briefly, 96-well plates were coated with the appropriate capture antibody in PBS overnight at room temperature. Plates were blocked with 1% bovine serum albumin in PBS for 1 h at room temperature, following which samples or standards were added and incubated overnight at 4° C. Adhering antigen was detected by sequential incubation with the respective

biotin-conjugated antibody for 1 h, and horseradish peroxidase-conjugated streptavidin for 20 minutes (each in PBS + 1% BSA). All preceding steps were separated by 3x washing steps with phosphate buffered saline + 0.05% Tween-20 (PBS-T). Fluorescence was developed by addition of 100 μ M 10-acetyl-3,7-dihydroxyphenoxazine and 0.3% H₂O₂ in PBS for 20 minutes at room temperature. Fluorescence was measured at an excitation of 540 nm and emission of 590 nm (SpectraMax M3, Molecular Devices).

Viability was routinely assessed for all treatment conditions by incubation with 0.5 mg/mL 3-(4,5-dimethylthiazol-2-yl)-2,5-diphenyltetrazolium bromide (MTT) for 30 min and measurement of the oxidized formazan end-product at 540 nm. All molecular analyses were normalized to the MTT absorbance level of the corresponding cell lysate to account for variance in cell number between conditions.

2.4.4. Immunocytochemistry

At the end of treatment, cells were washed 3x with HBSS supplemented with 1 mM Ca²⁺ and 0.5 mM Mg²⁺ and fixed in 5% PBS-buffered formalin (pH 7.4) for 10 minutes at room temperature. Each of the following sequential steps was preceded by washing 3x with PBS: fixed cells were blocked and permeabilized (PBS pH 7.4 supplemented with 1% HS and 0.1% Triton X-100 for 1 h), incubated with primary polyclonal rabbit Iba-1 (1:1000, Wako) and monoclonal mouse CD68 (ED-1, 1:500, AbDSerotec) antibodies (PBS pH 7.4 with 0.1% HS, overnight at 4° C), incubated with secondary Alexafluor® 647 conjugated donkey-anti-mouse (1:500, Life Technologies) and Alexafluor® 488 conjugated donkey-anti-rabbit (1:500, Life Technologies) antibodies (PBS with 0.1% HS, 2 h at room temperature), stained with Hoechst 33342 (cell permeable stain for DNA), and mounted using Fluoromount-G (Southern Biotech). Epifluorescence microscopy was performed using a Leica DMI6000-B microscope, and confocal

microscopy was performed on a Leica TCS-SPE inverted microscope. Post-processing was performed using ImageJ.

2.4.5. Cell Proliferation Assay

Proliferation was measured by the incorporation of the synthetic nucleotide 5-ethynyl-2'-deoxyuridine (EdU), and visualized using Click-iT® EdU Alexa Fluor® 555 Imaging Kit (Life Technologies) essentially according to manufacturer's protocol with modifications [31]. In brief, live cells were incubated with 10 μ M EdU for 24 hours at 37° C, 5% CO₂ and subsequently fixed and permeabilized as above. Fixed cells were then incubated for 30 min at 37°C in 100 mM Tris buffer (pH 8.5) with 50m M ascorbic acid, 10 mM CuSO₄, and 10 μ M Alexafluor 555 azide. After three washings in PBS pH 7.4, immunolabelling for Iba-1 and nuclear counterstaining with Hoechst 33342 was performed as outlined above. Basic images were taken using confocal microscopy. For quantification of proliferation, images were systematically acquired using epifluorescence microscopy on a 4 × 4 grid resulting in 16 images per condition, to eliminate acquisition bias. Images were quantified by automated analysis using custom written macros in Image J.

2.5. In-vivo Studies

2.5.1. Animals

Long-Evans rat pups (Charles River Laboratories, Quebec) were used in the experiment. Each pup was randomly assigned to receive the following treatment: (1) Saline (n=4, control), (2) (RADA)₄ (n=4), and (3) (RADA)₄-IKVAV (n=4). The rats were housed in a 12/12 h light/dark cycle with access to food and water *ad lib*. Animal procedures were approved by The Animal Care and Use Committee, Health Sciences, at the University of Alberta.

2.5.2. Intracerebral Injections

Eight-day-old rat pups were randomly selected to receive stereotactic injections of 1 μ l with either saline, 1% w/v (RADA)₄, or 1% (RADA)₄-IKVAV solution. Pups were anesthetized through a nose cone with 4% isoflurane and maintained at 2-2.5%. Pups were fixed in position on Kopf stereotaxic apparatus. An incision was made in the scalp to expose the cranial sutures. Injections were made at: 2.3 mm posterior to bregma, 3.0 mm lateral from the midline, and 1.0 mm deep. The solution was slowly injected by hand with a 5 μ L Hamilton syringe and needle (30g1/2), over 1 minute and the needle left in place for 10 minutes to prevent pressure changes, before being removed. The skin incision was sutured and the animals were then placed in an incubator at 35°C for 30 min before they were returned to their dam. Sites of interest for the needle tract and anatomy are shown in the supplemental materials (Figures A5.2 and A5.3, respectively)

2.5.3. Histology

Rat pups were euthanized 7 days post injection. Brains were harvested, frozen in isopentane, and stored at -80°C until use. Fresh frozen brains were cut with a cryostat (Leica Cryocut 1800) and 14 μ m thick coronal sections were collected at the injection site for subsequent histological processing. Prior to labelling, sections were fixed in neutral buffer formalin. For immunohistochemical analyses, the following primary antibodies were used: (1) polyclonal rabbit anti-GFAP (1/1500, DakoCytomation) antibody was used to determine the number of activated astrocytes present, (2) rabbit anti-fractin polyclonal (1/1500, Millipore) to detect damaged axons, and (3) mouse anti rat CD68 antibody (1/1000, AbDSerotec) were used to detect activated microglia. Primary antibodies were incubated overnight at 4°C. Sections were incubated with secondary antibodies for 1 hour at room temperature. Secondary antibodies used

were goat anti-rabbit (1/400, Vector) and rat adsorbed horse anti mouse IgG (1/200, Vector). Colour development was detected with ABC (Vector Laboratories, Vectastain ABC Kit) and DAB (Vector Laboratories, Peroxidase Substrate Kit DAB). Areas of interest were detected with a light microscope (Leica model DM2000) at 100X magnification and positive cells were analyzed at 400X magnification at the injection site. The computer program Leica Application Suite (Las EZ) version 3.0 was used to capture the images for scoring. Cell counting (CD68 and fractin) and densitometry (GFAP) was performed using the ImageJ program.

2.5.4. Statistical Analyses

Overall significance was assessed using analysis of variance, with Tukey's multiple comparison post-hoc analysis between groups. Pairwise comparisons were assessed using a Mann-Whitney U test. A p value of ≤ 0.05 was considered significant. Data are presented as the mean \pm SEM (Standard Error Mean). Each reported n indicates an independent experiment from a separate culture preparation.

3. Results

3.1. Nanoscale Morphology

Nanoscaffold morphology for mixtures of (RADA)₄ with 0%, 10%, 25%, 50%, and 100% volume (RADA)₄-IKVAV were characterized using TEM (Figure 5.2). Nanofibers, 5-10 nm in thickness with continuous length, are visible in every condition. Dispersed morphology of individual nanofibers (0%, 10%, and 25% (RADA)₄-IKVAV) is decreasingly prevalent with increasing amounts of (RADA)₄-IKVAV, where extensive aggregation becomes visible above 50% (RADA)₄-IKVAV.

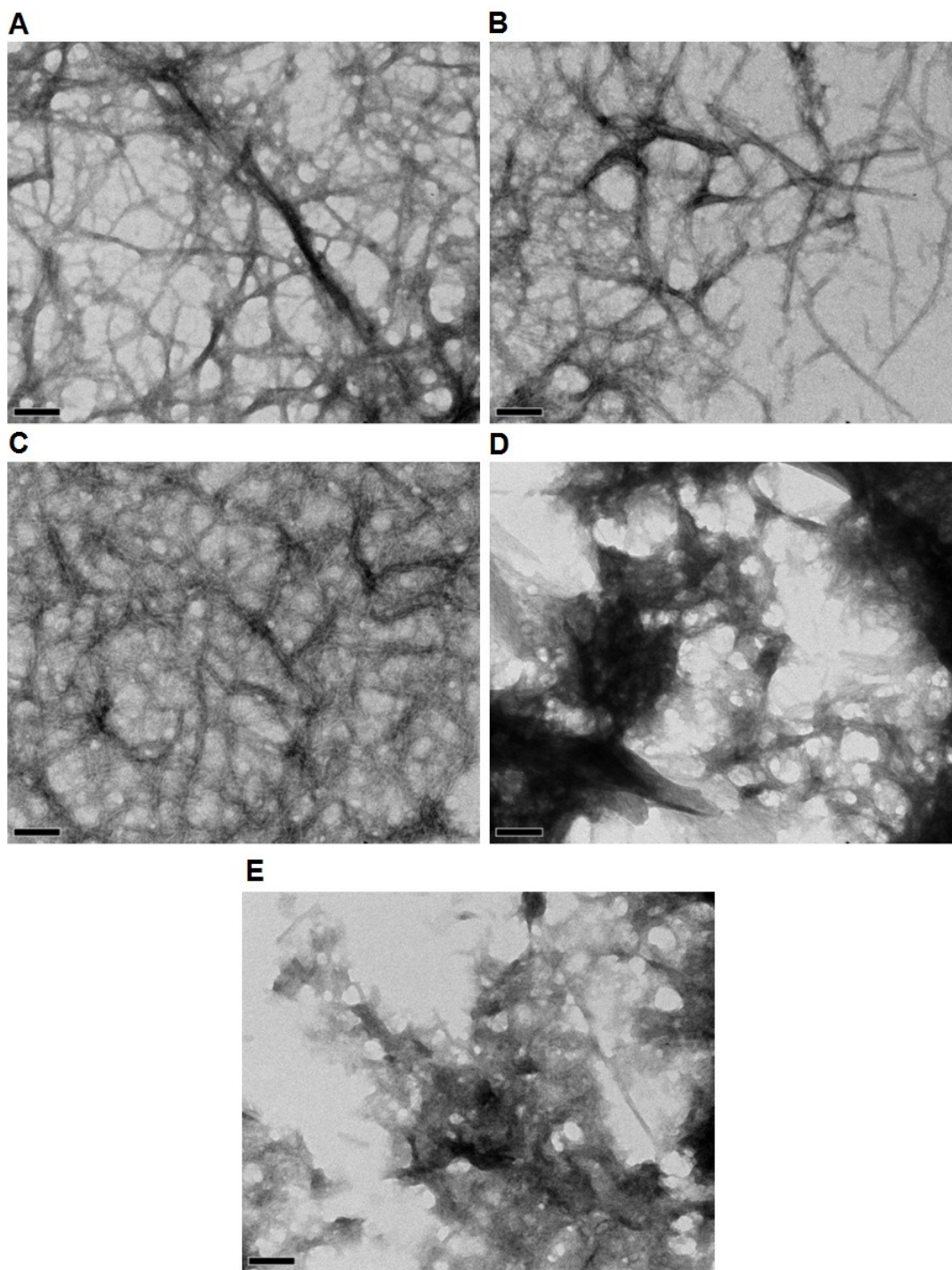


Figure 5.2. Transmission electron microscopy of (A) 0% / 100%, (B) 10% / 90%, (C) 25% / 75%, (D) 50% / 50%, and (E) 100% / 0% mixtures of (RADA)₄-IKVAV / (RADA)₄. All samples were stained with 4% uranyl acetate and imaged at 1% w/v in TNC buffer upon 30 minutes of sonication and 24 hours of incubation at 37°C. Scale bars are all 100 nm.

3.2. *Primary Microglial Culture*

Given the presence of aggregates for < 50%(RADA)₄-IKVAV concentrations, cell culture was carried out with microglia seeded onto a standard microglia adhesion coating poly-L lysine (PLL) control, and nanoscaffolds composed of 0%, 10%, and 25% (RADA)₄-IKVAV mixtures in (RADA)₄. Microglia were subsequently activated by introducing 0.1-1.0 µg/mL lipopolysaccharide (LPS) to the culture media. Microglia morphology was characterized using confocal immunofluorescence (Figure 5.3), using microglial markers CD68 (red) and IBA1 (green), as well as Hoescht 33342 nuclear staining (blue). It was apparent that microglia presented a heterogeneous morphology, typical of cultured ramified microglia, including cells with extended thin and thick processes, rod-like structures, and a limited number of amoeboid shapes [33, 34]. Visually, microglia tended to exhibit increased ramification, in terms of a greater number of smaller processes, in the presence of any (RADA)₄ mixture.

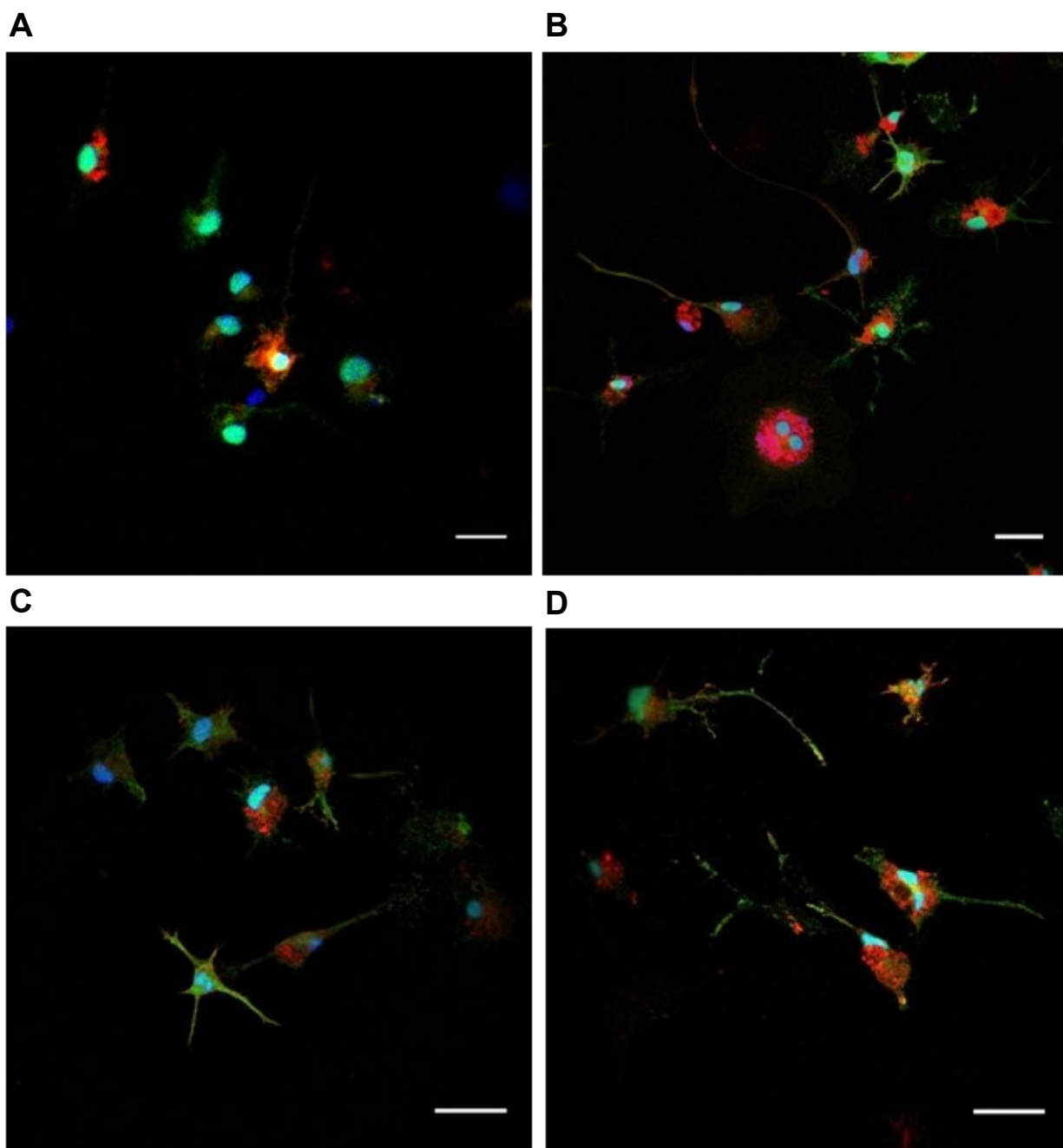


Figure 5.3. Representative confocal immunofluorescence micrographs of microglia seed onto 1% w/v mixtures of (A) Poly-L Lysine, (B) 0% / 100%, (C) 10% / 90%, and (D) 25% / 75% mixtures of (RADA)₄-IKVAV / (RADA)₄. Labels include IBA1 (green), CD68 (red), and Hoescht. Scale bars are 25 μm.

In order to assess microglia response to the presence of the SAP nanoscaffolds, pro-inflammatory cytokines IL-1 β , and TNF- α , and nitrite release were measured (Figure 5.4 A-D). For all measured pro-inflammatory molecules, no significant changes were observed in the presence of any (RADA)₄ mixture relative to the PLL-coated control surface. LPS was used to stimulate an inflammatory response in cultured microglia to determine if the matrix had any priming or sensitizing effects on microglia. LPS treatment resulted in a marked increase of IL-1 β , TNF- α , and NO (estimated by nitrite release assay) release, above the corresponding result in the absence of LPS for all conditions. No significant differences in LPS-stimulated cytokine and nitrite release was observed between PLL and any of the (RADA)₄ mixtures, nor between the (RADA)₄ and (RADA)₄-IKVAV conditions, regardless of LPS concentration. Viability, as measured using MTT assay, increased on average for every (RADA)₄ nanoscaffold condition upon the addition of LPS. All conditions, except 75% (RADA)₄, showed a significant increase ($p < 0.05$) in microglial viability. No significant MTT differences were observed in the unstimulated LPS condition.

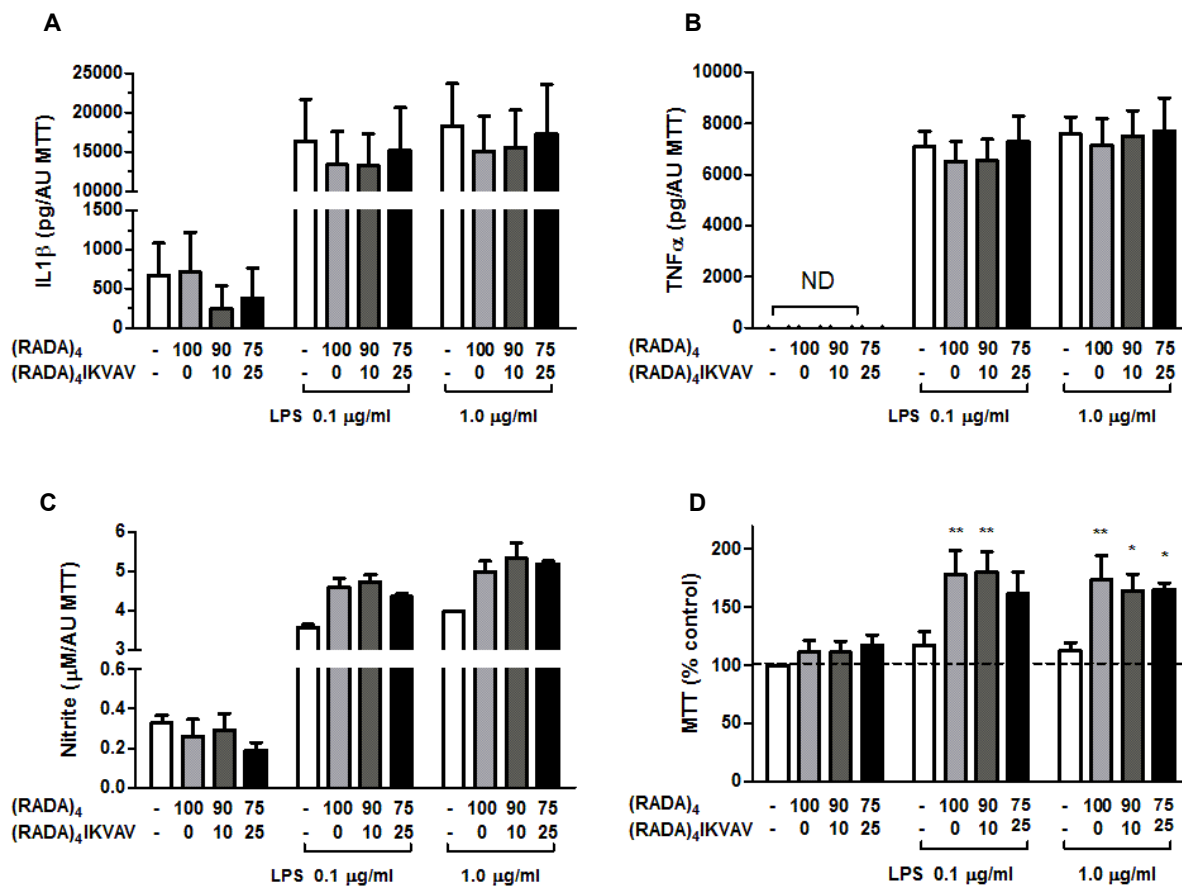


Figure 5.4. ELISA results for IL-1 β (A) and TNF- α (B) cytokine release of microglia culture. Analysis of nitrite release (C) and cell number from MTT assay (D). 1% w/v mixtures of 0:100, 10:90, 25:75 (RADA)₄-IKVAV:(RADA)₄ were compared to the PLL control. Groups were exposed with 0 μ g/ml, 0.1 μ g/ml, and 1.0 μ g/ml LPS. All cytokine and nitrite groups were normalized with their respective MTT assay results. (-) represent PLL control, $n=4$ (2 technical replicates and 2 experimental replicates) for all groups (* $p<0.05$, ** $p<0.01$), and data represents mean \pm SEM.

The overall MTT oxidation may be affected by an increase in the number of cells as well as an increase in metabolic activity. Thus, we sought to determine if the proliferation rate and total cell adhesion of microglia was affected by the presence of (RADA)₄ nanoscaffolds. Microglial proliferation was measured by incorporation of the synthetic nucleotide EdU and visualized by high throughput microscopy (Figure 5.5 A-E). As observed in prior conditions, the morphology of the microglia in all (RADA)₄ mixtures is defined by cells with spreading somata and increased processes when compared to PLL. Microglial proliferation was increased in the unstimulated condition for all (RADA)₄ nanoscaffold compositions, however proliferation did not differ from the PLL condition with the addition of LPS. Rates of proliferation did not have significant differences between (RADA)₄ mixtures without LPS, but did have an increasing trend on average. The total number of cells counted per condition was only higher in the presence of the LPS untreated 100% and 90% (RADA)₄ and 1.0 mg/ml LPS treated 100% (RADA)₄ matrices.

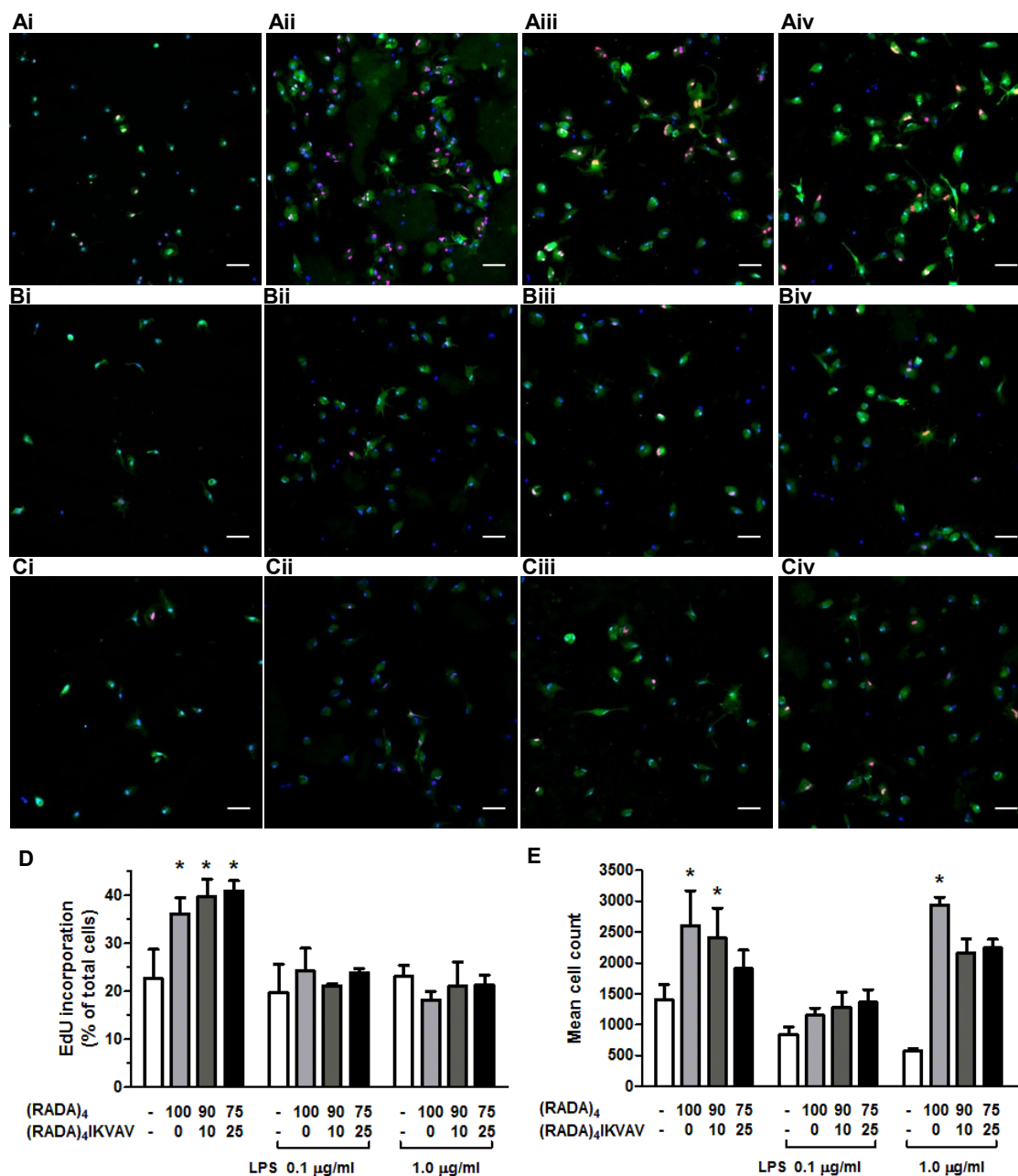


Figure 5.5. Proliferation analysis of primary microglia culture. Confocal immunofluorescent imaging visualizing proliferation of primary microglia activated with (A) 0 µg/ml (con), (B) 0.1 µg/ml, and (C) 1.0 µg/ml LPS, and cultured on substrates (i) PLL, (ii) 0% / 100%, (iii) 10% / 90%, (iv) 25% / 75% (RADA)₄-IKVAV / (RADA)₄. EdU (orange) stained new DNA while morphology was labelled by IBA1 (green) and DAPI (blue). Scale bars are 50 µm. Proliferation was imaged by epifluorescence and quantified (D) by counting EdU and DAPI labelled nuclei, in 12 sequential images per sample, where $n=4$ (* $p<0.05$). Mean cell counts (E) are also shown. (-) represent PLL control, and data represents mean \pm SEM.

3.3. *Animal Study*

Microglia activation at the site of the intracerebral injection was detected using the CD68 antibody against tissue samples. Systems using (RADA)₄ and (RADA)₄-IKVAV showed a trend towards an increase in the number of activated microglia compared to the saline treatment, however, this effect was not significant and a power analysis did not suggest significance would emerge with increasing replicates (Figure 5.6A). Under conditions of injury, astrocytes increase the expression and therefore production of GFAP. All treatment groups had a comparable GFAP immunodensity expression, and were not significantly different (Figure 5.6B). Fractin was used to detect damaged axons, an indicator of grey matter injury. No positive cells in all three treatment groups were detected (Figure 5. 6C).

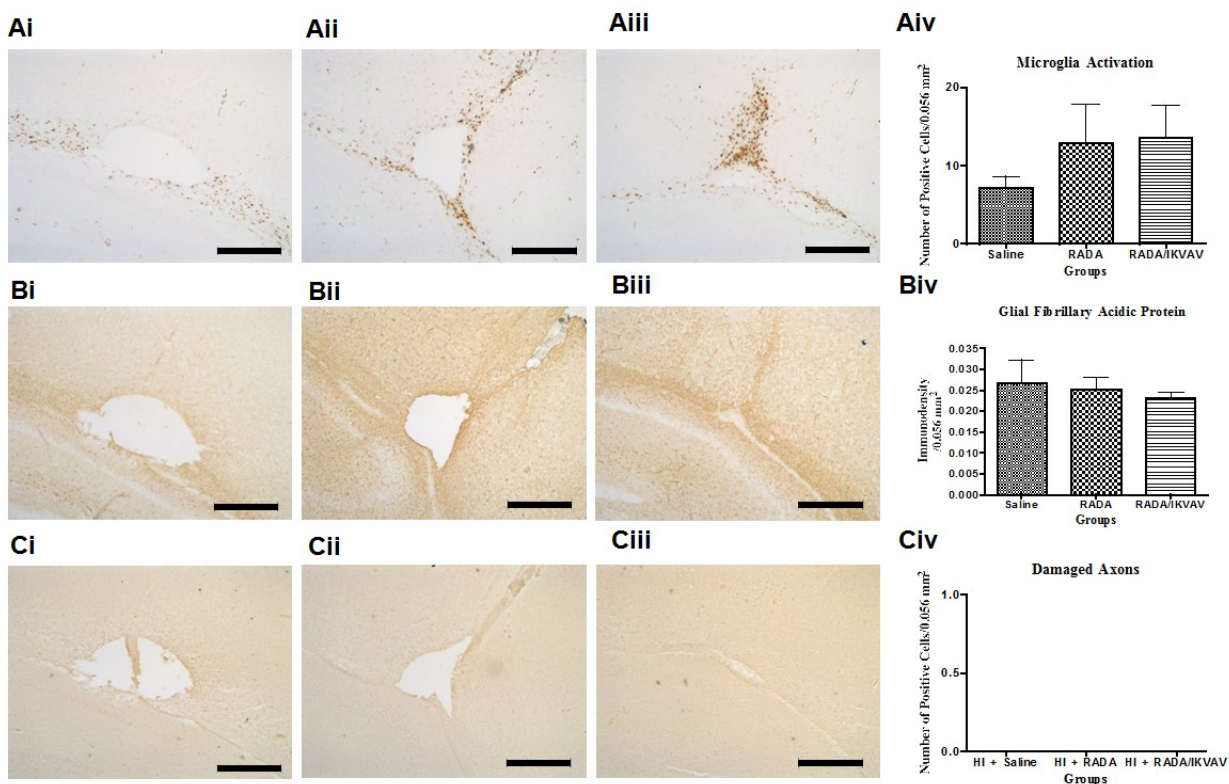


Figure 5.6. Histology and immunohistochemistry of postnatal rat pup, 7 days post intracerebral injection. Areas of interest are located at 5x magnification, centered in the field of view, and analyzed at 40x. Injections of respective solutions occurred on P8 and brain tissue was analyzed one week post surgery. The first row represents CD68 (Ai-iv), a marker for active microglia. Exposure to treatments did not cause significant changes in microglia cell counts. The second row represents GFAP (Bi-iv), a marker for astrocytes. Treatments did not cause significant changes in GFAP immunodensity. Finally, the third row represents Fractin (Ci-iv), a marker for damaged axons. No positive cells were detected surrounding the injection site. Scale bars are 0.5 mm. Saline $n=3$, (RADA)₄ $n=4$, (RADA)₄-IKVAV $n=4$. Data analyzed represents mean \pm SEM.

4. Discussion

Overall, the (RADA)₄ mixtures self-assembled into nanoscaffolds despite their decreasing meshed nanofiber morphology with the increasing addition of (RADA)₄-IKVAV. Microglia adhered to 100%, 90%, and 75% (RADA)₄, were not activated by the presence of nanoscaffolds any more than PLL. This was shown with ramified morphology and comparably low NO secretion and cytokine release. When compared to microglia on PLL, they exhibited higher measured MTT with the addition of any amount of LPS, had a higher overall cell count, and proliferation was progressively greater with the addition of IKVAV. When this matrix was injected intracerebrally, there was no significant astrocyte and microglia activity, nor was there any axonal damage.

The introduction of (RADA)₄-IKVAV, and the consequent presence of relatively hydrophobic residues isoleucine, valine, and alanine, likely increases the peptide's overall hydrophobicity and may be responsible for increased nanofiber aggregation. The presence of these hydrophobic residues may further affect the self-assembly of (RADA)₄ as it is influenced by electrostatic and, more strongly, hydrophobic interactions [35]. The (RADA)₄ morphology previously used in successful neural tissue culture by Zhang *et al.* was characterized as having a sparse 10 nm thick nanofiber network [36]. In this work, we tried to maintain this morphology for systems that incorporated 0%, 10%, and 25% (RADA)₄-IKVAV. Additionally, the *in vivo* study used both 100% (RADA)₄ and (RADA)₄-IKVAV to assess the host-response of the fully functionalized laminin-derived peptide.

By morphology, primary microglia are not apparently activated into an inflammatory state by the matrix, as cells are extending processes in a surveilling manner, similar or greater than the PLL control. An increase in CD68 immunolabelling may be related to an increase in cytoplasmic

granules and potential lysosomal activity, suggesting that the matrix may be consumed with no adverse effects on the ramified microglia. With the addition of LPS, the noteworthy increases in IL-1 β , TNF- α , nitrite, and MTT (to a lesser extent) on both PLL and (RADA)₄ based nanoscaffolds were expected from the antigenic nature of this molecule [37], and demonstrate that microglia remain competent in the presence of the nanoscaffold. Similarly, as IL-1 β , TNF- α , and nitrite secretions were neither attenuated nor exacerbated as compared to the PLL control or to any of the tested (RADA)₄ mixtures, there was no evidence of a priming or sensitization of microglia by the presence of the foreign nanoscaffold material. Although no beneficial anti-inflammatory properties are apparent due to the presence of (RADA)₄ or (RADA)₄-IKVAV, these nanoscaffolds demonstrate robust biocompatibility with or without an LPS host response. This is comparable to microglia studies with peptide modified hyaluronic acid hydrogels [38-43], and poly(ethylene glycol) based hydrogels [44], and other self-assembling nanoscaffolds [45]. However, due to the increased MTT signal in both ramified and active microglia when seeded into SAPs, there may be some additional response incurred by the (RADA)₄, such as proliferation and/or increased adhesion.

Over the time course of treatment, LPS has an inhibitory effect on proliferation in PLL and (RADA)₄ groups, which is consistent with the early inflammatory response of microglia, i.e. secretion of inflammatory factors, migration, and phagocytosis followed at later time points by proliferation at the site of injury [46 - 48]. When LPS was added to (RADA)₄/(RADA)₄-IKVAV, proliferation did not increase relative to the PLL control, which may reflect increased cell count significance being limited to one group. On the other hand, proliferation rate increased in all the LPS unstimulated (RADA)₄/(RADA)₄-IKVAV conditions, as did their overall cell count for 100% and 90% (RADA)₄. It is likely that these gains were due to proliferation in the first 24-

hour period of the experiment. Moreover, in the presence of LPS, microglia retract processes and take on an amoeboid morphology. This was observed less in the presence of matrix, suggesting the microglia also remained more adherent in the (RADA)₄/(RADA)₄-IKVAV conditions. This may explain overall higher, although not always significant, cell counts when compared to their respective PLL controls, especially with low proliferation rates upon LPS stimulation.

As we did not observe significant differences between (RADA)₄ and (RADA)₄-IKVAV for all assays, including microglial morphology, release of cytokines and inflammatory factors, and proliferation, it is possible that microglia do not respond to the specific presence of the IKVAV motif as neurons may [49]. Additionally, as there is a diminished morphological difference between the nanostructure of (RADA)₄ and (RADA)₄-IKVAV at the ratios tested in the biocompatibility assays, it is unlikely that the results have been affected by non-specific changes in the nanoscaffold structure. A similar increase in microglia proliferation with a Fmoc-Phe3 SAP was also observed by Chronopoulos *et al.* [45]. Herein, levels of MTT in SAP seeded microglia may be a result of increased metabolism as the cells may consume the nanoscaffold, also noted by abundant CD68 labelled cytoplasmic granules (Fig. 3). The nanostructure and assembly of (RADA)₄ has distinct similarities to amyloid plaques, for which microglia are known to consume aggregates of both invasive and non-invasive amyloid plaques alike [50-52]. This may be beneficial for a biomaterial as consumption of the matrix without any sensitization of the inflammatory process will lead to complete removal of the matrix over time during healing of wounded tissue.

Microglia response in the animal brain reflects that of the tissue culture in (RADA)₄, and (RADA)₄-IKVAV as there is no significant migration of cells to the site of injection.

Furthermore, indication of astrogliosis is no greater than that shown in saline injections, and damaged axons are not observed in any system studied. In both homogeneous microglia cell culture systems and complex brain tissue, (RADA)₄ has shown favourable biocompatibility, and is unaffected by the addition of the IKVAV into the SAP system. This was comparable to a study performed on hydrogels injected into the brain, where little difference was noted compared to response incurred by the injection [43]. Tysseling *et al.* similarly employed IKVAV *via* a self-assembling peptide amphiphile vehicle to promote spinal tissue repair, and a significant reduction in astrogliosis was noted over 11 weeks [53]. Chen *et al.* also noted a similar astrocyte decrease from IKVAV after 3 weeks in their (RADA)₄ SAP transplant [25]. Our system was observed after seven days with minor injury to assess base response, including microglia. Any benefit from IKVAV may become apparent over a longer term or upon inflicting a more serious injury.

5. Conclusions

Favourable biocompatibility was determined for SAP (RADA)₄ matrices and mixtures of (RADA)₄-IKVAV in primary microglia culture and *in vivo* brain tissue. Microglia, being the major cell type for the neural host response, were not activated in the presence of (RADA)₄ and did not differ in response when exposed to highly antigenic LPS, as compared to controls. Microglia did not increasingly release or show sensitization of release of inflammatory factors including cytokines and nitric oxide. In brain tissue, no increased microglia activity was present in this site of injection due to the nanoscaffold. Glial scarring and axonal damage were also not apparent. In light of these results, (RADA)₄ SAPs make an excellent candidate for localized brain tissue therapeutics and engineering applications, as they do not change tissue response, for better or worse. (RADA)₄ self-assembly in physiological conditions makes it easy to work with,

it can be made with a multitude of bioactive ligands and drugs, and it does not change surrounding tissue as a base system. Furthermore, microglia effectively adhere to and are apparently consuming the matrix without adverse effects, making it a potential drug delivery target for a multifunctional cell type directly involved in many neuro-inflammatory and degenerative disorders, but may also allow for effective break down and removal upon healing. Thus, its potential as a tuneable neural tissue scaffolding and drug delivery system is considerable and warrants further investigation.

6. Acknowledgements

The authors would like to gratefully thank Ed Armstrong for animal work and Katherine Shen for histology. KK & LDU would like to acknowledge Terry Sereda, Paul Semchuk, and Jack Moore for peptide synthesis assistance and Ron Koss for electron microscopy support. The authors are grateful for financial support from NSERC, NINT-NRC, AIHS, Alberta Health Services, the Davey Endowment for Brain Research, and WCHRI.

7. References

1. Cao H, Liu T, Chew SY. The application of nanofibrous scaffolds in neural tissue engineering. *Advanced Drug Delivery Reviews* 2009;61:1055–1064.
2. Anderson DG, Levenberg S, Langer R. Nanoliter-scale synthesis of arrayed biomaterials and application to human embryonic stem cells. *Nat Biotechnol* 2004;22(7):863–866.
3. Flaim CJ, Chien S, Bhatia SN. An extracellular matrix microarray for probing cellular differentiation. *Nat Methods* 2005;2(2):119–125.
4. Stupp SI. Biomaterials for regenerative medicine. *MRS Bull* 2005;30(7):546-53.
5. MacPhee CE, Woolfson DN. Engineered and designed peptide-based fibrous biomaterials. *Curr Opin Solid State Mater Sci* 2004;8(2):141-9.
6. Holmes TC. Novel peptide-based biomaterial scaffolds for tissue engineering. *Trends Biotechnol* 2002;20(1):16-21.
7. Gelain F, Bottai D, Vescovi A, Zhang S, Designer self-assembling peptide nanofiber scaffolds for adult mouse neural stem cell 3-dimensional cultures, *PLoS ONE* 2006;1(1): e119
8. Zimmermann DR, Dours-Zimmermann MT. Extracellular matrix of the central nervous system from neglect to challenge. *Histochem Cell Biol* 2008;130:635-53.
9. Lau LW, Cua R, Keough MB, Haylock-Jacobs S, Yong VW. Pathophysiology of the brain extracellular matrix: a new target for remyelination. *Nat Rev Neurosci* 2013;14:722-9.
10. Ulrich TA, de Juan Pardo EM, Kumar, S. The mechanical rigidity of the extracellular matrix regulates structure, motility, and proliferation of glioma cells. *Cancer Res* 2009;69(10):4167-74.

11. Zhang SG. Fabrication of novel biomaterials through molecular self-assembly. *Nat Biotechnol* 2003;21(10):1171-8.
12. Holmes TC, de Lacalle S, Su X, Liu GS, Rich A, Zhang SG. Extensive neurite outgrowth and active synapse formation on self-assembling peptide scaffolds. *ProcNatlAcadSci U S A* 2000;97(12):6728-33.
13. Zhang SG, Holmes TC, Dipersio CM, Hynes RO, Su X, Rich A. Self complementary oligopeptide matrices support mammalian-cell attachment. *Biomaterials* 1995;16(18):1385-93.
14. Kisiday J, Jin M, Kurz B, Hung H, Semino C, Zhang S. Self-assembling peptide hydrogel fosters chondrocyte extracellular matrix production and cell division: implications for cartilage tissue repair. *ProcNatlAcadSci U S A* 2002;99(15):9996-10001.
15. Zhang SG, Gelain F, Zhao X. Designer self-assembling peptide nanofiber scaffolds for 3D tissue cell cultures. *Seminars in Cancer Biology* 2005;15:413-420.
16. Gallin, JL, Snyderman R. *Inflammation basic principles and clinical correlates* 1999. 3rd ed. Raven Press, New York.
17. Polikov VS, Tresco PA, Reichert WM. Response to brain tissue to chronically implanted neural electrodes. *J. Neurosci. Meth.* 2005;148:1-18
18. Kettenmann H, Hanisch UK, Noda M, Verkhratsky A. Physiology of microglia. *Physiological Reviews* 2011;91(2):461-553
19. Anderson MA, Ao Y, Sofroniew V. Heterogeneity of reactive astrocytes. *Neuroscience Letters* 2014;565:23-29

20. Leonardo GC, Eakin AK, Ajmo JM, Gottschall PE. Vesican and brevian and expressed with distinct pathology in neonatal hypoxic-ischemic injury. *Journal of Neuroscience Research* 2008;86:1106-14
21. Silva GA, Czeisler C, Niece KL, Beniash E, Harrington DA, Kessler JA, Stupp SI, Selective differentiation of neural progenitor cells by high-epitope density nanofibers, *Science* 2004;303:1352–1355.
22. Parmar M, Skogh C, Björklund A, Campbell K, Regional specification of neurosphere cultures derived from subregions of the embryonic telencephalon, *Mol Cell Neurosci* 2002;21:645–656.
23. Wu S, Suzuki Y, Ejiri Y, Noda T, Bai h, Kitada M, Kataoka K, Ohta M, Chou H, Ide C, Bone marrow stromal cells enhance differentiation of cocultured neurosphere cells and promote regeneration of injured spinal cord, *J Neurosci Res* 2003;72:343–351.
24. Alsberg E, Anderson KW, Albeiruti A, Rowley JA, Mooney DJ, Engineering growing tissues, *Proc Nat Acad Sci U.S.A* 2002;99:12025–12030.
25. Cheng TY, Chen MH, Chang WH, Huang MY, Wang TW, Neural stem cells encapsulated in a functional self-assembled peptide hydrogel for brain tissue engineering, *Biomaterials* 2013;8:2005–2016.
26. Applied Biosystems, ABI 433A Peptide Synthesizer User Guide, 2004;V1.
27. Dawes JC, *Biological techniques for transmission and scanning electron microscopy*. Ladd Research Industries, Inc. 1984.
28. Siao, C-J, Tsirka, SE, Tissue plasminogen activator mediates microglia activation via its finger domain through annexin II, *Neurosci* 2002;22:3352–3358.

29. Lai AY, Todd KG. 2006. Hypoxia-activated microglial mediators of neuronal survival are differentially regulated by tetracyclines. *Glia* 2006;53:809–816.
30. Griess P. Bemerkungen zu der Abhandlung der HH. Weselsky und Benedikt "Uebereinigige Azoverbindungen". *Berichte Dtsch Chem Ges* 1989;12:426–428.
31. Tsikas D. Analysis of nitrite and nitrate in biological fluids by assays based on the Griess reaction: appraisal of the Griess reaction in the L-arginine/nitric oxide area of research. *J Chromatogr B Analyt Technol Biomed Life Sci* 2007;851:51–70.
32. Salic A, Mitchison TJ. A chemical method for fast and sensitive detection of DNA synthesis *in vivo*. *Proc Nat Acad Sci* 2008;105(7):2416-2420.
33. Suzumura A, Marunouchi T. Morphological transformation of microglia *in vitro*. *Brain Research* 1991;545:301-306.
34. Szabo M, Gulya K. Development of the microglial phenotype in culture. *Neuroscience* 2013;241:280-295.
35. Kabiri M, Bushnak I, McDermot MT, Unsworth LD. Toward a mechanism of ionic self-complementary self-assembly: role of water molecules and ions. *Biomacromolecules* 2013;14(11):3943-3950.
36. Koutsopoulos S, Zhang S. Long-term three-dimensional neural tissue cultures in functionalized self-assembling peptide hydrogels, Matrigel and Collagen I. *Acta Biomaterialia* 2012; <http://dx.doi.org/10.1016/j.actbio.2012.09.010>
37. Nakamura Y, Si QS, Kataoka K. Lipopolysaccharide-induced microglia activation in culture: temporal profiles of morphological change and release of cytokines and nitric oxide. *Neurosci Res* 1999;35(2):95-100.

38. Peppas NA, Hilt JZ, Khademhosseini A, Langer R. Hydrogels in biology and medicine: From molecular principles to bionanotechnology. *Adv Mater* 2006;18:1345-1360.
39. Duconseille E, Woerly S, Kelche C, Will B, Cassel J-C. Polymeric hydrogels placed into a fimbria-fornix lesion cavity promote fiber (re)growth: A morphological study in the rat. *Restor Neurol Neuros* 1998;13:193-203.
40. Prestwich GD. Hyaluronic acid-based clinical biomaterials derived for cell and molecule delivery in regenerative medicine. *J. Control. Release* 2011;155:193-199.
41. Shu XZ, Ahmad S, Liu YC, Prestwich GD. Synthesis and evaluation of injectable, *in situ* crosslinkable synthetic extracellular matrices for tissue engineering. *J Biomed Mater Res A* 2006;79:902-912.
42. Mithieux SM, Tu Y, Korkmaz E, Braet F, Weiss AS. *In situ* polymerization of tropoelastin in the absence of chemical cross-linking. *Biomaterials* 2009;30:431-435.
43. Nguyen MK, Lee DS. Injectable biodegradable hydrogels. *MacromolBiosci* 2010;10:563-579.
44. Bjugstad KB, Lampe K, Kern DS, Mahoney M. Biocompatibility of poly(ethylene glycol)-based hydrogels in the brain: an analysis of the glial response across space and time. *J Biomed Mater Res A* 2010;95(1):79-91.
45. Chronopoulou L, Togna AR, Guarguaglini G, Masci G, Glammaruco F, Togna GI, Palocci C. Self-assembling peptide hydrogels promote microglia cells proliferation and NGF production. *Soft Matter* 2012;8:5784-5790.
46. Hinojosa AE, Borja GB, Juan CL, Madrigal JLM. CCL2/MCP-1 modulation of microglial activation. *J Neuroinflammation* 2011;8:77.

47. Gomes C, Ferreira R, George J, Sanches R, Rodrigues DI, Gonçalves N, Cunha RA. Activation of microglial cells triggers a release of brain-derived neurotrophic factor (BDNF) inducing their proliferation in an adenosine A_{2A} receptor-dependent manner: A_{2A} receptor blockade prevents BDNF release and proliferation of microglia. *J Neuroinflammation* 2013;10:16.
48. Matsushita Y, Nakajima K, Tokyama Y, Kurihara T, Kohsaka S. Activation of microglia by endotoxin suppresses the secretion of glial cell line-derived neurotrophic factor (GDNF) through the action of protein kinase C α (PKC α) and mitogen-activated protein kinases (MAPKs). *J Neuroscience Research* 2008;86:1959-1971.
49. Milner R, Campbell IL. Cytokines regulate microglial adhesion to laminin and astrocyte extracellular matrix via protein kinase c-dependent activation of the α 6 β 1 integrin. *The J Neuroscience* 2002;22(5):1562-1572.
50. Lakshmanan A, Cheong DW, Accardo A, Fabrizio ED, Riekel C, Hauser CAE. Aliphatic peptides show similar self-assembly to amyloid core sequences, challenging the importance of aromatic interactions in amyloidosis. *Proc Nat Acad Sci* 2013;110(2):519-524.
51. Weldon DT, Rogers SD, Ghilardi JR, Finke MP, Cleary, JP, O'Hare E, Esler WP, Maggio JE, Mantyh PW. Fibrillar β -amyloid induces nitric oxide synthase, and loss of a select population of neurons in rat CNS *in vivo*. *The J Neuroscience* 1998;18(6):2161-2173.
52. Koenigsknecht J, Landreth G. Microglial phagocytosis of fibrillar β -amyloid through a β ₁ integrin-dependent mechanism. *The J Neuroscience* 2002;24(44):9838-9846.

53. Tysseling-Mattiace VM, Sahni V, Niece KL, Birch D, Czeisler C, Fehlings MG, Stupp SI, Kessler JA. Self-assembling nanofibers inhibit glial scar formation and promote axon elongation after spinal cord injury. *J Neuroscience* 2008;28(14):3814-3823

Chapter 6.

Summary and Outlook

The purpose of this chapter is to summarize the findings of this project, including pertinent discoveries from each chapter and how they address the initial questions of the proposed biomaterial. The future direction and outlook will also be explored.

Of the many approaches to designing biological interfacial nanomaterials for neural tissue engineering, capable of controlled peptide delivery, self-assembling peptide nanoscaffolds have many inherently desirable qualities. They form nanofiber-based nanoscaffolds that emulate natural extracellular matrices (ECMs) in physiological salts and temperatures, are relatively simple to synthesize with automated peptide chemistry, and are flexible to append with bioactive peptides to direct cellular behaviour, and proteolytically-tuned cleavage sites for on-demand release.

In this thesis, the self-assembling peptide (RADA)₄ was used as a platform for matrix metalloproteinase 2 (MMP-2) triggered peptide cleavage, which is secreted during inflammation, and was eventually used to direct neural cell differentiation. The high and low activity MMP-2 peptide substrates chosen were GPQG+IASQ and GPQG+PAGQ, respectively, where the '+' is the expected cleavage site. Neurotrophic analogues were attached to these peptides to be released and induce neural differentiation and viability. These peptides include the brain-derived neurotrophic factor MVG and the ciliary neurotrophic analogue DGGL.

Initially, time-based morphology and fractal dimension of these modified self-assembling peptides were studied and it was assured that these peptides were capable of forming the expected nanofibers with the added peptide cleavage sites. Fully formed nanofibers were present in all conditions with extensive bundling with the addition of the cleavage peptide. The addition of proline with the cleavage sites was noted as a potential promoter of bundling of these

nanofibers. The nanostructures continue to develop, however fractal dimensions, indicative of scale independent continuous morphology, are noteworthy beyond two hours. This suggested that the system may allow for diffusion or steric limitations for peptide release. Depending on the additional peptides and individual amino acids like proline, the nature of the self-assembly changes, which may lead to interesting studies where isolating these amino acids may allow for specific changes in morphologies.

Despite evidence of self-assembly, this material is not guaranteed to be labile for MMP-2 proteolysis. The peptide cleavage was assayed over a monthly time-frame, observing cleavage fragments. Product formation depended on active enzyme levels, peptide substrate (hydrogel) concentration and time, but sequence dependency was not apparent unless MMP-2 concentrations were excessive to natural physiology (>1 nM). Further, the nanofibers were visibly fragmented, likely due to proteolysis, in transmission electron microscope images. This allows for a drug delivery system that cleaves at the site of interest, only with protease, and maintains a self-assembled architecture upon cleavage. A study where this nanoscale architecture is assayed based on concentration and potential re-assembly over time may prove edifying to the biomolecular physics of these systems.

As a nanoscaffold and drug delivery vehicle intended for neural cells and tissues, a basic study demonstrating neural cell interaction and peptide release response is essential to determine the efficacy of this system. These peptides were used as a 2D cell culture substrate with the laminin peptide IKVAV to promote cell culture. PC-12 cells were used due to their sensitivity to bio-specific adhesion and neurotrophic drug-induced differentiation. This system was shown to enhance cell attachment with minimal amounts of IKVAV, MMP-2 induced peptide cleavage, and visible differentiation and neural signalling in both MVG and DGGL groups. As this was a

cell line, it allowed for an effective and sensitive demonstration of this nanoscaffold's capability. However, its relevance to mammalian physiology is not strong, therefore testing this system with primary neuronal culture or some form of neuroinflammatory animal model that responds to neurotrophic rescue may be a logical next step.

Despite its positive response inducing neural differentiation, this nanoscaffold was not guaranteed to be accepted by the central nervous system's immune cells. In the final study of this thesis, (RADA)₄ with integrated IKVAV was used to assess neural biocompatibility. As such, primary rat microglia, used as indicator cells for innate immunity in the brain, were seeded into this system and had no active or deleterious effect. In addition, these cells didn't respond negatively to these peptides when injected intracerebrally *in vivo*. Favourable biocompatibility was ascertained, and further studies could use microglia's inflammatory response, in which MMP-2 is secreted to degrade natural ECMs, to evaluate the response of the released neurotrophic peptide in this study. This system could also be corroborated *in vivo*, observing activated microglia and astrocytes.

The concluded work performed in this thesis allowed for the understanding and evaluation of a biofunctional, self-assembling, on-demand drug delivering nanoscaffold. With the appropriate modifications, this system can be used to engineer a variety of release cues and rates, as well as directed cell behaviours.

Sources Consulted

Allen TM, Cullis PR. Liposomal drug delivery systems: from concept to clinical applications.

Adv Drug Deliv Rev. 2013;65:36-48.

Alsberg E, Anderson KW, Albeiruti A, Rowley JA, Mooney DJ, Engineering growing tissues,

Proc Nat AcadSci U.S.A 2002;99:12025–12030.

Anand P, Kunnumakkara AB, Newman RA, Aggarwal BB. Bioavailability of curcumin:

problems and promises. Mol Pharm. 2007;4(6):807-18.

Ananthanarayanan B, Little L, Schaffer DV, Healy KE, Tirrell M. Neural stem cell adhesion and

proliferation on phospholipid bilayers functionalized with RGD peptides. Biomaterials.

2010;31:8706-15.

Anderson AA, Kendal CE, Garcia-Maya M, Kenny AV, Morris-Triggs SA, Wu T, et al. A

peptide from the first fibronectin domain of NCAM acts as an inverse agonist and stimulates

FGF receptor activation, neurite outgrowth and survival. J Neurochem. 2005;95(2):570-83.

Anderson DG, Levenberg S, Langer R. Nanoliter-scale synthesis of arrayed biomaterials and

application to human embryonic stem cells. Nat Biotechnol 2004;22(7):863–866.

Anderson MA, Ao Y, Sofroniew V. Heterogeneity of reactive astrocytes. Neuroscience Letters

2014;565:23-29

Andrew T. Jacovina, Fengming Zhong, Elena Khazanova, Emil Lev, Arunkumar B. Deora,

Katherine A. Hajjar. Neuritogenesis and the nerve growth factor-induced differentiation of

PC-12 cells requires annexin II-mediated plasmin generation. J Biol Chem.

2001;276(52):49350-8.

- Angeloni NL, Bond CW, Tang Y, Harrington DA, Zhang S, Stupp SI, et al. Regeneration of the cavernous nerve by Sonic hedgehog using aligned peptide amphiphile nanofibers. *Biomaterials*. 2011;32(4):1091-101.
- Antos JM, Francis MB. Selective tryptophan modification with rhodium carbenoids in aqueous solution. *J Am Chem Soc*. 2004;126(33):10256-7.
- Antos JM, McFarland JM, Iavarone AT, Francis MB. Chemoselective tryptophan labeling with rhodium carbenoids at mild pH. *J Am Chem Soc*. 2009;131(17):6301-8.
- Aota S, Nomizu M, Yamada K. The short amino acid sequence Pro-His-Ser-Arg-Asn in human Fibronectin enhances cell-adhesive function. *J Biol Chem*. 1994;269(40):24756-61.
- Applied Biosystems. ABI 433A peptide synthesizer user guide. 2004;1.
- Asahi M, Asahi K, Jung J, Zoppo GJd, Fini ME, Lo EH. Role for matrix Metalloproteinase 9 focal cerebral ischemic: effects of gene knockout and enzyme inhibition with BB-94. *J Cereb Blood Flow Metab*. 2000;20:1681-9.
- Baker AE, Bergin FG, Leaper DJ. Matrix metalloproteinases, their tissue inhibitors and colorectal cancer staging. *Br J Surg*. 2000;87(9):1215-21.
- Bakota EL, Aulisa L, Galler KM, Hartgerink JD. Enzymatic cross-linking of a nanofibrous peptide hydrogel. *Biomacromolecules*. 2011;12(1):82-7.
- Bakota EL, Sensoy O, Ozgur B, Sayar M, Hartgerink JD. Self-assembling multidomain peptide fibers with aromatic cores. *Biomacromolecules*. 2013;14(5):1370-8.
- Bakota EL, Wang Y, Danesh FR, Hartgerink JD. Injectable multidomain peptide nanofiber hydrogel as a delivery agent for stem cell secretome. *Soft Matter*. 2011;12:1651-7.

- Bancaud A, Beaudouin J, Ellenberg J, Huet S, Daigle N, Mozziconacci J. Molecular crowding affects diffusion and binding of nuclear proteins in heterochromatin and reveals the fractal organization of chromatin. *EMBO J.* 2009;28(24):3785-3798. <http://onlinelibrary.wiley.com/doi/10.1038/emboj.2009.340/abstract>. doi: 10.1038/emboj.2009.340.
- Banwell EF, Abelardo ES, Adams DJ, Birchall MA, Corrigan A, Donald AM, et al. Rational design and application of responsive α -helical peptide hydrogels. *Nat Mater.* 2009;8(7):596-600.
- Barbucci R. *Hydrogels*. Milan, Italy: Springer-Verlag; 2009.
- Barras FM, Pasche P, Bouche N, Aebischer P, Zurn AD. Glial cell line-derived neurotrophic factor released by synthetic guidance channels promotes facial nerve regeneration in the rat. *J Neurosci Res.* 2002;70:746-55.
- Baslé E, Joubert N, Pucheault M. Protein chemical modification on endogenous amino acids. *Chem Biol.* 2010;17(3):213-27.
- Beck K, Hunter I, Engel J. Structure and function of laminin: anatomy of a multidomain glycoprotein. *FASEB J.* 1990;4(2):148-60.
- Beglova N, LeSauter L, Ekiel I, Saragovi HU, Gehring K. Solution structure and internal motion of a bioactive peptide derived from nerve growth factor. *J Biol Chem.* 1998;273(37):23652-8.
- Beniash E, Hartgerink JD, Storrer H, Stendahl JC, Stupp SI. Self-assembling peptide amphiphile nanofiber matrices for cell entrapment. *Acta Biomater.* 2005;1:387-97.

- Bernardes GJL, Chalker JM, Errey JC, Davis BG. Facile conversion of cysteine and alkyl cysteines to dehydroalanine on protein surfaces: versatile and switchable access to functionalized proteins. *J Am Chem Soc.* 2008;130(15):5052-3.
- Bjugstad KB, Lampe K, Kern DS, Mahoney M. Biocompatibility of poly(ethylene glycol)-based hydrogels in the brain: an analysis of the glial response across space and time. *J Biomed Mater Res A* 2010;95(1):79-91.
- Bloch J, Fine EG, Bouche N, Zurn AD, Aebischer P. Nerve growth factor- and neurotrophin-3-releasing guidance channels promote regeneration of the transected rat dorsal root. *Exp Neurol.* 2001;172(2):425-32.
- Bramham CR, Messaoudi E. BDNF function in adult synaptic plasticity: The synaptic consolidation hypothesis. *Prog Neurobiol.* 2005;76:99-125.
- Brunner J. New photolabelling and crosslinking methods. *Annu Rev Biochem.* 1995;62:483-514.
- Burdick JA, Ward M, Liang E, Young MJ, Langer R. Stimulation of neurite outgrowth by neurotrophins delivered from degradable hydrogels. *Biomaterials.* 2006;27(3):452-9.
- Cambon K, Hansen SM, Venero C, Herrero AI, Skibo G, Berezin V, et al. A synthetic neural cell adhesion molecule mimetic peptide promotes synaptogenesis, enhances presynaptic function, and facilitates memory consolidation. *J Neurosci.* 2004;24(17):4197-204.
- Cao H, Liu T, Chew SY. The application of nanofibrous scaffolds in neural tissue engineering. *Adv Drug Deliv Rev.* 2009;61:1055-64.
- Caprini A, Silva D, Zanoni I, Cunha C, Volontè C, Vescovi A, et al. A novel bioactive peptide: assessing its activity over murine neural stem cells and its potential for neural tissue engineering. *N Biotechnol.* 2013;30(5):552.

- Ceulemans A, Zgavc T, Kooijman R, Hachimi-Idrissi S, Sarre S, Michotte Y. The dual role of the neuroinflammatory response after ischemic stroke: modulatory effects of hypothermia. *J Neuroinflammation*. 2010;7(1):74.
- Chalker JM, Bernardes GJ, Lin YA, Davis BG. Chemical modification of proteins at cysteine: opportunities in chemistry and biology. *Chem Asian J*. 2009;4(5):630-40.
- Chau Y, Luo Y, Cheung ACY, Nagai Y, Zhang S, Kobler James B, et al. Incorporation of a matrix metalloproteinase-sensitive substrate into self-assembling peptides - A model for biofunctional scaffolds. *Biomaterials*. 2008;29:1713-9.
- Chau Y, Luo Y, Cheung ACY, Nagai Y, Zhang S, Kobler JB, et al. Incorporation of a matrix metalloproteinase-sensitive substrate into self-assembling peptides - A model for biofunctional scaffolds. *Biomaterials*. 2008;29:1713-9.
- Chen G, Heim A, Riether D, Yee D, Milgrom Y, Gawinowicz MA, et al. Reactivity of functional groups on the protein surface: development of epoxide probes for protein labeling. *J Am Chem Soc*. 2003;125(27):8130-3.
- Cheng AL, Hsu CH, Lin JK, Hsu MM, Ho YF, Shen TS, et al. Phase I clinical trial of curcumin, a chemopreventive agent, in patients with high-risk orpre-malignant lesions. *Anticancer Res*. 2001;21(4B):2895-900.
- Cheng TY, Chen MH, Chang WH, Huang MY, Wang TW, Neural stem cells encapsulated in a functional self-assembled peptide hydrogel for brain tissue engineering, *Biomaterials* 2013;8:2005–2016.

- Chohan MO, Li B, Blanchard J, Tung Y, Heaney AT, Rabe A, et al. Enhancement of dentate gyrus neurogenesis, dendritic and synaptic plasticity and memory by a neurotrophic peptide. *Neurobiol Aging*. 2011;32(8):1420-34.
- Choi S, Park J, Lee K, Lee S, Jeon WB. Improved neural progenitor cell proliferation and differentiation on poly(lactide-co-glycolide) scaffolds coated with elastin-like polypeptide. *J Biomed Mater Res Part B Appl Biomater*. 2013;101(8):1329-39.
- Chonopoulou L, Togni AR, Guarguaglini G, Masci G, Glammaruco F, Togni GI, Palocci C. Self-assembling peptide hydrogels promote microglia cells proliferation and NGF production. *Soft Matter* 2012;8:5784-5790.
- Chung W, Merzlyak A, Yoo SY, Lee S. Genetically engineered liquid-crystalline viral films for directing neural cell growth. *Langmuir*. 2010;26(12):9885.
- Cigognini D, Satta A, Colleoni B, Silva D, Donegà M, Antonini S, et al. Evaluation of early and late effects into the acute spinal cord injury of an injectable functionalized self-assembling scaffold. *PloS one*. 2011;6(5):e19782.
- Cooke MJ, Zahir T, Phillips SR, Shah DSH, Athey D, Lakey JH, et al. Neural differentiation regulated by biomimetic surfaces presenting motifs of extracellular matrix proteins. *J Biomed Mater Res A*. 2010;93(3):NA.
- Costa A. Hausdorff (box-counting) fractal dimension, 2011. <<http://www.mathworks.com/MATLABcentral/fileexchange/30329-hausdorff--box-counting--fractal-dimension>>
- Creasey RG, Voelcker NH, Schultz CJ. Investigation of self-assembling proline- and glycine-rich recombinant proteins and peptides inspired by proteins from a symbiotic fungus using

- atomic force microscopy and circular dichroism spectroscopy. *Biochim Biophys Acta*. 2012;1824:711-22.
- Cuello AC, Bruno M, Leon W. P3-380: A β -induced nerve growth factor trophic disconnection in Alzheimer's disease. *Alzheimers Dement*. 2008;4(4):T633.
- Cui G, Shao S, Yang J, Liu J, Guo H. Designer self-assemble peptides maximize the therapeutic benefits of neural stem cell transplantation for Alzheimer's disease via enhancing neuron differentiation and paracrine action. *Mol Neurobiol*. 2015.
- Cunha C, Panseri S, Villa O, Silva D, Gelain F. 3D culture of adult mouse neural stem cells within functionalized self-assembling peptide scaffolds. *Int J Nanomedicine*. 2011;6:943-55.
- Dai W, Belt J, Saltzman WM. Cell-binding peptides conjugated to poly(ethylene glycol) promote neural cell aggregation. *Nat Biotechnol*. 1994;12:797-801.
- Dallérac G, Zerwas M, Novikova T, Callu D, Leblanc-Veyrac P, Bock E, et al. The neural cell adhesion molecule-derived peptide FGL facilitates long-term plasticity in the dentate gyrus in vivo. *Learn Memory*. 2011;18(5):306-13.
- Dawes JC, *Biological techniques for transmission and scanning electron microscopy*. Ladd Research Industries, Inc. 1984.
- Debeir T, Saragovi HU, Cuello AC. A nerve growth factor mimetic TrkA antagonist causes withdrawal of cortical cholinergic boutons in the adult rat. *Proc Natl Acad Sci*. 1999;96(7):4067-72.
- del Pozo-Rodríguez A, Pujals S, Delgado D, Solinís MA, Gascón AR, Giralt E, et al. A proline-rich peptide improves cell transfection of solid lipid nanoparticle-based non-viral vectors. *J Control Release*. 2008;133(2009):52-9.

- Dhoot NO, Tobias CA, Fischer I, Wheatley MA. Peptide-modified alginate surfaces as a growth permissive substrate for neurite outgrowth. *J Biomed Mater Res A*. 2004;71A(2):191-200.
- Dong H, Paramonov SE, Aulisa L, Bakota EL, Hartgerink JD. Self-assembly of multidomain peptides: balancing molecular frustration controls conformation and nanostructure. *J Am Chem Soc*. 2007;129(41):12468-72.
- Duconseille E, Woerly S, Kelche C, Will B, Cassel J-C. Polymeric hydrogels placed into a fimbria-fornix lesion cavity promote fiber (re)growth: A morphological study in the rat. *RestorNeurol Neuros* 1998;13:193-203.
- Durbeej M. Laminins. *Cell Tissue Res*. 2010;339:259-68.
- Ellis-Behnke RG, Liang Y, You S, Tay DKC, Zhang S, So K, et al. Nano neuro knitting: peptide nanofiber scaffold for brain repair and axon regeneration with functional return of vision. *PNAS*. 2006;103(13):5054-9.
- Englander O, Oates W, Paravastu A, Cheng L. An effective continuum approach for modeling non-equilibrium structural evolution of protein nanofiber networks. *J Chem Phys*. 2011;135(5):15. <http://dx.doi.org/10.1063/1.3622489>. doi: 10.1063/1.3622489.
- Fatin-Rouge N, Starchev K, Buffle J. Size effects on diffusion processes within agarose gels. *Biophysical Journal*. 2004;86(5):2710-9.
- Fernández-Carneado J, Kogan MJ, Castel S, Giralt E. Potential peptide carriers: amphipathic proline-rich peptides derived from the N-terminal domain of γ -zein. *Angw Chem Int Ed*. 2004;43:1811-4.

- Ferrari D, Los M, Bauer MKA, Vandenabeele P, Wesselborg S, Schulze-Osthoff K. P2Z purinoreceptor ligation induces activation of caspases with distinct roles in apoptotic and necrotic alterations of cell death. *FEBS Lett.* 1999;447(1):71-5.
- Fichman G, Gazit E. Self-assembly of short peptides to form hydrogels: design of buildingblocks, physical properties and technological applications. *Acta Biomater.* 2014;10:1671-82.
- Fine EG, Decosterd I, Papalioezos M, Zurn AD, Aebischer P. GDNF and NGF released by synthetic guidance channels support sciatic nerve regeneration across a long gap. *Eur J Neurosci.* 2002;15(4):589-601.
- Fine SM, Maggirwar SB, Elliott PR, Epstein LG, Gelbard HA, Dewhurst S. Proteasome blockers inhibit TNF- α release by lipopolysaccharide stimulated macrophages and microglia: implications for HIV-1 dementia. *J Neuroimmunol.* 1999;95(1):55-64.
- Flaim CJ, Chien S, Bhatia SN. An extracellular matrix microarray for probing cellular differentiation. *Nat Methods* 2005;2(2):119–125.
- Flavin MP, Zhao G, Ho LT. Microglial tissue plasminogen activator (tPA) triggers neuronal apoptosis in vitro. *Gila.* 2000;29(4):347-54.
- Fonseca KB, Granja PL, Barrias CC. Engineering proteolytically-degradable artificial extracellular matrices. *Prog Polym Sci.* 2014;39:2010-29.
- French P. Hausdorff dimension by the box counting method. 2007. <<http://www.mathworks.com/MATLABcentral/fileexchange/15918-hausdorff-dimension-by-the-box-counting-method>>

- Gagnon P, Huang X, Therrien E, Keillor JW. Peptide coupling of unprotected amino acids through in situ p-nitrophenyl ester formation. *Tetrahedron Lett.* 2002;43:7717-9.
- Galler KM, Aulisa L, Regan KR, D'Souza RN, Hartgerink JD. Self-assembling multidomain peptide hydrogels: designed susceptibility to enzymatic cleavage allows enhanced cell migration and spreading. *J Am Chem Soc.* 2010;132(9):3217.
- Gallin, JL, Snyderman R. *Inflammation basic principles and clinical correlates* 1999. 3rd ed. Raven Press, New York.
- Garcia-Bennett AE, Kozhevnikova M, König N, Zhou C, Leao R, Knöpfel T, et al. Delivery of differentiation factors by mesoporous silica particles assists advanced differentiation of transplanted murine embryonic stem cells. *Stem Cells Transl Med.* 2013;2(11):906-15.
- Geckil H, Xu F, Zhang X, Moon S, Demirci U. Engineering hydrogels as extracellular matrix mimics. *Nanomedicine.* 2010 April;5(3):469-84.
- Gelain F, Bottai D, Vescovi A, Zhang S, Designer self-assembling peptide nanofiber scaffolds for adult mouse neural stem cell 3-dimensional cultures, *PLoS ONE* 2006;1(1): e119
- Gelain F, Cigognini D, Caprini A, Silva D, Colleoni B, Donegá M, et al. New bioactive motifs and their use in functionalized self-assembling peptides for NSC differentiation and neural tissue engineering. *Nanoscale.* 2012;4:2946-57.
- Gelain F, Panseri S, Antonini S, Cunha C, Donega M, Lowery J, et al. Transplantation of nanostructured composite scaffolds results in the regeneration of chronically injured spinal Cords. *ACS Nano.* 2011;5(1):227-36.

- Gelain F, Silva D, Caprini A, Taraballi F, Natalello A, Villa O, et al. BMHP1-derived self-assembling peptides: hierarchically assembled structures with self-healing propensity and potential for tissue engineering applications. *ACS nano*. 2011;5(3):1845.
- Gelain F, Unsworth LD, Zhang S. Slow and sustained release of active cytokines from self-assembling peptide scaffolds RID A-7231-2011. *J Controlled Release*. 2010;145(3):231-9.
- Gomes C, Ferreira R, George J, Sanches R, Rodrigues DI, Gonçalves N, Cunha RA. Activation of microglial cells triggers a release of brain-derived neurotrophic factor (BDNF) inducing their proliferation in an adenosine A_{2A} receptor-dependent manner: A_{2A} receptor blockade prevents BDNF release and proliferation of microglia. *J Neuroinflammation* 2013;10:16.
- Gomes ME, Reis RL. Biodegradable polymers and composites in biomedical applications: from catgut to tissue engineering. *Int Mater Rev*. 2004;49(5):261-73.
- Görizt C, Dias DO, Tomilin N, Barbacid M, Shupliakov O, Frisén J. A pericyte origin of spinal cord scar tissue. *Science*. 2011;333:238-42.
- Griess P. Bemerkungen zu der Abhandlung der HH. Weselsky und Benedikt "Uebereinige Azoverbindungen". *Berichte Dtsch Chem Ges* 1989;12:426-428.
- Groblewska M, Mroczko B, Gryko M, Pryczynicz A, Guzińska-Ustymowicz K, Kędra B, et al. Serum levels and tissue expression of matrix metalloproteinase 2 (MMP-2) and tissue inhibitor of metalloproteinases 2 (TIMP-2) in colorectal cancer patients. *Tumor Biol*. 2014 January;35:3793-802.
- Grothe C, Haastert K, Jungnickel J. Physiological function and putative therapeutic impact of the FGF-2 system in peripheral nerve regeneration — lessons from in vivo studies in mice and rats. *Brain Res*. 2006;51(2):293-9.

Gundlach HG, Moore S, Stein WH. The reaction of iodoacetate with methionine. *J Biol Chem.* 1959;234(7):1761-4.

Guo J, Leung KKG, Su H, Yuan Q, Wang L, Chu T, et al. Self-assembling peptide nanofiber scaffold promotes the reconstruction of acutely injured brain. *Nanomedicine.* 2009;5(3):345-51.

Guo J, Su H, Zeng Y, Liang Y, Wong WM, Ellis-Behnke RG, et al. Reknitting the injured spinal cord by self-assembling peptide nanofiber scaffold. *Nanomedicine.* 2007;3(4):311-21.

Haller MF, Saltzman WM. Nerve growth factor delivery systems. *J Control Release.* 1998;53:1-6.

Hamley IW. Self-assembly of amphiphilic peptides. *Soft Matter.* 2011;7:4122-38.

Hansen U, Bruckner P. Macromolecular specificity of collagen fibrillogenesis: fibrils of collagens I and XI contain a heterotypic alloyed core and a collagen I sheath. *J Biol Chem.* 2003 September 26;278(39):37352-9.

Harston GWJ, Tee YK, Blockley N, Okell TW, Thandeswaran S, Shaya G, et al. Identifying the ischaemic penumbra using pH-weighted magnetic resonance imaging. *Brain.* 2015;138(1):36-42.

Hartgerink JD, Beniash E, Stupp SI. Self-assembly and mineralization of peptide-amphiphile nanofibers. *Science.* 2001;294:23.

Hashimoto M, Hatanaka Y. Recent progress in diazirine-based photoaffinity labeling. *Eur J Org Chem.* 2008(15):2513-23.

Hausdorff F. Dimension und äußeres Maß. *Mathematische Annalen.* 1919;79:157-9.

- Hauser CAE, Zhang S. Designer self-assembling peptide nanofiber biological materials. *Chem Soc Rev*. 2010 August;39(8):2780-90.
- Hinojosa AE, Borja GB, Juan CL, Madrigal JLM. CCL2/MCP-1 modulation of microglial activation. *J Neuroinflammation* 2011;8:77.
- Hiraoka M, Kato K, Nakaji-Hirabayashi T, Iwata H. Enhanced survival of neural cells embedded in hydrogels composed of collagen and laminin-derived cell adhesive peptide. *Bioconjugate Chem*. 2009;20(5):976-83.
- Hoare TR, Kohane DS. Hydrogels in drug delivery: Progress and challenges. *Polymer*. 2008;Volume 49(Number 8):1993-2007.
- Hochman-Mendez C, Cantini M, Moratal D, Salmeron-Sanchez M, Coelho-Sampaio T. A fractal nature for polymerized laminin. *PloS one*. 2014;9(10):e109388.
- Hoffman AS. Hydrogels for biomedical applications. *Adv Drug Deliv Rev*. 2012;64:18-23.
- Hollis ER, Tuszynski MH. Neurotrophins: potential therapeutic tools for the treatment of spinal cord injury. *Neurotherapeutics*. 2011;8:694-703.
- Holmes TC, de Lacalle S, Su X, Liu G, Rich A, Zhang S. Extensive neurite outgrowth and active synapse formation on self-assembling peptide scaffolds. *PNAS*. 2000;97(12):6728-33.
- Holmes TC. Novel peptide-based biomaterial scaffolds for tissue engineering. *Trends Biotechnol* 2002;20(1):16-21.
- Hooker JM, Esser-Kahn AP, Francis MB. Modification of aniline containing proteins using an oxidative coupling strategy. *J Am Chem Soc*. 2006;128(49):15558-9.

Hooker JM, Kovacs EW, Francis MB. Interior surface modification of bacteriophage MS2. *J Am Chem Soc.* 2004;126(12):3718-9.

Hosseinkhani H, Hiraoka Y, Li C, Chen Y, Yu D, Hong P, et al. Engineering three-dimensional collagen-IKVAV matrix to mimic neural microenvironment. *ACS Chem Neurosci.* 2013;4(8):1229-35.

Houweling DA, Lankhorst AJ, Gispen WH, Bär PR, Joosten EAJ. Collagen containing neurotrophin-3 (NT-3) attracts regrowing injured corticospinal axons in the adult rat spinal cord and promotes partial functional recovery. *Exp Neurol.* 1998;153(1):49-59.

Hu Q, Katti PS, Gu Z. Enzyme-responsive nanomaterials for controlled drug delivery. *Nanoscale.* 2014;6:12273-86.

Huang EJ, Reichardt LF. Neurotrophins: roles in neuronal development and function. *Annu Rev Neurosci.* 2001;24:677-736.

Huang L, Wu Z, Zhuge Q, Zheng W, Shao B, Wang B, et al. Glial scar formation occurs in the human brain after ischemic stroke. *Int J Med Sci.* 2014;11(4):344.

Hule R, Nagarkar R, Hammouda B, Schneider J, Pochan D. Dependence of self-assembled peptide hydrogel network structure on local fibril nanostructure. *Macromolecules.* 2009;42(18):7137-45.

Ichiyama T, Campbell IL, Furukawa S, Catania A, Lipton JM. Autocrine α -melanocyte-stimulating hormone inhibits NF- κ B activation in human glioma. *J Neurosci Res.* 1999;58(5):684-9.

Ishii K, Nakamura M, Dai H, Finn TP, Okano H, Toyama Y, et al. Neutralization of ciliary neurotrophic factor reduces astrocyte production from transplanted neural stem cells and

- promotes regeneration of corticospinal tract fibers in spinal cord injury. *Journal of Neuroscience Research*. 2006 December;84(8):1669-81.
- Itoh S, Matsuda A, Kobayashi H, Ichinose S, Shinomiya K, Tanaka J. Effects of a laminin peptide (YIGSR) immobilized on crab-tendon chitosan tubes on nerve regeneration. *J Biomed Mater Res Part B Appl Biomater*. 2005;73B(2):375-82.
- Iwasaki M, Wilcox JT, Nishimura Y, Zweckberger K, Suzuki H, Wang J, et al. Synergistic effects of self-assembling peptide and neural stem/progenitor cells to promote tissue repair and forelimb functional recovery in cervical spinal cord injury. *Biomaterials*. 2013;35:2617-29.
- Jacobson J, Kiselyov V, Bock E, Berezin V. A peptide motif from the second Fibronectin module of the neural cell adhesion molecule, NCAM, NLIKQDDGGSPIRHY, is a binding site for the FGF receptor. *Neurochem Res*. 2008;33(12):2532-9.
- Janeway CA, Travers P, Walport M, Shlomchik MJ. Responses to alloantigens and transplant rejection. In: *Immunobiology: the immune system in health and disease*. New York: Garland Science; 2001.
- Jelinek HF, Elston N, Zietsch B. Fractal analysis: pitfalls and revelations in neuroscience. In: Alt W, editor. *Fractals in biology and medicine mathematics and biosciences in interaction*. ; 2005. p. 85-94.
- Jenkins P, Laughter M, Lee D, Lee Y, Freed C, Park D. A nerve guidance conduit with topographical and biochemical cues: potential application using human neural stem cells. *Nanoscale Res Lett*. 2015;10(1):1-7.

- Jeon WB, Park BH, Choi SK, Lee K, Park J. Functional enhancement of neuronal cell behaviors and differentiation by elastin-mimetic recombinant protein presenting Arg-Gly-Asp peptides. *BMC Biotechnol.* 2012;12(1):61.
- Jha RK, Chakraborti S, Kern TL, Fox DT, Strauss CEM. Rosetta comparative modeling for library design: Engineering alternative inducer specificity in a transcription factor. *Proteins.* 2015;83:1327-40.
- Jiang X, Namura S, Nagata I. Matrix metalloproteinase inhibitor KB-R7785 attenuates brain damage resulting from permanent focal cerebral ischemia in mice. *Neurosci Lett.* 2001;305(1):41-4.
- Joester A, Faissner A. The structure and function of tenascins in the nervous system. *Matrix Biol.* 2001;20(1):13-22.
- Jucker M, Kleinman HK, Ingram DK. Fetal rat septal cells adhere to and extend processes on basement membrane, laminin, and a synthetic peptide from the laminin A chain sequence. *J Neurosci Res.* 1991;28:507-17.
- Kabiri M, Bushnak I, McDermot MT, Unsworth LD. Toward a mechanism of ionic self-complementary self-assembly: role of water molecules and ions. *Biomacromolecules* 2013;14(11):3943-3950.
- Kafi MA, Kim T, Kim H, Yea C, Choi J. Effects of nanopatterned RGD peptide layer on electrochemical detection of neural cell chip. *Biosens Bioelectron.* 2010;26(4):1359-65.
- Kakimura J, Kitamura Y, Takata K, Umeki M, Suzuki S, Shibagaki K, et al. Microglia activation and amyloid- β clearance induced by exogenous heat-shock proteins. *FASEB J.* 2002;16(6):601-3.

- Kam L, Shain W, Turner JN, Bizios R. Selective adhesion of astrocytes to surfaces modified with immobilized peptides. *Biomaterials*. 2002;23(2):511-5.
- Kelamangalath L, Smith GM. Neurotrophin treatment to promote regeneration after traumatic CNS injury. *Front Biol*. 2013;8(5):486-95.
- Kenny GD, Bienemann AS, Tagalakis AD, Pugh JA, Welser K, Campbell F, et al. Multifunctional receptor-targeted nanocomplexes for the delivery of therapeutic nucleic acids to the brain. *Biomaterials*. 2013;34:9190-200.
- Kettenmann H, Hanisch UK, Noda M, Verkhaty A. Physiology of microglia. *Physiological Reviews* 2011;91(2):461-553
- Kim D, Martin DC. Sustained release of dexamethasone from hydrophilic matrices using PLGA nanoparticles for neural drug delivery. *Biomaterials*. 2006;27(15):3031-7.
- Kim J, Chu HS, Park KI, Won J, Jang J. Elastin-like polypeptide matrices for enhancing adeno-associated virus-mediated gene delivery to human neural stem cells. *Gene Ther*. 2012;19(3):329.
- Kim SI, Na H, Ding Y, Wang Z, Lee SJ, Choi ME. Autophagy promotes intracellular degradation of type I collagen induced by transforming growth factor (TGF)- $1\beta^*$. *J Biol Chem*. 2012;287(15):11677-88.
- Kim Y, Ho SO, Gassman NR, Korlann Y, Landorf EV, Collart FR, et al. Efficient site-specific labeling of proteins via cysteines. *Bioconjugate Chem*. 2008;19(3):786-91.
- Kingham PJ, Pocock JM. Microglial secreted cathepsin B induces neuronal apoptosis. *Journal of Neurochemistry*. 2001;76(5):1475-84.

- Kiryushko D, Kofoed T, Skladchikova G, Holm A, Berezin V, Bock E. A synthetic peptide ligand of neural cell adhesion molecule (NCAM), C3d, promotes neuritogenesis and synaptogenesis and modulates presynaptic function in primary cultures of rat hippocampal neurons. *J Biol Chem.* 2003;278(14):12325-34.
- Kiselyov VV, Skladchikova G, Hinsby AM, Jensen PH, Kulahin N, Soroka V, et al. Structural basis for a direct Interaction between FGFR1 and NCAM and evidence for a regulatory role of ATP. *Structure.* 2003;11(6):691-701.
- Kisiday J, Jin M, Kurz B, Hung H, Semino C, Zhang SG. Self-assembling peptide hydrogel fosters chondrocyte extracellular matrix production and cell division: implications for cartilage tissue repair. *Proc Natl Acad Sci U S A* 2002;99(15):9996-10001.
- Knight GT, Sha J, Ashton RS. Micropatterned, clickable culture substrates enable in situ spatiotemporal control of human PSC-derived neural tissue morphology. *Chem Commun.* 2015;51:5238-41.
- Knowles JR. Photogenerated reagents for biological receptor-site labeling. *Acc Chem Res.* 1972;5(4):155-60.
- Koenigsknecht J, Landreth G. Microglial phagocytosis of fibrillar β -amyloid through a β_1 integrin-dependent mechanism. *The J Neuroscience* 2002;24(44):9838-9846.
- Kogan M, Dalcol I, Gorostiza P, Lopez-Iglesias C, Pons R, Pons M, et al. Supramolecular properties of the proline-rich γ -zein N-terminal domain. *Biophys J.* 2002;83:1194-204.
- Könnecke H, Bechmann I. The role of microglia and matrix metalloproteinases involvement in neuroinflammation and gliomas. *Clin Dev Immunol.* 2013;2013:914104.

- Korsmeyer RW. Diffusion controlled systems: hydrogels. In: Tarcha PJ, editor. *Polymers for controlled drug delivery*. CRC Press Inc.; 1991.
- Koutsopoulos S, Zhang SG. Long-term three-dimensional neural tissue cultures in functionalized self-assembling peptide hydrogels, Matrigel and Collagen I. *Acta Biomater*. 2012;xxx:xxx.
- Kyle S, Aggeli A, Ingham E, McPherson MJ. Production of self-assembling biomaterials for tissue engineering. *Trends Biotechnol*. 2009;27(7):423-33.
- Lai AY, Todd KG. 2006. Hypoxia-activated microglial mediators of neuronal survival are differentially regulated by tetracyclines. *Glia* 2006;53:809–816.
- Lakhan SE, Kirchgessner A, Hofer M. Inflammatory mechanisms in ischemic stroke: therapeutic approaches. *J Transl Med*. 2009;7(1):97.
- Lakshmanan A, Cheong DW, Accardo A, Fabrizio ED, Riekkel C, Hauser CAE. Aliphatic peptides show similar self-assembly to amyloid core sequences, challenging the importance of aromatic interactions in amyloidosis. *Proc Nat AcadSci* 2013;110(2):519-524.
- Laterra J, Keep R, Betz LA, Goldstein GW. Blood-brain barrier. In: Siegel GJ, Agranoff BW, Albers RW, Fisher SK, Uhler MD, editors. *Basic neurochemistry: molecular, cellular and medical aspects*, 6th edition. Philadelphia: Lippincott-Raven; 1999. p. 763.
- Lau LW, Cua R, Keough MB, Haylock-Jacobs S, Yong VW. Pathophysiology of the brain extracellular matrix: a new target for remyelination. *Nat Rev Neurosci* 2013;14:722-9.
- Law B, Tung C. Proteolysis: A biological process adapted in drug delivery, therapy, and imaging. *Bioconjugate Chem*. 2009;20(9):1683-965.
- Law B, Tung C. Structural modification of protease inducible preprogrammed nanofiber precursor. *Biomacromolecules*. 2008;9(2):421-5.

- Lee KY, Mooney DJ. Hydrogels for Tissue Engineering. *Chem Rev.* 2001;101(7):1869-78.
- Leonardo GC, Eakin AK, Ajmo JM, Gottschall PE. Vesican and brevian and expressed with distinct pathology in neonatal hypoxic-ischemic injury. *Journal of Neuroscience Research* 2008;86:1106-14
- Lévesque SG, Shoichet MS. Synthesis of enzyme-degradable, peptide-cross-linked dextran hydrogels. *Bioconjugate Chem.* 2007;18(3):874-85.
- Li B, Wanka L, Blanchard J, Liu F, Chohan MO, Iqbal K, et al. Neurotrophic peptides incorporating adamantane improve learning and memory, promote neurogenesis and synaptic plasticity in mice. *FEBS Lett.* 2010;584(15):3359-65.
- Li Q, Chau Y. Neural differentiation directed by self-assembling peptide scaffolds presenting laminin-derived epitopes. *J Biomed Mater Res A.* 2010;94(3):688-99.
- Li R, Kong Y, Ladisch S. Nerve growth factor-induced neurite formation in PC12 cells is independent of endogenous cellular gangliosides. *Glycobiology.* 1998;8(6):597-603.
- Liu Y, Ye H, Satkunendrarajah K, Yao GS, Bayon Y, Fehlings MG. A self-assembling peptide reduces glial scarring, attenuates post-traumatic inflammation and promotes neurological recovery following spinal cord injury. *Acta Biomater.* 2013;9:8075-88.
- Livnah O, Bayer EA, Wilchek M, Sussman JL. Three-dimensional structures of avidin and the avidin-biotin complex. *Biochemistry.* 1993;90:5079-80.
- Lomander A, Hwang W, Zhang S. Hierarchical self-assembly of a coiled-coil peptide into fractal structure. *Nano Lett.* 2005;5.
- Lonardo, E. Parish, C. L., Ponticelli S, Marasco D, Ribeiro D, Ruvo M, Falco SD, et al. A small synthetic cripto blocking peptide improves neural induction, dopaminergic differentiation,

- and functional integration of mouse embryonic stem cells in a rat model of Parkinson's disease. *Stem Cells*. 2010;28:1326-37.
- Lopes R, Betrouni N. Fractal and multifractal analysis: A review. *Med Image Anal*. 2009;13:634-49.
- Lu P, Yang H, Jones LL, Filbin MT, Tuszynski MH. Combinatorial therapy with neurotrophins and cAMP promotes axonal regeneration beyond sites of spinal cord injury. *J Neurosci*. 2004;24(28):6402-9.
- Lucivero V, Prontera M, Mezzapesa DM, Petruzzellis M, Sancilio M, Tinelli A, et al. Different roles of matrix metalloproteinases-2 and -9 after human ischaemic stroke. *Neurol Sci*. 2013 December 1;28:165-70.
- Luo C, Sun J, Sun B, He Z. Prodrug-based nanoparticulate drug delivery strategies for cancer therapy. *Trends Pharmacol Sci*. 2014;35(11):556-66.
- MacArthur MW, Thornton JM. Influence of proline residues on protein conformation. *J Mol Biol*. 1991;218(2):397-412. <http://www.ncbi.nlm.nih.gov/pubmed/2010917>. doi: 10.1016/0022-2836(91)90721-H.
- MacEwan SR, Chilkoti A. Applications of elastin-like polypeptides in drug delivery. *J Control Release*. 2014;190:314-30.
- MacPhee CE, Woolfson DN. Engineered and designed peptide-based fibrous biomaterials. *Curr Opin Solid State Mater Sci*. 2004;8(2):141-9.
- Madduri S, Gander B. Growth factor delivery systems and repair strategies for damaged peripheral nerves. *J Control Release*. 2012;161:274-82.

- Mahler A, Reches M, Rechter M, Cohen S, Gazit E. Rigid, self-assembled hydrogel composed of a modified aromatic dipeptide. *Adv Mater*. 2006;18(11):1365-70.
- Markó K, Kohidi T, Hádinger N, Jelitai M, Mezo G, Madarász E. Isolation of radial glia-like neural stem cells from fetal and adult mouse forebrain via selective adhesion to a novel adhesive peptide-conjugate. *PloS one*. 2011;6(12):e28538.
- Massa SM, Yang T, Xie Y, Shi J, Bilgen M, Joyce JN, et al. Small molecule BDNF mimetics activate TrkB signaling and prevent neuronal degeneration in rodents. *J Clin Invest*. 2010;120(5):1774-85.
- Massia SP, Holecko MM, Ehteshami GR. In vitro assessment of bioactive coatings for neural implant applications. *J Biomed Mater Res A*. 2004;68A(1):177-86.
- Masuda T, Sakuma C, Kobayashi K, Kikuchi K, Soda E, Shiga T, et al. Laminin peptide YIGSR and its receptor regulate sensory axonal response to the chemoattractive guidance cue in the chick embryo. *J Neurosci Res*. 2009;87(2):353-9.
- Matsushita Y, Nakajima K, Tokyama Y, Kurihara T, Kohsaka S. Activation of microglia by endotoxin suppresses the secretion of glial cell line-derived neurotrophic factor (GDNF) through the action of protein kinase C α (PKC α) and mitogen-activated protein kinases (MAPKs). *J Neuroscience Research* 2008;86:1959-1971.
- Matsuzawa M, Weight FF, Potember RS, Liesi P. Directional neurite outgrowth and axonal differentiation of embryonic hippocampal neurons are promoted by a neurite outgrowth domain of the B2-chain of laminin. *Int J Devl Neuroscience*. 1996;14(3):283-95.
- Maude S, Ingham E, Aggeli A. Biomimetic self-assembling peptides as scaffolds for soft tissue engineering. *Nanomedicine*. 2013;8(5):823-47.

- Mayet N, Choonara YE, Kumar P, Tomar LK, Tyagi C, Du Toit LC, et al. A comprehensive review of advanced biopolymeric wound healing systems. *J Pharm Sci.* 2014 August;103(8):2211-30.
- McDaniel JR, Radford DC, Chilkoti A. A unified model for de novo design of elastin-like polypeptides with tunable inverse transition temperatures. *Biomacromolecules.* 2013;14(8):2866-72.
- McFarland JM, Francis MB. Reductive alkylation of proteins using iridium catalyzed transfer hydrogenation. *J Am Chem Soc.* 2005;127(39):13490-1.
- Mehban N, Zhu B, Tamagnini F, Young FI, Wasmuth A, Hudson KL, et al. Functionalized α -helical peptide hydrogels for neural tissue engineering. *ACS Biomater Sci Eng.* 2015;1(6):431-9.
- Meiners S, Nur-e-Kamal MSA, Mercado MLT. Identification of a neurite outgrowth-promoting motif within the alternatively spliced region of human Tenascin-C. *J Neurosci.* 2001;21(18):7215.
- Mercado MLT, Nur-e-Kamal A, Liu H, Gross SR, Movahed R, Meiners S. Neurite outgrowth by the alternatively spliced region of human Tenascin-C is mediated by neuronal $\alpha 7\beta 1$ integrin. *J Neurosci.* 2004;24(1):238-47.
- Milner R, Campbell IL, Cytokines regulate microglial adhesion to laminin and astrocyte extracellular matrix via protein kinase c-dependent activation of the $\alpha 6\beta 1$ integrin. *The J Neuroscience* 2002;22(5):1562-1572.
- Minchiotti G. Nodal-dependant Cripto signaling in ES cells: from stem cells to tumor biology. *Oncogene.* 2005;24(37):5668-75.

- Mithieux SM, Tu Y, Korkmaz E, Braet F, Weiss AS. *In situ* polymerization of tropoelastin in the absence of chemical cross-linking. *Biomaterials* 2009;30:431-435.
- Miyagi M, Rao KCS. Proteolytic ¹⁸O-Labeling Strategies for Quantitative Proteomics. *Mass Spectrom Rev.* 2007;26:121-36.
- Monera OD, Sereda TJ, Zhou NE, Kay CM, Hodges RS. Relationship of sidechain hydrophobicity and alpha-helical propensity on the stability of the single-stranded amphipathic alpha-helix. *J Pept Sci.* 1995;1(5):319-29.
- Montague PR, Friedlander MJ. Expression of an intrinsic growth strategy by mammalian retinal neurons. *Proc Natl Acad Sci U S A.* 1989;86:7223-7.
- Moore K, MacSween M, Shoichet M. Immobilized concentration gradients of neurotrophic factors guide neurite outgrowth of primary neurons in macroporous scaffolds. *Tissue eng.* 2006;12(2):267-78.
- Mura S, Nicolas J, Couvreur P. Stimuli-responsive nanocarriers for drug delivery. *Nat Mater.* 2013;12(11):991.
- Nagase H, Fields GB. Human matrix metalloproteinase specificity studies using collagen sequence-based synthetic peptides. *Biopolymers.* 1996;40:399-416.
- Nagase H, Woessner JF. Matrix metalloproteinases. *J Biol Chem.* 1999 July 30;274(31):21491-4.
- Naghdi P, Tiraihi T, Ganji F, Darabi S, Taheri T, Kazemi H. Survival, proliferation and differentiation enhancement of neural stem cells cultured in three-dimensional polyethylene glycol RGD hydrogel with tenascin. *J Tissue Eng Regen Med.* 2014:n/a.

- Nakajima K, Shimojo M, Hamanoue M, Ishiura S, Sugita H, Kohsaka S. Identification of elastase as a secretory protease from cultured rat microglia. *J Neurochem.* 1992;58(4):1401-8.
- Nakajima K, Tsuzaki N, Shimojo M, Hamanoue M, Kohsaka S. Microglia isolated from rat brain secrete a urokinase-type plasminogen activator. *Brain Res.* 1992;577(2):285-92.
- Nakamura Y, Si QS, Kataoka K. Lipopolysaccharide-induced microglia activation in culture: temporal profiles of morphological change and release of cytokines and nitric oxide. *Neurosci Res* 1999;35(2):95-100.
- Nakanishi H. Microglial functions and proteases. *Mol Neurobiol.* 2003;27:163-76.
- Nakanishi H. Microglial proteases: strategic targets for neuroprotective agents. *Curr Neuropharmacol.* 2003;1(1):99-108.
- Neiendam JL, Køhler LB, Chistensen C, Li S, Pedersen MV, Ditlevsen DK, et al. An NCAM-derived FGF-receptor agonist, the FGL-peptide, induces neurite outgrowth and neuronal survival in primary rat neurons. *J Neurochem.* 2004;91(4):920-35.
- Netzel-Arnett S, Sang QX, Moore WG, Navre M, Birkedal-Hansen H, Van Wart HE. Comparative sequence specificities of human 72- and 92-kDa gelatinases (type IV collagenases) and PUMP (matrilysin). *Biochemistry.* 1993 June 29;32(25):6427-32.
- Nguyen MK, Lee DS. Injectable biodegradable hydrogels. *MacromolBiosci* 2010;10:563-579.
- Niece KL, Hartgerink JD, Donners, Jack J J M, Stupp SI. Self-assembly combining two bioactive peptide-amphiphile molecules into nanofibers by electrostatic attraction. *J Am Chem Soc.* 2003;125(24):7146-7.

- Nielsen J, Gotfryd K, Li S, Kulahin N, Soroka V, Rasmussen KK, et al. Role of glial cell line-derived neurotrophic factor (GDNF)-neural Cell adhesion molecule (NCAM) interactions in induction of neurite outgrowth and identification of a binding site for NCAM in the heel region of GDNF. *J Neurosci.* 2009;29(36):11360.
- Nishioku T, Hashimoto K, Yamashita K, Liou S, Kagamiishi Y, Maegawa H, et al. Involvement of cathepsin E in exogenous antigen processing in primary cultured murine microglia. *J Biol Chem.* 2002;277(7):4816-22.
- Nowakowski GS, Dooner MS, Valinski HM, Mihaliak AM, Quesenberry PJ, Becker PS. A specific heptapeptide from a phage display peptide library homes to bone marrow and binds to primitive hematopoietic stem cells. *Stem Cells.* 2004;22:1030-8.
- Ogo S, Uehara K, Abura T, Fukuzumi S. pH-dependent chemoselective synthesis of α -amino acids. Reductive amination of α -keto acids with ammonia catalyzed by acid-stable iridium hydride complexes in water. *J Am Chem Soc.* 2004;126:3020-1.
- Oh HH, Lu H, Kawazoe N, Chen G. Differentiation of PC12 cells in three-dimensional collagen sponges with micropatterned nerve growth factor. *Biotechnol Prog.* 2012 May;28(3):773-9.
- Ojo B, Rezaie P, Gabbott PL, Cowely TR, Medvedev NI, Lynch MA, et al. A neural cell adhesion molecule-derived peptide, FGL, attenuates glial cell activation in the aged hippocampus. *Exp Neurol.* 2011;232:318-28.
- O'Leary PD, Hughes RA. Design of potent peptide mimetics of brain-derived neurotrophic factor. *J Biol Chem.* 2003;278(28):25738-44.
- Ontaneda D, Rae-Grant A. Management of acute exacerbations in multiple sclerosis. *Ann Indian Acad Neurol.* 2009;12(4):264-72.

- Orive G, Anitua E, Pedraz JL, Emerich DF. Biomaterials for promoting brain protection, repair and regeneration. *Nat Rev Neurosci.* 2009;10(10):682-92.
- Pal D, Chakrabarti P. Cis peptide bonds in proteins: Residues involved, their conformations, interactions and locations. *J Mol Biol.* 1999;294(1):271.
<http://www.ingentaconnect.com/content/ap/mb/1999/00000294/00000001/art03217>.
- Palsler AL, Norman AL, Saffell JL, Reynolds R. Neural cell adhesion molecule stimulates survival of premyelinating oligodendrocytes via the fibroblast growth factor receptor. *J Neurosci Res.* 2009;87(15):NA.
- Pankov R, Yamada K. Fibronectin at a glance. *J Cell Sci.* 2002;115:3861-563.
- Parish CL, Arenas E. Stem-cell-based strategies for the treatment of Parkinson's disease. *Neurodegenerative Dis.* 2007;4:339-47.
- Parmar M, Skogh C, Björklund A, Campbell K, Regional specification of neurosphere cultures derived from subregions of the embryonic telencephalon, *Mol Cell Neurosci* 2002;21:645–656.
- Pearse DD, Pereira FC, Marcillo AE, Bates ML, Berrocal YA, Filbin MT, et al. cAMP and Schwann cells promote axonal growth and functional recovery after spinal cord injury. *Nat Med.* 2004;10(6):610-6.
- Peluffo H, González P, Arís A, Acarin L, Saura J, Villaverde A, et al. RGD domains neuroprotect the immature brain by a glial-dependent mechanism. *Ann Neurol.* 2007;62(3):251-61.
- Peppas NA, Hilt JZ, Khademhosseini A, Langer R. Hydrogels in biology and medicine: From molecular principles to bionanotechnology. *Adv Mater*2006;18:1345-1360.

- Petanceska S, Canoll P, Devi LA. Expression of rat cathepsin S in phagocytic cells. *J Biol Chem.* 1996;271(8):4403-9.
- Peters A, Brey DM, Burdick JA. High-throughput and combinatorial technologies for tissue engineering applications. *Tissue Eng Part B Rev.* 2009 September;15(3):225-39.
- Piantino J, Burdick JA, Goldberg D, Langer R, Benowitz LI. An injectable, biodegradable hydrogel for trophic factor delivery enhances axonal rewiring and improves performance after spinal cord injury. *Exp Neurol.* 2006;201(2):359-67.
- Pittman RN, Williams AG. Neurite penetration into collagen gels requires Ca²⁺-dependent metalloproteinase activity. *Dev Neurosci.* 1989;11(1):41-51.
- Polikov VS, Tresco PA, Reichert WM. Response to brain tissue to chronically implanted neural electrodes. *J. Neurosci. Meth.* 2005;148:1-18
- Powell SK, Rao J, Roque E, Nomizu M, Kuratomi Y, Yamada Y, et al. Neural cell response to multiple novel sites on laminin-1. *J Neurosci Res.* 2000;61(3):302-12.
- Prestwich GD. Hyaluronic acid-based clinical biomaterials derived for cell and molecule delivery in regenerative medicine. *J. Control. Release* 2011;155:193-199.
- Qiu WQ, Walsh DM, Ye Z, Vekrellis K, Zhang J, Podlisny MB, et al. Insulin-degrading enzyme regulates extracellular levels of amyloid b-protein by degradation. *J Biol Chem.* 1998;273:32730-8.
- Qiu WQ, Ye Z, Kholodenko D, Seubert P, Selkoe DJ. Degradation of amyloid β -protein by a metalloprotease secreted by microglia and other neural and non-neural cells. *J Biol Chem.* 1997;272(10):6641-6.

- Ramos-Cabrer P, Campos F, Sobrino T, Castillo J. Targeting the ischemic penumbra. *Stroke*. 2011;42(1 Suppl):S11.
- Raspa A, Saracino GAA, Pugliese R, Silva D, Cigognini D, Vescovi A, et al. Complementary co-assembling peptides: from In silico studies to in vivo application. *Adv Funct Mater*. 2014;24(40):6317-28.
- Reichardt LF. Neurotrophin-regulated signalling pathways. *Phil Trans R Soc B*. 2006;361(1473):1545-64.
- Rodríguez-Seguí S, Pla-Roca M, Engel E, Planell J, Martínez E, Samitier J. Influence of fabrication parameters in cellular microarrays for stem cell studies. *J Mater Sci: Mater Med*. 2009 July;20(7):1525-33.
- Romanic AM, White RF, Arleth AJ, Ohlstein EH, Frank C B. Matrix metalloproteinase expression increases after cerebral focal ischemia in rats: inhibition of matrix metalloproteinase-9 reduces Infarct size. *Stroke*. 1998;29(5):1020-30.
- Romano NH, Madl CM, Heilshorn SC. Matrix RGD ligand density and L1CAM-mediated Schwann cell interactions synergistically enhance neurite outgrowth. *Acta Biomater*. 2015;11:48-57.
- Romano NH, Sengupta D, Chung C, Heilshorn SC. Protein-engineered biomaterials: nanoscale mimics of the extracellular matrix. *Biochim Biophys Acta*. 2011;1810(3):339-49.
- Romero MI, Rangappa N, Garry MG, Smith GM. Functional regeneration of chronically injured sensory afferents into adult spinal cord after neurotrophin gene therapy. *J of Neurosci*. 2001;21(21):8408-16.

- Rosenberg GA, Estrada EY, Dencoff JE. Matrix metalloproteinases and TIMPs are associated with blood-brain barrier opening after reperfusion in rat brain. *Stroke*. 1998;29(10):2189.
- Rozners E. Recent advances in chemical modification of peptide nucleic acids. *J Nucleic Acids*. 2012;2012:518162-8.
- Ruoslahti E. RGD and other recognition sequences for integrins. *Annu Rev Cell Dev Biol*. 1996;12(1):697-715.
- Russmann V, Seeger N, Zellinger C, Hadamitzky M, Pankratova S, Wendt H, et al. The CNTF-derived peptide mimetic Cintrofin attenuates spatial-learning deficits in a rat post-status epilepticus model. *Neurosci Lett*. 2013;556:170-5.
- Ryan RE, Sloane BF, Sameni M, Wood PL. Microglial cathepsin B: an immunological examination of cellular and secreted species. *J Neurochem*. 1995;65(3):1035-45.
- Salic A, Mitchison TJ. A chemical method for fast and sensitive detection of DNA synthesis *in vivo*. *Proc Nat AcadSci* 2008;105(7):2416-2420.
- Santoso S, Hwang W, Hartman H, Zhang S. Self-assembly of surfactant-like peptides with variable glycine tails to form nanotubes and nanovesicles. *Nano Lett*. 2002;2(7):687-91.
- Saracino GA, Gelain F. Modelling and analysis of early aggregation events of BMHP1-derived self-assembling peptides. *J Biomol Struct Dyn*. 2014;32(5):759-75.
- Schense JC, Hubbell JA. Three-dimensional migration of neurites is mediated by adhesion site density and affinity. *J Biol Chem*. 2000;275(10):6813-8.
- Schlick TL, Ding Z, Kovacs EW, Francis MB. Dual-surface modification of the tobacco mosaic virus. *J Am Chem Soc*. 2005;127(11):3718-23.

- Schneider A, Garlick JA, Egles C. Self-assembling peptide nanofiber scaffolds accelerate wound healing. *PloS one*. 2008;3(1):e1410.
- Secher T, Novitskaia V, Berezin V, Bock E, Glenthøj B, Klementiev B. A neural cell adhesion molecule-derived fibroblast growth factor receptor agonist, the FGL-peptide, promotes early postnatal sensorimotor development and enhances social memory retention. *Neuroscience*. 2006;141(3):1289-99.
- Segal RA, Greenberg ME. Intracellular signaling pathways activated by neurotrophic factors. *Annual review of neuroscience*. 1996;19(1):463-89.
- Semino CE, Kasahara J, Hayashi Y, Zhang S. Entrapment of migrating hippocampal neural cells in three-dimensional peptide nanofiber scaffold. *Tissue Eng*. 2004;10(3-4):643-55.
- Seow WY, Hauser CAE. Short to ultrashort peptide hydrogels for biomedical uses. *Mater Today*. 2014;17(8):381-8.
- Shaikh AK, Mohammad QD, Ullah MA, Ahsan MM, Rahman A, Shakoor MA. Effect of dexamethasone on brain oedema following acute ischemic stroke. *Mymensingh Med J*. 2011;20(3):450-8.
- Shamji MF, Jing L, Chen J, Hwang P, Ghodsizadeh O, Friedman AH, et al. Treatment of neuroinflammation by soluble tumor necrosis factor receptor Type II fused to a thermally responsive carrier. *J Neurosurg Spine*. 2008;9(2):221-8.
- Shamji MF, Whitlatch L, Friedman AH, Richardson WJ, Chilkoti A, Setton LA. An injectable and in situ-gelling biopolymer for sustained drug release following perineural administration. *Spine*. 2008;33(7):748-54.

- Shields DC, Schaecher KE, Saido TC, Banik NL. A putative mechanism of demyelination in multiple sclerosis by a proteolytic enzyme, calpain. PNAS. 1999;96(20):11486-91.
- Shields DC, Tyor WR, Deibler GE, Hogan EL, Banik NL. Increased calpain expression in activated glial and inflammatory cells in experimental allergic encephalomyelitis. PNAS. 1998;95(10):5768-72.
- Shin MK, Kim HG, Kim KL. A novel trimeric peptide, Neuropep-1-stimulating brain-derived neurotrophic factor expression in rat brain improves spatial learning and memory as measured by the Y-maze and Morris water maze. J Neurochem. 2011;116:205-16.
- Shu XZ, Ahmad S, Liu YC, Prestwich GD. Synthesis and evaluation of injectable, *in situ* crosslinkable synthetic extracellular matrices for tissue engineering. J Biomed Mater Res A2006;79:902-912.
- Siao, C-J, Tsirka, SE, Tissue plasminogen activator mediates microglia activation via its finger domain through annexin II, Neurosci 2002;22:3352–3358.
- Siegel GJ, Chauhan NB. Neurotrophic factors in Alzheimer's and Parkinson's disease brain. Brain Res Rev. 2000;33:199-227.
- Silva D, Natalello A, Sani B, et al. Synthesis and characterization of designed BMHP1-derived self-assembling peptides for tissue engineering applications. Nanoscale. 2013;5:704-718. <http://search.credoreference.com/content/entry/igidictist/nanoscale>.
- Silva GA, Czeisler C, Niece KL, Beniash E, Harrington DA, Kessler JA, Stupp SI, Selective differentiation of neural progenitor cells by high-epitope density nanofibers, Science 2004;303:1352–1355.

- Sinclair SM, Bhattacharyya J, McDaniel JR, Gooden DM, Gopaldaswamy R, Chilkoti A, et al. A genetically engineered thermally responsive sustained release curcumin depot to treat neuroinflammation. *J Control Release*. 2013;171:38-47.
- Singh A, Thornton ER, Westheimer FH. The photolysis of diazoacetylchymotrypsin. *J Biol Chem*. 1962;237(9):PC3008.
- Singh HD, Bushnak I, Unsworth LD. Engineered peptides with enzymatically cleavable domains for controlling the release of model protein drug from “soft” nanoparticles. *Acta Biomater*. 2012(8):636-45.
- Skaper SD. The biology of neurotrophins, signalling pathways, and functional peptide mimetics of neurotrophins and their receptors. *CNS Neurol Disord Drug Targets*. 2008;7(1):46-62.
- Soille P, Rivest J. On the validity of fractal dimension measurements in image analysis. *J Vis Commun Image Represent*. 1996;7(3):217-29.
- Soroka V, Kiryushko D, Novitskaya V, Rønn LCB, Poulsen FM, Holm A, et al. Induction of neuronal differentiation by a peptide corresponding to the homophilic binding site of the second Ig module of the neural cell adhesion molecule. *J Biol Chem*. 2002;277(27):24676-83.
- Spicer CD, Davis BG. Selective chemical protein modification. *Nat Commun*. 2014;5:4740.
- Sporns O, Edelman GM, Crossin KL. The neural cell adhesion molecule (N-CAM) inhibits proliferation in primary cultures of rat astrocytes. *Proc Natl Acad Sci*. 1995;92(2):542-6.
- Stephanopoulos N, Freeman R, North HA, Sur S, Jeong SJ, Tantakitti F, et al. Bioactive DNA-peptide nanotubes enhance the differentiation of neural stem cells into neurons. *Nano Lett*. 2015;15(1):603.

- Stewart DE, Sarkar A, Wampler JE. Occurrence and role of cis peptide bonds in protein structures. *J Mol Biol.* 1990;214(1):253-260. <http://www.sciencedirect.com/science/article/pii/002228369090159J>. doi: 10.1016/0022-2836(90)90159-J.
- Stohwasser R, Giesebrecht J, Kraft R, Müller E, Häusler KG, Kettenmann H, et al. Biochemical analysis of proteasomes from mouse microglia: Induction of immunoproteasomes by interferon- γ and lipopolysaccharide. *Glia.* 2000;29(4):355-65.
- Strizzi L, Bianco C, Normanno N, Salomon D. Cripto-1: a multifunctional modulator during embryogenesis and oncogenesis. *Oncogene.* 2005;24(37):5731-41.
- Stupp SI. Biomaterials for regenerative medicine. *MRS Bull* 2005;30(7):546-53.
- Sun PZ, Zhou J, Sun W, Huang J, van Zijl, Peter C M. Detection of the ischemic penumbra using pH-weighted MRI. *J Cereb Blood Flow Metab.* 2007;27(6):1129-36.
- Sun W, Incitti T, Migliaresi C, Quattrone A, Casarosa S, Motta A. Viability and neuronal differentiation of neural stem cells encapsulated in silk fibroin hydrogel functionalized with an IKVAV peptide. *J Tissue Eng Regen Med.* 2015.
- Sun W, Valloran JJ, Zabara A, Mezzenga R. Controlling enzymatic activity and kinetics in swollen mesophases by physical nano- confinement†. *Nanoscale.* 2014;6:6853-9.
- Suzumura A, Marunouchi T. Morphological transformation of microglia *in vitro*. *Brain Research* 1991;545:301-306.
- Szabo M, Gulya K. Development of the microglial phenotype in culture. *Neuroscience* 2013;241:280-295.

- Tagalakis AD, Lee DHD, Bienemann AS, Zhou H, Munye MM, Saraiva L, et al. Multifunctional, self-assembling anionic peptide-lipid nanocomplexes for targeted siRNA delivery. *Biomaterials*. 2014;35:8406-15.
- Takai N, Nakanishi H, Tanabe K, Nishioku T, Sugiyama T, Fujiwara M, et al. Involvement of caspase-like proteinases in apoptosis of neuronal PC12 cells and primary cultured microglia induced by 6-hydroxydopamine. *J Neurosci Res*. 1998;54(2):214-22.
- Tanaka Y, Kohler JJ. Photoactivatable crosslinking sugars for capturing glycoprotein interactions. *J Am Chem Soc*. 2008;130(11):3278-9.
- Taraballi F, Natalello A, Campione M, Villa O, Doglia SM, Paleari A, et al. Glycine-spacers influence functional motifs exposure and self-assembling propensity of functionalized substrates tailored for neural stem cell cultures. *Front Neuroeng*. 2010;3:NA.
- Tatham AS, Shewry PR. Elastomeric proteins: biological erties and functions. Abductin forms the. *TIBS*. 2000;25:567-71.
- Tavakol S, Saber R, Hoveizi E, Aligholi H, Ai J, Rezayat SM. Chimeric self-assembling nanofiber containing bone marrow homing peptide's motif induces motor neuron recovery in animal model of chronic spinal cord injury; an in vitro and in vivo investigation. *Mol Neurobiol*. 2015.
- Teng KK, Angelastro JM, Cunningham ME, Greene LA. Cultured PC12 cells chapter 21: a model for neuronal function, differentiation, and survival. In: *Cell Biology*. Elsevier Inc.; 2006. p. 171-6.
- Theiler J. Estimating fractal dimension. *J Opt Soc Am A*. 1990;7(6):1055-73.

- Thelen K, Kedar V, Panicker AK, Schmid R, Midkiff BR, Maness PF. The neural cell adhesion molecule L1 potentiates integrin-dependent cell migration to extracellular matrix proteins. *J Neurosci*. 2002;22(12):4918.
- Thid D, Holm K, Eriksson PS, Ekeröth J, Kasemo B, Gold J. Supported phospholipid bilayers as a platform for neural progenitor cell culture. *J Biomed Mater Res A*. 2008;84A(4):940-53.
- Thundilmadathil J. Click chemistry in peptide science: a mini-review. Synthesis of clickable peptides and applications. *Chemistry Today*. 2013;31(2):34-7.
- Tilley SD, Francis MB. Tyrosine-selective protein alkylation using π -allylpalladium complexes. *J Am Chem Soc*. 2006;128:1080-1.
- Timpl R, Rohde H, Robey PG, Rennard SI, Foidart JM, Martin GR. Laminin--a glycoprotein from basement membranes. *J Biol Chem*. 1979;254(19):9933.
- Tiwari G, Tiwari R, Sriwastawa B, Bhati L, Pandey S, Pandey P, et al. Drug delivery systems: An updated review. *Int J Pharm Investig*. 2012 March;2(1):2-11.
- Toh WS, Loh XJ. Advances in hydrogel delivery systems for tissue regeneration. *Mater Sci Eng C Mater Biol Appl*. 2014;45:690-7.
- Tomaselli KJ, Damsky CH, Reichardt LF. Interactions of a neuronal cell line (PC12) with laminin, collagen IV, and fibronectin: identification of integrin-related glycoproteins involved in attachment and process outgrowth. *J Cell Biol*. 1987;105:2347-58.
- Tsikis D. Analysis of nitrite and nitrate in biological fluids by assays based on the Griess reaction: appraisal of the Griess reaction in the L-arginine/nitric oxide area of research. *J Chromatogr B Analyt Technol Biomed Life Sci* 2007;851:51–70.

- Turk BE, Huang LL, Piro ET, Cantley LC. Determination of protease cleavage site motifs using mixture-based oriented peptide libraries. *Nat Biotechnol.* 2001 July;19(7):661-7.
- Tutton MG, George ML, Eccles SA, Burton S, Swift RI, Abulafi AM. Use of plasma MMP-2 and MMP-9 levels as a surrogate for tumor expression in colorectal cancer patients. *Int J Cancer.* 2003 June;107:541-50.
- Tysseing-Mattiace VM, Sahni V, Niece KL, Birch D, Czeisler C, Fehlings MG, et al. Self-assembling nanofibers inhibit glial scar formation and promote axon elongation after spinal cord injury. *J Neurosci.* 2008;28(14):3814-23.
- Tzafriri AR, Bercovier M, Parnas H. Reaction Diffusion Model of the Enzymatic Erosion of Insoluble Fibrillar Matrices. *Biophys J.* 2002;83(2):776-93.
- Uhlig T, Kyprianou T, Martinelli FG, Oppici CA, Heiligers D, Hills D, Calvo XR, Varhaert P. The emergence of peptides in the pharmaceutical business: From exploration to exploitation. *EuPA.* 2014;4:58-69
- Ulery BD, Nair LS, Laurencin CT. Biomedical applications of biodegradable polymers. *J Polym Sci , Part B: Polym Phys.* 2011;49(12):832-64.
- Ulrich TA, de Juan Pardo EM, Kumar, S. The mechanical rigidity of the extracellular matrix regulates structure, motility, and proliferation of glioma cells. *Cancer Res* 2009;69(10):4167-74.
- Urry DW. Physical chemistry of biological free energy transduction as demonstrated by elastic protein-based polymers. *J Phys Chem B.* 1997;101:11007-28.

- Vauthey S, Santoso S, Gong H, Watson N, Zhang S. Molecular self-assembly of surfactant-like peptides to form nanotubes and nanovesicles. *Proc Natl Acad Sci U S A*. 2002 April 16;99(8):5355-60.
- von Maltzahn G, Vauthey S, Santoso S, Zhang S. Positively charged surfactant-like peptides self-assemble into nanostructures. *Langmuir*. 2003;19:4332-7.
- Wadhwa R, Lagenaur CF, Cui XT. Electrochemically controlled release of dexamethasone from conducting polymer polypyrrole coated electrode. *J Control Release*. 2006;110(3):531-41.
- Wang W, Chau Y. Self-assembled peptide nanorods as building blocks of fractal patterns. *Soft Matter*. 2009;5:4893-8.
- Weldon DT, Rogers SD, Ghilardi JR, Finke MP, Cleary, JP, O'Hare E, Esler WP, Maggio JE, Mantyh PW. Fibrillar β -amyloid induces nitric oxide synthase, and loss of a select population of neurons in rat CNS *in vivo*. *The J Neuroscience* 1998;18(6):2161-2173.
- Weledji EP, Assobb JC. The ubiquitous neural cell adhesion molecule (N-CAM). *Ann Med Surg (Lond)*. 2014;3(3):77-81.
- Wierzbicka-Patynowski I, Schwarzbauer JE. The ins and outs of fibronectin matrix assembly. *J Cell Sci*. 2003;116(16):3269-76.
- Willerth SM, Sakiyama-Elbert SE. Approaches to neural tissue engineering using scaffolds for drug delivery. *Adv Drug Deliv Rev*. 2007;59(4):325-38.
- Williams BAR, Chaput JC. Synthesis of peptide-oligonucleotide conjugates using a heterobifunctional crosslinker. *Curr Protoc Nucleic Acid Chem*. 2010;Chapter 4:Unit4.41.

- Williams CM, Engler AJ, Slone RD, Galante LL, Schwarzbauer JE. Fibronectin expression modulates mammary epithelial cell proliferation during acinar differentiation. *Cancer Res.* 2008;68(9):3185-92.
- Winter JO, Cogan SF, Rizzo JF. Neurotrophin-eluting hydrogel coatings for neural stimulating electrodes. *J Biomed Mater Res Part B Appl Biomater.* 2007;81B(2):551-63.
- Worthington P, Pochan DJ, Langhans SA. Peptide Hydrogels - Versatile Matrices for 3D Cell Culture in Cancer Medicine. *Front Oncol.* 2015;5:92.
- Wu S, Suzuki Y, Ejiri Y, Noda T, Bai h, Kitada M, Kataoka K, Ohta M, Chou H, Ide C, Bone marrow stromal cells enhance differentiation of cocultured neurosphere cells and promote regeneration of injured spinal cord, *J Neurosci Res* 2003;72:343–351.
- Yamada KM. Adhesive recognition sequences. *J Biol Chem.* 1991;266(20):12809.
- Yan Q, Yin Y, Li B. Use new PLGL-RGD-NGF nerve conduits for promoting peripheral nerve regeneration. *Biomed Eng Online.* 2012;11(1):36.
- Yao L, Damodaran G, Nikolskaya N, Gorman AM, Windebank A, Pandit A. The effect of laminin peptide gradient in enzymatically cross-linked collagen scaffolds on neurite growth. *J Biomed Mater Res A.* 2010;92(2):484-92.
- Yao L, Wang S, Cui W, Sherlock R, O'Connell C, Damodaran G, et al. Effect of functionalized micropatterned PLGA on guided neurite growth. *Acta Biomater.* 2009;5(2):580-8.
- Yoshida T, Lai TC, Kwon GS, Sako K. pH- and ion-sensitive polymers for drug delivery. *Expert Opin Drug Deliv.* 2013;10(11):1497-513.
- Yu TT, Shoichet MS. Guided cell adhesion and outgrowth in peptide-modified channels for neural tissue engineering. *Biomaterials.* 2005;26(13):1507-14.

- Yu X, Bellamkonda RV. Tissue-engineered scaffolds are effective alternatives to autografts for bridging peripheral nerve gaps. *Tissue eng.* 2003;9(3):421-30.
- Yurchenco P, Patton B. Developmental and pathogenic mechanisms of basement membrane assembly. *Curr Pharm Des.* 2009;15(12):1277-94.
- Zhang SG, Gelain F, Zhao X. Designer self-assembling peptide nanofiber scaffolds for 3D tissue cell cultures. *Semin Cancer Biol.* 2005 October;15(5):413-20.
- Zhang SG, Holmes T, Lockshin C, Rich A. Spontaneous assembly of a self-complementary oligopeptide to form a stable macroscopic membrane. *Proc Natl Acad Sci.* 1993;90:3334-8.
- Zhang SG, Holmes TC, DiPersio CM, Hynes RO, Su X, Rich A. Self-complementary oligopeptide matrices support mammalian cell attachment. *Biomaterials.* 1995 March 23;16:1385-93.
- Zhang SG. Fabrication of novel biomaterials through molecular self-assembly. *Nat Biotechnol.* 2003;21(10):1171-8.
- Zhang ZX, Zheng QX, Wu YC, Hao DJ. Compatibility of neural stem cells with functionalized self-assembling peptide scaffold *In vitro.* *Biotechnol Bioprocess Eng.* 2010;15:545-55.
- Zhao X, Zhang SG. Designer self-assembling peptide materials. *Macromol Biosci.* 2007 January 5;7(1):13-22.
- Zhong Y, Bellamkonda RV. Controlled release of anti-inflammatory agent α -MSH from neural implants. *J Control Release.* 2005;106(3):309-18.
- Zhou J, van Zijl P. Defining an acidosis-based ischemic penumbra from pH-weighted MRI. *Transl Stroke Res.* 2012;3(1):76-83.

Zhuang X, Xiang X, Grizzle W, Sun D, Zhang S, Axtell RC, et al. Treatment of brain inflammatory diseases by delivering exosome encapsulated anti-inflammatory drugs from the nasal region to the brain. *Mol Ther*. 2011;19(10):1769-79.

Zimmermann DR, Dours-Zimmermann MT. Extracellular matrix of the central nervous system from neglect to challenge. *Histochem Cell Biol* 2008;130:635-53.

Appendix A - Supplemental Figures

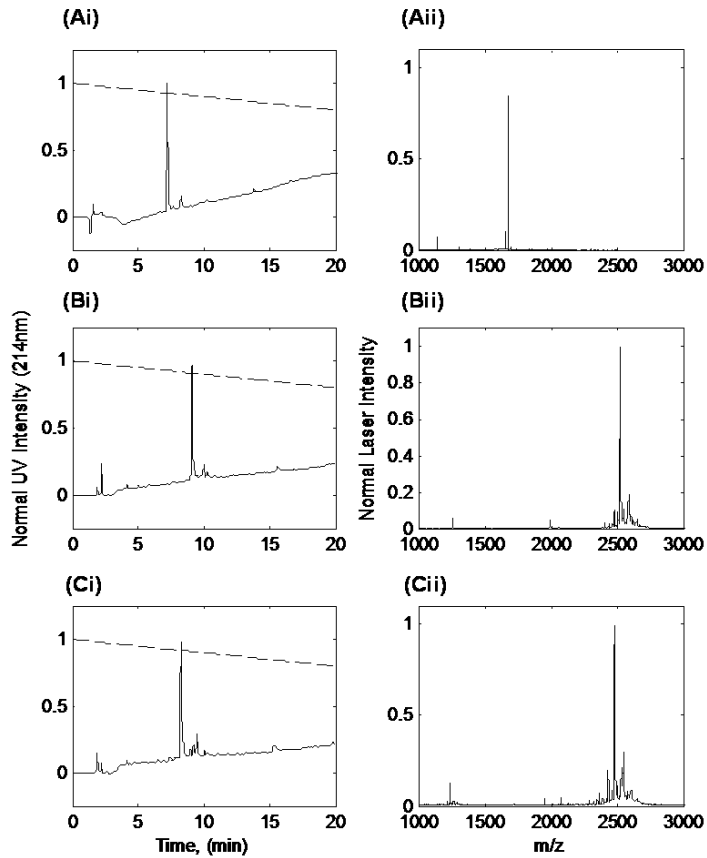


Figure A2.1. Representative (i) HPLC (i) and (ii) MALDI TOF/TOF mass spectrometry (ii) of purified peptide $(\text{RADA})_4$, $(\text{RADA})_4\text{-GG-GPQG+IASQ}$, and $(\text{RADA})_4\text{-GG-GPQG+PAGQ}$, shown in A, B, and C, respectively. Purities were determined to be above 95% by measuring the comparative areas under the major curve in the HPLC spectra. Major peaks in the MALDI spectra are at 1671.8, 2525.2, and 2478.8 m/z which reflect the theoretical molecular weights. All peaks were normalized to their respective maxima.

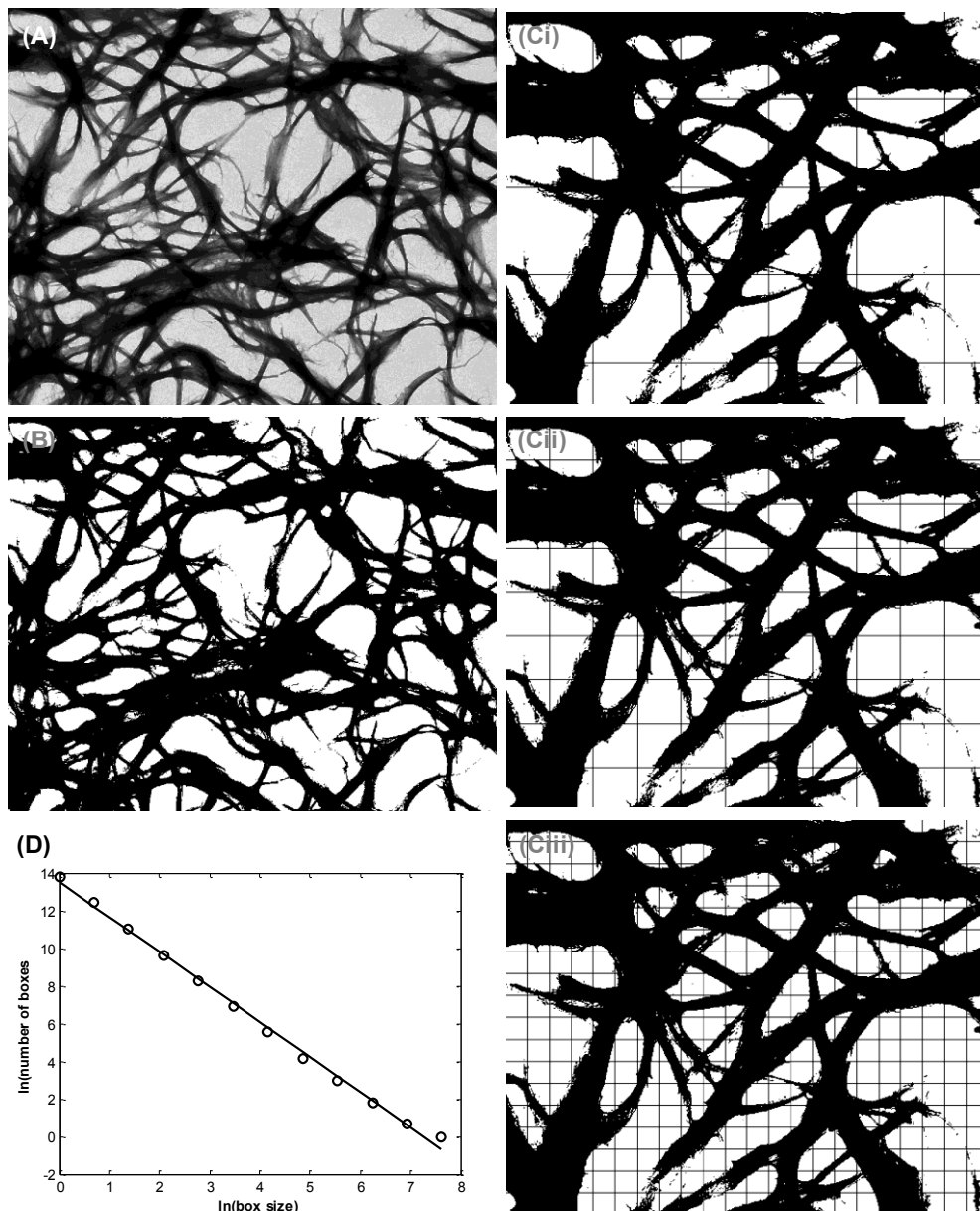


Figure A2.2. Example of image processing for Hausdorff boxcount method. (A) Transmission electron microscopy, (B) gray scale and background filtering off image (MATLAB functions `im2bw` and `imfill`), various grid sizes used to count pixels ($D(r)$) based on radius or dimension (r) for points of the box-count line, and a linear plot from the log of the box count curve. The negative slope of the linear curve is the box-count dimension (D_H), this dimension being 1.8.

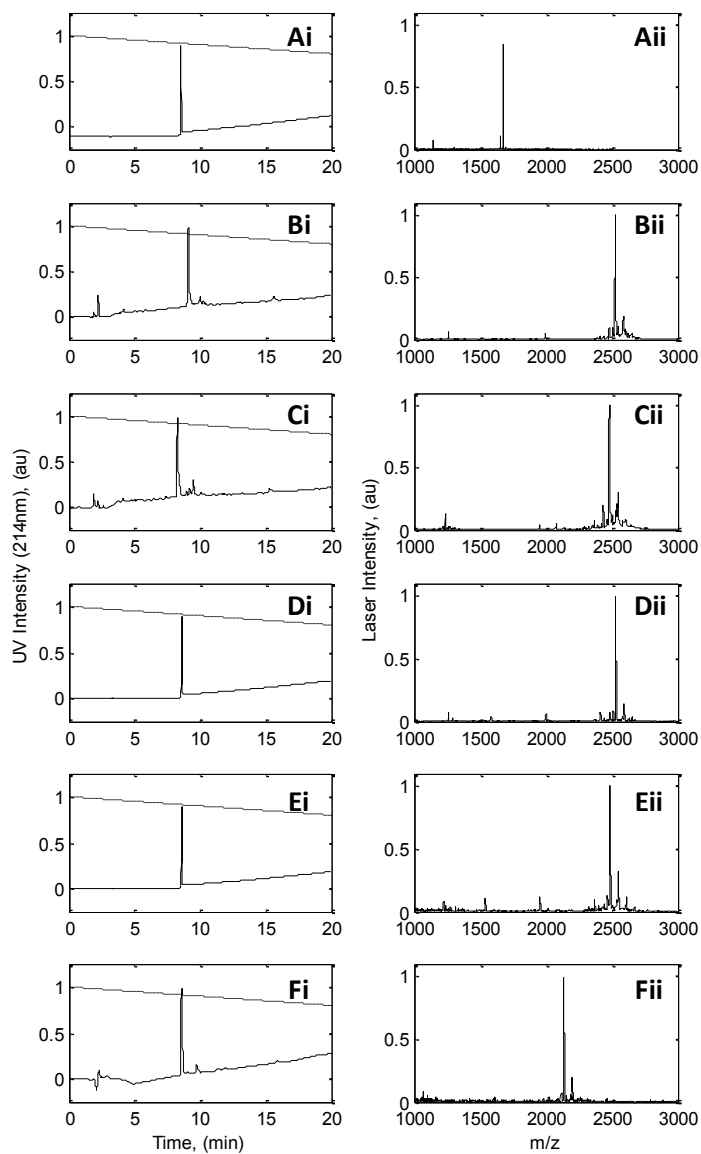


Figure A3.1. HPLC and MALDI TOF/TOF mass spectrometry, i and ii respectively, of purified peptide A) (RADA)₄, (B) (RADA)₄-GPQG+IASQ, (C) (RADA)₄-GPQG+PAGQ, (D) (RADA)₄-IQPGSAQG, (E) (RADA)₄-PQGAQGPG and (F) (RADA)₄-GPQG₈₊. Purities were determined to be above 95% by measuring the comparative areas under the major curve in the HPLC spectra. Respective major peaks in the MALDI spectra are at 1671.8, 2525.2, 2478.8, 2525.2, 2478.8, and 2132.1 m/z which reflect the theoretical molecular weights. All peaks were normalized to their respective maxima.

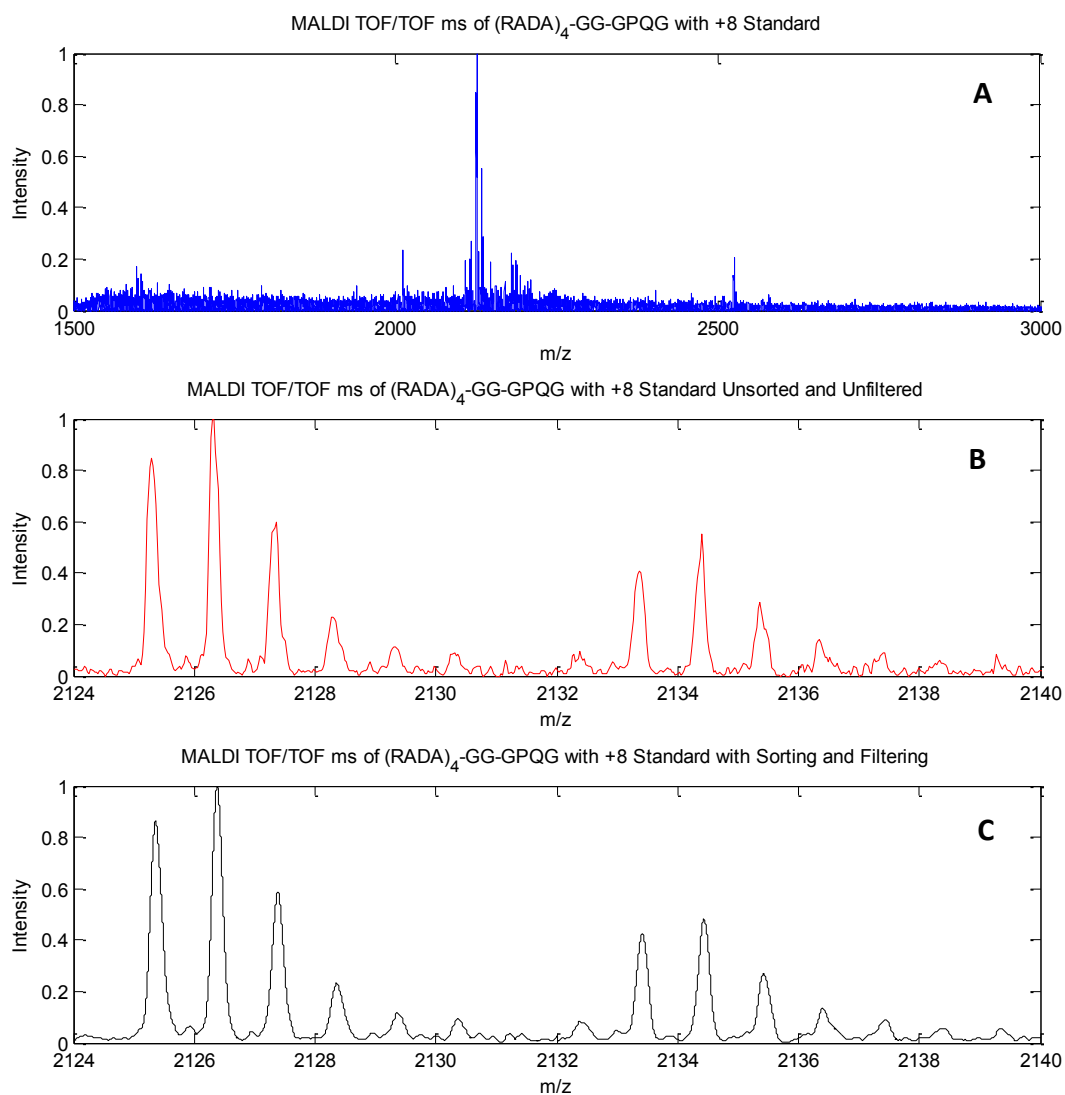


Figure A3.2. MALDI TOF/TOF mass spectrometry of worked example for enzyme product formation analysis. Raw spectra (A) of whole data set. Spectra of raw unfiltered data (B) in range of interest with product isotopic envelope (left) and standard envelope (right). Selected, filtered, and curve fitted spectra (C) where the area (trapezoidal rule) under the right envelope divided by the left equates to the product formed relative to the concentration of the standard.

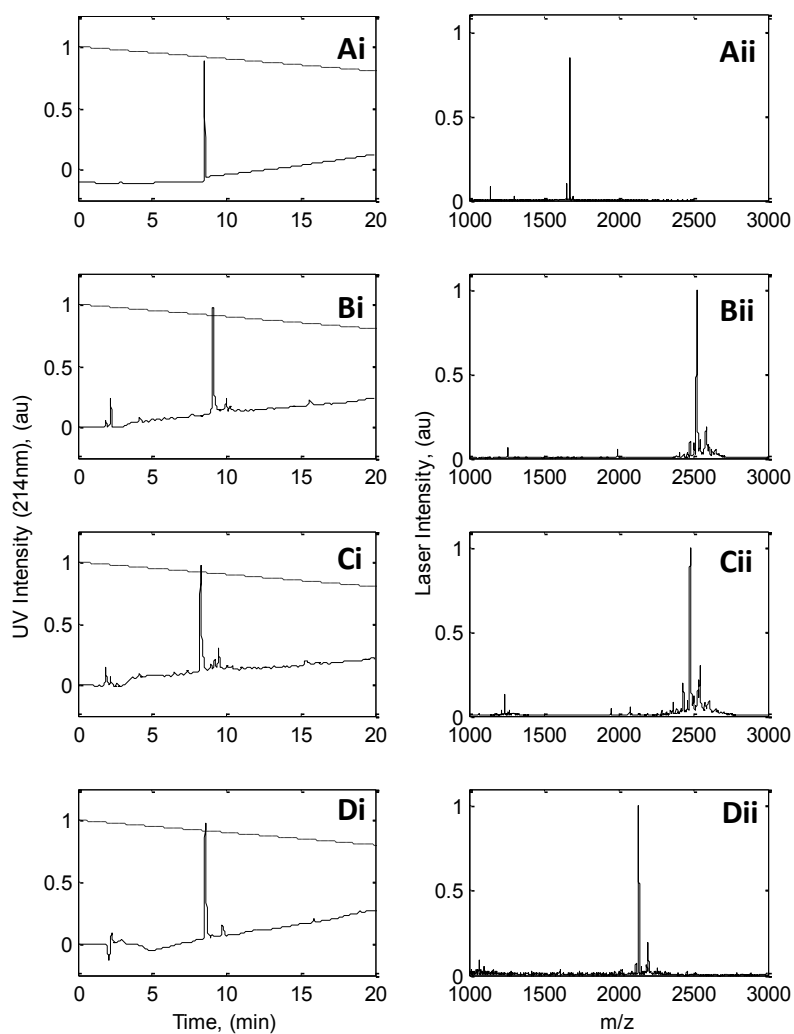


Figure A4.1. HPLC and MALDI TOF/TOF mass spectrometry, i and ii respectively, of purified peptide (RADA)₄ (A), (RADA)₄-GPQG+IASQ (B), (RADA)₄-GPQG+PAGQ (C), and (RADA)₄-GPQG₈₊ (D) shown in A, B, and C, respectively. Purities were determined to be above 95% by measuring the comparative areas under the major curve in the HPLC spectra. Respective major peaks in the MALDI spectra are at 1671.8, 2525.2, 2478.8, and 2132.1 m/z which reflect the theoretical molecular weights. All peaks were normalized to their respective maxima.

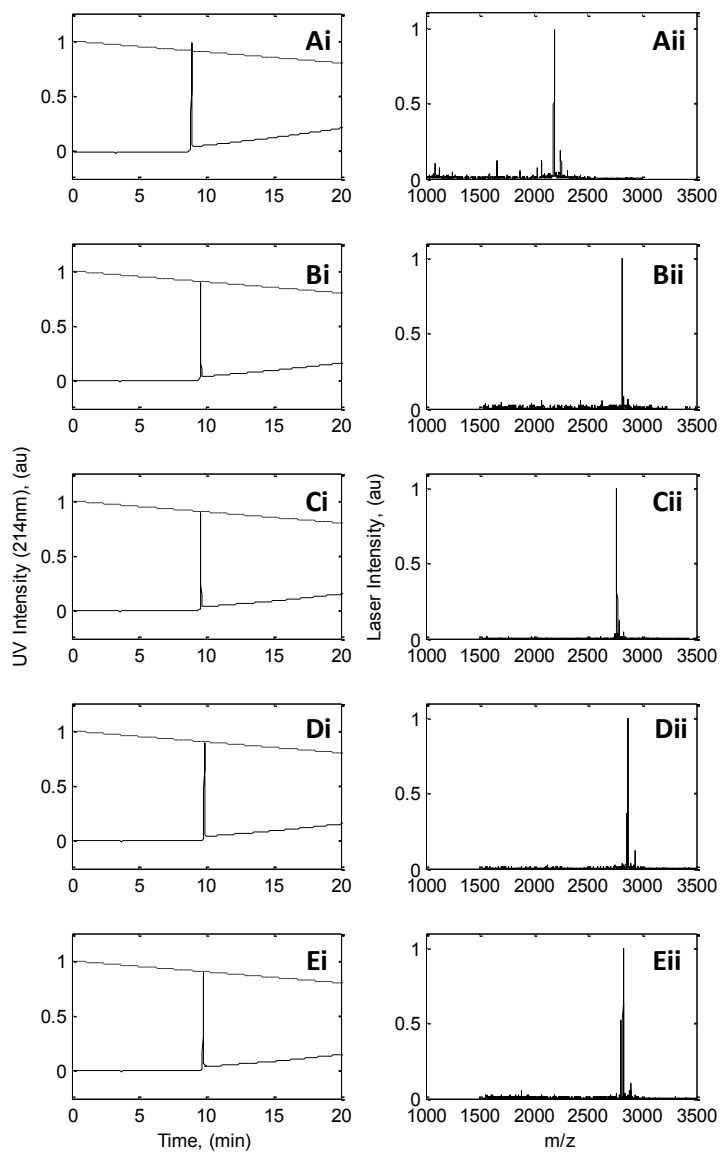


Figure A4.2. HPLC and MALDI TOF/TOF mass spectrometry, i and ii respectively, of purified peptide (RADA)₄-IKVAV (A), (RADA)₄-GPQG+IASQ-MVG (B), (RADA)₄-GPQG+PAGQ-MVG (C), (RADA)₄-GPQG+IASQ-DGGL (D), and (RADA)₄-GPQG+PAGQ-DGGL (E). Purities were determined to be above 95% by measuring the comparative areas under the major curve in the HPLC spectra. Respective major peaks in the MALDI spectra are at 2182.4, 2812.01, 2765.95, 2866.98, and 2820.91 m/z, which reflect the theoretical molecular weights. All peaks were normalized to their respective maxima.

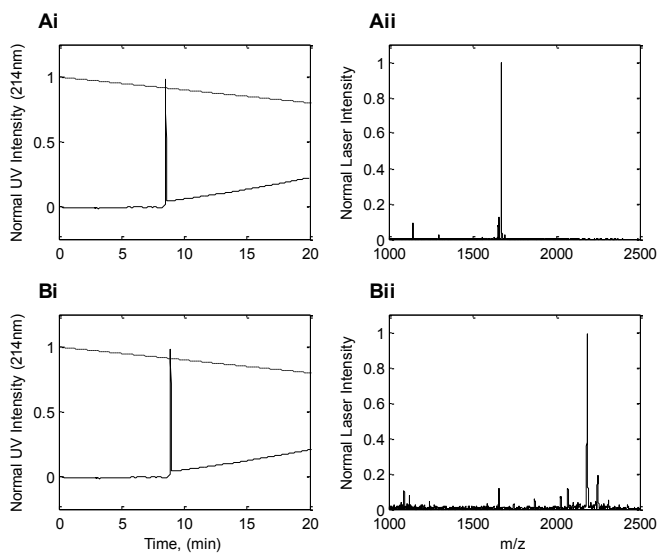


Figure A5.1. HPLC and MALDI TOF/TOF mass spectrometry, i and ii respectively, of purified peptide (RADA)₄ and (RADA)₄-IKVAV, shown in A and B, respectively. Purities are above 95% and major peaks in the ms are at 1671.8 and 2182.4 m/z, which reflect the theoretical molecular weights. All peaks were normalized to their respective maxima.

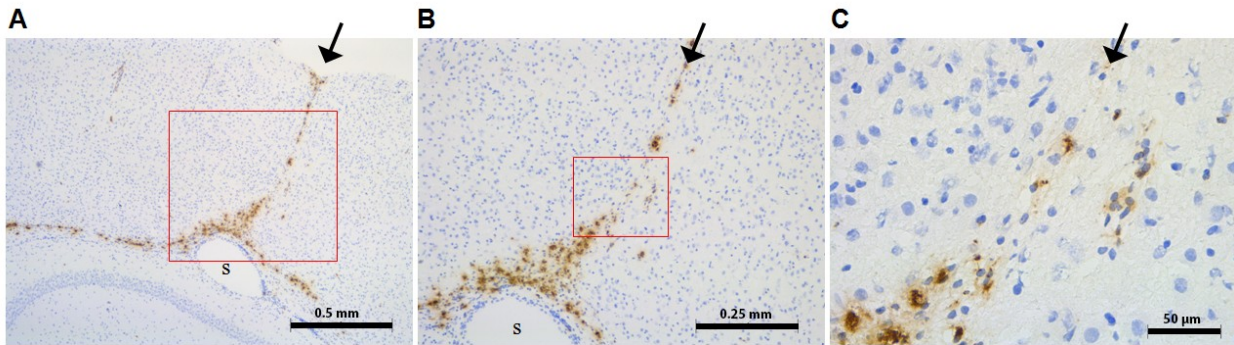


Figure A5.2. Representative image for the histological analyses. The areas of interest were located under 5X (A) and (B) 10X magnification to ensure the location of the injection tract and site. The final image for analyses were taken at 40X magnification (C). The red boxes indicate the area that was magnified in the following sections. S = site of injection. Arrows refers to the injection tract. Scale bars are (A) 0.5 mm, (B) 0.25 mm, and (C) 50 μm . Tract is immunolabeled by CD68.

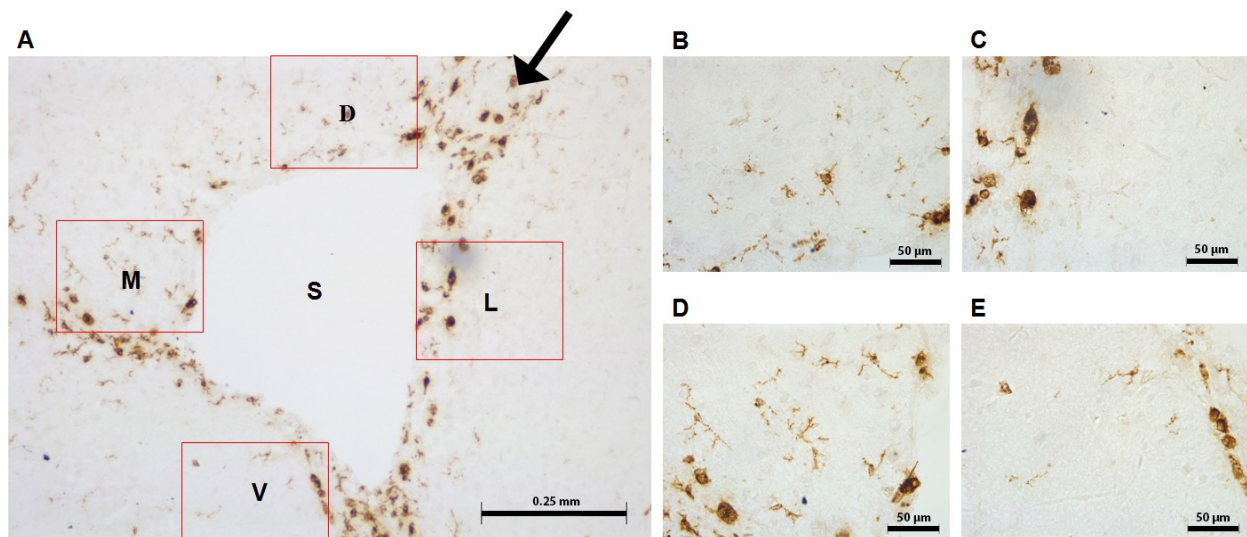


Figure A5.3. Representative images for histological analyses. Areas of interest are located at 10X magnification and centered in the field of view (A). Positive cells are counted at 40X magnification in 4 areas surrounding the injection site. The areas are dorsal (B), lateral (C), medial (D), and ventral (E) to the injection site. Red boxes indicate positions where images were taken at 40X for counting. S = site of injection, D = dorsal, L = lateral, M = medial, V = ventral. Arrow represents the injection tract. Scale bars are (A) 0.25 mm and (B-E) 50 μm . Tract is immunolabeled by CD68.

Appendix B - MATLAB Code

```

% Hausdorff Dimension MATLAB Code

close all;
clc; clear;

% Load Function

I = imread('inputImage.jpg');

% These function are theshold, fill, and edge functions to be used at
% discretion is image requires contour tracing to these degrees
% These are embedded in the function as well so disable them here or in the
% function body
% Particularly difficult images were made negative by Adobe Photoshop®

% B = im2bw(I, graythesh(I)); % Disabled
% F = imfill(B, 'holes'); % Disabled
% E = edge(double(F)); % Disabled

% Hausdorff Dimension is HD
% fractalF is a function to find the hausdorff dimension via the box counting
method
% by French P.
% email: p.french@ee.ucl.ac.uk
% web: www.ee.ucl.ac.uk/~pfrench
% retrieved from:
% http://www.mathworks.com/MATLABcentral/fileexchange/15918-hausdorff-
dimension-by-the-box-counting-method

[x,y,p,BF,x2,y2,p2,BF2,HD] = fractalF(E);

% The function is as follows

%%%%%%%%%%%%%
% this is used to find the hausdorff dimension via the box counting method
% email: p.french@ee.ucl.ac.uk
% web: www.ee.ucl.ac.uk/~pfrench
%%%%%%%%%%%%%

Function fractalF(p)

clear
clc
table = [,2];

% load up original image and convert to gray-scale
% p = imread('inputImage.jpg'); % Disabled; this can be loaded internally
%p = rgb2gray(P);

figure(1)
imshow(p)

```

```

% detect the edge of image 'p' using the Canny algorithm
% this gives edge as 'e2'
bw = im2bw(p, graythresh(p));
e = edge(double(bw));
fi = imfill(bw, 'holes');
op = imerode(fi, strel('disk',4));
e2 = edge(double(op));
figure(2)
imshow(e2)

% once we have e2, set up a grid of blocks across the image
% and scan each block to see if the edge occupies any of the blocks.
% If a block is occupied then flag it and record it in boxCount --
% store both size of blocks (numBlocks) and no of occupied boxes (boxCount)
% in table()
Nx = size(e2,1);
Ny = size(e2,2);

for numBlocks = 1:25

    sizeBlocks_x = floor(Nx./numBlocks);
    sizeBlocks_y = floor(Ny./numBlocks);

    flag = zeros(numBlocks,numBlocks);
    for i = 1:numBlocks
        for j = 1:numBlocks
            xStart = (i-1)*sizeBlocks_x + 1;
            xEnd = i*sizeBlocks_x;

            yStart = (j-1)*sizeBlocks_y + 1;
            yEnd = j*sizeBlocks_y;

            block = e2(xStart:xEnd, yStart:yEnd);

            flag(i,j) = any(block(:)); %mark this if ANY part of block is
true
        end
    end
    boxCount = nnz(flag);
    table(numBlocks,1) = numBlocks;
    table(numBlocks,2) = boxCount;
end

% from the above table of discrete points, take a line of best fit and plot
% the raw data (ro) and line of best fit (r-)
x = table(:,1); % x is numBlocks
y = table(:,2); % y is boxCount

p = polyfit(x,y,1);
BestFit = polyval(p,x);

figure(3)
hold on
grid on
plot(x,y, 'ko','LineWidth',1)

```

```

plot(x,BestFit, 'k-', 'LineWidth',2)
xlabel('Number of blocks, N', 'FontSize',12)
ylabel('Box Count, N(s)', 'FontSize',12)

% calculate Hausdorff Dimension
x2 = log(x);
y2 = log(y);

p2 = polyfit(x2,y2,1);
BestFit2 = polyval(p2,x2);

figure(4)
hold on
grid on
plot(x2,y2, 'bo', 'LineWidth',1)
plot(x2,BestFit2, 'b-', 'LineWidth',2)
xlabel('Number of blocks, log N', 'FontSize',12)
ylabel('Box Count, log N(s)', 'FontSize',12)

HausdorffDimension = p2(:,1)

% MADLI Product Formation MATLAB Code

clear; clc;
close all;

% Load data
Data0 = dlmread(InputFile.txt);

% This variable sets the cut-off for the filter
windowSize = 5;
% This variable is determined by the size of the data
S = size(Data0);
Product0 = []; Standard0 = [];
% Set ranges here based on locations in raw data
range1 = XXXX; range2 = XXXX; range3 = XXXX; range4 = XXXX;
rangeA = range1:0.001:range2; rangeB = range3:0.001:range4;
ProductA = []; StandardA = [];
% The code sorts through any columns of data
for n = 1:2:S(2)-1
    Product0X = []; Standard0X = [];
    Product0Y = []; Standard0Y = [];
% This code sorts out the data based on the expected isotopic envelopes
for m = 1:S(1)
    X = Data0(m,n);
    Y = Data0(m,n+1);
if X >= range1 && X <= range2
    Product0X = [Product0X;X];
    Product0Y = [Product0Y;Y];
else
end
if X >= range3 && X <= range4
    Standard0X = [Standard0X;X];
    Standard0Y = [Standard0Y;Y];

```

```

else
end
end
% This code filters and curve fits the collected data, then organizes it
% and calculates the area under the respective curves
    StandFilt = filter(ones(1,windowSize)/windowSize,5,Standard0Y);
    StandSpli = spline(Standard0X,StandFilt,rangeB)';
    Standard0 = [Standard0, StandSpli];
    StandardA = [StandardA; trapz(rangeB,StandSpli./max(StandSpli))];
    ProdFilt = filter(ones(1,windowSize)/windowSize,5,Product0Y);
    ProdSpli = spline(Product0X,ProdFilt,rangeA)';
    Product0 = [Product0, ProdSpli];
    ProductA = [ProductA; trapz(rangeA,ProdSpli./max(StandSpli))];
end

% Plots the example
figure;
subplot(3,1,1)
plot(Data0(:,1),Data0(:,2)/max(Data0(:,2)));
xlabel('m/z'); ylabel('Intensity'); xlim([1500 3000]);
title('MALDI TOF/TOF ms of (RADA)_4-GG-GPQG with +8 Standard')
subplot(3,1,2)
plot(Data0(:,1),Data0(:,2)/max(Data0(:,2)), 'r-');
xlabel('m/z'); ylabel('Intensity'); xlim([2124 2140]);
title('MALDI TOF/TOF ms of (RADA)_4-GG-GPQG with +8 Standard Unsorted and
Unfiltered')
subplot(3,1,3)
plot(rangeA',Product0(:,1)/max(Product0(:,1)), 'k-
',rangeB',Standard0(:,1)/max(Product0(:,1)), 'k-')
xlabel('m/z'); ylabel('Intensity');
title('MALDI TOF/TOF ms of (RADA)_4-GG-GPQG with +8 Standard with Sorting and
Filtering')

% Calculates the percent product
Percent = 100 * StandardA(1) / ProductA(1)

```

Appendix C - Supplemental Methods

1. Peptide Synthesis

1.1. Overview

Solid phase peptide synthesis was used to produce peptides by standard 9-fluorenylmethoxycarbonyl (Fmoc) chemistry. In this type of chemistry the alpha nitrogen of the amino acids is protected with the base labile Fmoc group and the side chains are protected with acid labile groups based on a trityl (triphenylmethyl) group. The N-protected amino acid residue is anchored via its carboxyl group to an amino acid resin to yield an amide linked peptide that ultimately produces a C-terminal amide peptide. After coupling, the excess reactants are removed by filtration and washings. The N-terminal protecting group is removed (deprotection) allowing the addition of the next N-protected amino acid by activation of its α -carboxylic acid (coupling). During these operations, side-chain functional groups of amino acids must be masked with protecting groups that are stable in the reaction conditions used during peptide elongation. The peptide is assembled from the C-terminus to the N-terminus (C \rightarrow N) by repetitive cycles (deprotection/coupling) until the desired sequence of amino acids is obtained. At the end, the peptide is cleaved from the resin and the side chain protecting groups removed. Peptide synthesis involves numerous repetitive steps resulting in excess reagents and side chains separated from the growing and insoluble peptide simply by filtration and washings, and all the synthesis steps can be performed in the same vessel without any transfer of material.

All methods outlined below were developed by Applied Biosystems® for use with the model ABI 433A peptide synthesizer. The materials, techniques and sequence of events adhered to, or were modified from, the following manual: Applied Biosystems. ABI 433A peptide synthesizer user guide. 2004 March;1.

1.2. Materials

N-dimethylformamide (DMF), Acetonitrile (ACN) (99.8%), pyridine (99.8%), potassium cyanate (KCN) (96.0%), ninhydrin (97%), methanol (MeOH) (99.8%), 1-2 ethandithiol (98%), dimethyl sulphide (99%), N,N-dimethylformamide (99.8%), dichloromethane (99.8%), N,N-diisopropylethylamine (99.5% biotech. grade), piperidine (99.5% biotech. grade), 1-cyano-2-ethoxy-2-oxoethylidenaminoxy)dimethylamino-morpholino-carbenium hexafluorophosphate (COMU) (97%), ethyl (hydroxyimino)cyanoacetate (97%), trifluoroacetic acid (TFA) (99%), triisopropylsilane (99%), and α -cyano-4-hydroxycinnamic acid (HCCA) were all purchased from Sigma (Oakville, ON). N-methyl pyrrolidone (NMP) was purchased from Applied Biosystems (Burlington, ON). Ethanol (EtOH) (95%) was purchased from the University of Alberta Biological Stores. Loaded wang resins and Fmoc amino acids were from ChemPep (Wellington, FL). All other reagents were of the highest quality available.

1.3. Fmoc Amino Acid Cartridge Preparation

Fmoc amino acids were weighed on wax paper in 10 X the required molarity (0.1 mmol). Dry fmoc amino acids were poured into cartridges using folded wax paper, freshly capped, and sealed with a capping tool. The metal septum tabs were removed from the cartridge top. The pusher block was moved to the far left and latch secured. An empty cartridge was placed in the first position in the guideway (under the needles), which was ejected at the cycle beginning as the first step. Amino acid cartridges were placed left to right, N to C-terminal next to the empty first cartridge, with the amino acid label facing outside and barcode facing the instrument. As preloaded resins were used, the C-terminal amino acid was on the resin. The amino acid in the cartridge after the empty first cartridge then represents the amino acid just before the C--terminal

amino acid. The pusher block was placed against the cartridges. The barcode scan function was not used in this synthesis procedure.

1.4. COMU/Oxyrna Preparation

0.45 M COMU / Oxyrna / DMF solutions were prepared by weighing out 0.5 M dry reagents, being 21.17 g COMU and 8.14 g Oxyrna per 100 mL DMF, and poured into the 450 ml bottle. The bottle was recapped and shaken until COMU/Oxyrna was dissolved. The increased volume due to COMU and Oxyrna reduces the concentration from 0.5 M to 0.45 M. The Bottle 5 delivery line was thoroughly dried with a kimwipe. A new, polyethylene, reagent line filter was attached onto the end of the Bottle 5 delivery line every change of solvents. A bottle seal was also replaced every time and Bottle 5 was screwed into the ratchet cap on the peptide synthesizer. The stability of the 0.45M COMU/Oxyrna/DMF remains constant at room temperature up to 6 weeks from manufacturer testing. The solution turned yellow after a few days, which does not have any adverse affect on the chemistry.

1.5. Preparing N-diisopropylethylamine (DIEA)

2.0 M DIEA was used. This was diluted in NMP accordingly. This was placed in Bottle 7. A bottle seal needs to be replaced each time this is topped up.

1.6. Other Reagents

Make certain the COMU/Oxyrna, DIEA, piperidine, methanol (MeOH), NMP, DMF are topped up to allow for full synthesis. Respectively, cycles for full bottles are approximately 50, 65, 225, N.A., 120, N.A., where N.A. almost negligible. All bottle should be checked during repeated synthesis. All bottle seals should be replaced during any reagent top ups.

1.7. Loading the Reactor Vessel (RV)

Loaded resin was measured out on wax paper based on the following calculation: Molar Scale (0.10 mmol) / Resin Molar Loading (mmol/g) = Mass in RV (g). Select the scaled RV (0.1 mmol, 8 ml). The RV was held in a vertical position and placed in a RV filter on the protruding “knife-edge” found inside the openings on both ends of the RV. The filter formed a seal with the knife edge as the RV caps were screwed in place. The caps were tightened until a firm resistance was felt, indicating that a seal has formed between the filter and the knife edge. This was visually checked by looking through the open end of the RV, observing a flat and smooth filter shape, with no protrusions beyond the knife edge. The appropriate amount of resin was added to the RV. The filter was placed on the knife edge of the open end of the RV and the screw was tightened on the cap. The RV was placed in the RV holder.

1.8. FastMoc Cycles Chosen:

Loaded Resin - NMP Washes - D

Each Residue - Double Couple (DC) - BADEIADEF

Loaded Resin - Final Deprotection - BIDc

The modules are briefly summarized:

Module A - Dissolving Amino Acid, Time = 7.6 minutes

At the beginning of module A, the old cartridge was ejected and the new cartridge was advanced.

NMP (2.1g) and 0.9 mmol of 0.45 M COMU/Oxyma in DMF (2.0 g) were added to the

cartridge. The amino acid was dissolved via mixing for 6 minutes. COMU was completely removed by flushing with NMP and nitrogen dried.

Module B - Piperidine Deprotection, Time = 2.9 minutes

This module began with one NMP resin wash. 22% piperidine/ NMP solution was introduced and allowed for a 2 minute deprotection. The RV was drained and a second treatment with a 22% piperidine solution was performed. The valve blocks were then thoroughly rinsed. Deprotection continued for an additional 7.6 minutes during module A.

Module D - NMP Washes, Time = 2.5 minutes

The RV was drained and the resin was washed 4 times with NMP.

Module E - Add DIEA and Transfer to RV, Time = 2.1 minutes

At the beginning of the module, 1 ml of 2 M DIEA in NMP was added to the cartridge, to initiate the activation of the amino acid. The activated amino acid solution was then transferred from the cartridge to the RV.

Module F - Clean Cartridge, Couple, Drain and NMP Washes, Time = 9.3 minutes

The amino acid cartridge was washed 2 times with NMP. This NMP is transferred to the Activator Vessel and for later modules to wash the resin in the RV. Coupling occurred during cartridge washing, and continued for another 4.5 minutes. The RV was drained and the resin was washed with the NMP from the Activator Vessel. In this module, step # 22 was changed from time 9 to Time 40 to increase the coupling time to 15.5 minutes.

1.9. Ninhydrin Quality Control

Quality control was routinely assessed with ninhydrin. Each test tube was weighed to the nearest tenth of a milligram, and then 2–3 ml MeOH was added. 2–3 drops of acetic acid was then added. After the synthesis, MeOH was used for washing. As such, resin off the side of the tube was rinsed with MeOH, the liquid was removed with a pipette upon resin settling, the resin was washed once with MeOH and the liquid was removed again with a pipette, the remaining MeOH was vacuum aspirated as the test tube was gently tilted and gently. The test tubes were dried in a centrifugal vacuum evaporator for one hour. The dried resin samples were weighed in each test tube to the nearest 0.1 mg. Using a Pasteur pipette, Ninhydrin reagents were added to the blank (empty tube) and samples. The following proportions were applied:

Monitor 1: Phenol (3.2g/ml) / EtOH ~ 75 μ l

Monitor 2: KCN (0.2mM) / Pyridine ~ 100 μ l

Monitor 3: Ninhydrin (0.5mg/ml) / EtOH ~ 75 μ l

The test tubes were then incubated in a heating block at 100°C for 5 minutes. When the heating was finished, the tubes were removed and 4.8 ml of 60% EtOH was immediately added for a final volume of 5 ml. The tubes were vortexed to mix the solution thoroughly. The resin was allowed to settle to the bottom of the tubes. 60% EtOH was used to zero a spectrophotometer. The absorbance of each sample was read (and the blank) at 570 nm. The sample was pipetted into the cuvette. The μ mol/g of amine was calculated as follows:

$$\mu\text{mol/g} = \frac{[\text{Abs sample} - \text{Abs blank}] \times \text{dilution (mL)} \times 10^6}{[\text{Extinction coefficient} \times \text{sample weight (mg)}]}$$

Where the dilution is 5 ml and the extinction coefficient is $1000 \text{ m}^{-1}\text{cm}^{-1}$. The percent coupling was calculated as follows:

$$\% \text{ coupled} = [1 - \text{amine } (\mu\text{mol/g})] / [10^3 \times \text{Resin Molar Loading (mmol/g)}] \times 100$$

Where the resin molar loading is given per resin by the supplier.

1.10. Cleavage Cocktail

A filter was prepared to retain the resin particles either by placing a polypropylene frit into a disposable polypropylene syringe. The filter was clamped over a round-bottom flask containing at least a 10-fold excess of cold ($-20 \text{ }^\circ\text{C}$) diethyl ether. A cleavage cocktail of (84/2/2/2/10) TFA, H_2O , and triisopropylsilane, 1-2 ethanedithiol, and dimethyl sulphide was added dropwise to the filter. The support was rinsed with a small volume (5 ml) of cleavage cocktail. The ether was then chilled in ice bath overnight. The precipitate was collected by centrifugation. Wash the precipitate at least three times with cold ether to remove any residual scavengers. The peptide was dissolved in glacial acetic acid, frozen, and lyophilized.

1.11. Peptide Purification

Self-assembling peptide were made soluble in 35% DMF and diluted until solution is clear. These were loaded onto a 5 ml rheodyne loop of a liquid chromatography system at 5 mL/ min flow. A Zorbax Eclipse C18 reverse-phase semi-preparative 9.4 x 250 mm column (Agilent Technologies) was used with a 1%/min H_2O -ACN (0.1%TFA) loading. Larger columns are recommended for higher yields, if available. Outputs were collected every minute and analyzed by matrix-assisted laser desorption/ionization time of flight (MALDI-TOF/TOF) and high pressure liquid chromatography (HPLC) to determine pure fractions. These were frozen and

lyophilized. ABI 4800MALDI-TOF/TOF mass-spectrometry was used to assess sample masses. HCCA matrix concentrations of 10 mg/ml were suspended in 1:1 ACN:H₂O (0.1% TFA). Peptide solutions at 1 mg/ml were also dissolved in ACN:H₂O (0.1% TFA). 1 µl peptide solutions were spotted, allowed to dry, matrix solutions were spotted on these, and also allowed to dry. Samples were assessed using HPLC with a Luna C18 reverse phase 4.6 x 250 mm column and a 1 ml/min 2%/min H₂O-ACN (0.1%TFA) loading. Samples were loaded into HPLC vials at 1 mg/ml, dissolved in ACN:H₂O (0.1% TFA) and injected at 20 µl. These parameters were varied accordingly to enhance the signal to noise ratio.

2.0. Transmission Electron Microscopy (TEM) Preparation

(RADA)₄ samples were pipetted, in 5ul aliquots, onto 200 mesh perforated formvar carbon coated copper grids (Ted Pella, Redding, CA). All samples were collected after 30 minutes of sonication. 5 µl of a 4% aqueous uranyl acetate stain was then applied to samples for 5 minutes. In between steps, sample and stain were filter-dried using filter paper wedges cut from Whatman filter paper pieces. The negative staining technique was after Dawes (1984). Grids were placed into the grid holder of a transmission electron microscope. All TEM was performed on a Philips FEI Morgagni transmission electron microscope.

3.0. MMP-2 Enzymatic Treatment

This is an adapted protocol from Chau *et al.*(2008).

Peptides were dissolved to 1.0% w/v in TNC buffer (50 mM TrisHCl, 150 mM NaCl, 1 mM CaCl₂, pH 7.4). These samples were sonicated for 30 minutes for break up nanofibers, and allowed to self-assemble for 24 hours at 4°C. All peptide samples were normalized using a basis of (RADA)₄ % w/v for all solution concentrations meaning they were weighed out in excess,

multiplied by the ratio of the (RADA)₄ modified peptide to (RADA)₄. Groups were centrifuged at 3000 RMP for 1 minute in an Eppendorf® microfuge. Half of the supernatant was removed and topped up with TNC buffer at least 10 times. The pH was routinely checked with the collected supernatant to assure a pH of 7.4. Following this, a 5:3 ACN:H₂O solution was added for to create a final 1:1 ACN:H₂O mixture. Depending on the starting volume the amount will vary. This was done to prevent self-assembly from creating error in non-uniform solutions when stock solutions are aliquoted. The larger volumes will reduce error and can be dried and re-suspended to the correct working volumes.

In these experiments, hydrogel samples of 10 µl were desired. The diluted peptide solutions were sonicated for 30 minutes and quickly aliquoted in 0.2 mL PCR Tubes. These were then vacuum dried (or lyophilized, if equipment is available). These tubes were filled with 7.5 µl MilliQ water and subsequently sonicated for another 60 minutes. To prevent confounds due to condensation or non-level fluid, these tubes were quickly spun down in a Corning LSE™ Mini Microcentrifuge at 2000 x g. These were allowed to self-assemble at 4°C for 24 hours. 2.5 µl of four times working concentration active MMP-2 was carefully pipetted onto the sample surface under cold-room conditions with a multi-pipetter to prevent error due to premature digestion. Samples were incubated at 37°C to initiate proteolysis. To halt the reaction, 75 µl ACN, 65 µl H₂O and 0.1% TFA solution was added to a final 150 µl volume. Half (5 µl) of this mixture was collected and added to a deuterated standard solution for quantitative MALDI-TOF assessment. The standard mixture was 100 µl H₂O, 0.1% TFA, and 5 µl of the 0.3 mg/ml deuterated standard (this needed to be optimized depending on conditions). These solutions were sonicated briefly and 1 µl was spotted onto a 4800 compatible MALDI plate. HCCA matrix concentrations of 10 mg/mL were suspended in 1:1 ACN:H₂O (0.1% TFA). The product was determined by the

trapezoidal rule, upon filtering and curve fitting the data with a spline, and then comparing the area under the curve of the product (2122 - 2130 m/z) and standard (2132 - 2140 m/z) isotopic envelopes. This should also account for the baseline of the data. MatLab (The MathWorks®) functions used were filter, spline, and trapz. Concentrations were determined by back calculating from the known molarity of the standard.

4.0. 2D PC-12 Cell Culture Preparation

4.1. Materials

The PC-12 cell strain originated from ATCC (Manassas, VA); cells were processed and cultured according to the supplier's product sheet PC-12 (ATCC® CRL-1721™). Under all conditions, culture medium refers to complete growth medium, which was composed of 80% v Advanced RPMI, 10% v Horse Serum (HS), 5% v Fetal Bovine Serum (FBS), 2.5% v 200mM l-glutamine, 2.5% 10 m v g/ml penicillin/10 I.U, streptomycin (Sigma Aldrich, Burlington, ON). Cells were housed in liquid nitrogen in vials containing 1.5ml aliquots of 5×10^5 to 1×10^6 viable cells/ml.

4.2. Culture and Coatings

Frozen cell inoculums were rapidly thawed in a water bath at 37°C for approximately 2 minutes. Vials were removed from the water bath, sprayed with 70% ethanol to reduce contamination and carried into a biosafety laminar-flow hood where further operations were carried out under aseptic conditions. Biosafety hoods were sterilized by UV exposure for 30 minutes. The contents of vials were transferred into 50 ml falcon tubes with 9 ml of culture media and centrifuged at 200 x g for 5 minutes. The supernatant was removed and discarded leaving a pellet at the bottom. 5 mls of fresh culture medium was added to the falcon tube. The

pellet was suspended by aspirating cells 4 or 5 times through a 20 ml syringe equipped with a 22 gauge needle. The cell suspension was transferred into 150 cm², Corning® T-150 flasks (catalog #430825) containing 25 ml of media and incubated at 37° in 5% CO₂air atmosphere.

Cells were allowed to reach a density of 2-4 x 10⁶ viable cells/ml before subculturing.

Subcultures of cells used for study were expanded in 75 cm², Corning® T-175 flasks (catalog #431464) each containing 10 -15 mls of media. Cell suspensions were processed as above in terms of centrifugation, aspiration, and incubation prior to being seeded into culture. Appropriate aliquots of cell suspension was added to the flasks with medium seeded at 5 x 10⁵ to 1 x 10⁶ viable cells/ml or use subcultivation ratio of 1:2 to 1:4. Culture vessels were placed in an incubator at 37°C in 5% CO₂air atmosphere. Further subculture passage occurred when cell density reached between 2-4 x 10⁶ viable cells/ml. The media was renewed every 2 to 3 days. Cells were passaged 4 times before discarding.

Cell viability was routinely assessed by first centrifuging cells 200 x g for 5 minutes, flushing pellets with fresh media through a 20 ml syringe with a 22g needle, then staining them with 1:1 trypan blue (0.4%)/cell suspension. The mixed solution was mounted into a BIO-RAD TC10 dual chamber counting slide, and inserting the slide into a BIO-RAD TC10 Automated Cell Counter. A viability of 80% live counted cells was acceptable for seeding.

Many different cell types have been shown to bind to ECMs. One ECM provided was Collagen IV; PC-12 cells attach and change their behaviour in the presence of collagen IV. Collagen was handled according to Sigma-Aldrich (Oakville, ON) product sheet human placenta Bornstein and Traub Type IV Collagen (catalogue number C5533). The powder was dissolved in sterile 0.2% acetic acid at a concentration of 2mg/ml at room temperature. This mixture was further diluted 1:10 in sterile Milli-Q water and stored at 4°C until use. 24-transwell tissue

culture plates were coated under aseptic conditions by dispensing 100ul of collagen into each well, which left to sit for 1h. The solution was aspirated and the uncovered plates were exposed to UV for 30 min. Tissue culture plates were left to dry overnight (for 14 to 18 hs) in the BioSafety Hood, covered, and stored at 4°C until needed. Before use, each well was rinsed twice, at 10 min intervals, with 500 ul of sterile PBS.

An emulated ECM was provided in the form of (RADA)₄ mixtures. 1 % (w/v) (RADA)₄ mixtures in H₂O were sonicated for 60 minutes and 20 µL was pipetted into each well of a 24-well culture plate. Carefully, 80 µl of modified TNC buffer was added and incubated for 24 hours at 4° C. Buffer was aspirated and wells were washed with 200µL of advanced RPMI three times before addition of cells. Cells were seeded onto SAP scaffolds 200 µl volumes at 5×10⁴ cells / ml. Seeding was repeated two more times, with a 1 hour period between and set to rest overnight before an experiment.

4.0. 2D Microglia Cell Culture Preparation

4.1. Materials

Lidocaine HCl was all purchased from Sigma (Oakville, ON). Loaded wang resins and Fmoc amino acids were from ChemPep (Wellington, FL). Horse serum (HS), fetal bovine serum (FBS), Dulbecco's modified Eagle Medium/Ham's F-12 (DMEM/F-12, 1:1), Hank's balanced saline solution (HBSS), 0.25% trypsin/EDTA, and penicillin/streptomycin were from Gibco (Life Technologies, Burlington, ON).

4.2. Culture and Coatings

According to Siao and Tsirka (2007), mixed glial cultures were used to isolate rat microglia after 2 weeks incubation at 37°C. In male postnatal day 1-2 Sprague-Dawley rat pups, whole brains were removed and dissected. The meninges were removed and the collected tissues were dissociated by trypsin and mechanically triturated. Following this, cultures of mixed cell types were grown in 75 cm² flasks coated with poly-L-lysine. Cells were sustained in basal media with a 1:1 of Dulbecco's modified Eagle medium : Ham's F-12 supplement and supplemented with 200 U/mL penicillin, 200 µg/mL streptomycin and 10% FBS in a 37° C, 5% CO₂ humidified incubator. After 2 weeks, cells were assessed for confluence, and microglia were isolated. This included a 10 minute 15 mM lidocaine treatment in DMEM/F-12 with 20 mM HEPES to buffer the media outside the incubator. This was followed by 5 minutes rocking (100 rpm at 37° C). These cells were DMEM/F-12 washed prior to plating in 24 well plates. Microglia were then treated with glial conditioned basal media for 16 hours. This was done to promote recovery from the isolation procedure and improved adhesion. Media with DMEM/F-12 supplemented with 1% FBS was used for the duration of all experiments. Immunofluorescence microscopy was used to

determine microglia purity ($\geq 95\%$) via microglia-specific markers (IBA1) and were compared to total nuclear staining (Hoechst). The Animal Care and Use Committee, The University of Alberta, Health Sciences, approved all animal procedures.

1 % (w/v) (RADA)₄ was made soluble in 18 MΩ reverse osmosis H₂O by 60 minutes of sonication. 20 μL per well was then pipetted into 24-well plates. TNC buffer was added in 180 μL increments and incubated for overnight at 4° C. Buffer was removed from all wells. They were subsequently washed with 500 μL of DMEM/F-12X 3 before pipetting cells. Microglia at 1×10^6 cells / ml was added in 0.5 mL increments for SAP scaffolds and poly-L-lysine seeding. All assays were performed 24 hours upon seeding.